



University
of Glasgow

Mulligan, Andrew (2004) *Studies of model adsorbate systems*. PhD thesis.

<http://theses.gla.ac.uk/4872/>

Copyright and moral rights for this thesis are retained by the author

A copy can be downloaded for personal non-commercial research or study, without prior permission or charge

This thesis cannot be reproduced or quoted extensively from without first obtaining permission in writing from the Author

The content must not be changed in any way or sold commercially in any format or medium without the formal permission of the Author

When referring to this work, full bibliographic details including the author, title, awarding institution and date of the thesis must be given

Studies of Model Adsorbate Systems

by

Andrew Mulligan

A thesis presented in partial fulfilment for the degree of Doctor of Philosophy
in the Faculty of Science of the University of Glasgow

Chemistry Department

December 2004

©Andrew Mulligan

Abstract

In the first part of this thesis we perform the first structural study to examine the interaction of furan and tetrahydrofuran (THF) on Cu(111), using Normal incidence X-ray standing wavefield absorption (NIXSW) and temperature programmed desorption (TPD). NIXSW experiments showed THF adopts an atop adsorption site, with furan adopting a displaced atop site. We attribute the displaced adsorption site of furan to the effects of adsorbate-adsorbate interactions, the magnitude of which are significant in comparison to the strength of the furan-copper interaction. Finally, we note that the adsorption of THF on Cu(111) is significantly stronger than that observed for furan. We attribute this observation to the effects of C-H...Cu interactions between THF and the copper surface.

The study of adsorbates on the Cu(111) surface was continued by an extensive study of the interaction of crotonaldehyde, butaldehyde, crotyl alcohol and 1-butanol and the effects upon adsorption induced by the presence of atomic sulphur and the sulphur containing moiety methyl thiolate. This work began by initial characterisation of the adsorption of sulphur and dimethyl disulphide (DMS), which subsequently forms methyl thiolate, on Cu(111). X-ray photoelectron spectroscopy (XPS), ultraviolet photoelectron spectroscopy (UPS) and low energy electron diffraction (LEED) observations are consistent with those of previous work for both the S/Cu(111) and DMS/Cu(111) systems. Work function measurements performed during sulphur adsorption show that with increasing sulphur work function initially increases linearly up to formation of the $(\sqrt{7}\times\sqrt{7})R19.1^\circ$ structure, where we observe a sudden increase. We propose these observations to be consistent with initial development of a CuS like structure prior to $(\sqrt{7}\times\sqrt{7})R19.1^\circ$ formation. Upon $(\sqrt{7}\times\sqrt{7})R19.1^\circ$ formation the surface undergoes significant surface reconstruction and this is signalled by the sudden increase in work function.

Work function measurements of methyl thiolate adsorption on Cu(111) show the opposite effect to that induced by sulphur. We observe a linear decrease in work function with increasing coverage up until a decrease of 1.8 eV at methyl thiolate saturation. These observations are consistent with a strong molecular dipole associated with the molecule being orientated anti-parallel to that of the surface dipole causing a reduction in magnitude of the surface dipole and therefore of work function. This hypothesis is consistent with the results of previous theoretical work.

Finally, we perform the first TPD measurements of the desorption of DMS from Cu(111). We observe desorption of DMS multilayers at 154 K followed by no further desorption products until dissociation of methyl thiolate. Dissociation is observed to take place between 325 and 475 K with desorption of methane and ethane observed. Following desorption we observe atomic sulphur to remain on the surface but no dissociated carbon.

In TPD experiments on the clean Cu(111) surface we observe the adsorption of crotonaldehyde and butaldehyde to be molecular and reversible, while that of crotyl alcohol and 1-butanol results in a small amount of dissociation. We propose the adsorption of each of the molecules can be interpreted by use of an electrostatic model involving the interaction of the surface dipole and that associated with the molecule. In the presence of atomic sulphur, at any surface coverage, the dissociation of crotyl alcohol and 1-butanol is inhibited, with sulphur acting in a site blocking mechanism. In addition, the presence of sulphur results in an increase in magnitude of the surface dipole resulting in an increased interaction between the molecule and the surface. To maximise this effect, orientation changes of the adsorbed molecules are also observed. The greatest effect is observed to take place on crotonaldehyde, which we attribute to crotonaldehyde having the largest dipole moment.

In the presence of methyl thiolate we observe significantly different results. Methyl thiolate is observed to produce no significant effect on the stability of either crotonaldehyde or butaldehyde adsorption. However, the adsorption of crotyl alcohol and 1-butanol is completely destabilised in the presence of methyl thiolate. These observations are attributed to the effects of hydrogen bonding between the alcohol molecules and the methyl group resulting in preferential adsorption on the methyl thiolate rather than the copper surface followed by nucleation to form multilayers. Further to our proposed electrostatic model we also propose a reaction mechanism consistent with both our own results and those of catalytic work to explain the increased selectivity to crotyl alcohol formation during hydrogenation of crotonaldehyde on Cu catalysts.

In the second half of this thesis we turn our attention to the study of nanoscale aluminium oxide films grown on NiAl(110) using Al2p photoemission. Adsorption of oxygen at room temperature results in a predominately amorphous like Al₂O₃ phase.

However, in addition we also observe a small γ -like Al_2O_3 component. Annealing of this layer results in a change to a predominately γ -like Al_2O_3 structure followed by a change to α -like Al_2O_3 upon annealing to 1273 K. Adsorption of oxygen at 823 K results in formation of a γ -like Al_2O_3 layer, which once again transforms to α -like Al_2O_3 upon annealing to 1273 K. Significantly, we observe the α -like Al_2O_3 layers formed after annealing to contain significant amounts of metallic aluminium, which we attribute to either "pin holes" or segregated aluminium metal in the oxide layer. Further cycles of adsorption and annealing results in both additional oxide formation and the filling of vacancies in the α -like Al_2O_3 layer resulting in the layer becoming more aluminium rich. However, despite this we continue to observe the presence of "pin holes" or segregated aluminium metal in the oxide layer.

In the final chapter, we perform the first ever enantio-sensitive second harmonic generation (ES-SHG) measurements from the adsorbate-metal systems, 2-butanol/Cu(111) and 1-(1-naphthyl)ethylamine (NEA)/Cu(111). Using this new application of the surface second harmonic technique we show chiral discrimination of adsorbate layers can be achieved and enantiomeric excess monitored. In addition to this we show for the first time that the adsorbed chiral molecule, NEA, can reversibly imbue the electronic structure of the metal surface with chirality, without physically restructuring the metal surface atoms. This phenomenon is previously unobserved and has strong implications for the functionality of metal surfaces and enantioselective catalysis.

Contents

Abstract	i
Contents	iv
Acknowledgements	viii
Publications	ix
Acronyms and Abbreviations used in this Thesis	x

Chapter 1: Introduction

1.1	Introduction	1
1.2	References	3

Chapter 2: Theory

2.1	Introduction	5
2.2	Techniques	5
2.2.1	Temperature Programmed Desorption (TPD)	5
2.2.2	Surface Sensitivity of Electrons	6
2.2.3	Auger Electron Spectroscopy (AES)	8
2.2.4	X-ray Photoelectron Spectroscopy (XPS)	9
2.2.5	Ultraviolet Photoelectron Spectroscopy (UPS)	10
2.2.6	Low Energy Electron Diffraction (LEED)	12
2.2.7	Normal Incidence X-ray Standing Wavefield (NIXSW)	16
2.2.7.1	Adsorption Site Determination by Real Space Triangulation	20
2.2.7.2	Non-dipole Effects in NIXSW	23
2.2.8	Second Harmonic Generation (SHG)	24
2.3	References	

Chapter 3: Experimental

3.1	Introduction	35
3.2	Experimental (TPD/AES Chamber)	35
3.2.1	Obtaining UHV Conditions	35
3.3	Experimental Procedures for the TPD/AES Chamber	38

3.3.1	Sample Preparation	38
3.3.2	TPD	39
3.3.3	AES/LEED	41
3.3.3.1	RFA Electron Detection in LEED Experiments	41
3.3.3.2	RFA Electron Detection in AES Experiments	42
3.4	Experimental (UPS/XPS Chamber)	43
3.4.1	Obtaining UHV Conditions	43
3.5	Experimental Procedures for the UPS/XPS Chamber	46
3.5.1	Sample Preparation	46
3.5.2	General Experimental Procedures	49
3.5.3	XPS	49
3.5.4	UPS	50
3.5.5	CHA Electron Detection in UPS and XPS Experiments	52
3.6	Experimental (SHG Apparatus)	54
3.7	Experimental (SRS Station 6.3)	55
3.7.1	System Design	55
3.7.2	Experimental Procedures	56
3.8	Experimental (SRS Station 4.1)	57
3.8.1	System Design	57
3.8.2	Experimental Procedures	58
3.9	References	59

Chapter 4: TPD and NIXSW Investigation of Furan and Tetrahydrofuran Adsorption on Cu(111)

4.1	Introduction	60
4.2	Results	61
4.2.1	Initial Characterisation – TPD	61
4.2.2	NIXSW	65
4.3	Discussion	74
4.4	Conclusions	77
4.5	References	78

Chapter 5: Adsorption of Sulphur and Dimethyl Disulphide on Cu(111)

5.1	Introduction	79
5.1.1	Sulphur	79
5.1.2	Dimethyl Disulphide	82
5.2	Results and Discussion	85
5.2.1	Sulphur	85
5.2.2	Dimethyl Disulphide	95
5.3	Conclusions	103
5.3.1	Sulphur	103
5.3.2	Dimethyl Disulphide	104
5.4	References	105

Chapter 6: A Model Study of Crotonaldehyde Hydrogenation

6.1.1	Introduction	107
-------	--------------	-----

Part 1: The Adsorption of Crotonaldehyde and Related Molecules on Cu(111) and the Effects of Sulphur Co-adsorption

6.1.2	Results	112
6.1.2.1	Adsorption on Clean Cu(111) – TPD	112
6.1.2.1	UPS and XPS	118
6.1.2.3	Adsorption on S/Cu(111) Surfaces – TPD	123
6.1.2.4	UPS and XPS	132
6.1.3	Discussion	138

Part 2: Co-adsorption of Crotonaldehyde and Related Molecules with Methyl Thiolate on Cu(111)

6.2.1	Results	144
6.2.1.1	TPD	144
6.2.1.2	UPS and XPS	151
6.2.2	Discussion	163

Part 3: Summary of the Co-adsorption of Crotonaldehyde and Related Molecules with S and Methyl Thiolate on Cu(111)

6.3.1	Summary	167
6.3.2	Conclusions	173

Chapter 7: Growth of Nanoscale Aluminium Oxide Films on NiAl(110)

7.1	Introduction	176
7.2	Results	180
7.2.1	Room Temperature Adsorption	180
7.2.2	Effects of Annealing	188
7.2.3	Multiple Adsorption and Annealing Cycles	193
7.3	Discussion	202
7.4	Conclusions	212
7.5	References	214

Chapter 8: Enantio-Sensitive Second Harmonic Generation:- Developing a Unique Probe of Chiral Interfaces

8.1	Introduction	216
8.1.1	Enantiomer Sensitive Second Harmonic Generation (ES-SHG)	217
8.1.2	2-Butanol	221
8.1.3	1-(1-Naphthyl) Ethylamine	222
8.2	Results	223
8.2.1	Initial Characterisation – 2-Butanol	223
8.2.2	1-(1-Naphthyl) Ethylamine	229
8.2.3	Second Harmonic Generation – 2-Butanol	233
8.2.4	1-(1-Naphthyl) Ethylamine	238
8.3	Discussion	244
8.4	Conclusions	249
8.5	References	250

<u>Summary and Forward Look</u>	253
--	------------

Acknowledgements

I would like to thank my supervisor Dr Malcolm Kadodwala for his constant support and guidance during the course of my PhD. Without his constant help and dedication this project would not have been made possible. Likewise, I am indebted to both Gilles and Shona, my fellow PhD students, whose help and assistance was always forthcoming. Over the years, many project students have passed through our lab and helped perform experiments, namely Susan, Owain, Craig, Sarah, Dale, Marcus, Antti, Niall and Martin and I would like to thank all of them for their help.

Over the first two years of my PhD, some 13 weeks were spent at the synchrotron radiation source in Daresbury. I would like to express my gratitude to the staff involved with us during this time, Dr Vin Dhanak and George Miller whose advice and technical assistance proved invaluable. My thanks also go to the staff and students of the Nottingham University Nanoscience Group for some light relief from the daily grind of synchrotron work. It was reassuring to know some people spent more time at Daresbury than we did.

A great deal of thanks are also due to all of the academic and technical staff of the chemistry department. In particular I would like to extend my thanks to Dr David Lennon, Prof. David Jackson and Prof. John Winfield for helpful comments over the years. Additionally, advice and support has been much appreciated from John Gillan and Jim Bannon, Jarnail Bhumbra, William McCormack and Arlene Douglas and Stuart MacKay who have helped keep the project on track when things have failed.

Also invaluable in keeping the work on track have been Tim and Dave, Ali and Iain and Ewan and Iain who were always happy to help with the heavy lifting. Many thanks.

Many thanks to my long suffering family for their support over what seems to them like an age spent at university. It's much appreciated.

Last but certainly not least, I'd like to thank my friends from both in and out of the chemistry department who haven't had a mention already, Bev, David, Euan, Paula, Iain, Allon, Claire, Fiona, Gordon, Graeme, Andy, Martyn, Stoon, Chris, all the guys in or associated with the band(s) and the countless others I've probably forgotten to mention.

Publications

- ◆ Shona M. Johnston, Andrew Mulligan, Vin Dhanak and Malcolm Kadodwala
The structure of disordered chemisorbed oxygen on Cu(111)
Surface Science 519 (2002) 57

- ◆ Shona M. Johnston, Andrew Mulligan, Vin Dhanak and Malcolm Kadodwala
The structure of methanol and methoxy on Cu(111)
Surface Science 530 (2003) 111

- ◆ Shona M. Johnston, Andrew Mulligan, Vin Dhanak and Malcolm Kadodwala
The bonding of Acetone on Cu(111)
Surface Science 548 (2004) 5

- ◆ Andrew Mulligan, Shona M. Johnston, George Miller, Vin Dhanak and Malcolm Kadodwala
A TPD and NIXSW investigation of furan and tetrahydrofuran adsorption on Cu(111)
Surface Science 541 (2003) 3

- ◆ Andrew Mulligan, Ian Lane, Gilles B. D. Rousseau, Lutz Hecht, Shona M. Johnston, David Lennon and Malcolm Kadodwala
Chiral discrimination within disordered adlayers on metal surfaces
Chemical Communication (21) (2004) 2492

- ◆ Andrew Mulligan, Ian Lane, Gilles B. D. Rousseau, Lutz Hecht, Shona M. Johnston, David Lennon and Malcolm Kadodwala
Going beyond the physical: Instilling chirality on to the electronic structure of a metal surface
Accepted Angewandte Chem

- ◆ Andrew Mulligan, Vin Dhanak and Malcolm Kadodwala
A high resolution photoemission study of nanoscale aluminium oxide films on NiAl(110)
Submitted to Journal of Physical Chemistry

Acronyms and Abbreviations used in this Thesis

AES	Auger Electron Spectroscopy
AFM	Atomic Force Microscopy
ARUPS	Angle Resolved Ultra Violet Photoemission Spectroscopy
CAE	Constant Analyser Energy
CCD	Charge Coupled Device
CD	Circular Dichroism
CD-SHG	Circular Dichroism Second Harmonic Generation
CHA	Concentric Hemispherical Analyser
DMS	Dimethyl Disulphide
EELS	Electron Energy Loss Spectroscopy
ES-SHG	Enantio-Sensitive Second Harmonic Generation
FCC	Face Centred Cubic
HCP	Hexagonal Close Packed
HREELS	High Resolution Electron Energy Loss Spectroscopy
IMFP	Inelastic Mean Free Path
L	Langmuir ($1L = 1 \times 10^{-6}$ Torr exposure for 1s)
LD	Linear Difference
LD-SHG	Linear Difference Second Harmonic Generation
LEED	Low Energy Electron Diffraction
LEEM	Low Energy Electron Microscopy
LEIS	Low Energy Ion Scattering
ML	Monolayer
NEA	1-(1-Naphthyl) Ethylamine
NEXAFS	Near Edge X-ray Absorption Fine Structure
NIXSW	Normal Incidence X-ray Standing Wavefield
OA-SHG	Optically Active Second Harmonic Generation
ORD	Optical Rotation Dispersion
ORD-SHG	Optical Rotation Dispersion Second Harmonic Generation
QMS	Quadrupole Mass Spectrometer
RFA	Retarding Field Analyser
SH	Second Harmonic
SHG	Second Harmonic Generation
SNR	Signal-to-Noise Ratio
STM	Scanning Tunnelling Microscopy
THF	Tetrahydrofuran

THT	Tetrahydrothiophene
TPD	Temperature Programmed Desorption
TSP	Titanium Sublimation Pump
UHV	Ultra High Vacuum
UPS	Ultraviolet Photoelectron Spectroscopy
XPS	X-ray Photoelectron Spectroscopy

Chapter 1: Introduction

1.1 Introduction

The study of model adsorbate systems has been at the heart of surface science for many years. In the work presented here we continue this tradition using both well-established and new surface science techniques to examine a variety of adsorbate systems of current scientific interest. In the initial results reported here (chapters 4-6) we continue a programme of work undertaken in the Glasgow University Surface Science group examining small organic molecules on metal and semiconductor surfaces. This previous work has focussed on factors such as structure and bonding, aromaticity, reactivity and the effects of co-adsorbates [1-11] and we continue to focus on some of these topics here. In the following chapters (chapters 7 and 8), we turn our attention to the study of two topics of wide scientific interest, namely the growth and properties of nanoscale aluminium oxide layers and development of a new technique for the study of chiral adsorbate-metal systems.

In the first results chapter (chapter 4) we present work examining the bonding of both furan and tetrahydrofuran (THF) on Cu(111) using the TPD and NIXSW techniques. Practical interest in these systems lies in examining the mechanisms involved in the heteroatom removal process used extensively in the petrochemical industry [12] and from the electronics industry where heterocycles are being studied for use as conducting polymers [13]. In addition to this, the study allows us to compare the bonding of an aromatic heterocycle with its non-aromatic equivalent. This extends both our previous work on heterocycles and on the structure and bonding of oxygen containing species, allowing new insights into the adsorption mechanisms of the molecules on metal surfaces.

Chapters 5 and 6 continue our work studying the adsorption of organic molecules on the Cu(111) surface. In these chapters we examine the adsorption of crotonaldehyde and related molecules and study the effects upon their adsorption in the presence of sulphur and the sulphur-containing moiety, methyl thiolate. On transition metal catalysts, sulphur has traditionally been considered to have a poisoning effect on catalytic reactions [14,15], with its presence undesirable in catalytic experiments. However, recent work by Hutchings et al. [16-19] has demonstrated the promotional effects of sulphur during the selective hydrogenation

of crotonaldehyde to crotyl alcohol on copper catalysts. Additionally, previous work in our group has demonstrated promotional effects on the adsorption of organic molecules on Cu(111). In this study we aim to use surface science techniques to rationalise the results of these catalytic observations, while also probing the underlying mechanisms of our observations and comparing them with the work carried out in the lab previously.

Chapter 7 concerns the growth and properties of nanoscale aluminium oxide films on the NiAl(110) surface. These aluminium oxide films have been the topic of wide scientific interest due to their potential use in a wide range of applications. These include use in anti-corrosion and coating technologies and as insulating material in microelectronic devices. In addition to this, a great deal of interest has been focussed on their study for use as mimics of the Al₂O₃ support material used commonly in heterogeneous catalysis. Given the wide-ranging interest in these films, they have been the subject of extensive previous study, including the study of aluminium oxide growth on NiAl(110) [20-28]. However, despite this interest and the range of techniques that have been applied to the system, a number of properties of the films formed remain controversial. In particular, the homogeneity and phase of the oxides formed by differing preparation methods remains a topic of debate. Hence, in this study we use Al2p photoemission to study the resultant oxide films formed by a number of different preparation methods, studying the oxidation process from the initial stages through to the effects of multiple adsorption and annealing cycles. Using one technique to study the whole process and examining different preparation conditions we believe allows us to provide additional information to the work that has gone previously.

Finally, in chapter 8 we return to the study of organic molecules on the Cu(111) surface. However, we use a new application of the second harmonic generation (SHG) technique, enantio-sensitive-SHG (ES-SHG), to achieve chiral discrimination of adsorbate-metal interfaces. The study of chirality is a topic, which has received extensive attention due to the lucrative chemical industry, which utilises single enantiomers of chiral molecules in many products ranging from pharmaceuticals to colourings and flavourings. At present the main route to obtain particular enantiomers of molecules has been homogeneous asymmetric synthesis. However, production of single enantiomer products by enantioselective heterogeneous catalysis has showed some promise [29, 30]. In these experiments a conventional catalyst is modified by a chiral molecule (modifier) resulting in the product reflecting

the chirality of the modifier. However, at present only a qualitative understanding of the mechanism of this process exists. Previous surface science experiments attempting to study the process have been performed on model adsorbate systems. However, the range of problems that can be addressed have been limited by the need to use high-resolution STM images to achieve chiral discrimination. Unfortunately, however, high-resolution STM images cannot be obtained for transitionally disordered and complex overlayers, which are the conditions most relevant to catalytic systems. Hence, the development of a non-invasive, optical probe of surface chirality would be an ideal complement to existing STM techniques. In this chapter we present the first results obtained following development of the ES-SHG technique and demonstrate its potential usefulness in probing the mechanism of a chiral modifier on a metal catalyst.

1.2 References

- [1] P. Milligan, J. McNamarra, B. Murphy, B. C. C. Cowie, D. Lennon and M. Kadodwala, *Surf. Sci.* 413 (1998), 166
- [2] P. K. Milligan, B. Murphy, B. C. C. Cowie, D. Lennon and M. Kadodwala, *Surf. Sci.* 430 (1999), 45
- [3] A. Sotiropoulos, P. K. Milligan, B. C. C. Cowie, and M. Kadodwala, *Surf. Sci.* 444 (2000), 52
- [4] P. K. Milligan, B. Murphy, B. C. C. Cowie, D. Lennon and M. Kadodwala, *J. Phys. Chem. B*, 105 (2001) 140
- [5] S. M. Johnston, G. Rousseau, V. Dhanak and M. Kadodwala, *Surf. Sci.* 477 (2001) 163
- [6] P. K. Milligan, B. Murphy, B. C. C. Cowie, D. Lennon and M. Kadodwala, *J. Phys. Chem. B*, 105 (2001) 5231
- [7] G. B. D. Rousseau, V. Dhanak and M. Kadodwala, *Surf. Sci.* 494 (2001) 251
- [8] G. B. D. Rousseau, N. Bovet, S. M. Johnston, D. Lennon V. Dhanak and M. Kadodwala, *Surf. Sci.* 511 (2002) 190
- [9] S. M. Johnston, A. Mulligan, V. Dhanak and M. Kadodwala, *Surf. Sci.* 519 (2002) 57
- [10] S. M. Johnston, A. Mulligan, V. Dhanak and M. Kadodwala, *Surf. Sci.* 530 (2003) 111
- [11] S. M. Johnston, A. Mulligan, V. Dhanak and M. Kadodwala, *Surf. Sci.* 548 (2004) 5
- [12] E. Furimsky, *Appl. Catal.* 6 (1983) 159

- [13] A. Tsumura, L. Tossi, H.E. Katz, *Science* 268 (1995) 270
- [14] D.S. Newsome, *Catalysis Rev.-Sci. Eng.* 21 (1980) 275
- [15] C.T. Campbell and B.E. Koel, *Surf. Sci.* 183 (1987) 100
- [16] G.J. Hutchings, F. King, I.P. Okoye, M.P. Padley and C.H. Rochester, *J. of Catal.* 148 (1994) 464
- [17] G.J. Hutchings, F. King, I.P. Okoye, M.B. Padley, C.H. Rochester, *J. of Catal.* 148 (1994) 453
- [18] J.E. Bailie and G.J. Hutchings, *J. of Mol. Catal A: Chemical* 177 (2002) 209
- [19] J.E. Bailie, H.A. Abdullah, J.A. Anderson, N.V. Richardson, N. Hodge, J.G. Zhang, A. Burrows, C.J. Kiely and G.J. Hutchings *Phys. Chem. Chem. Phys.* 3 (2001) 4113
- [20] H. Isem and G. R. Castro, *Surf. Sci.* 211/212 (1989) 865
- [21] A. Y. Lozovoi, A. Alavi and M. W. Finnis, *Phys. Rev. Lett.* 85 (3) (2000) 610
- [22] A. Y. Lozovoi, A. Alavi and M. W. Finnis, *Comp. Phy. Comm.* 137 (2001) 174
- [23] R. M. Jaeger, H. Kühlenbeck, H. –J. Freund, M. Wuttig, W. Hoffmann, R. Franchy and H. Ibach, *Surf. Sci.* 259 (1991) 235
- [24] J. Libuda, F. Winkelmann, M. Bäumer, H. –J. Freund, Th. Bettrams, H. Neddermeyer and K. Müller, *Surf. Sci.* 318 (1994) 61
- [25] K. F. McCarty, *Surf. Sci.* 474 (2001) L165
- [26] M. B. Lee, J. H. Lee, B. G. Frederick and N. V. Richardson, *Surf. Sci.* 448 (2000) L207
- [27] T. T. Lay, M. Yoshitake and B. Mebarki, *J. Vac. Sci. Technol. A* 20 (6) (2002) 2027
- [28] M. Yoshitake, B. Mebarki and T. T. Lay, *Surf. Sci.* 511 (2002) L313
- [29] M.A. Keane and G. Webb, *J. Mol. Catal.* 73 (1992) 91
- [30] S.P. Griffiths, P. Johnston and P.B. Wells, *App. Catal. A: General*, 191 (2000)

Chapter 2: Theory

2.1 Introduction

In this chapter a brief description of the techniques used during the completion of work presented in this thesis will now be given. The techniques of interest here are: Temperature Programmed Desorption (TPD), X-ray Photoelectron Spectroscopy (XPS), Ultraviolet Photoelectron Spectroscopy (UPS), Auger Electron Spectroscopy (AES), Low Energy Electron Diffraction (LEED), Normal Incidence X-ray Standing Wavefield (NIXSW) and Second Harmonic Generation, (SHG). More extensive and detailed descriptions of the TPD, AES, XPS, UPS, and LEED techniques can be found in references 1 and 2, with a full review of the NIXSW technique given in reference 3. Additional information on SHG can be found in references 15-23.

2.2 Techniques

2.2.1 Temperature Programmed Desorption (TPD)

In a basic TPD experiment, a linear heating ramp is applied to an adsorbate-covered surface. As the temperature applied to the sample rises, the thermal energy available to the system increases and desorption is observed when sufficient energy is available for breaking adsorbate-surface bonds. Desorption from the surface is then monitored using a quadrupole mass spectrometer (QMS) tuned to detect the species of interest and placed close to the sample. Under UHV, desorbing gases are continuously pumped from the system at a significantly faster rate than that of desorption. Hence, the pressure rise in the chamber is proportional to desorption rate and peaks present in the corresponding pressure-temperature curve represent different adsorption states. The temperature at which a peak maximum occurs is denoted T_{\max} and indicates that at that temperature the rate of desorption is at a maximum.

Several different pieces of information can be obtained by use of the TPD technique. Firstly, the area under a TPD curve can be used as a measure of relative surface coverage. Hence, relative surface coverage of different adsorption states or co-adsorbate-induced changes to molecular packing density can be measured. Additionally, TPD measurements can be used to obtain quantitative information on

the activation energy of desorption, rate constant for desorption and the order of desorption. Finally, the TPD technique can be used as a probe of surface reactions by using the QMS to monitor gas phase products. This then allows investigation of the reaction mechanisms involved in surface reactions. However, in the work contained within this thesis, we primarily use the TPD technique in two ways. Firstly, we use the technique to identify desorption from multilayer and monolayer states. This is easily achieved using TPD measurements since the first adsorbed layer is more strongly bound than subsequent condensed layers and additionally, the multilayer state does not saturate with increasing coverage. This information is then used to reproducibly generate saturated monolayers for further experiments. Secondly, we use TPD as a method of "fingerprinting" adsorbate-surface bond strength, by monitoring shifts in T_{\max} , and the effects on strength of interaction induced by the presence of co-adsorbates. In other words, whether the presence of co-adsorbates can stabilise or destabilise molecular adsorption.

2.2.2 Surface Sensitivity of Electrons

Prior to discussing each of the electron spectroscopy techniques individually, it is useful to consider why electrons make ideal probes of surfaces. Additionally, this is useful in showing how experiments can be tailored to maximise surface sensitivity, a property we make use of in the experiments performed in chapter 7.

The surface sensitivity of an electron is critically dependent upon a parameter called the inelastic mean free path (IMFP). This is defined as the distance an electron can travel before its intensity decays to $1/e$ (0.368) of its initial value through scattering processes and therefore can be used as an index of the distance an electron can travel before losing energy. A small value of IMFP represents an electron with a high probability of energy loss and the ability to only travel a short distance before being adsorbed. These electrons are highly surface sensitive with a limited penetration depth into the solid and are therefore ideal for use in surface science experiments.

The IMFP of electrons is generally accepted to be only very weakly dependent on material. However, a strong dependence on electron kinetic energy is observed and is shown pictorially in figure 1.

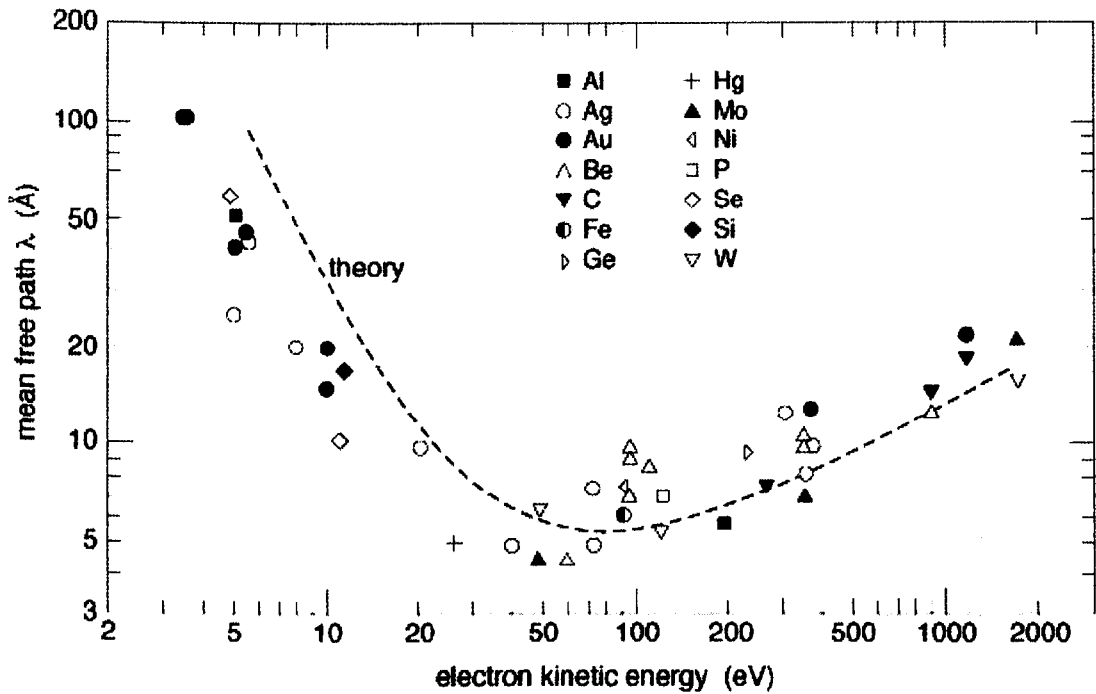


Figure 1. Schematic diagram of “Universal Curve” showing variation of inelastic mean free path with kinetic energy. Taken from reference 4.

The graph in figure 1 can be explained with the following rationale. At energies below 30 eV the main process of energy loss is removed, plasmon excitation, and hence, mean free path increases quickly. At electron energies above 50 eV, the IMFP is proportional to the square root of the kinetic energy and therefore directly proportional to electron velocity. From this, the increase in IMFP is understandable since the faster an electron travels, the faster the electron will pass through the solid and hence the less chance of energy loss. This results in a range between around 30-100 eV where surface sensitivity is greatest.

In the XPS experiments we perform in Glasgow we are unable to make full use of this feature of electron emission. Our lab-based source has a fixed electron energy and hence, it is not possible to tune the emitted electron energy to provide maximum surface sensitivity. Therefore, in chapter 7 we use synchrotron radiation, which does allow us to tune the emitted electron energy and hence obtain data with maximum surface sensitivity.

2.2.3 Auger Electron Spectroscopy (AES)

AES is a surface specific technique used during experiments performed in this thesis to both monitor surface cleanliness and, in conjunction with LEED, to calculate sulphur coverage. A schematic diagram of the Auger process is shown in figure 2.

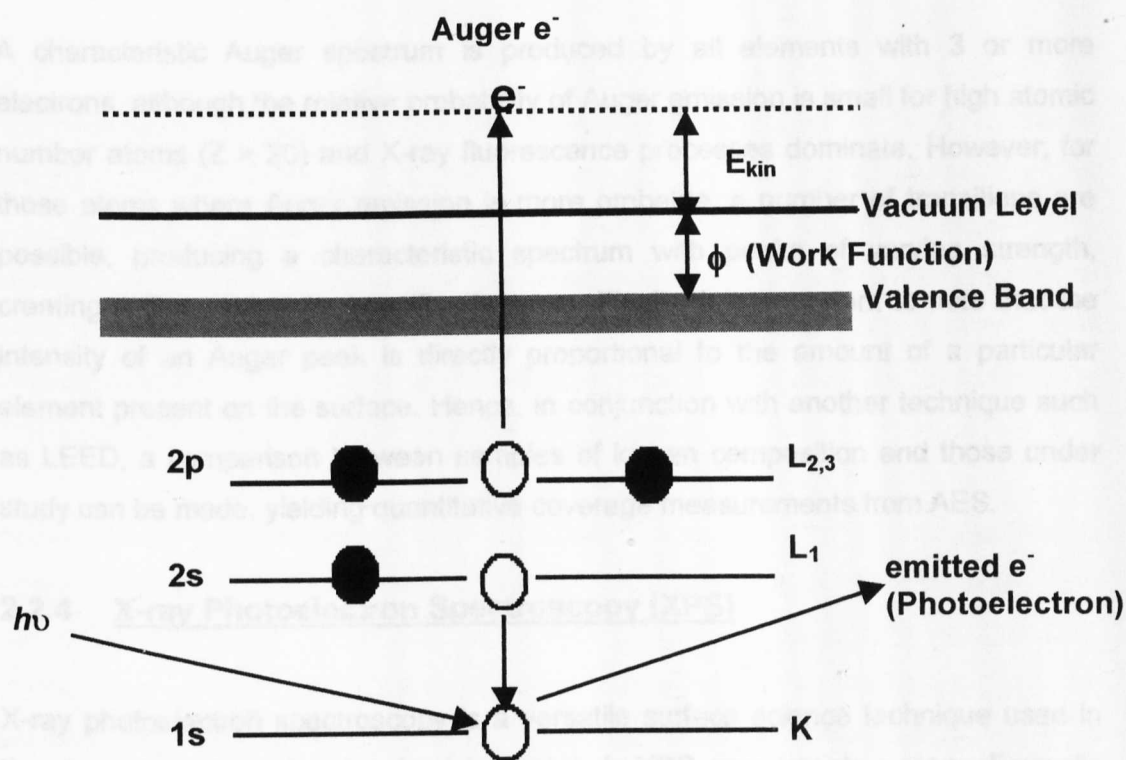


Figure 2. Schematic representation of the Auger process.

The process takes place in three stages and is initiated when a beam of electrons or photons impinge on an atom and induce emission of a core level electron. This leaves behind a positive hole, which can then be neutralised by an electron transition from a level of lower binding energy. The energy released in this transition can then either be removed from the atom as a photon, in the form of fluorescence, or go on to transfer its energy to a third electron. It is this third electron that is known as the Auger electron. The Auger electron has sufficient energy to escape into the vacuum level and has kinetic energy, E_{kin} , described by the following equation: -

$$E_{kin} = E_k - E_{L1} - E_{L2,3} - \phi \quad (1)$$

where ϕ represents work function, the minimum energy required to remove an electron from the solid to the vacuum. From equation 1 it can be seen that, in contrast to photoemission, the kinetic energy of the Auger electron is independent of the incident electron or photon beam and depends only on the binding energies of the electrons of the atom under study. Hence, the process is atom specific and can be used in elemental identification on single crystal surfaces by monitoring the kinetic energies of emitted electrons.

A characteristic Auger spectrum is produced by all elements with 3 or more electrons, although the relative probability of Auger emission is small for high atomic number atoms ($Z > 20$) and X-ray fluorescence processes dominate. However, for those atoms where Auger emission is more probable, a number of transitions are possible, producing a characteristic spectrum with peaks of varying strength, creating a "fingerprint" for specific elements. Finally, it is important to note that the intensity of an Auger peak is directly proportional to the amount of a particular element present on the surface. Hence, in conjunction with another technique such as LEED, a comparison between samples of known composition and those under study can be made, yielding quantitative coverage measurements from AES.

2.2.4 X-ray Photoelectron Spectroscopy (XPS)

X-ray photoelectron spectroscopy is a versatile surface science technique used in the characterisation of molecular adsorbates. In XPS experiments a monochromatic beam of X-ray photons is used to induce the emission of core level electrons from an atom (see figure 1). The kinetic energy of the emitted photoelectron is given by the equation: -

$$E_{\text{kin}} = h\nu - E_B \quad (2)$$

where $h\nu$ is the incident photon energy and E_B represents the binding energy of the electron. Hence, based on this description, a photoelectron spectrum would simply show the density of occupied states of an atom shifted up in energy by $h\nu$ and therefore can be used for the purposes of elemental identification. The assumption made in this statement is that the energy and spatial distribution of the electrons remaining after photoemission is exactly the same as in the initial state. In this

situation, the binding energy could then be directly linked to the negative orbital energy of the emitted electron. This approximation is known as Kóopmans' theorem. However, in reality the final state of the photoemitted electrons will be influenced by the remaining electrons in the system relaxing to different energy states. Two processes contribute to this, the intra-atomic relaxation shift, E_A and the interatomic relaxation shift, E_R .

$$E_{\text{kin}} = h\nu - E_B + E_A + E_R \quad (3)$$

The intra-atomic relaxation shift describes the process where other electrons relax in energy to lower energy states to partially screen the hole created by the photoemitted electron and therefore make more energy available to the out-going electron. The interatomic relaxation shift takes account of the effect produced by an atom placed in or on a surface such as a metal. In this situation the weakly bound valence electrons of the metal will be very mobile and will screen the hole efficiently leading to further energy available to the outgoing electron.

These effects are generally of the magnitude of a few eV and do not significantly effect interpretation of XPS data. However, the chemical environment of an atom can affect both these factors and the original binding energies. As a result of this, XPS can be used to provide information on the chemical environment of a particular element. For instance, atoms in a high oxidation state will exhibit binding energies higher than that of the same atom in a lower binding energy state. The positive charge on the atom results in increased Coulombic attraction between electrons and the nucleus and therefore causes a shift in core levels to higher binding energy.

Finally, it should be noted that like AES, the intensity of a photoelectron peak is directly related to the amount of a particular element on a surface. Therefore, like AES, quantitative coverage measurements can be made.

2.2.5 Ultraviolet Photoelectron Spectroscopy (UPS)

UPS is a technique closely related to XPS. However, where XPS is employed to study strongly bound core electrons, UPS is utilised as a probe of loosely bound valence electrons and is an excellent technique for studying the electronic structure of surfaces and adsorbates. In UPS experiments performed here, a He(I) discharge

lamp producing incident photons at 21.22 eV is used. This produces sufficient energy to induce valence level emission into the vacuum level, making it ideal for studying the weakly bound valence levels associated with chemical bond formation. The kinetic energy of the valence band emitted electrons can be seen to originate from their binding energies, in the same manner to XPS, given by: -

$$E_{\text{kin}} = h\nu - E_B + \phi \quad (4)$$

In the application of UPS to adsorbate covered systems presented here we have utilised the technique for "fingerprinting". This ideally involves comparison between the UP spectrum from an adsorbate with that of its gas phase spectrum. When molecular orbitals are involved in bonding to a surface they are electronically perturbed from the position of the electronically unperturbed molecule. Hence, by aligning the gas phase and adsorbate spectra using a deep lying orbital not involved in bonding we can identify orbitals involved in surface bonding by relative shifts in the adsorbate spectrum.

In addition to the study of adsorbates, UPS is also a useful probe of the electronic structure of surfaces. In solids, the outer valence electrons will form an energy band. In the case of first row transition metals this arises from the overlap of the 3d and 4s electrons and results in the formation of a d and sp band. In the case of Cu, the main subject of study in this thesis, the d band is filled and the Fermi level cuts the sp band. This results in UP spectra characterised by intense d band emission around 2-3 eV below the Fermi level and only weak emission from the low density of states sp band. Thus qualitative information regarding substrate electronic structure can be gained from UPS measurements.

One further aspect of UPS measurements is utilised in the work presented in this thesis, the measurement of work function. The work function of a system can be measured by simply considering the width of a UP spectrum from Fermi level where electrons of highest kinetic energy will be emitted, effectively $h\nu - \phi$ and where the lowest kinetic energy electrons are emitted (where the electrons have just overcome the work function barrier and are "emitted" with zero kinetic energy). The work function can then be calculated using the equation: -

$$\phi = h\nu - W \quad (5)$$

where W is the width of the UP spectrum and the photon energy is known to be 21.22 eV for He(I) discharge. Changes to work function induced by adsorbates then manifest as changes in the low kinetic energy tail.

2.2.6 Low Energy Electron Diffraction (LEED)

In a basic LEED experiment, a beam of electrons with kinetic energy in the range 20 to 1000 eV, are elastically back scattered from a surface. Electrons in this energy range are ideal probes of surfaces as they have de Broglie wavelengths in the range 2.74-0.388 Å which are of the same magnitude as the interatomic spacings of a single crystal surface. Hence, these electrons can undergo diffraction, producing patterns related to the periodicity of the surface.

To investigate the properties of this technique further we begin by the simplest case of diffraction from a one-dimensional array of periodicity, a (i.e. lattice constant = a). A representation of this simple array with electrons scattering at an angle θ_a from the array is shown in figure 3.

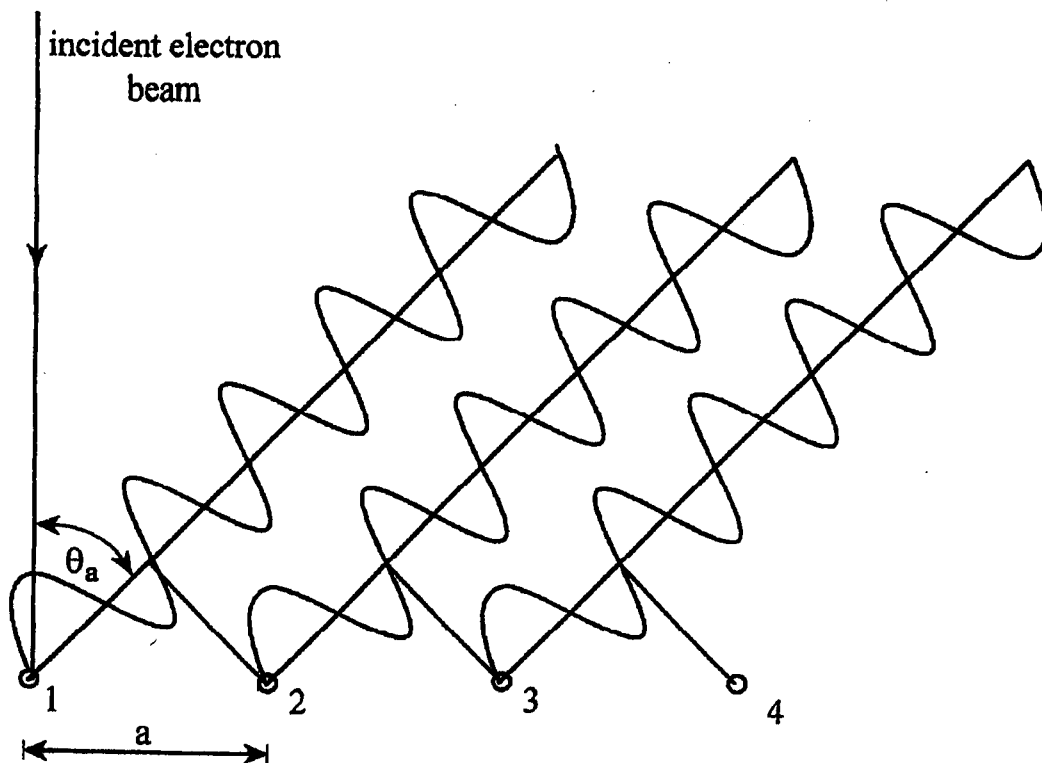


Figure 3. Schematic diagram of the diffraction beam of electrons from a hypothetical one dimensional array of point scatterers of equal spacing a . From reference 1.

From consideration of the diagram in figure 3, we can see that for constructive interference of the scattered waves to take place

$$n\lambda = a \sin\theta_a \quad (6)$$

where $n = 0, \pm 1, \pm 2, \pm 3 \dots$ with the wavelength described by

$$\lambda = \frac{h}{mv} \quad (7)$$

where h is Planck's constant, m is mass and v is velocity.

We will now develop a description for the condition for diffraction using electron wavevectors and reciprocal lattice vectors. Hence, with the magnitude of the incident wavevector generated by the electron described as

$$|\mathbf{k}_0| = \frac{2\pi}{\lambda} \quad (8)$$

Combining equations 7 and 8 and substituting into equation 6 gives

$$|\mathbf{k}_0| \sin\theta_a = \left(\frac{2\pi}{a}\right)n \quad (9)$$

With reference to equations 7 and 8 it can be seen that $|\mathbf{k}_0|$ is in fact related to momentum (mv) of the electron. Therefore, by consideration of figure 4 we can see that $|\mathbf{k}_0| \sin\theta_a$ is in fact the component of momentum parallel to the surface, k_{\parallel} of the incident electron wavevector.

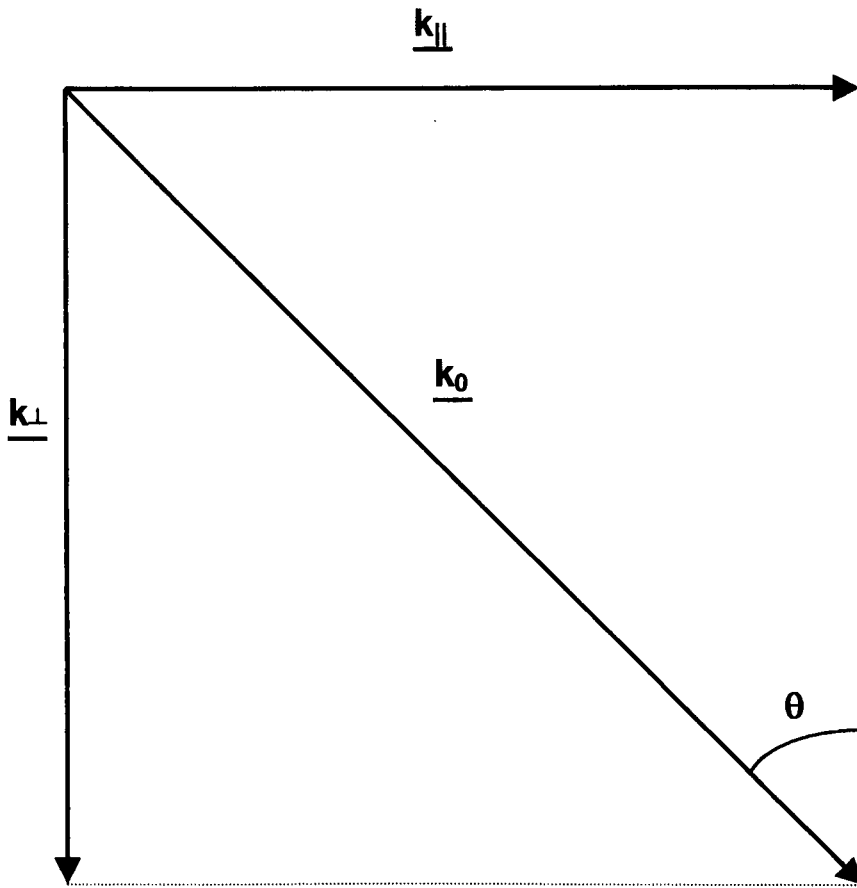


Figure 4. Parallel and perpendicular components of incident electron wavevector \mathbf{k}_0 with $|\mathbf{k}_{||}| = |\mathbf{k}_0| \sin \theta$ and $|\mathbf{k}_{\perp}| = |\mathbf{k}_0| \cos \theta$.

Additionally, from equation 10 it can be seen that parallel momentum can only be exchanged with the surface in quantised units of $2\pi/a$ since n can only take values of $0, \pm 1, \pm 2, \pm 3, \dots$. Hence $\{2\pi/a\}$ is the magnitude of the one dimensional reciprocal lattice vector associated with diffraction of the electron beam. In physical terms the implication of this is that for the electrons incident on the surface, (i.e. normal to the surface) initially with no parallel momentum, to produce diffracted beams, they must undergo a change in direction. For this to occur, the electron must undergo exchange in parallel momentum with the one-dimensional lattice in quantised values of $2\pi/a$, thereby conserving momentum. Therefore, the change in parallel momentum, $\Delta \mathbf{k}_{||}$, can be expressed as

$$\Delta \mathbf{k}_{||} = |\mathbf{k}_0| \sin \theta_a = \left(\frac{2\pi}{a} \right) n \quad (10)$$

Having satisfied the conditions for diffraction from a one-dimensional array, we now consider adding a second periodic array in an orthogonal direction to the first with lattice periodicity b instead of a . Following a similar derivation to that for the previous direction we obtain the following:

$$\Delta \mathbf{k}_{\parallel} = |\mathbf{k}_0| \sin \theta_b = \left(\frac{2\pi}{b} \right) m \quad (11)$$

where $m = 0, \pm 1, \pm 2, \pm 3, \dots$. Thus to observe diffraction from a two-dimensional array both equations 10 and 11 must be satisfied simultaneously. This results at the points of intersection of the one-dimensional reciprocal lattice rods in the a and b directions. In this situation, exchange of parallel momentum is restricted to a two-dimensional reciprocal lattice vector (\mathbf{G}), given by

$$\mathbf{G} = \Delta \mathbf{k}_{\parallel} = n \frac{2\pi}{a} + m \frac{2\pi}{b} \quad (12)$$

Therefore we can now adopt an expression from which a reciprocal lattice generated by an associated real space lattice can be constructed.

$$\mathbf{G} = n\mathbf{a}^* + m\mathbf{b}^* \quad (13)$$

where $|\mathbf{a}^*| = \frac{2\pi}{|\mathbf{a}|} \quad (14)$

$$|\mathbf{b}^*| = \frac{2\pi}{|\mathbf{b}|} \quad (15)$$

$$\mathbf{a} \cdot \mathbf{b}^* = \mathbf{a}^* \cdot \mathbf{b} = 0 \quad (16)$$

where \mathbf{a} and \mathbf{b} are the vectors of the surface two-dimensional array and \mathbf{a}^* and \mathbf{b}^* are the corresponding reciprocal lattice vectors. Hence from these equations it can be seen that a large distance in real space will be small in reciprocal space and vice versa and also that \mathbf{a} and \mathbf{b} are perpendicular to \mathbf{a}^* and \mathbf{b}^* . From this we then have a condition for diffraction given by

$$\mathbf{k}_0^{\parallel} = \mathbf{k}_s^{\parallel} + \mathbf{G} \quad (17)$$

where \mathbf{k}_s^{\parallel} is the parallel component of the scattered electron.

As an alternative to this approach, Ewald Sphere Construction is a geometrical representation of equation 17. Using this approach, it is possible to calculate both the number of diffracted beams emerging from a surface at a given beam energy and also the angle of the diffracted beams with a particular real space direction. Figures 5a and 5b show Ewald sphere construction used to determine both beam number (5a) and angle (5b). The approach involves drawing a circle (representation of a sphere but in two dimensions) with radius $|k_0|$, within which the total number of diffracted beams emerging from the surface will be contained in figure 5a and the angle made with each diffracted beam will be given in 5b at the point of intersection of the sphere with the reciprocal lattice rods.

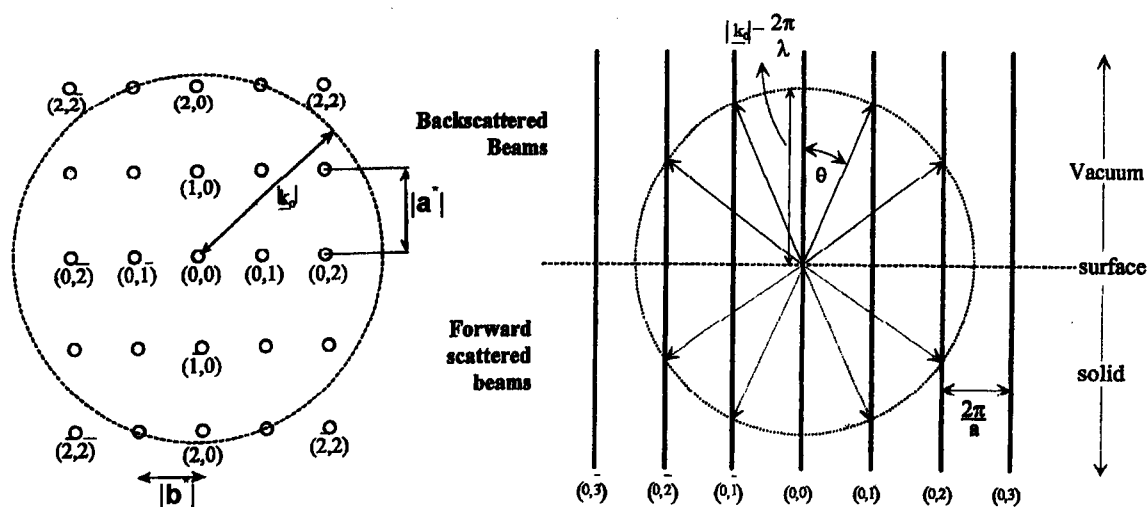


Figure 5. Ewald Sphere (Circle) Construction. From reference 1.

2.2.7 Normal Incidence X-ray Standing Wavefield (NIXSW)

The technique of Normal Incidence X-ray Standing Wavefield (NIXSW) is used in surface science to provide quantitative structural information on the local registries of adsorbates on single crystal surfaces and unlike LEED and SXRD the experiment has no requirement for surface long-range order. In a NIXSW experiment X-ray radiation with the appropriate wavelength to generate a Bragg reflection at normal incidence strikes the crystal surface. Interference between the incident and backscattered waves generates a standing wavefield in the solid with nodal planes lying parallel to the Bragg scattering planes and with a separation equal to that of the scattering planes. This wave penetrates both into the surface by an order of μm

and also extends outward above the crystal surface. A schematic diagram of the effect is shown in figure 6.

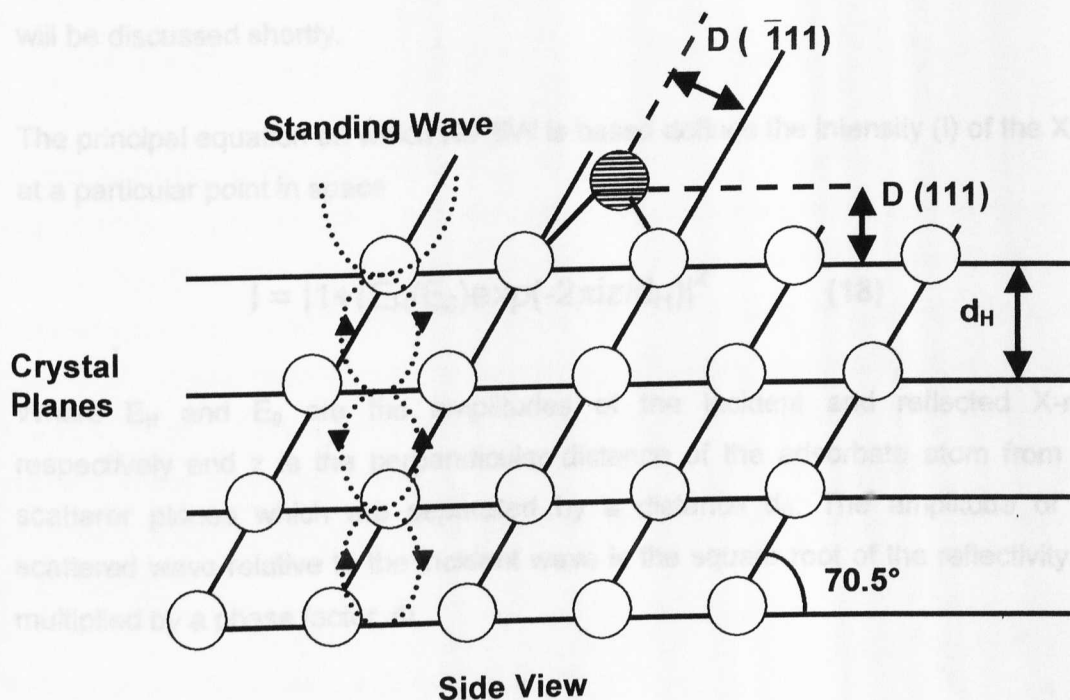


Figure 6. Schematic diagram of an X-ray standing wavefield in a single crystal. The (111) and ($\bar{1}\bar{1}\bar{1}$) coherent positions (D) are also shown.

Clearly the amount of X-ray absorption experienced by a surface or adsorbate atom depends on its position in relation to the standing wavefield. When the photon energy is scanned through a range of reflectivity associated with the standing wavefield, its phase changes in a way that can be modelled. The location of the adsorbate atom relative to the bulk scattering planes can be determined by modelling the X-ray absorption profile of the atom, obtained while the photon energy is scanned. This can be achieved by monitoring the intensity of the emitted photoelectrons, the Auger emission or alternatively the X-ray fluorescence.

An inherent difficulty associated in performing NIXSW measurements lies in obtaining sufficient signal to noise ratio (SNR) in NIXSW profiles when studying the adsorption of light elements such as oxygen and fluorine on transition metal surfaces. This problem arises due to the disparity between the standing wave energy required to meet the Bragg condition of the metal and the 1s ionisation energy of the elements. This results in a small ionisation cross section for 1s ionisation. However, photoemission experiments generally have a better SNR than

that using Auger emission, and indeed in the experiments reported here the best SNR was obtained by monitoring O1s photoemission. However, the use of core level emission does add a complication to the analysis of NIXSW profiles and this will be discussed shortly.

The principal equation on which NIXSW is based defines the intensity (I) of the XSW at a particular point in space.

$$I = |1 + (E_H/E_0)\exp(-2\pi iz/d_H)|^2 \quad (18)$$

Where E_H and E_0 are the amplitudes of the incident and reflected X-rays respectively and z is the perpendicular distance of the adsorbate atom from the scatterer planes which are separated by a distance d_H . The amplitude of the scattered wave relative to the incident wave is the square root of the reflectivity, R , multiplied by a phase factor, Φ ,

$$E_H/E_0 = \sqrt{R} \exp(i\Phi) \quad (19)$$

Using this we can now re-write equation 18.

$$I = 1 + R + 2\sqrt{R} \cos(\Phi - (2\pi z / d_H)) \quad (20)$$

This analysis applies only for a single adsorbate molecule at a single fixed position in a rigid lattice. In reality, adsorbates on metal surfaces may be distributed throughout a number of adsorption sites due to the effects of vibrational or static disorder or both. This can be accounted for by taking a distribution of z -values such that

$$\int_0^{d_H} f(z) dz = 1 \quad (21)$$

Hence, using this, the absorption profile is given by

$$I = 1 + R + 2\sqrt{R} \int_0^{d_H} f(z) \cos(\Phi - (2\pi z / d_H)) dz \quad (22)$$

which can also be written in the form

$$I = 1 + R + 2f_{co} \sqrt{R} \cos(\Phi - (2\pi D / d_H)) \quad (23)$$

in terms of the coherent fraction, f_{co} , and the coherent position, D . These two parameters essentially define how the obtained absorption profiles vary in relation to surface structure and are obtained by use of an automated fitting program [5]. D is a value between 0 and 1 lattice spacings, which for a well defined site represents the height of the atom above the nearest (111) plane, while f_{co} is a value, again between 0 and 1, representing the uncertainty in the position of the atom with respect to the scattering planes. Profiles fitted to a coherent fraction of 0 would represent a completely ill defined position, while 1 would be a position with no uncertainty.

It is convenient to re-write equation 23 in the form:

(24)

$$I = f_{co} (1 + R + 2\sqrt{R} \cos(\Phi - (2\pi D / d_H))) + (1 - f_{co})(1 + R)$$

A simpler method of relating the coherent fraction and coherent position to the actual distribution is given by

$$f_{co} \exp(2\pi i D / d_H) = \int_0^{d_H} f(z) \exp(2\pi i z / d_H) dz \quad (25)$$

This final equation shows that f_{co} is actually a reflection of the distribution of heights above the scattering plane associated with an adsorbate and can provide an indication of the occupation of multiple adsorption sites. This equation also allows for the construction of an Argand diagram representing the measured parameters D and f_{co} .

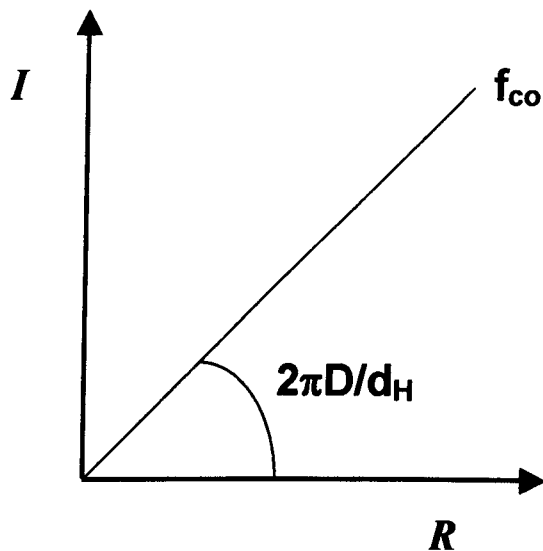


Figure 7. Argand diagram representation of coherent fraction, f_{co} , and coherent position, D . The axes are labelled I for imaginary and R for real.

In the case of multiple site adsorption, this method can be useful in determining the relative occupation of different adsorption sites.

2.2.7.1 Adsorption Site Determination by Real Space Triangulation

For an adsorbate on a (111) surface plane there are four principal adsorption sites, atop, bridge, fcc and hcp (figure 8). In order to unambiguously assign an adsorption site from NIXSW measurements, the position of an atom (i.e. f_{co} and D values) is obtained in both the (111) and $(\bar{1}11)$ planes, allowing adsorption site to be obtained by real space triangulation. In reality, this is achieved by measurement of the (111) direction D and f_{co} values from which the expected $(\bar{1}11)$ values can be calculated for each of the possible adsorption sites. Comparison of theoretically calculated values with those obtained by experiment then allows adsorption site determination.

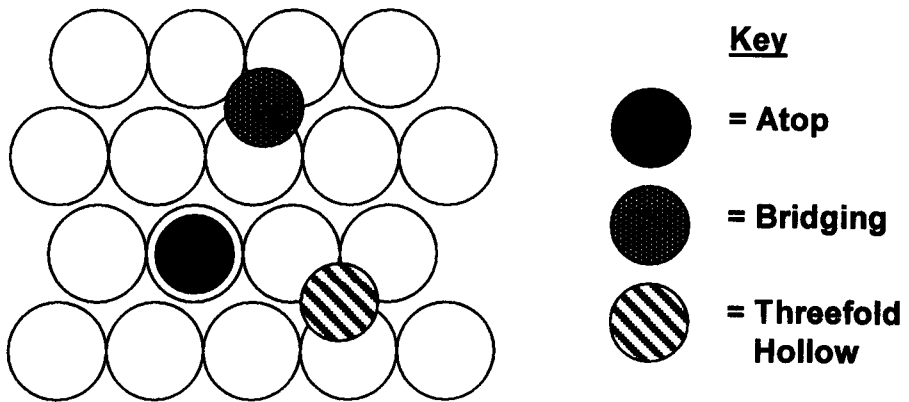


Figure 8. Schematic diagram of the three principal adsorption sites on a (111) surface. Threefold hollow sites can be in the form of either fcc or hcp sites.

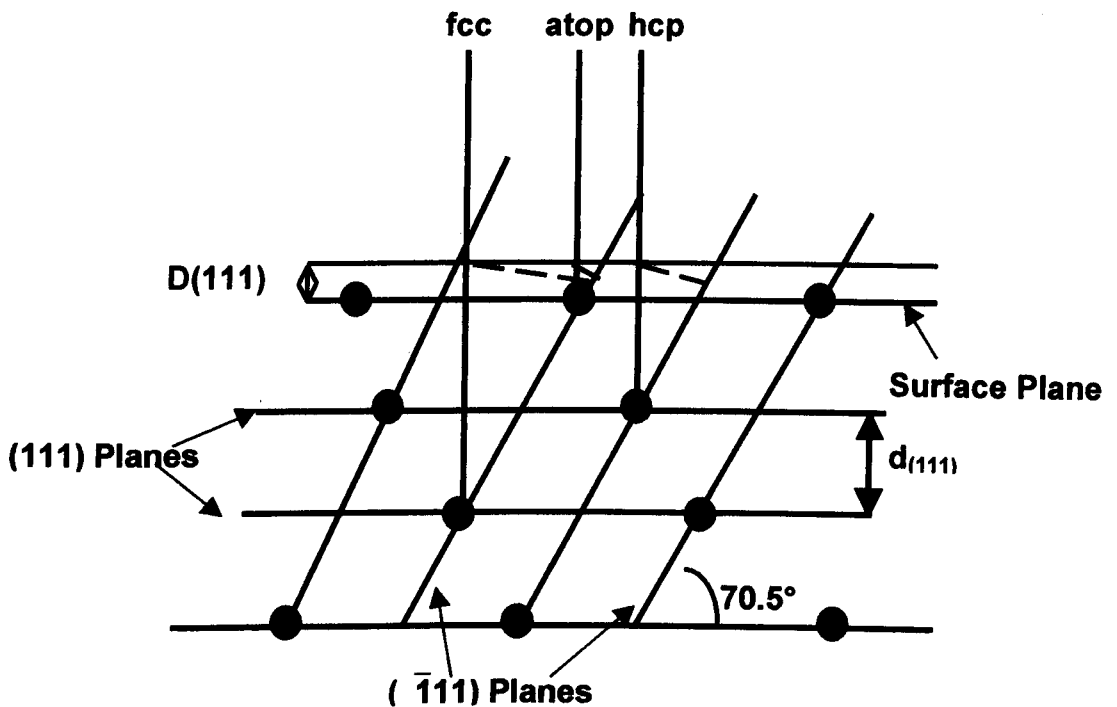


Figure 9. Schematic diagram showing the principal adsorption sites on a (111) surface with respect to both the (111) and $(\bar{1}11)$ planes used in NIXSW experiments. Adapted from reference 6.

The ($\bar{1}11$) plane D and f_{co} values for each adsorption site can be calculated from the corresponding (111) experimental data using the following equations:

$$\text{Atop:} \quad D(\bar{1}11) = D(111)/3 \quad (26)$$

$$f_{co}(\bar{1}11) = f_{co}(111) \quad (27)$$

$$\text{Bridge:} \quad D(\bar{1}11) = D(111)/3 + d_{111}/2 \quad (28)$$

$$f_{co}(\bar{1}11) = f_{co}(111)/3 \quad (29)$$

$$\text{FCC:} \quad D(\bar{1}11) = (D(111) + 2d_{111})/3 \quad (30)$$

$$f_{co}(\bar{1}11) = f_{co}(111) \quad (31)$$

$$\text{HCP:} \quad D(\bar{1}11) = (D(111) + d_{111})/3 \quad (32)$$

$$f_{co}(\bar{1}11) = f_{co}(111) \quad (33)$$

The procedure outlined above works perfectly for a single well-defined adsorption site with a high coherent fraction. However, in the situation where a lower coherent fraction is obtained, there is a possibility of multiple adsorption sites and an Argand diagram representation must be constructed. In this situation a diagram is constructed showing the experimental ($\bar{1}11$) data plotted along with vectors representing each of the well-defined adsorption sites given by the above equations. By standard vector manipulation it is then possible to assign a combination of sites which result in the observed data.

Finally, it can be seen from the above equations for a bridge adsorption site that the site is defined by a f_{co} one third of the other vectors. This results from the fact that there are three inequivalent adsorption sites with respect to the ($\bar{1}11$) plane for this adsorption geometry. The first site corresponds to one with a layer spacing value of $D(111)/3$, while the other two to values of $(D(111)/3 + d_{111}/2)$. This results in two opposing vectors of relative length $1/3$ and $2/3$, which combine to give an overall vector with a coherent position given by $(D(111)/3 + d_{111}/2)$ and a coherent fraction $1/3$ of the original value.

2.2.7.2 Non-dipole Effects in NIXSW

As mentioned earlier, to obtain sufficient SNR in NIXSW experiments it is often preferable to monitor photoemitted electrons rather than Auger. This results in a complication to the NIXSW analysis arising from non-dipole effects.

These non-dipole effects manifest themselves in standing wave measurements by influencing the angular distribution of photoemitted core electrons. Observations of this type of effect were initially noted in both theoretical [7] and experimental [8,9] work on noble gases. However, a number of subsequent NIXSW studies [10-12] have noted that non-dipole effects have a substantial influence on the interpretation of NIXSW measurements. By necessity, in a NIXSW experiment, the emitted photoelectrons are detected in a direction "backwards" to the direction of propagation of the X-rays. Conversely, the detector is in the "forward" direction with respect to the reflected beam. Hence, if the angular distribution of the photoelectrons is influenced by non-dipole effects, there will be a backward/forward asymmetry in the photoemission and incident and reflected components will be detected with differing efficiencies.

Obviously, these effects must be taken account of in the analysis of NIXSW data. This has been achieved by an inclusion of a dimensionless term, Q , in NIXSW analysis of photoelectron derived profiles. In the earliest attempt to compensate for non-dipole effects in NIXSW [10], Q was used to define the ratio of photoemission intensity in the forward and backward direction as

$$(1 + Q)(1 - Q) \quad (34)$$

Incorporating this into equation 24 and re-writing in terms of the angular derivative of the total cross-section, $d\sigma/d\Omega$, gives the signal detected in a given direction during a NIXSW experiment:

$$\frac{d\sigma}{d\Omega} \propto \left| 1 + R \frac{(1+Q)}{(1-Q)} + \sqrt{R} f_{\text{co}} \left(\frac{(1+Q)}{(1-Q)} \right)^{1/2} \cos \left(\Phi - \frac{2\pi D}{d_H} \right) \right| \quad (35)$$

More recent theoretical work on non-dipole effects on NIXSW measurements has been performed by Vartanyants and Zegenhagen [11]. The results of this work produced a more complete description of the effects above, which included an additional term into the analysis, Δ , associated with the scattering phase shift differences. Although this work produced a theoretically fuller description, calibration experiments by Lee and co-workers [12] found that omitting Δ from NIXSW analysis results in systematic errors introduced into D and f_{co} smaller than the typical random errors associated with each. Hence in the NIXSW analysis reported here we have only used Q in our fitting routine.

Determining the actual Q value of an atom is done experimentally, by NIXSW measurements from condensed multilayers. Measurements of the Q value for O containing atoms have been made in previous experiments carried out in our lab [13,14] and have determined Q to be 0.25.

2.2.8 Second Harmonic Generation (SHG)

The technique of second harmonic generation is both a useful and powerful tool in examining the structural and electronic properties of interfaces with the technique being used to study systems such as buried interfaces, adsorption processes and the electronic structure of metals. In addition to this, SHG is a useful probe of surface chirality due to its specificity to non-centrosymmetric environments or molecules and the large asymmetries generated. However, despite SHG having been a topic of scientific interest for over 40 years, many aspects of the process are not fully understood theoretically. This is particularly true for SHG from metal surfaces where a number of mechanisms can contribute to the overall SHG signal. In addition to this, the use of SHG for chiral discrimination is a relatively new use of SHG and theoretically not fully developed. In the experiments reported in chapter 8, we perform the first ever chiral discrimination experiments from chiral adsorbates on a metal surface. Hence, a combined theoretical description of both the metal and adsorbates has never been developed. However, we present here a theoretical description of the experiments performed in chapter 8 based on the information currently available.

A full derivation of the SHG process from first principles can be found in reference 15, as well as several other texts, with numerous other articles available relating to specific systems. We begin here by exploring the underlying theory behind SHG

from chiral molecules and metal surfaces based on the work of Schanne-Klein et al. in reference 16 on SHG from chiral molecules and Sipe et al. on metals in reference 17. The geometry of SHG from a layer is defined in figure 10.

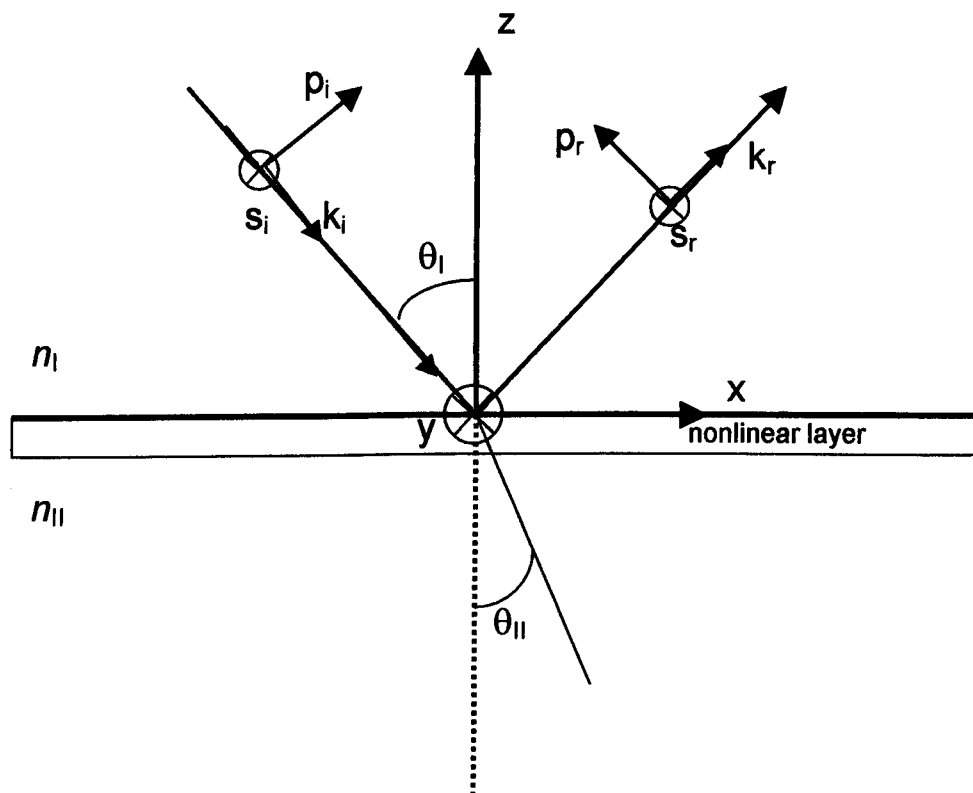


Figure 10. Geometry of surface SHG. θ_I is the angle of incidence of the laser beam with frequency ω . k_i is the incident wave vector in the x - z plane with z normal to the surface, with the reflected second harmonic in the k_r direction. The polarisation of the electric field is defined by p, s and k .

In the model proposed in the figure above we make a number of assumptions and simplifications in the following derivation. The thickness of the interface is considered to be much smaller than that of the optical wavelength to remove propagation effects. Also we neglect the effects of multiple reflections as they do not introduce dephasing between the optical parameters. Here we also assume the linear index of refraction of the molecular layer to be the same as that of the substrate, reducing the problem to that of two semi-infinite media on either side of the surface defined medium I with $n_I=1$ and medium II with index n_{II} . This model means the electric field in the molecular layer is then related to that outside the

layers by the usual Fresnel coefficients, $t_p^{||}$ for p polarisation and $t_s^{||}$ for s polarisation.

Starting with this model we define the electric field of the light as

$$\mathbf{E}(r,t) = \mathbf{E}(\omega)e^{i(kr-\omega t)} + \text{c.c} \quad (36)$$

with c.c representing the complex conjugate. The electric field generates a nonlinear polarisation in the interface of which we are interested in terms associated with the second order given by the following equation:

$$\mathbf{P}(2\omega) = \chi^{eee}: \mathbf{E}^{||}(\omega)\mathbf{E}^{||}(\omega) + 2\chi^{eem}: \mathbf{E}^{||}(\omega)\mathbf{B}^{||}(\omega) \quad (37)$$

and the nonlinear magnetisation is given by

$$\mathbf{M}(2\omega) = \chi^{mee}: \mathbf{E}^{||}(\omega)\mathbf{E}^{||}(\omega) \quad (38)$$

where $\mathbf{E}^{||}$ and $\mathbf{B}^{||}$ are respectively the electric and magnetic fields in medium II related by

$$\mathbf{B}^{||} = \mathbf{n}_i^{||} \times \mathbf{E}^{||} \quad (39)$$

$$\text{where } \mathbf{n}_i^{||} = n_{||}(\sin\theta_{||}\hat{\mathbf{x}} - \cos\theta_{||}\hat{\mathbf{z}}) \quad (40)$$

At this point we have left a number of variables used above undefined, namely χ^{eee} , χ^{eem} and χ^{mee} . These terms define the second order susceptibility generated by the electric dipole, χ^{eee} , and the magnetic dipole and electric quadrupolar terms combined together and represented by χ^{eem} and χ^{mee} . χ^{eem} is associated with the magnetic interaction occurring at the fundamental frequency, while χ^{mee} is associated with the harmonic. These terms are at the heart of the SHG technique and are determined by orientational averaging of all the molecules on the surface, each of which is characterised by the molecules hyperpolarisability factor, β . To fully explain some aspects of SHG, as we will show later, we must use a 27 element

second order susceptibility tensor. For clarity we have omitted the χ^2 terms and show only the associated subscripts.

$$\begin{pmatrix} xxx & xyy & xzz & xyz & xzy & xzx & xxz & xxy & xyx \\ yxx & yyy & yzz & yyz & yzy & yzx & yxz & yxy & yyx \\ zxx & zyy & zzz & zyz & zzy & zzx & zxz & zxy & zyx \end{pmatrix} \quad (41)$$

In the special situation of SHG in a purely electric dipole approximation, the last three pairs of columns in 41 can be contracted, since both $E^{||(\omega)}$ in equation 37 can be considered equivalent. Therefore we have:

$$\begin{pmatrix} xxx & xyy & xzz & xyz & xxz & xxy \\ yxx & yyy & yzz & yyz & yxz & yxy \\ zxx & zyy & zzz & zyz & zxz & zxy \end{pmatrix} \quad (42)$$

Taking account of the symmetry of the interface of interest can reduce the non-vanishing components of this tensor still further. The different faces of a number of metal single crystals have been explored in detail by Sipe et al. [17]. The topmost layer of the (111) face of copper has C_{3v} symmetry. However, taking into account additional surface layers (SHG has been reported to come from the top 100 Å of the surface [20]) results in symmetry consistent with C_{3v} . Using this symmetry, the authors have calculated the non-vanishing tensor elements to be:

$$\begin{pmatrix} xxx & -xyy & 0 & 0 & xxz & 0 \\ 0 & 0 & 0 & yyz & 0 & -yxy \\ zxx & zyy & zzz & 0 & 0 & 0 \end{pmatrix} \quad (43)$$

The SH signal detected in SHG experiments can be described in the simplest terms as different components of the electric-dipole (and magnetic) susceptibility components in differing relative contributions. In particular, the relative weights and contributions of these elements can be significantly affected by using different

polarisations of fundamental and detected radiation. In chapter 8, we make use of this particular feature of SHG. In that chapter, we wish to measure the chirality of our adsorbate layer but for almost all experimental geometries we observe the signal generated by the metal surface (SH_{metal}) to be significantly greater than that of the adsorbate (SH_{ads}) [19,20]. Under these circumstances changes to the metal dominated signal would only be observed if the electronic structure of the metal had been imbued with chirality by the adsorbate molecules. To overcome this problem we use particular combinations of polarised fundamental and detected radiation. Specifically, we perform two types of experiments, one using p-polarised incident radiation and the second using s-polarised incident light. When using p-polarised light, the electric field will be polarised in the x and z plane. Hence, only particular elements of the susceptibility tensor associated with those components of the radiation will be non-vanishing. These are shown in equation 44.

$$\begin{pmatrix} \text{XXX} & 0 & 0 & 0 & \text{XXZ} & 0 \\ 0 & 0 & 0 & 0 & 0 & 0 \\ \text{ZXX} & 0 & \text{ZZZ} & 0 & 0 & 0 \end{pmatrix} \quad (44)$$

Similarly, for s-polarised radiation only tensor elements interacting with incident light associated with incident radiation in the y direction will be non-vanishing. These are shown in equation 45.

$$\begin{pmatrix} 0 & -xyy & 0 & 0 & 0 & 0 \\ 0 & 0 & 0 & 0 & 0 & 0 \\ 0 & zyy & 0 & 0 & 0 & 0 \end{pmatrix} \quad (45)$$

Using either p or s-polarised radiation and detecting only s-polarised SH should result in no SH signal according to either of the tensors above. However, in early work on Cu(111), Tom et al. [18] observed a measurable rotational anisotropy, which is not consistent with the above model. This model is based on a purely free electron response of the metal but both Tom's work and subsequent experiments [21,22] have shown the response is more complicated. Indeed, the SH response of a metal can also contain signal arising from bulk quadrupole effects and/or signal generated as a result of interband transitions. The work of Lüpke et al. [21] during

resonance studies of Cu(111) concluded that bulk electric quadrupole contributions are relatively small and that the main component of the signal is due to an interband transition associated with the zzz tensor element. In our own study we expect a resonance enhancement between the copper and the SH radiation as has been observed previously [18,22]. Hence, if we now return to consider the relevance of the theory presented already to our own work, we can overcome the problem of the dominating SH_{metal} signal. If we use s-polarised incident radiation and detect close to s-polarisation, a number of components of the susceptibility tensor no longer contribute to the overall signal, in particular the resonantly enhanced zzz component. Under these circumstances (as we show in chapter 8) SH_{metal} is significantly reduced and SH_{ads} becomes detectable. In the alternative experiments we perform using p-polarised incident radiation the metal signal dominates and includes a contribution from the interband transition associated with the zzz component.

In a similar manner to the metal, the adsorbate layer also has associated susceptibility tensors. The electric dipole contribution to the SH signal from the adsorbate layer can once again be described by a 18 component tensor and as before, the non-vanishing elements are reduced further due to surface isotropy, which results in a layer with C_{∞} symmetry. The electric dipole associated susceptibility tensor for a chiral adsorbate layer, which has C_{∞} symmetry, is shown in equation 46.

$$\begin{pmatrix} 0 & 0 & 0 & xyz & xxz & 0 \\ 0 & 0 & 0 & yyz & -yxz & 0 \\ zxx & zyy & zzz & 0 & 0 & 0 \end{pmatrix} \quad (46)$$

It is worth noting at this point that the elements associated with chirality are those containing three different terms, i.e. xyz . Measuring different enantiomers of a molecule should result in a change in sign of these elements but the magnitude should remain the same. Hence, the signal generated by a racemic layer should produce a SH signal between that of the two enantiomers. As we did for the metal surface, we now consider the effects of polarisation on the adsorbate layer. Firstly, if the incident radiation is p-polarised, the following elements are non-vanishing:

$$\begin{pmatrix} 0 & 0 & 0 & 0 & \text{xxz} & 0 \\ 0 & 0 & 0 & 0 & -\text{yxz} & 0 \\ \text{zxx} & 0 & \text{zzz} & 0 & 0 & 0 \end{pmatrix} \quad (47)$$

And similarly for s-polarised incident radiation.

$$\begin{pmatrix} 0 & 0 & 0 & 0 & 0 & 0 \\ 0 & 0 & 0 & 0 & 0 & 0 \\ 0 & \text{zyy} & 0 & 0 & 0 & 0 \end{pmatrix} \quad (48)$$

This initially suggests a possible problem to the measurements we wish to make in chapter 8 of chiral adsorbates. If we use s-polarised incident radiation to reduce the metal component as described previously, we also have only one non-vanishing tensor element associated with the adsorbate layer. Additionally, this element is not associated with chirality. Hence, the measurements we make in chapter 8 are theoretically impossible under a purely electric dipole mechanism. However, chiral SHG measurements using s-polarised radiation have been made previously [16].

The origin of chiral SHG measurements from a variety of different molecules has been investigated by Hache et al. [23], concluding that we must go beyond a purely electric dipole approximation and include the effects of electric quadrupolar and magnetic dipolar contributions. In SHG, it is difficult to differentiate between these contributions and hence, the authors have combined them together into “magnetic” terms associated with the fundamental (χ^{eem}) and harmonic (χ^{mee}) frequency. Unlike for the tensor elements associated with the electric dipole, the magnetic and electric components associated with the “magnetic” tensors will not be equivalent and hence we must use our original 27-element tensor. The χ^{eem} components associated with a chiral adsorbate layer are:

$$\begin{pmatrix} 0 & 0 & 0 & xyz & xzy & xzx & xxz & 0 & 0 \\ 0 & 0 & 0 & yyz & yzy & -yzx & -yxz & 0 & 0 \\ zxx & zyy & zzz & 0 & 0 & 0 & 0 & zxy & -zyx \end{pmatrix}$$

(49)

For the magnetic tensor elements, the components associated with chirality are those with two or more terms the same, i.e. xyx , xxx , zyz , etc. As before, we wish to consider the non-vanishing elements under the polarisation conditions described already. In this instance when the electric component of the radiation is polarised in the x and z directions, the magnetic component will be polarised in the y direction and vice versa. We will begin by considering p-polarisation (with respect to the electric field).

$$\begin{pmatrix} 0 & 0 & 0 & 0 & xzy & 0 & 0 & 0 & 0 \\ 0 & 0 & 0 & 0 & yzy & 0 & 0 & 0 & 0 \\ 0 & 0 & 0 & 0 & 0 & 0 & 0 & zxy & 0 \end{pmatrix} \quad (50)$$

Similarly, for s-polarisation (with respect to the electric field).

$$\begin{pmatrix} 0 & 0 & 0 & xyz & 0 & 0 & 0 & 0 & 0 \\ 0 & 0 & 0 & yyz & 0 & 0 & 0 & 0 & 0 \\ 0 & 0 & 0 & 0 & 0 & 0 & 0 & 0 & -zyx \end{pmatrix} \quad (51)$$

It can be seen that in equation 51 we still observe a chiral component yyz even when the radiation is s-polarised. Hence, chiral SHG measurements would be theoretically possible. We now also repeat this analysis for the second magnetic component associated with the harmonic frequency, χ^{mee} . The tensor elements associated with this are shown in equation 52.

$$\begin{pmatrix} 0 & 0 & 0 & xyz & xzy & xzx & xxz & 0 & 0 \\ 0 & 0 & 0 & yyz & yzy & -yzx & -yxz & 0 & 0 \\ zxx & zyy & zzz & 0 & 0 & 0 & 0 & 0 & 0 \end{pmatrix} \quad (52)$$

For p-polarised radiation (with respect to the electric field).

$$\begin{pmatrix} 0 & 0 & 0 & 0 & xzy & 0 & 0 & 0 & 0 \\ 0 & 0 & 0 & 0 & yzy & 0 & 0 & 0 & 0 \\ 0 & 0 & 0 & 0 & 0 & 0 & 0 & 0 & 0 \end{pmatrix} \quad (53)$$

Similarly, for s-polarised radiation (with respect to the electric field).

$$\begin{pmatrix} 0 & 0 & 0 & xyz & 0 & 0 & 0 & 0 & 0 \\ 0 & 0 & 0 & yyz & 0 & 0 & 0 & 0 & 0 \\ 0 & 0 & 0 & 0 & 0 & 0 & 0 & 0 & 0 \end{pmatrix} \quad (54)$$

Hence, from this analysis we can see that chiral components of the susceptibility tensors associated with the magnetic contributions (χ^{em} and χ^{me}) remain when the incident radiation is either p or s-polarised. Hence, in our experiments in chapter 8 we expect any chiral response from the adsorbate layer to be generated by magnetic contributions to the SH signal. However, measurements using p-polarised light which show a chiral response could be generated by either electric or magnetic contributions but as described already the signal would be metal dominated. Hence for a chiral response the adsorbate would have to imbue the metal in some way with chirality, either physically or electronically. If this occurred, the symmetry of the surface would also have to change from C_{3v} to one consistent with chirality, e.g. C_{∞} .

Therefore, the measurements we make in chiral experiments monitor changes to the frequency doubled outgoing light induced by changes to the chiral components of the electronic and magnetic second order susceptibility tensors. The reflected second harmonic electric field is defined as

$$E_{s,p}^r(2\omega) = \frac{i4\pi\omega / ct_{s,p}^{||/||}}{n_{||} \cos \theta_{||}} \left[\mathbf{P}(2\omega) - \mathbf{n}_r^{||} \times \mathbf{M}(2\omega) \right]_{s,p} \quad (55)$$

with

$$\mathbf{n}_r^{||} = n_{||} (\sin \theta_{||} \hat{\mathbf{x}} + \cos \theta_{||} \hat{\mathbf{z}}) \quad (56)$$

Continuing the derivation from this point, it has been shown that equation 56 can be re-written as a function of the s and p polarised components. Hence, by detecting the frequency doubled SH signal at particular polarisations we can monitor particular parts of both the electric and magnetic components as described. In the experiments in chapter 8 we utilise the effects of altering both the in-going and the out-going light polarisation to perform the experiments reported. However, we do not perform the experiments with the intention of separating out individual components or making measurements of them. Hence, we will not continue the derivation to this further stage as we do not make measurements of this type in chapter 8.

2.3 References

- [1] G. Attard and C. Barnes, Surfaces, Oxford University Press, Oxford, 1998
- [2] D.P. Woodruff and T.A. Delchar, Modern Techniques of Surface Science – Second Edition, Cambridge University Press, Cambridge, 1994
- [3] D.P. Woodruff, Prog. Surf. Sci. 57 (1998) 1
- [4] A. Zangwill, Physics at Surfaces, Cambridge Univ. Press. and references therein
- [5] NIXSW99#1 R.G. Jones, Dept. of Chemistry, University of Nottingham
- [6] D.P. Woodruff, B.C.C. Cowie, A.R.H.F. Ettema, J. Phys. Condens. Matter, 6 (1994) 10633
- [7] J.W. Copper, Phys. Rev. A 47(1993) 1841
- [8] B. Krassig, M. Jung, D.S. Gemmel, E.P. Gemmel, E.P. Kanter, T. LeBrun, S.H. Southworth, L. Young, Phys. Rev. Lett. 75 (1995) 4736
- [9] M. Jung, B. Krassig, D.S. Gemmel, E.P. Kanter, T. LeBrun, S.H. Southworth, L. Young, Phys. Rev. A 54 (1996) 2127
- [10] G. J. Jackson, B. C. C. Cowie, D. P. Woodruff, R. G. Jones, M. S. Kariapper, C. Fisher, A. S. Y. Chan and M. Butterfield, Phys. Rev. Lett 84 (2000) 2346

- [11] I. A. Vartanyants and J. Zegenhagen, *Solid State Comm.* 113 (2000) 299
- [12] J. J. Lee, C. J. Fisher, D. P. Woodruff and R. G. Jones, *Surf. Sci.* 494 (2001) 166
- [13] A. Sotiropoulos, P. Milligan, B.C.C. Cowie, M. Kadaodwala, *Surf. Sci.* 444 (2000) 52
- [14] S.M. Johnston, G. Rousseau, V. Dhanak, M. Kadodwala, *Surf. Sci.* 477 (2001) 163
- [15] P.F. Brevet, *Surface Second Harmonic Generation, Cahiers De Chimie, Presses Polytechniques et Universities Romandes*
- [16] M.C. Schanne-Klein, F. Hache, A. Roy and C. Flytzanis, *J. Chem. Phys* 108 (22) (1998) 9436
- [17] J.E. Sipe, D.J. Moss and H.M. van Driel, *Phys. Rev. B*, 35(3) (1987) 1129
- [18] H.W.K. Tom and G.D. Aumiller, *Phys. Rev. B*, 33 (12) (1986) 8818
- [19] H.W.K. Tom, C.M. Mate, X.D. Zhu, J.E. Crowell, T.F. Heinz, G.A. Somorjai and Y.R. Shen, *Phys. Rev. Lett.* 52 (1984) 348
- [20] J. E. Sipe, D. J. Moss and H. M. van Driel, *Phys. Rev. B*, 35 (1987) 1129
- [21] G. Lüpke, D.J. Bottomley and H.M. van Driel, *Phys. Rev. B*, 49 (24) (1994) 17303
- [22] M.Y. Jiang, G. Pajer and E. Burstein, *Sur. Sci.* 242 (1991) 306
- [23] F. Hache, H. Mesnil, and M.C. Schanne-Klein, *J. Chem. Phys* 115 (14) (2001) 6707

Chapter 3: Experimental

3.1 Introduction

This chapter gives a brief outline of the experimental apparatus and techniques used during the course of experiments presented in this thesis. Two separate UHV systems were used in the chemistry department at Glasgow. The first system was equipped with TPD, AES and LEED capabilities, while the second was used to obtain UPS and XPS data and in conjunction with the laser/optics set-up make SHG measurements. In addition to these systems, stations 6.3 and 4.1 of the Daresbury Laboratory were also used in the work presented here.

3.2 Experimental (TPD/AES Chamber)

3.2.1 Obtaining UHV Conditions

Figure 1 shows a picture of the TPD/AES chamber in Glasgow, with a schematic diagram of the pumping arrangement shown in figure 2. The chamber is equipped with LEED/AES and TPD capabilities and uses a system of four pumps to obtain UHV conditions. The chamber is initially pumped to a pressure of 1×10^{-2} mbar by a Edwards rotary pump (E2M8). At this pressure, the turbomolecular pump (Varian V-250) is switched on and is capable of pumping the chamber to a pressure of around 1×10^{-7} mbar. At this point, the entire chamber is baked, by placing ceramic heaters on the table (figure 1) and covering it with two clad steel covers. Separate heating tapes are used to bake the section below the table, with any exposed sections covered by aluminium foil. The ion pump (Varian Vac-Ion Plus 300 Triode) is equipped with a separate heater. Bake-out is stopped when the chamber reaches a pressure of 2×10^{-7} mbar. At this point the TSP is degassed by firing every ten minutes at a working current of 45-50 A for one hour. The ion pump is also degassed at this point by being switched on and off regularly over the course of several hours. In addition, it was found to work more effectively, if after bake-out, the pump was briefly used with approximately 1×10^{-5} mbar of argon leaked into the chamber. After this procedure was carried out, the ion pump was only used with the chamber already at a pressure of 3×10^{-9} mbar or below. The TSP and ion pumps were never operated at the same time as this was found to have a detrimental effect on the overall base pressure. After degassing of the ion gun (PSP Vacuum

Technology), QMS (RC RGA Hiden Analytical), LEED/AES electron gun (RVL, VG Microtech) and ion gauge, a base pressure of 2×10^{-10} mbar was obtained.

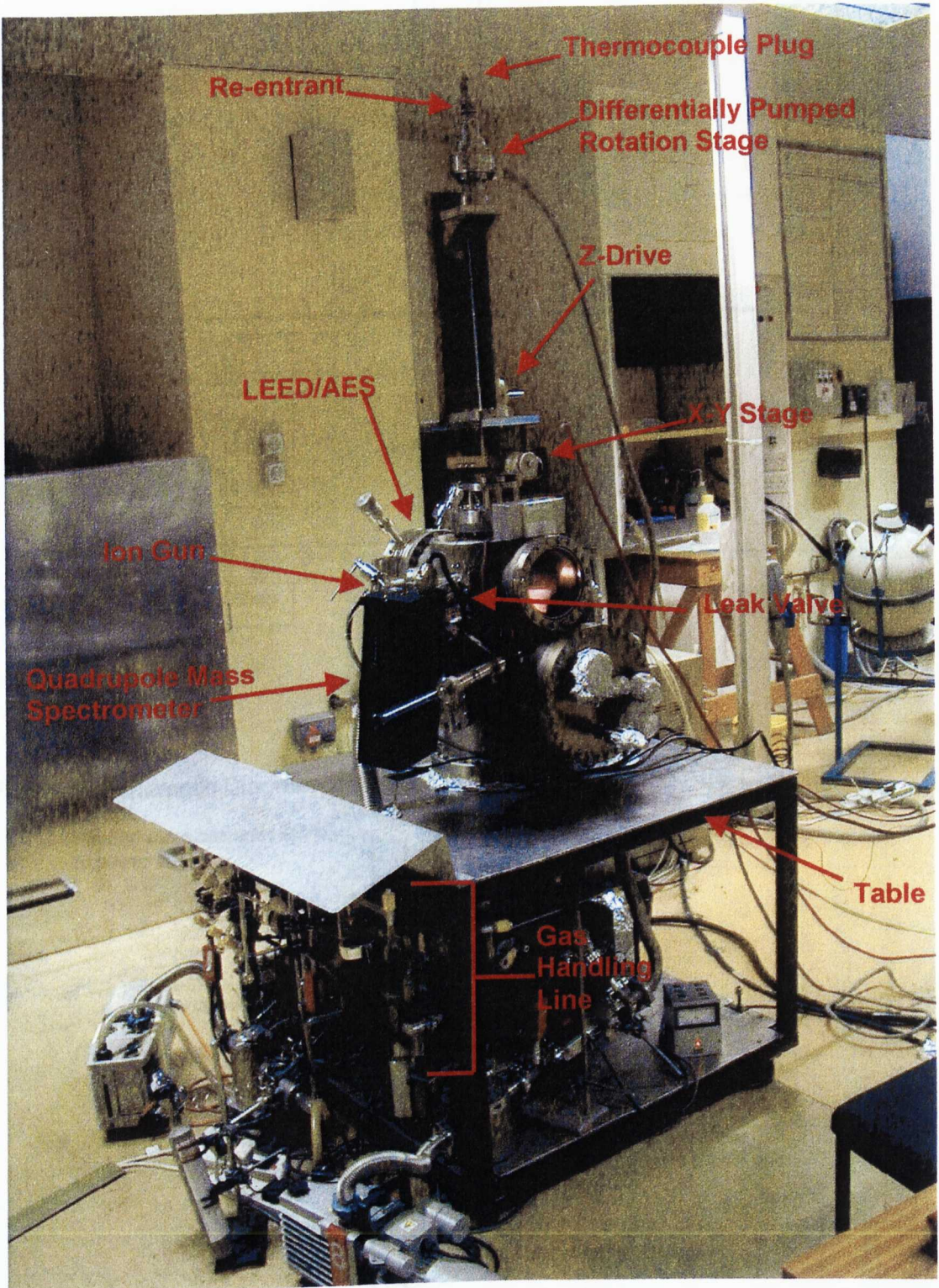


Figure 1. Labelled diagram of TPD/AES Chamber.

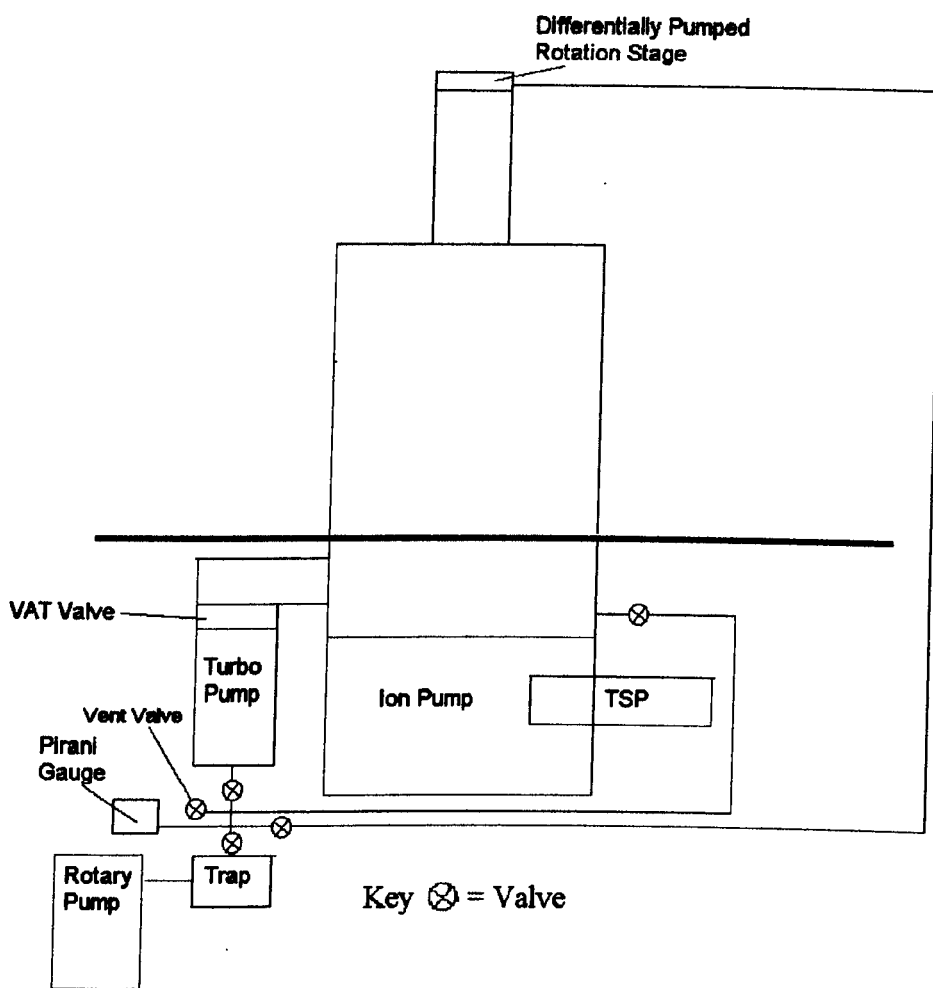


Figure 2. Schematic Diagram of pumping arrangement of TPD/AES Chamber.

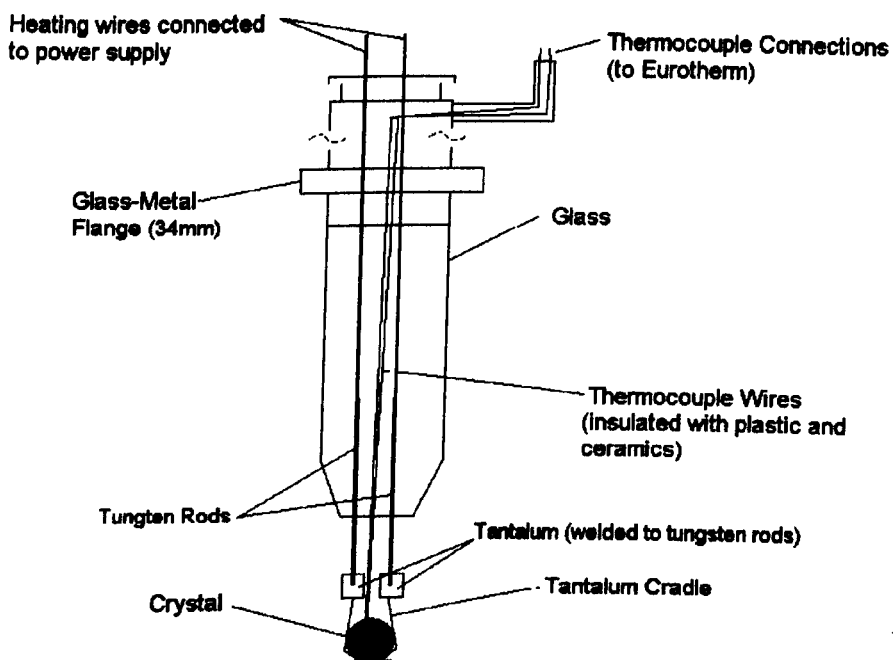


Figure 3. Schematic diagram of sample re-entrant from TPD/AES Chamber

3.3 Experimental Procedures for the TPD/AES Chamber

3.3.1 Sample Preparation

The Cu(111) single crystal was mounted onto the sample re-entrant shown in figure 3. The single crystals are held in a tantalum cradle that is in turn spot-welded to two tungsten rods protruding from a glass finger at the bottom of the re-entrant. This is then attached to the rest of the re-entrant, made from metal, by means of a glass to metal flange.

The crystal could be cooled to ca.100 K by filling the glass re-entrant with liquid nitrogen and heated resistively by means of the TSP power supply (CVT SNC 1) connected to the two tungsten rods. Both of these processes rely on good thermal contact between the crystal and the sample holder to achieve adequate heating and cooling of the crystal and care had to be taken to maintain good contact during sample holder construction.

Crystal temperature was measured by means of a chromel/alumel thermocouple made from two separate wires of chromel and alumel twisted together and inserted into a hole in the top of the crystal. These were then separated and insulated by means of ceramics and plastic tubing above the crystal and connected at the top of the chamber to two separate chromel/alumel connections. These were in turn attached to a Eurotherm box.

The copper crystals were cleaned in-situ by cycles of argon ion bombardment and annealing. Bombardment cycles lasted between 20 and 60 minutes with drain currents between 10 and 14 μ A. After bombardment samples were annealed for a period of 20 minutes at a temperature of 823 K, with crystal quality and cleanliness checked by AES and LEED.

Due to the extremes of temperature (i.e. 100-823 K) the re-entrant was subjected to, it was found that after a period of time stress on the welds or on the glass finger would cause either or both to fail. This would result in the manipulator having to be removed from the system and the glass finger/sample holder sections having to be repaired or replaced.

3.3.2 TPD

TPD experiments were performed by, firstly, dosing the crystal using a high precision leak valve attached to directional doser, at the appropriate temperature using gas from the gas handling line (figure 4). The gas-line is pumped by a combination of rotary pump (Edwards RV5) and diffusion pump (Edwards) to a base pressure of 1×10^{-3} mbar. During the course of these experiments both liquid and gas samples were used. In the case of gas samples, the line was pumped down and a pressure sufficient to fill the line was released into it. However, for liquid samples this was achieved by simply opening the line to the sample and allowing vapour into the gas line. In addition, prior to use, liquid samples were purified by three freeze/pump/thaw cycles, with purity subsequently checked using the QMS. In the case of both, samples were dosed onto the crystal using a "back-filling" method. This involved the crystal being above the directional doser with its back to the end of the tube. Exposures are measured in units of mbar.s, with pressures being measured by an ion gauge with no correction for sensitivity.

To perform TPD experiments, the crystal was then lowered into a position directly in front of the QMS. The QMS was fitted with a linear drive, allowing it to be positioned close to the face of the crystal (~2 mm). Furthermore, a shield containing a 3mm aperture was placed over the head of the QMS to prevent detection of gas molecules desorbing from the sample holder and not the crystal (figure 5). A heating rate of 0.5 K/s was used to collect TPD spectra.

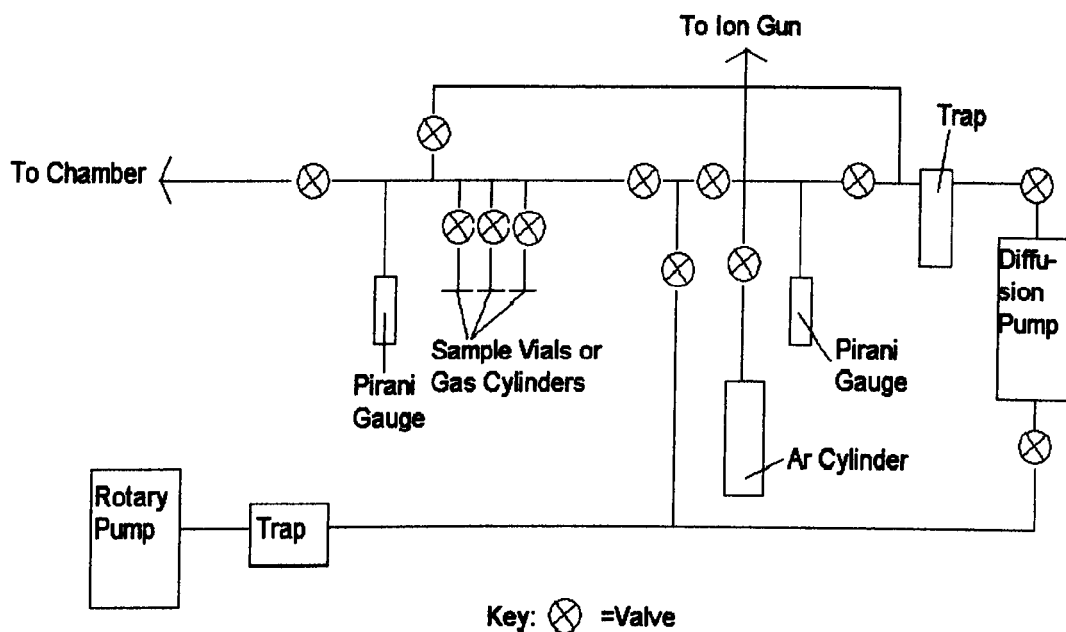


Figure 4. Schematic diagram of the TPD/AES Chamber gas handling line.

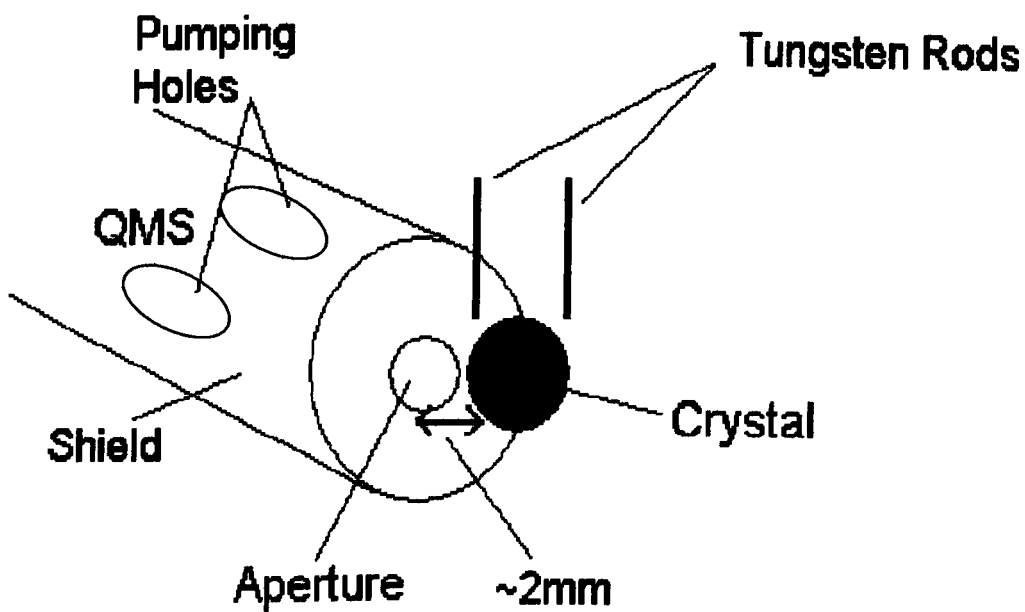


Figure 5. Crystal position during TPD experiments. Welds and thermocouple have been removed from the diagram for clarity.

3.3.3 AES/LEED

AES and LEED experiments were performed routinely to check for surface cleanliness and long range crystal order. These experiments were performed using an electron gun and retarding field analyser (RFA). The electron gun is operated in a range from 5-1000 eV for LEED and up to 3000 eV for AES experiments. Electrons are produced by a Thoria coated filament and are accelerated and focused into a beam by potentials applied to elements of the gun.

The RFA is fitted with a linear drive to allow it to be moved away from the crystal when not in use. However, over a period of time the mechanism was found to jam in place. As a result, the RFA was left in an extended position where the crystal could be moved close to the analyser rather than the other way around. This removed the need to use the retraction mechanism and posed no further problems during LEED, AES or TPD experiments.

RFA electron detection is described in the following sections.

3.3.3.1 RFA Electron Detection in LEED Experiments

A schematic diagram of an RFA electron detector is shown in figure 6. It effectively consists of a set of four meshes, labelled M1-M4, and a phosphor coated glass screen. In LEED mode, M1 has a negative potential (the retard potential) applied to it. This potential is set at a value close to that of the accelerating energy of the electron gun which, effectively prevents any inelastically scattered electrons from reaching the phosphor coated screen. The remaining three meshes are all earthed, with M2 and M3 usually connected by a central link. The screen is set at a potential of around +5 kV. The overall effect is for the RFA to effectively work as a high pass filter of inelastically scattered electrons allowing only elastically scattered electrons to make up the LEED pattern that can be viewed via the rear view port. LEED pictures can then be recorded using a CCD camera.

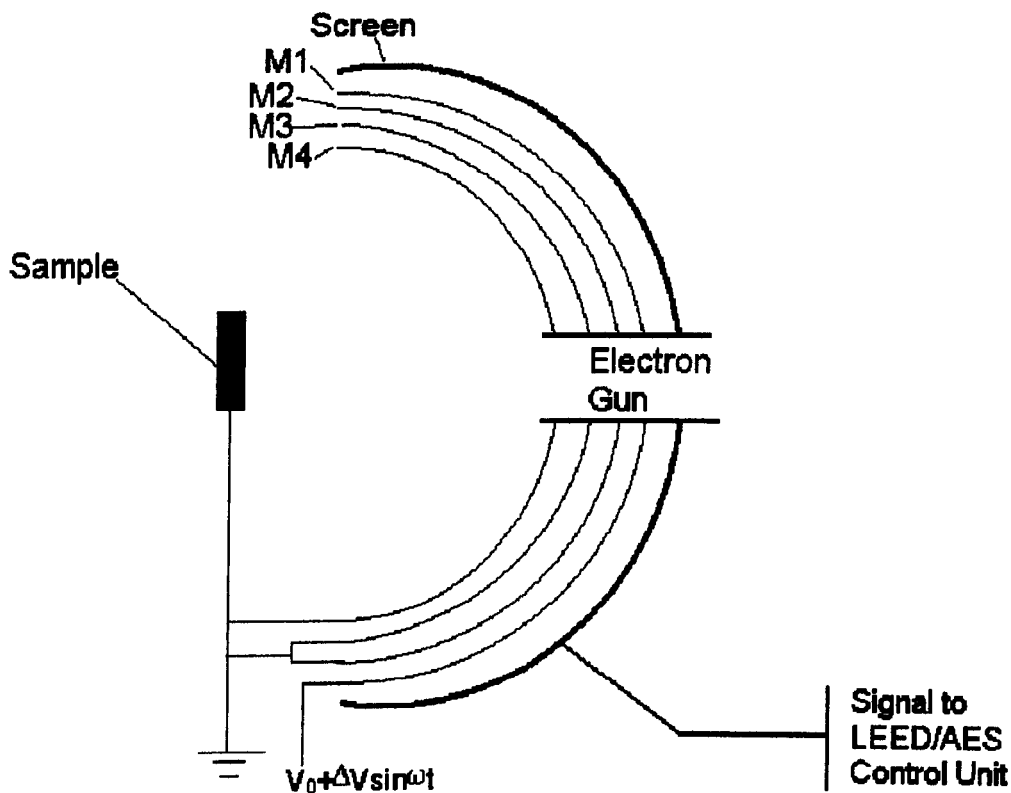


Figure 6. Schematic diagram of RFA.

3.3.3.2 RFA Electron Detection in AES Experiments

When the RFA is used in AES mode, meshes M2-M4 continue to be earthed. However, M1 has a ramped potential applied to it that is modulated sinusoidally. This mesh acts as a filter, with the effect of producing variations in current detected by the screen. Hence, if the electron energy distribution is $N(E)$ and the retarding potential is V_0 , then the current arriving at the detector will be given by the expression:

$$\int_{E_0}^{\infty} N(E) dE \quad (1)$$

In addition, an upper limit can be set on the integral, as the highest energy beam electrons emitted will have the primary beam energy, E_p :

$$\int_{E_0}^{E_p} N(E) dE \quad (2)$$

Hence, differentiation of the current gives the energy distribution $N(E)$. In practice, the experiment is performed by modulating the voltage on mesh M1 (i.e.

$V_0 + \Delta V \sin \omega t$), which in turn modulates the retarding potential E_0 . The current arriving at the screen can then be expressed as a sum of harmonics that is effectively a d.c. current, which is given by equation 2, and terms given in $\sin \omega t$, $\sin 2\omega t$, etc. The amplitude (A_1) of the first harmonic ($\sin \omega t$) is given by:

$$A_1 = \Delta E N(E_0) + \frac{\Delta E^3}{8} N''(E_0) + \frac{\Delta E^5}{192} N'''(E_0) + \dots \quad (3)$$

The amplitude (A_2) of the second harmonic ($\sin 2\omega t$) is given by:

$$A_2 = \frac{\Delta E^2}{4} N'(E_0) + \frac{\Delta E^4}{48} N'''(E_0) + \frac{\Delta E^6}{1536} N''''(E_0) + \dots \quad (4)$$

As is common in AES experiments the amplitude of the second harmonic was measured by means of a phase sensitive detector. There are two reasons for measuring the second harmonic signal as opposed to the first in AES experiments. Firstly, looking at a differentiated form of the second harmonic removes the constant background and amplifies any structure of interest, as well as separating any broad peaks into "double peaks". Secondly, substantial capacitive coupling takes place between the four meshes and the screen. This effect leads to a large first harmonic signal being measured due to the modulation of the capacitively coupled meshes. As a result, the second harmonic signal is measured in experiments. In all experiments reported here a modulation voltage of 4.4 V_{p-p} is used.

3.4 Experimental (UPS/XPS Chamber)

3.4.1 Obtaining UHV Conditions

Figure 7 shows a picture of the UPS/XPS chamber in Glasgow, with a schematic diagram of the pumping arrangement shown in figure 8. The chamber is equipped with a twin anode X-ray source (VG Microtech), UV source (VG Microtech) and a CLAM 2 electron energy analyser (VG Microtech), for performing X-ray and ultraviolet photoelectron spectroscopies. In addition, a quadrupole mass spectrometer (VG Gas) is installed for residual gas analysis, LEED optics (RVL, VG Microtech) and an EX03 ion gun (VG Microtech) for sample bombardment. The "pot" section at the bottom of the chamber is used for performing SHG experiments.

UHV conditions are obtained by a system of three pumps. Initially, the chamber is pumped to a pressure of 1×10^{-3} mbar by an Edwards rotary pump. At this pressure, the diffusion pump (Edwards EO4K) is then used and is capable of reducing the pressure to ca. 1×10^{-7} mbar. To obtain UHV conditions the chamber is encased in insulated metal covers and ceramic heaters (figure 7) are used to bake the chamber. The bakeout is removed when a pressure of around 2×10^{-7} mbar is achieved, which usually takes around 16 hours. When bakeout is complete, the TSP is fired continuously for five minutes, with the operating current gradually increased until the working current of 48 A is reached. After this, the TSP is fired for 60 seconds, once every 10 minutes in the first post bakeout hour, and subsequently once every 3 hours under normal operation. After degassing of the sample, QMS, X-ray source, ion gun, LEED electron gun and ion gauge a UHV base pressure of 1×10^{-10} mbar is achieved.

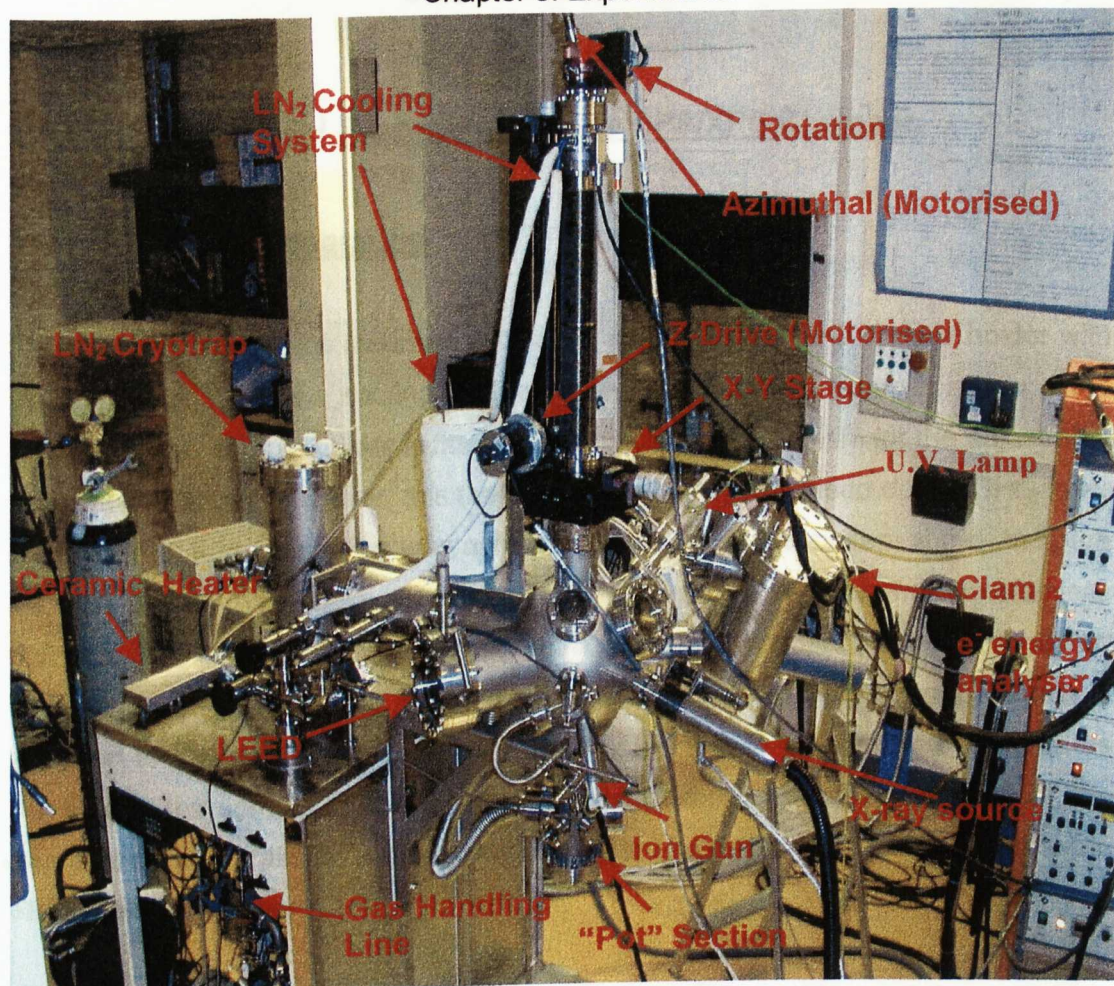


Figure 7. Labelled diagram of UPS/XPS Chamber.

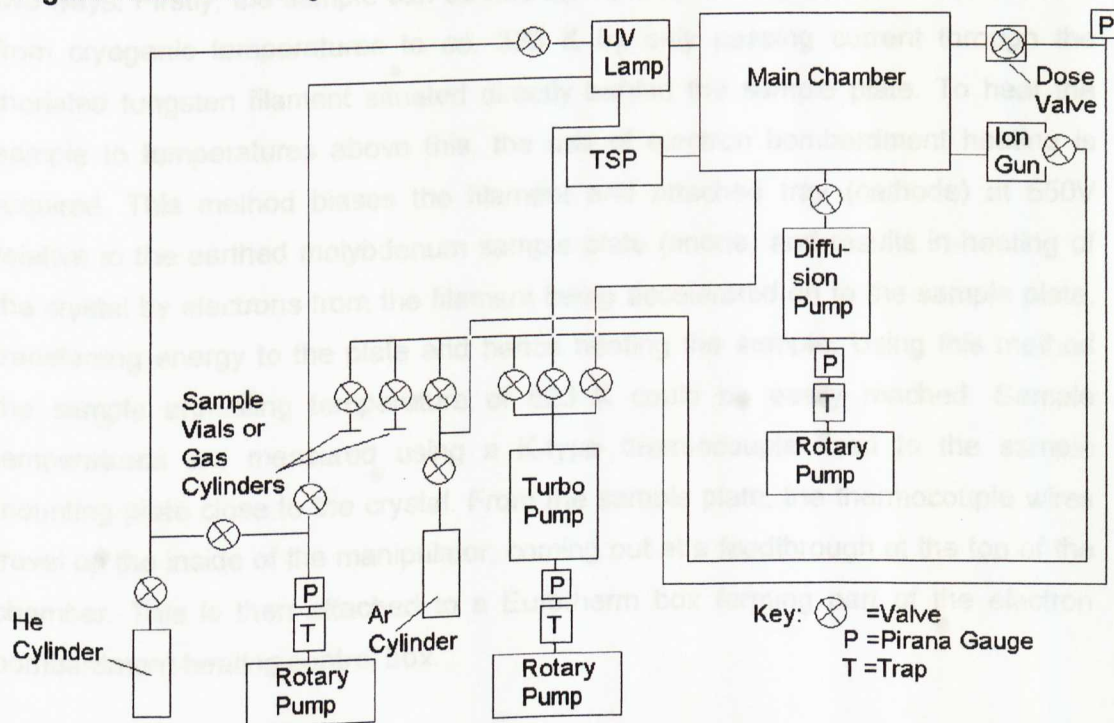


Figure 8. Schematic Diagram of pumping arrangement of UPS/XPS Chamber.

3.5 Experimental Procedures for the UPS/XPS Chamber

3.5.1 Sample Preparation

The Cu(111) crystal was mounted onto a VG manufactured SH2 sample holder with optional liquid nitrogen cooling and electron bombardment sample heater fitted (figure 9). This sample holder is fitted with a precision mechanism for the adjustment of azimuthal angle. However, this feature was generally only used during SHG laser experiments. Sample cooling was achieved by means of the system shown in figure 10. This system passes liquid nitrogen, condensed from dry gas, through stainless steel capillary tubing within the vacuum chamber, to a copper evaporator mounted close to the copper sample. In addition, flexible, high conductivity copper braid is attached to the evaporator, which allows the free end to be attached as close as possible to the sample to achieve lowest possible temperatures. Unfortunately, the attached copper braid limits the maximum angle of rotation of the azimuthal drive to 180° in either direction.

The electron bombardment heating accessory can be used to heat the sample in two ways. Firstly, the sample can be heated from room temperature to *ca.* 473 K or from cryogenic temperatures to *ca.* 333 K by only passing current through the thoriated tungsten filament situated directly behind the sample plate. To heat the sample to temperatures above this, the use of electron bombardment heating is required. This method biases the filament and attached tray (cathode) at 650V relative to the earthed molybdenum sample plate (anode) and results in heating of the crystal by electrons from the filament being accelerated on to the sample plate, transferring energy to the plate and hence heating the sample. Using this method the sample annealing temperature of 823 K could be easily reached. Sample temperatures are measured using a K-type thermocouple fixed to the sample mounting plate close to the crystal. From the sample plate, the thermocouple wires travel up the inside of the manipulator, coming out at a feedthrough at the top of the chamber. This is then attached to a Eurotherm box forming part of the electron bombardment heating control box.

The SH2 sample holder assembly is fixed to an Omniax Translator (MX Series, VG) allowing crystal movement in X, Y and Z planes as well as rotation (polar angle) and operation of the azimuthal rotation of the sample holder. Movement of the azimuthal and polar angles and translation in the Z direction is achieved by the use of three

rotary motion drives (RD, VG), controlled by computer, allowing for control of fine sample movements. X and Y motion is controlled manually using micrometers.

The copper crystals were cleaned in-situ by cycles of argon ion bombardment and annealing. Bombardment cycles lasted between 20 and 60 minutes with drain currents between 5 and 10 μA . After bombardment, samples were annealed for a period of 20 minutes at a temperature of 823 K, with crystal quality and cleanliness checked by XPS, UPS and LEED.

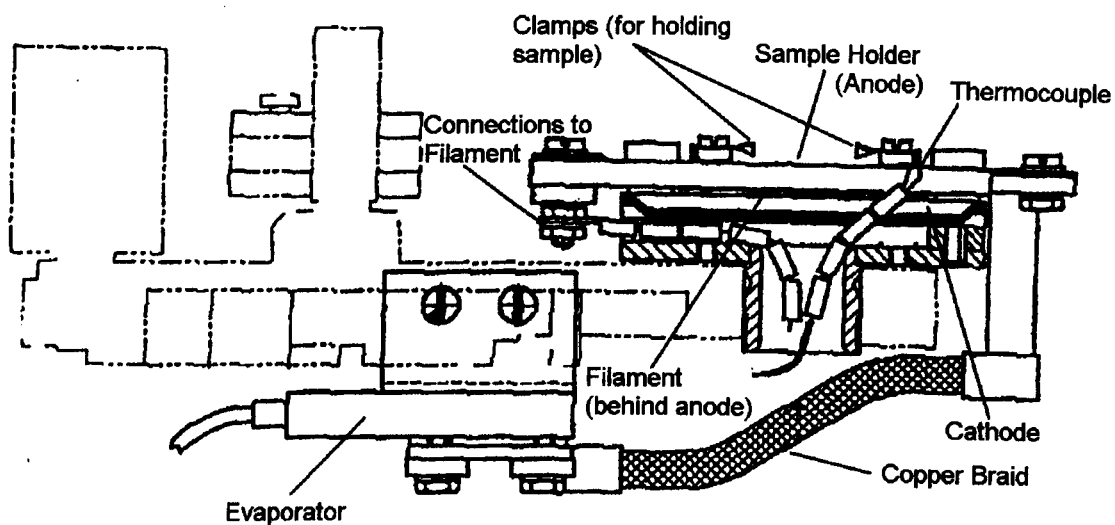


Figure 9. Schematic diagram of SH2 sample holder. Adapted from ref. 1.

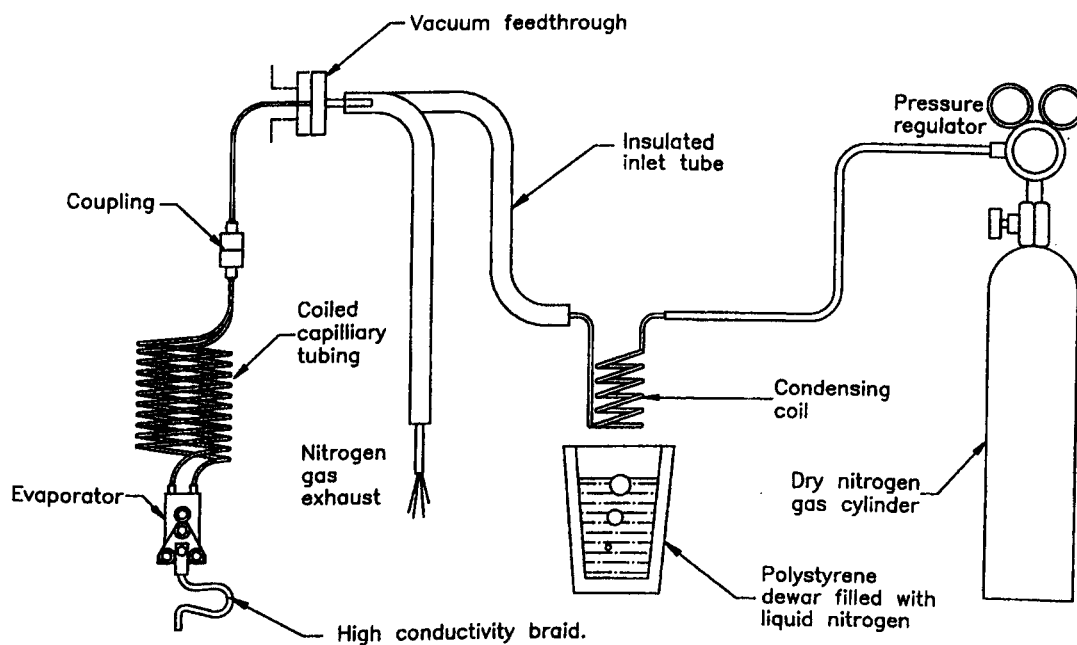


Figure 10. Schematic diagram of liquid nitrogen cooling system. Adapted from ref.

2.

3.5.2 General Experimental Procedures

XPS and UPS experiments were performed on samples prepared by dosing the appropriate amount of gas onto the sample at a suitable adsorption temperature from the gas handling line (figure 8). The gas handling line is pumped to a pressure of 1.3×10^{-3} mbar by an Edwards (RV5) rotary pump with lower pressures being reached should the attached turbomolecular pump (Varian) be used. The gas line was filled and gas subsequently dosed using the same methods as in section 3.3.2 for TPD measurements. XPS and UPS experiments could then be performed. Commonly XPS and UPS experiments took the form of sequential annealing experiments where, after dosing, the sample is heated to a temperature of interest and XPS or UPS spectra are subsequently recorded. Generally, during sequential annealing experiments, use of electron bombardment heating was kept to a minimum as it was found that its use could induce non-thermal reactions. This was attributed to electrons spilling around the sample plate, causing either a degree of polymerisation or dissociation of organic molecules adsorbed on the surface.

3.5.3 XPS

XPS experiments are performed using an unmonochromatised twin anode X-ray source (figure 11). X-rays are generated by electrons, emitted from one of two thorium coated tape filaments maintained close to earth potential, striking an anode maintained at a potential of +15 kV. The anode is constructed of copper coated in magnesium on one side and aluminium on the other. The X-rays produced arise from the filling of core holes generated by the incident electron beam superimposed on a continuum background due to bremsstrahlung. The use of magnesium and aluminium results in the dominant feature of the electron energy spectrum being due to the emission of K_{α} photons. For aluminium this gives an X-ray line at 1486.6 eV and 1253.6 eV for magnesium, although other X-ray lines are also present but are generally less than 1 % of the main K_{α} line. In the experiments presented here only the magnesium anode was used. A thin aluminium foil window is in place over the end of the X-ray source. This has two effects, firstly, it acts as a partial filter of unwanted X-ray lines, particularly oxygen and secondly, it prevents the anode potential affecting electrons in the analysis region. To improve photon flux from the source, the source is mounted on a 25mm linear retraction mechanism. This allows

the X-ray source to be extended into the chamber and placed close to the crystal (~ 5 mm) during XPS experiments and retracted clear when not in use. The anode is water cooled during experiments, with water supplied from a Model 8561 water box. The high voltage connection to the X-ray source also extends from the water box, which is in turn connected to the X-ray control unit.

Use of an unmonochromatised source of this type does have disadvantages. Although the main X-ray line generated is the K_{α} , other lines are also present, although small. These have the effect of causing satellite peaks in XPS spectra, which can be inconvenient or cause difficulties in interpretation. In addition, the dominant K_{α} of both aluminium and magnesium has a full width at half maximum of ~ 1.5 eV. This places a limit on the minimum line width of photoelectron features that we wish to detect. Hence, it is not possible to detect very small changes of width and position of photoelectron peaks.

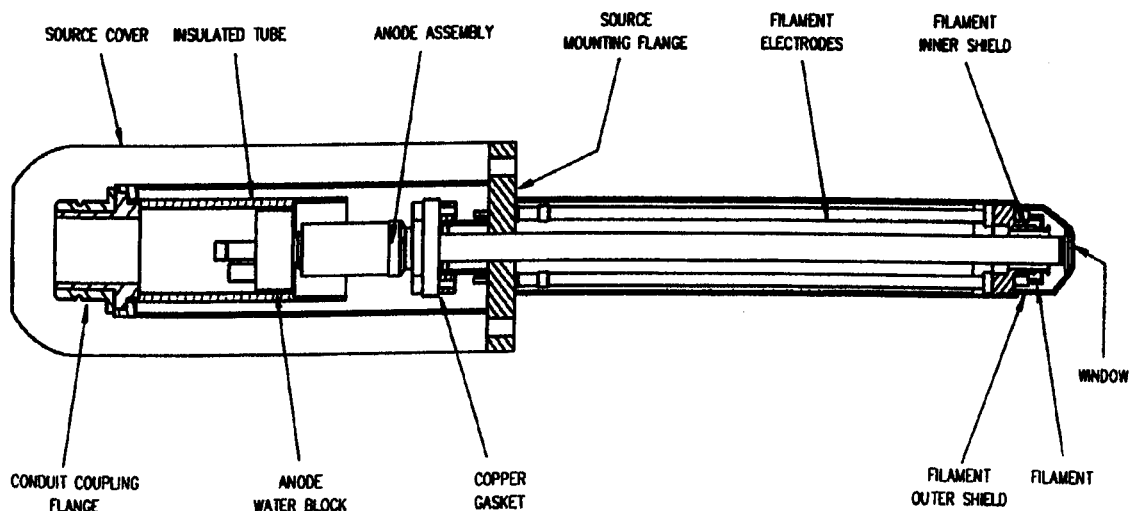


Figure 11. Schematic diagram of X-ray source. Adapted from ref. 3.

3.5.4 UPS

UPS experiments were performed using a VG Microtech gas discharge lamp (figure 12), using helium gas as the gas discharge medium. Discharge is achieved by slowly leaking gas into the lamp while an EHT start voltage of 5 kV is applied between the anode and cathode (situated at opposite ends of the quartz tube). The lamp is differentially pumped (figures 8 and 12) using a combination of rotary pump

(Edwards RV3) and turbomolecular pump (Varian, shared by the gas line) while gas is being leaked into the system. Chamber pressures of 1×10^{-7} mbar are usually required to obtain discharge after which the gas pressure is reduced to ca. 1.4×10^{-8} mbar and the operating voltage is automatically reduced to 600 V. At this pressure the helium gas fluoresces, producing a He I line with an energy of around 21.2 eV. He I discharge is used in all experiments reported here. During the course of experiments it is important to monitor helium pressure as reducing the pressure results in a greater proportion of He II to He I lines being produced by the lamp, altering UPS spectra. In addition, changes in helium pressure were found to alter the intensity of UP spectra obtained.

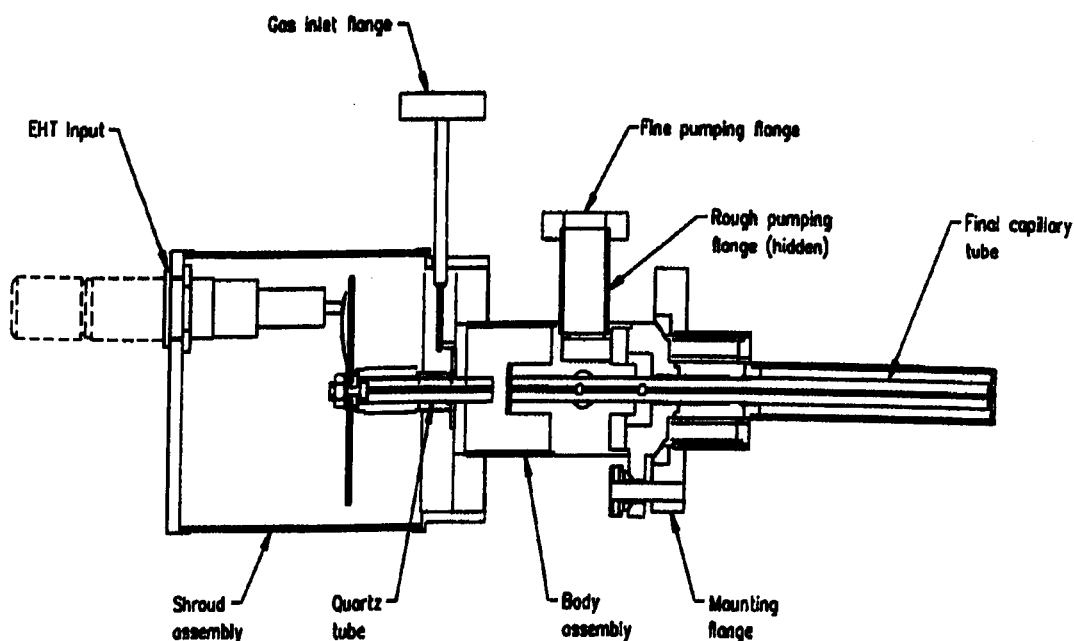


Figure 12. Schematic diagram of U.V. lamp. Adapted from ref. 4.

3.5.5 CHA Electron Detection in UPS and XPS Experiments

Electron detection in UPS and XPS experiments is achieved using a concentric hemispherical analyser (CHA). A schematic diagram of a CHA is shown in figure 13.

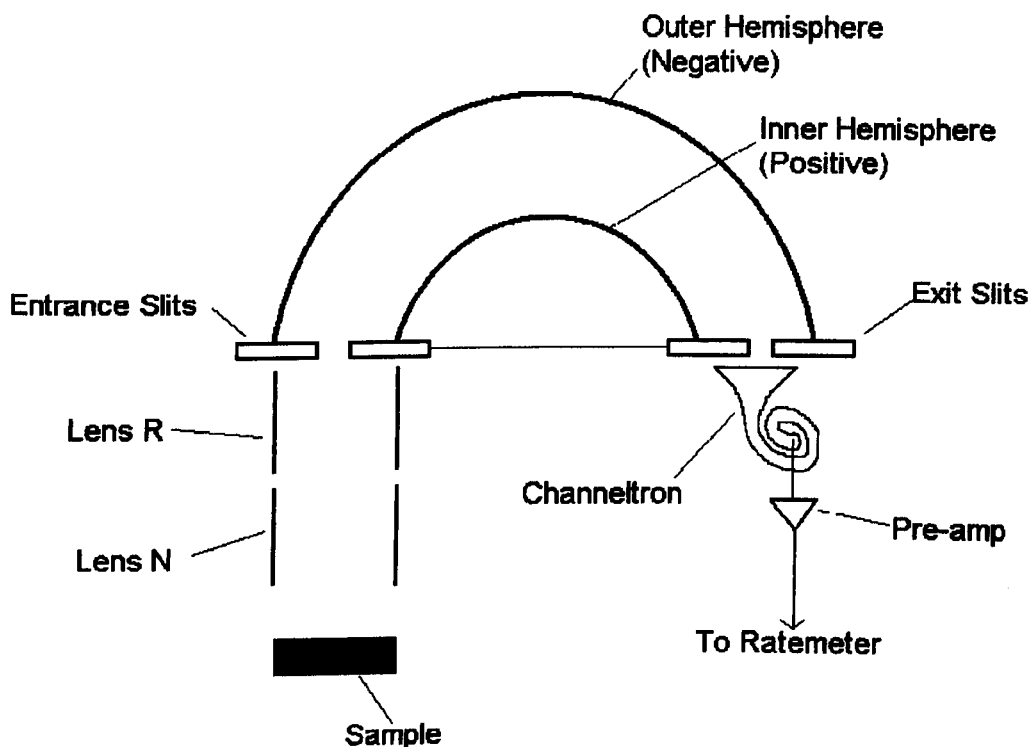


Figure 13. Schematic diagram of CHA.

The basic function of the analyser is to act as a narrow band filter, allowing only electrons of a particular energy to pass through. In practice this is achieved by retarding electrons coming into the analyser using the lenses R and N. Retarding the entering electrons has the effect of improving the resolving power of the analyser. Electrons then pass between two concentrically mounted hemispheres with equal and opposite potentials applied to them with respect to the retard potential. This causes high-energy electrons to strike the outer hemisphere (negative) while low energy electrons strike the inner hemisphere (positive) leaving only electrons of a desired energy to pass through to the channeltron. In reality, a spread of energies is passed through to the channeltron for analysis. This is effectively the intrinsic resolving power of the analyser and is governed by a combination of the analyser's physical design, geometry, and the potential difference applied between the hemispheres.

Electrons passing through the exit slits enter a single channeltron which acts as detector for the system. The channeltron is constructed of glass with the internal surfaces coated in a resistive material across which a potential is applied. Electrons striking the internal surface of the channeltron produce secondary emission that continues along the multiplier with an avalanche effect capable of generating 10^8 electrons from a single electron entering the channeltron. The entrance to the channeltron is maintained at a potential similar to the retard potential applied by the lenses. This varies along with the retard potential and effectively maintains a constant potential across the channeltron during scanning. The signal from the channeltron passes through a pre-amp and is then detected by a ratemeter.

Throughout the course of experiments the CHA was used in 1:1 mode, where both R and N lenses are set at the same potential. This effectively means a sample area equivalent to the size of the entrance slit is analysed. In addition all experiments were performed with the analyser in constant analyser energy (CAE) mode. In this mode of operation the pass energy is kept constant regardless of the kinetic energy. (Both 1:1 and CAE modes are generally accepted as producing best results for XPS). The pass energy used during all XPS experiments was 50 eV, while UPS experiments were performed with a pass energy of 10 eV.

XPS experiments were performed with the sample orientated 25° off normal emission with respect to the analyser and also in a position 25° off normal with respect to the X-ray source. This position is chosen as it is mid way between the X-ray source and the analyser, allowing both the analyser to be focused on the sample and the source to be moved close to it. UPS were performed with the sample normal to the analyser in all experiments reported here and with radiation from the helium lamp incident at 47° . Before commencing experiments the position of the sample was optimised with respect to the analyser by monitoring the number of counts produced at particular kinetic energies corresponding to the Cu 2s photoelectron peak or the d-orbital peak obtained during XPS or UPS respectively. The analyser is also equipped with magnetic trim coils that can be used to screen out the effects of magnetic fields within the analyser and with manual control over lens voltages to correct for variations in sample distances.

3.6 Experimental (SHG Apparatus)

Enantio-sensitive second harmonic generation experiments reported in chapter 8 were performed using the optical set up shown in figure 14. Experiments were performed using 8-12 ns pulses generated by a Nd: YAG laser (Quanta Ray-Spectra Physics GCR Series) producing fundamental 1064 nm radiation at a repetition rate of 10 Hz and ~3.6 mJ / pulse. The fundamental beam is passed first, through a polariser, followed by a $\lambda/2$ plate, allowing the incident polarisation to be varied. The incoming beam is subsequently defocused to 10 mm in diameter and passed through 532 nm filters, to remove any SH light produced by the optical elements themselves, before striking the copper surface at an angle of 60° with respect to the surface normal. The SH light generated is detected at an angle of 60° with respect to the surface normal after passing through a 1064 nm filter, polariser, and lens. The first of these, the 1064 nm filter, removes any light not undergoing SHG from the reflected beam, allowing detection of only 532 nm radiation. The polariser allows us to select the polarisation of the radiation we detect and the camera lens is used to focus the beam into the spectrograph and intensified CCD (Holospec, Keiser Optical Systems).

The system operates using a signal gating mechanism, with the time of the pulse delay and pulse width controlled by computer. This effectively means that we only record spectra in a small window after the laser pulse is triggered rather than recording background noise between pulses. In addition, background spectra recorded before laser light is passed into the chamber is automatically subtracted from the spectra being recorded during experiments by the data acquisition software. Due to the small signal levels associated with SHG experiments, spectra are recorded by accumulating the signal from a number of laser pulses, over a period of time.

Focussing and alignment of the system is achieved by use of a quartz plate. This is inserted just prior to the UHV system and generates a large SH signal. This signal is then focussed and optimised by making changes to the sample position, camera lens and detector focus until a clear, well defined SH peak is observed. The quartz plate is then removed and SHG measurements performed.

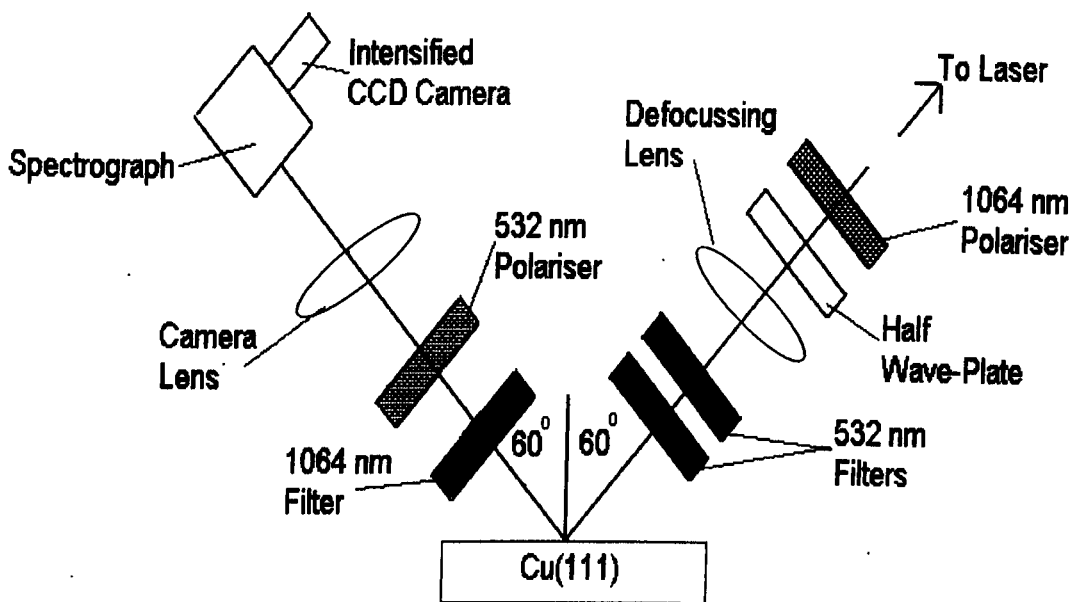


Figure 14. Schematic diagram of SHG optical layout.

3.7 Experimental (SRS Station 6.3)

3.7.1 System Design

NIXSW experiments described in chapter 4 were performed at the Central Laboratories of the Research Councils (CLRC) laboratory at Daresbury, at station 6.3 of the Synchrotron Radiation Source (SRS). Both the beamline and UHV end-chamber of this station have been described in detail elsewhere [5,6]. Briefly, radiation from the storage ring passes through a set of horizontal jaws, used to define the beam, followed by a filter rack consisting of 10 carbon foils. The purpose of the foil is to filter out the UV/visible components of the radiation, before reaching the monochromator. The beam is then focussed by a toroidal pre-mirror into the Bird and Tole monochromator. The desired energy is selected by movement of one of three pairs of crystals. For the purposes of the study in chapter 4, InSb(111) crystals were used providing energy in the range 1780-5200 eV. The X-ray beam leaves the monochromator and passes into the I_0 chamber. In this section, the beam current leaving the monochromator (I_0') is measured using beryllium foil, passes through a set of vertical and horizontal jaws, allowing the beam to be defined further, and is

finally measured by a second beam current monitor designated I_0 before entering the UHV end station. A schematic diagram of the beamline is depicted in figure 15.

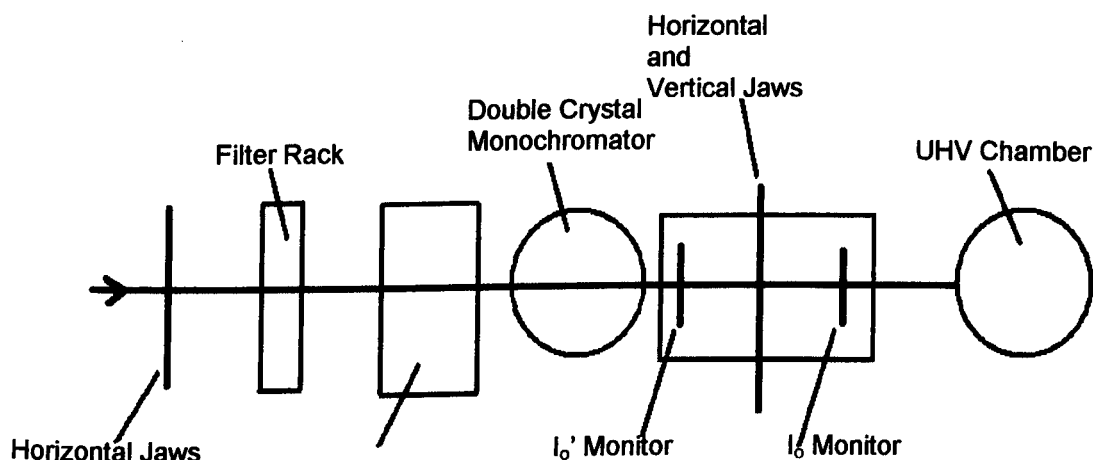


Figure 15. Schematic diagram of beamline 6.3.

The UHV end-chamber is equipped with LEED optics, a concentric hemispherical analyser (CHA) for photon-stimulated AES and X-ray photoelectron spectroscopy (XPS), as well as standard argon ion bombardment facilities. The sample is cooled to cryogenic temperatures (*ca.* 110 K) and annealed at 923 K using electron bombardment and liquid nitrogen cooling similar to that in section 3.4.2.1.

The intensity of the X-ray beam at the Daresbury Laboratory decreases over time and as a result, all NIXSW and XPS data acquired during the course of an experiment must be normalised to take account of this. A beam monitor exists within the chamber, close to the crystal, but as this is used as a measure of the XSW reflectivity in NIXSW experiments it cannot be used as a direct measure of beam current. Hence all NIXSW and XPS raw data presented here is divided by the beam current from the I_0 monitor located prior to the chamber.

3.7.2 Experimental Procedures

The Cu(111) sample was cleaned by cycles of argon ion bombardment (15 min, 3kV) and annealing to 923 K. Surface quality and cleanliness were verified by XPS and LEED.

Furan and THF were stored in a stainless steel gas handling line. Before use, samples were purified by three freeze/pump/thaw cycles. As in the corresponding

TPD experiments, samples were prepared by "back filling" of the UHV chamber while the crystal is maintained at cryogenic temperatures. Monolayer coverages were then obtained by heating the sample to temperatures appropriate to desorb multilayers (as indicated by TPD data) signalled by a significant decrease in XPS intensity.

NIXSW experiments were then performed on both (111) and ($\bar{1}11$) crystal planes by monitoring of the O1s photoemitted electrons.

3.8 Experimental (SRS Station 4.1)

3.8.1 System Design

Photoemission experiments described in chapter 7 were performed at the Central Laboratories of the Research Councils (CLRC) laboratory at Daresbury, at station 4.1 of the Synchrotron Radiation Source (SRS). Both the beamline and UHV end-chamber of this station have been described in detail elsewhere [7-9]. Briefly, the beamline is designed to operate in the energy range of $14 < h\nu < 170$ eV. This makes the beamline ideally suited for the study of shallow core and valence levels. The beamline is fitted with three in-situ interchangeable diffraction gratings, which are selected according to experimental requirements. Throughout the course of experiments grating two was used as all experiments were performed at 120 eV and this grating was the most suitable for use at this energy.

A schematic diagram of the beam line is shown in figure 16. Synchrotron radiation passes through both horizontal and vertical mirrors, being directed into the entrance slits and monochromator. The diffracted beam then passes through a further set of slits, and is directed into the chamber by a refocusing mirror.

The UHV end-chamber is equipped with LEED optics, UV lamp and X-ray source. A CLAM 2 concentric hemispherical analyser (CHA) was used to record all valence and core level spectra. In addition, the chamber is fitted with standard e-beam sample heating and argon ion bombardment facilities similar to those described in section 3.4.2.1.

No facilities were available to automatically record the intensity of the beam during experiments. Hence, beam currents were recorded manually at the start and end of

recording spectra and were found to not change significantly over the course of the relatively short scan times. However, to normalise the spectra recorded on different days/periods of time they have been divided by the manually recorded beam current at the start of each scan monitored prior to entering the chamber.

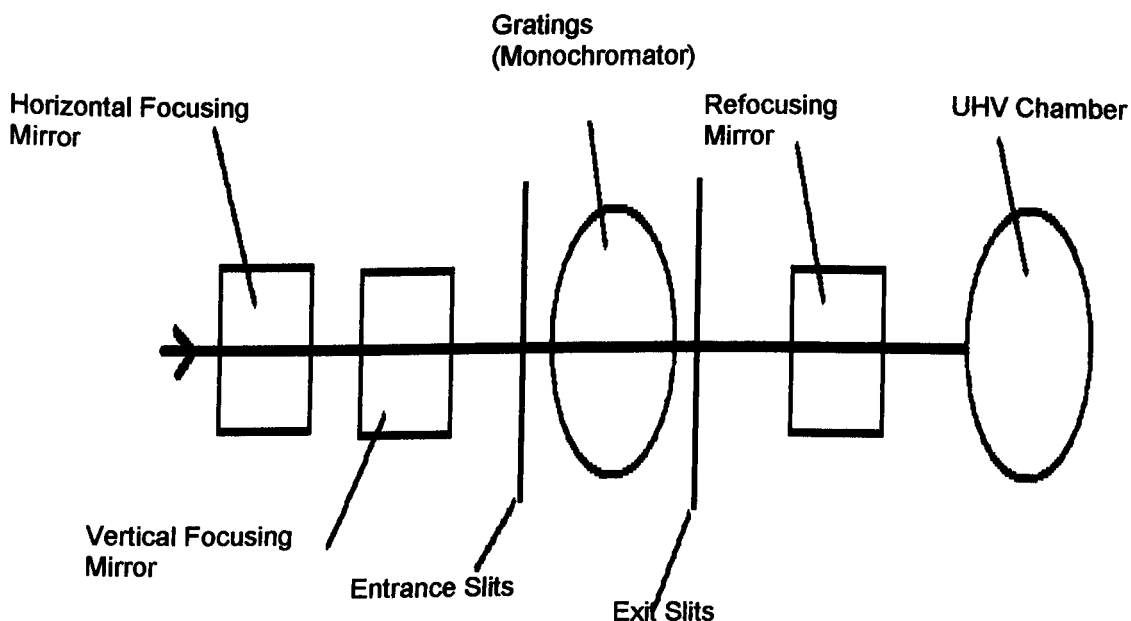


Figure 16. Schematic diagram of beamline 4.1.

3.8.2 Experimental Procedures

Al₂p X-ray photoemission spectra were recorded at normal emission with respect to the analyser and at an angle of 50° with respect to the photon beam. All Al₂p spectra were recorded using a photon energy of 120 eV. The O1s X-ray photoelectron spectra were recorded using the X-ray source at an angle of 73° with respect to the surface normal, at a photon energy of 1256.6 eV, and at 42° off normal with respect to the analyser. The core level spectra are background subtracted and are presented in binding energy, which was referenced to the E_F , determined from valence region scans performed immediately after core level spectra.

The NiAl(110) crystal was cleaned by cycles of argon ion bombardment (30 min, 3 kV) followed by annealing at 1100 K and repeated flashing to 1370 K over a 30 min

period. Crystal quality and cleanliness was verified by XPS, LEED and a sharp well defined Al2p photoemission spectrum.

Oxygen exposures from the stainless steel gas handling line were conducted in two ways. Initial adsorption experiments were performed by admitting oxygen into the main chamber at pressures ranging from 1×10^{-8} mbar.s to 1×10^{-6} mbar.s, dependent on dose, at ca. 300 K. Multiple adsorption and annealing cycles were performed by admitting oxygen into the chamber at a pressure of 1×10^{-6} mbar.s for 20 minutes at ca. 823 K followed by subsequent annealing to ca. 1273 K. Oxygen exposures were carried out with the crystal in a line of sight position and are quoted in units of mbar.s with pressures being measured by an ion gauge, with no correction for sensitivity.

3.9 References

- [1] Vacuum Generators Instruction Manual UI 428 94H
- [2] Vacuum Generators Instruction Manual UI 4208A
- [3] Vacuum Generators Instruction Manual, Twin Anode XR3E2 X-ray Source Systems, HA030001
- [4] Vacuum Generators Instruction Manual, Ultraviolet Sources, HA030005
- [5] A.A. MacDowell, D. Norman, J.B. West, J.C. Campuzano and R.G. Jones, Nuclear Instrum. Meth. Phys. Research A 246 (1986), 131
- [6] A. A. MacDowell, D. Norman, and J.B. West, Rev. Sci. Instrum. 57 (11) (1986), 2667
- [7] V.R. Dhanak, A.W. Robinson, G. van der Laan and G. Thornton, Rev. Sci. Instrum. 63 (1992) 1342
- [8] V.R. Dhanak, A.G. Shard, C.A. Muryn, P.L. Wincott and G. Thornton, J. Synchrotron Rad. 569 (1998) 569
- [9] http://srs.dl.ac.uk/info/STATION_INFO/stat4_1.html

Chapter 4: TPD and NIXSW Investigation of Furan and Tetrahydrofuran Adsorption on Cu(111)

4.1 Introduction

The adsorption of furan and tetrahydrofuran (THF) on Cu(111) is of interest from both practical and fundamental aspects. The adsorption of heterocyclic organic molecules on metal surfaces provides clear insights into the mechanisms involved in the heteroatom removal process extensively used in the petrochemical industry in the refining of petroleum feedstocks [1]. In addition, furan and other five-membered aromatic heterocycles are increasingly being studied for use in the electronics industry as conducting polymers [2]. These have a number of possible uses in device fabrication as components of integrated circuits.

From a fundamental aspect this study is of interest as it allows comparison of the bonding of an aromatic heterocycle with its non-aromatic equivalent. There has been a significant amount of work performed on studying the adsorption of aromatic heterocycles on metal surfaces. For example furan and thiophene have been shown to form bonds to metal surfaces involving the interaction of both the heteroatom and the aromatic π -system [3,4]. In the bonding of thiophene on Cu(111) [3], this dual interaction creates a coverage driven phase transition on the surface. The molecule can bond to the surface with the aromatic ring parallel to it, at low coverage, or in a more upright orientation, at higher coverages. A similar model has been suggested by Sexton [4] for the adsorption of thiophene on Cu(100). This study compared the adsorption of thiophene, furan and pyrrole on Cu(100) using TPD and EELS. Sexton proposed that furan forms a "bilayer" on the Cu(100) surface, with furan initially adsorbing in a flat lying orientation parallel to the surface and then additional furan molecules adsorbing on top of the first layer in an orientation perpendicular to the surface. The adsorption of furan on Cu(100) is molecular and reversible.

On the Ag(110) [5] surface, adsorption of both furan and 2,5-dihydrofuran were shown to be molecular and reversible also. On these surfaces however, there is no evidence for a second layer forming after monolayer adsorption of either molecule. In addition, furan adsorption has been examined on a number of other, more

reactive, transition metal surfaces. On these surfaces furan adsorption is no longer reversible, and hence is significantly different to the present study.

In contrast to aromatic heterocycles there have been very few studies of the saturated equivalents. The adsorption of tetrahydrothiophene (THT) on Mo(110) [6] has been investigated as part of a wide range study of the mechanism of the hydro-desulfurisation process. Unlike thiophene, no evidence was found to suggest that THT adopted more than a single adsorption geometry on the surface. The only previous study of THF adsorption performed by Wang and co-workers [7] examined its adsorption on the Al(111) surface. This study concluded that THF polymerises on the Al surface, hence making its adsorption significantly different to the adsorption of THF on Cu(111) in the present study. No other studies of THF adsorption have been performed.

In this study, we have used the techniques of TPD and NIXSW to perform the first structural study of the adsorption of furan and THF on Cu(111) in an attempt to understand the effects that saturating the aromatic ring of furan has on its interaction with the surface. Furan was found to adsorb in two chemisorbed states, which we have labelled α and β states, followed by multilayer adsorption, while THF was found to form only a single chemisorbed layer. Neither THF nor furan was found to decompose on the Cu(111) surface. After initial characterisation using TPD, NIXSW experiments were then performed on the chemisorbed THF and α -state furan layers. THF was found to adsorb in an atop adsorption site, with an oxygen to copper distance of 2.39 ± 0.04 Å, while furan adopts a displaced atop position with an oxygen to copper separation of 3.08 ± 0.08 Å. The displaced atop adsorption site of furan is attributed to the effects of adsorbate-adsorbate interactions, which are significant compared to the strength of the weak furan to copper interaction. The adsorption of THF is significantly stronger than that of furan, which we propose is due to the influence of C-H...Cu interactions between THF and the copper surface.

4.2 Results

4.2.1 Initial Characterisation – TPD

Initial characterisation experiments of the adsorption of furan and THF on Cu(111) were performed in Glasgow (TPD/AES Chamber) using TPD, AES and LEED.

These experiments were then followed up with NIXSW experiments performed on station 6.3 of the Daresbury Laboratory.

Figures 1a and 1b show nested TPD spectra from surfaces exposed to sequentially higher doses of THF and furan obtained by monitoring the evolution of their parent ions (68 and 72 amu for furan and THF respectively). Exposures are quoted in units of mbar.s, with pressures being measured by an ion gauge with no correction for sensitivity.

Both THF and furan adsorb reversibly on the Cu(111) surface. This is confirmed by AES and XPS (performed during NIXSW experiments at Daresbury), taken at the end of TPD/NIXSW experiments showing no carbon remaining on the surface and the lack of any other desorption products such as H₂ being evolved during TPD experiments.

TPD spectra of THF display two peaks at 173 and 136 K. The peak at 173 K saturates with increasing exposure and is assigned to desorption from a chemisorbed state. The peak at 136 K continues to increase in size with increasing exposure and is attributed to desorption from a condensed multilayer.

Increasing exposure of furan results in the development of four desorption peaks at 132, 140, 156 and 226 K. The state at 226 K is assigned to desorption from defect sites, while the peaks at 156 K and 140 K are assigned to chemisorbed states that have been labelled α and β respectively. The final state at 132 K is assigned to desorption of condensed multilayers.

Comparison of the adsorption of furan on Cu(111), in this study, with the data obtained by Sexton [4] in an equivalent study of furan adsorption on Cu(100) shows the adsorption on both surfaces to be qualitatively similar. As on Cu(111), TPD spectra from the Cu(100) surface shows the presence of two chemisorbed states, at 165 and 225 K. In this study, the presence of two chemisorbed states is attributed to the initial population of a flat-lying, π -bonded species followed by population of a second, less strongly bound bilayer state adsorbed on top of the first in a more upright geometry. Unfortunately, this is not a unique interpretation of the presence of two chemisorbed peaks observed in TPD spectra. In the same study, Sexton assigns the presence of two states in the thiophene/Cu(100) system as due to a coverage driven phase transition. The presence of two desorption peaks in the

thiophene/Cu(111) system has also been attributed to the presence of a coverage driven phase transition. In the phase transition model, desorption from the higher temperature state arises from a flat π -bonded state, while the state at lower temperature originates from a less strongly bound state in which the ring of the heterocycle is more inclined to the surface normal.

Unfortunately, none of the techniques used in this study allow us to unambiguously determine whether the presence of two chemisorbed states is as a result of a coverage driven phase transition or of the formation of a bilayer. However, in both models the α -state would originate from the desorption of furan from a chemisorbed state in which its aromatic ring was roughly flat to the surface. Finally, it is interesting to note that the desorption temperatures recorded on the Cu(100) surface are significantly higher than on the Cu(111) surface. Although on the more reactive (100) surface higher desorption temperatures may be expected, it is interesting to note that the α -state furan orientation is particularly strongly bound on the Cu(100) surface with a temperature of desorption 69 K higher than on the Cu(111) surface. β -state furan desorption takes place at 25 K higher on Cu(100), suggesting that the flat lying orientation of furan and as such the state involving the aromatic ring, may be particularly face sensitive.

From the TPD data it is clear that saturating the aromatic ring has significant effects on the bonding of the heterocyclic ring. The most obvious difference is that THF has only one chemisorbed state rather than the two displayed by furan. Another significant difference is that the THF chemisorbed state ($T_{\max} = 173$ K) is relatively more strongly bound than either the α - ($T_{\max} = 156$ K) or β - ($T_{\max} = 140$ K) states of furan.

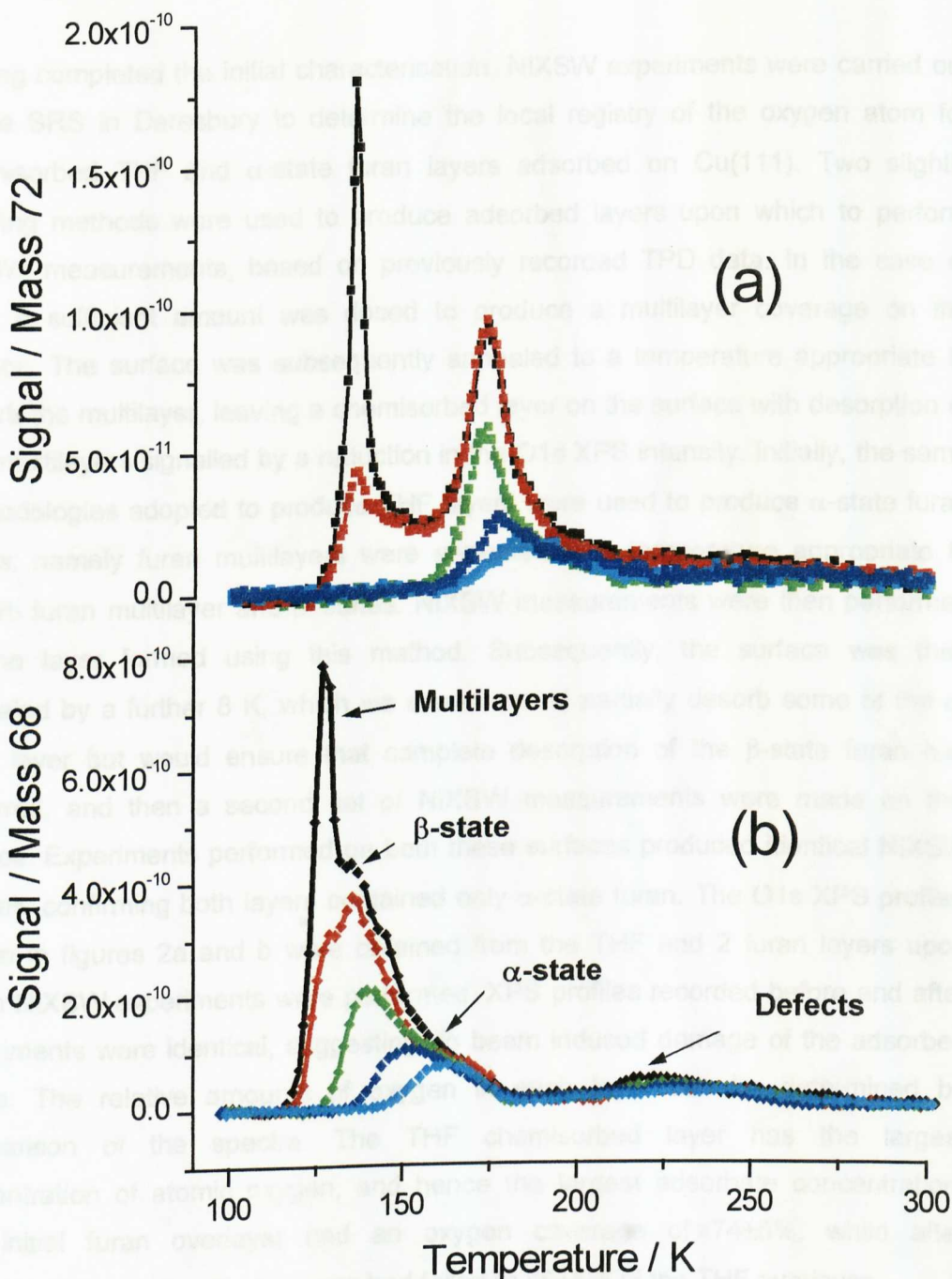


Figure 1a. TPD spectra showing the desorption of THF (parent ion 72 amu) from surfaces which had been dosed with sequentially higher exposures (0.5 (cyan), 1 (blue), 2 (green), 4 (red), 5 (black) $\times 10^{-6}$ mbar.s) at *ca.* 100 K are displayed. All spectra were collected with a heating rate of 0.5 K s^{-1} .

Figure 1b. TPD spectra showing the desorption of furan (parent ion 68 amu) from surfaces which had been dosed with sequentially higher exposures 1 (cyan), 2 (blue), 4 (green), 5 (red), 7 (black) $\times 10^{-6}$ mbar.s). Experimental conditions were identical to those in figure 1.

4.2.2 NIXSW

Having completed the initial characterisation, NIXSW experiments were carried out at the SRS in Daresbury to determine the local registry of the oxygen atom for chemisorbed THF and α -state furan layers adsorbed on Cu(111). Two slightly differing methods were used to produce adsorbed layers upon which to perform NIXSW measurements, based on previously recorded TPD data. In the case of THF, a sufficient amount was dosed to produce a multilayer coverage on the surface. The surface was subsequently annealed to a temperature appropriate to desorb the multilayer, leaving a chemisorbed layer on the surface with desorption of THF multilayers signalled by a reduction in the O1s XPS intensity. Initially, the same methodologies adopted to produce THF layers were used to produce α -state furan layers; namely furan multilayers were annealed to a temperature appropriate to desorb furan multilayer and β -states. NIXSW measurements were then performed on the layer formed using this method. Subsequently, the surface was then annealed by a further 8 K, which we expect would partially desorb some of the α -state layer but would ensure that complete desorption of the β -state furan had occurred, and then a second set of NIXSW measurements were made on this surface. Experiments performed on both these surfaces produced identical NIXSW profiles, confirming both layers contained only α -state furan. The O1s XPS profiles shown in figures 2a and b were obtained from the THF and 2 furan layers upon which NIXSW experiments were performed. XPS profiles recorded before and after experiments were identical, suggesting no beam induced damage of the adsorbed layers. The relative amounts of oxygen in each layer can be determined by comparison of the spectra. The THF chemisorbed layer has the largest concentration of atomic oxygen, and hence the largest adsorbate concentration. The initial furan overlayer had an oxygen coverage of $74\pm 5\%$, while after subsequent annealing its coverage had fallen to $45\pm 5\%$ of the THF overlayer.

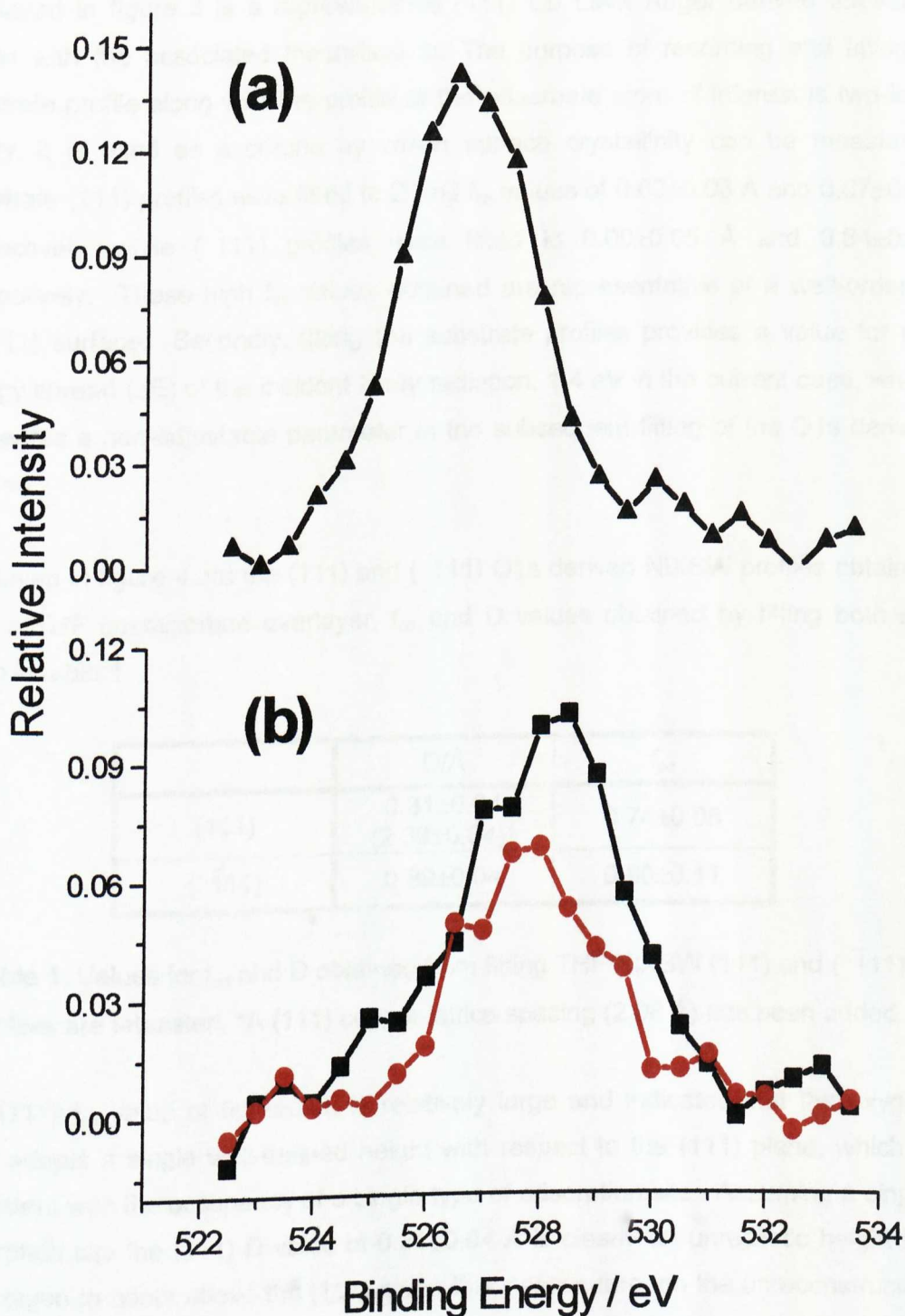


Figure 2a. XPS spectra of the O1s region collected using $h\nu = 2962$ eV for a THF overlayer that was formed by annealing condensed layers.

Figure 2b. XPS spectra of the O1s region collected using $h\nu = 2962$ eV for two furan overlayers that were formed by annealing condensed layers. The first furan spectrum (black) was collected from a surface, which had been heated, to a temperature that was just sufficient to desorb the β -state and multilayers. The second (red) was collected from the same layer which had been heated by a further 8 K.

Displayed in figure 3 is a representative (111) Cu LMM Auger derived substrate profile with the associated theoretical fit. The purpose of recording and fitting a substrate profile along with the profile of the adsorbate atom of interest is two-fold. Firstly, it is used as a criteria by which surface crystallinity can be measured. Substrate (111) profiles were fitted to D and f_{co} values of $0.00 \pm 0.03 \text{ \AA}$ and 0.87 ± 0.05 respectively, while $(\bar{1}11)$ profiles were fitted to $0.00 \pm 0.05 \text{ \AA}$ and 0.84 ± 0.05 respectively. These high f_{co} values obtained are representative of a well-ordered Cu(111) surface. Secondly, fitting the substrate profiles provides a value for the energy spread (ΔE) of the incident X-ray radiation, 1.4 eV in the current case, which is used as a non-adjustable parameter in the subsequent fitting of the O1s derived profiles

Displayed in figure 4 are the (111) and $(\bar{1}11)$ O1s derived NIXSW profiles obtained from a THF chemisorbed overlayer, f_{co} and D values obtained by fitting both are given in table 1.

	$D/\text{\AA}$	f_{co}
(111)	0.31 ± 0.04 $(2.39 \pm 0.04)^*$	0.74 ± 0.08
$(\bar{1}11)$	0.89 ± 0.04	0.80 ± 0.11

Table 1. Values for f_{co} and D obtained from fitting THF NIXSW (111) and $(\bar{1}11)$ profiles are tabulated. *A (111) copper lattice spacing (2.08 Å) has been added.

The (111) f_{co} value of 0.74 ± 0.08 is relatively large and indicates that the oxygen atom adopts a single well-defined height with respect to the (111) plane, which is consistent with the occupancy of a single type of adsorption site. Assuming a single adsorption site the (111) D value of $0.31 \pm 0.04 \text{ \AA}$ is clearly an unrealistic height for the oxygen to adopt above the (111) plane that passes through the unreconstructed surface. However, if the D (111) value is the height of the atom with respect to the first hypothetical plane above the surface, then a more realistic oxygen-surface height of 2.39 \AA ($0.31 \text{ \AA} + 1$ lattice spacing) is obtained.

With the height of the O atom above an unreconstructed (111) plane known, expected values of $(\bar{1}11)$ D and f_{co} atop, bridge and threefold (FCC and HCP) sites can be calculated. A comparison between the $(\bar{1}11)$ values calculated from the (111) data and the experimentally observed D and f_{co} values is made in table 2.

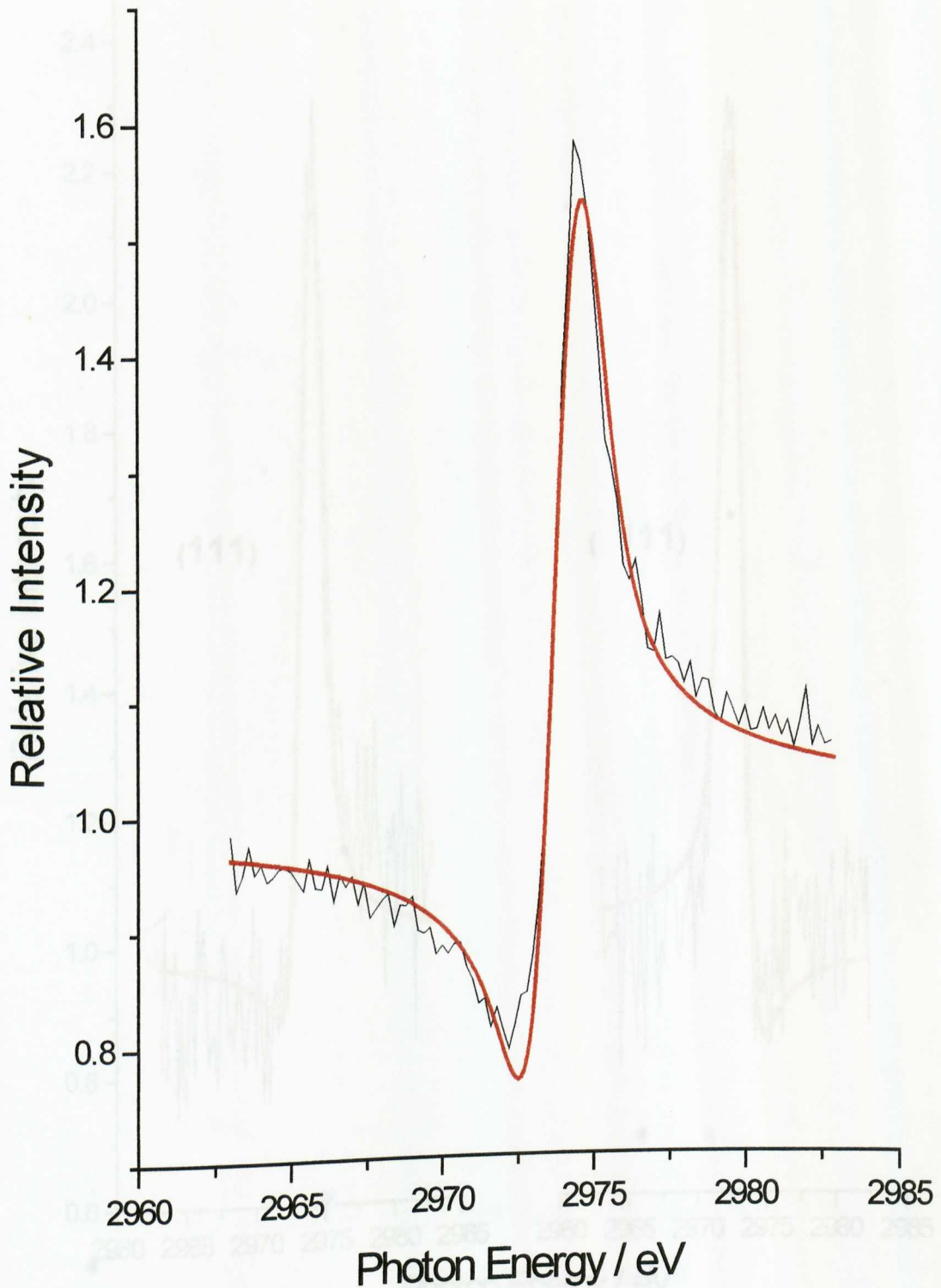


Figure 3. Experimental (black) and fitted (red) copper NIXSW profiles collected using the (111) plane. The parameters used to generate the fit are $D=0.00 \text{ \AA}$ and $f_{\text{co}}=0.87$ and an energy spread (ΔE) = 1.4eV.

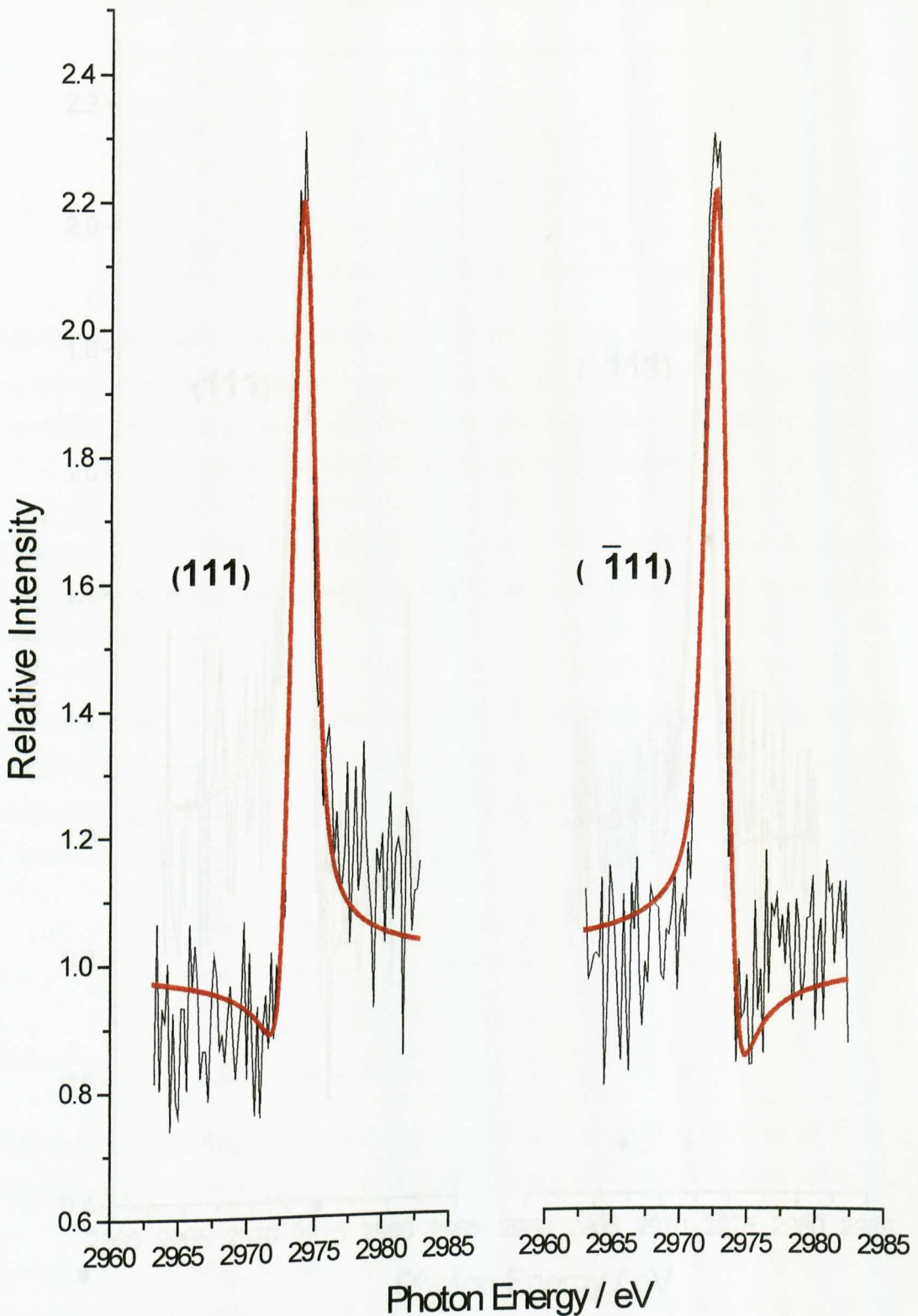


Figure 4. Experimental (black) NIXSW profiles and the corresponding fits (red) obtained from a chemisorbed THF overlayer using the (111) and ($\bar{1}11$) planes are shown.

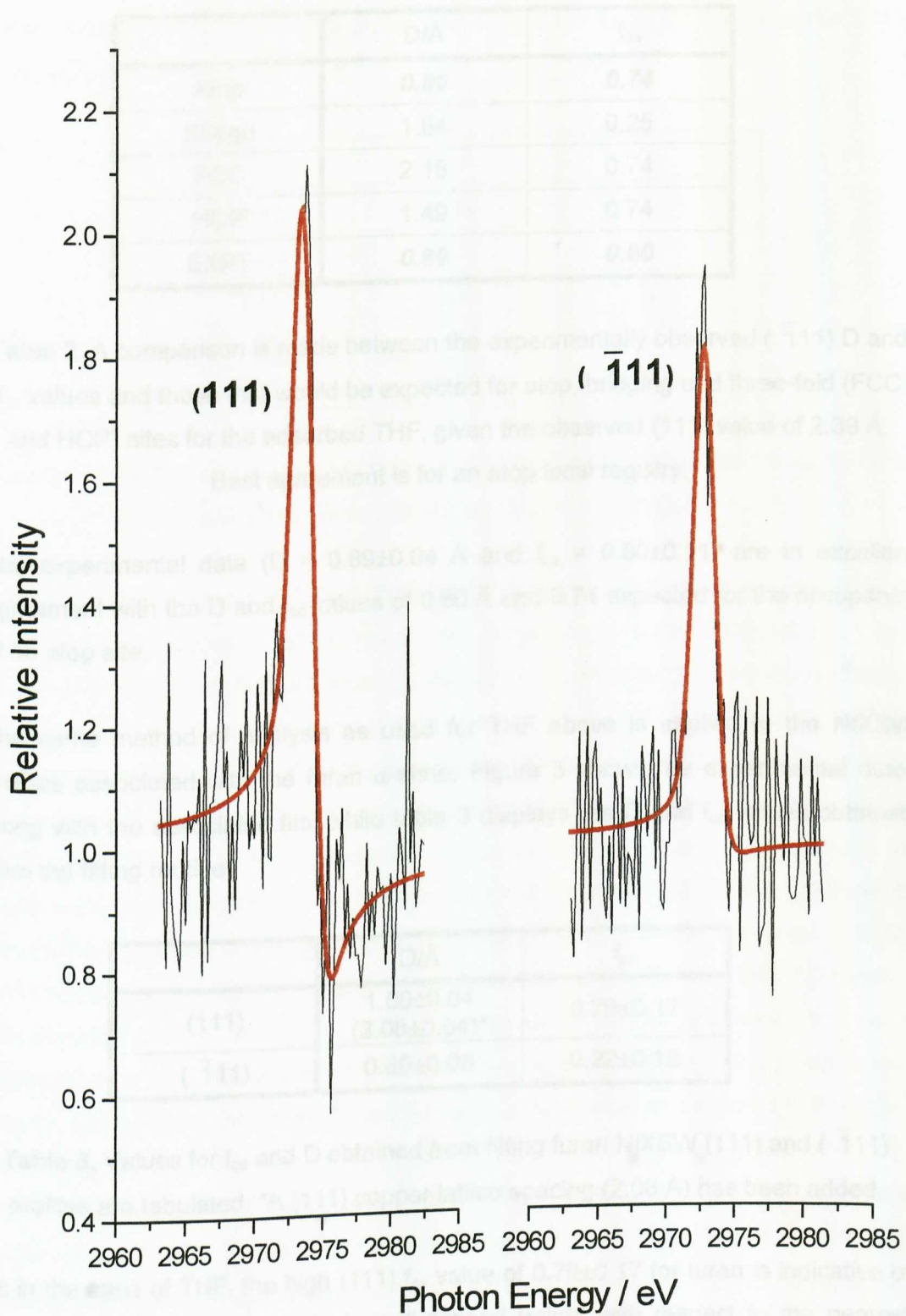


Figure 5. Experimental (black) NIXSW profiles and the corresponding fits (red) obtained from a chemisorbed furan overlayer using the (111) and ($\bar{1}11$) planes are shown. Identical profiles are obtained for both furan overlayers measured.

	D/Å	f_{co}
Atop	0.80	0.74
Bridge	1.84	0.25
FCC	2.18	0.74
HCP	1.49	0.74
EXPT	0.89	0.80

Table 2. A comparison is made between the experimentally observed ($\bar{1}11$) D and f_{co} values and those that would be expected for atop, bridging and three-fold (FCC and HCP) sites for the adsorbed THF, given the observed (111) value of 2.39 Å.

Best agreement is for an atop local registry.

The experimental data ($D = 0.89 \pm 0.04$ Å and $f_{co} = 0.80 \pm 0.11$) are in excellent agreement with the D and f_{co} values of 0.80 Å and 0.74 expected for the occupancy of an atop site.

The same method of analysis as used for THF above is applied to the NIXSW profiles associated with the furan α -state. Figure 5 shows the experimental data, along with the associated fits, while table 3 displays the D and f_{co} values obtained from the fitting routine.

	D/Å	f_{co}
(111)	1.00 ± 0.04 $(3.08 \pm 0.04)^*$	0.79 ± 0.17
($\bar{1}11$)	0.89 ± 0.08	0.22 ± 0.12

Table 3. Values for f_{co} and D obtained from fitting furan NIXSW (111) and ($\bar{1}11$) profiles are tabulated. *A (111) copper lattice spacing (2.08 Å) has been added.

As in the case of THF, the high (111) f_{co} value of 0.79 ± 0.17 for furan is indicative of the oxygen atom having a single well-defined height with respect to the nearest (111) plane, and hence implies the occupancy of a single type of adsorption site. Once again the D value of 1.00 ± 0.04 Å is too short to be a realistic oxygen-surface distance. Using the same arguments invoked for THF the addition of a lattice spacing (2.08 Å) to the D value gives a realistic oxygen-surface distance of 3.08 ± 0.04 Å. As before, the experimental ($\bar{1}11$) D and f_{co} values are compared with

those calculated for atop, bridging and three-fold sites using the experimental (111) data, table 4.

	D/Å	f_{co}
Atop	1.03	0.79
Bridge	2.07	0.26
FCC	0.33	0.79
HCP	1.72	0.79
EXPT	0.89	0.22

Table 4. A similar comparison made in table 2 for THF is made here for furan. The best agreement is for occupancy of an atop site.

The experimental D value ($D = 0.89 \pm 0.08$ Å) is in best agreement with the 1.03 Å expected for occupancy of an atop site. However, the experimental f_{co} value obtained in the ($\bar{1}11$) direction of 0.22 ± 0.12 is much smaller than the expected value of 0.79. The significance of this low f_{co} value is that there is a greater uncertainty in the position of the oxygen atom with respect to the ($\bar{1}11$) plane than was expected. There are a number of factors that can account for the reduction in the f_{co} value. Firstly, a reduction can be caused by dynamic disorder or secondly, by static atoms with a distribution of heights. The latter would occur if the oxygen atom adopted a displaced atop local registry or was in multiple adsorption sites. If furan were adsorbed in multiple adsorption sites, there would also be a range of D values, the differing values caused by different oxygen to copper distances for each particular site, and hence a significant reduction in the f_{co} of the (111) plane would also be observed. In the present case a high f_{co} value (0.79) is observed in the (111) direction and hence we rule out the possibility that furan adsorbs in multiple sites. In the case of a displaced local registry, the oxygen would still have a well-defined height with respect to the (111) plane, and hence a high (111) f_{co} value, but it would have a relatively broad distribution of heights with respect to the ($\bar{1}11$) plane, which would result in the observed small f_{co} value. This is consistent with our observations of this system and hence we attribute the reduction in f_{co} due to static disorder to be caused by displacement from an ideal atop adsorption site rather than adsorption in multiple adsorption sites. However, from the data in the present study, it is not possible to determine whether the dominant factor in reducing the f_{co} value in the

($\bar{1}11$) direction is caused by static or dynamic disorder. Indeed, we suggest that both effects play a role in reducing the observed f_{co} value.

The low f_{co} value observed for furan with respect to the ($\bar{1}11$) plane raises the question of why furan has a greater degree of static/dynamic disorder with respect to this plane than THF. The answer to this question lies in considering the relative bond strengths of α -state furan compared to THF. Both TPD and NIXSW show that furan is significantly less strongly bound to the copper surface than THF. This weak interaction with the surface would result in two effects being considerably larger for furan than for the THF molecules. Firstly, the adsorbate-adsorbate interactions within the α -state furan overlayer are likely to be significant compared to the weak adsorbate-surface interaction furan has with the surface. This is unlikely to be the case for the significantly more strongly bound THF molecules and would result in the furan molecule being "pulled" from a perfect atop position by lateral interactions with its neighbouring molecules. Secondly, the weak furan-surface interaction would result in a vibration parallel to the surface with an amplitude greater than would be observed for the more strongly bound THF. This reasoning, additionally supports our conclusion that the low f_{co} value observed for furan with respect to the ($\bar{1}11$) plane is due to a displaced atop site and not occupation of high symmetry sites.

Unfortunately, neither TPD nor NIXSW can be used to directly measure the orientation of either THF or furan. However, as discussed earlier and based on the results of previous studies, we have suggested that furan in the α -state is most likely to be adsorbed with its ring in a roughly flat lying geometry, parallel to the surface. No previous studies of THF adsorption exist that would aid us in accessing the probable orientation of THF. Indeed the only data from which a possible orientation can be inferred is the O1s XPS data in figures 2a and b, which provides a measure of its relative coverage. This data shows the initial α -state furan layer (which we believe to be roughly a saturated monolayer) to be approximately 74% of the saturated THF layer. We believe this indicates that both THF and furan adopt a similar orientation on the Cu(111) surface. We make this observation based on the fact that if THF was significantly more inclined toward the surface normal than furan we would observe significantly increased packing density and therefore a much larger O1s intensity than that observed here.

4.3 Discussion

The results of both TPD and NIXSW clearly show that THF interacts more strongly with Cu(111) than does furan, although both molecules have significantly longer D values than would be expected for a chemisorbed oxygen-containing moiety such as alkoxy or carboxylate species (typically in the range 1.80 to 1.90 Å [8,9,10]). THF has a shorter Cu-O separation, by 0.69 Å, and a higher desorption temperature, by 23 K, than α -state furan. Indeed the weakness of the α -state furan interaction is highlighted by the fact that the Cu-O distance for furan of 3.08 ± 0.04 Å is close to the expected van der Waals separation of 2.92 Å. Evidently, we must account for the significant disparity between the degree to which THF and furan interact with the Cu(111) surface.

The most obvious difference, which could play a role in bonding, is the aromatic nature of furan compared to THF. Furan adsorbed in the α -state could interact with the surface via both the lone pair electrons of the oxygen and through the π -orbitals of the aromatic ring. However, the results of experimental and theoretical work [11, 12] would suggest that the oxygen lone pair could have a more dominant role in bonding with the substrate than does the π system. Despite the contribution of the π system to the overall bonding interaction, furan is still less strongly bound than THF and in the β -state, where the interaction of the aromatic ring is reduced, the difference in bond strength only becomes larger. From these observations it would appear that the oxygen lone pair electrons of THF interact more strongly with Cu(111) than those of furan.

As a possible explanation for the observed disparity in bonding we must examine the differing orbital characteristics and numbers of lone pairs of electrons of the oxygen atoms interacting with the copper surface. The oxygen atom of furan has three sets of sp^2 hybridised orbitals. Two of these are involved in bonding to the neighbouring carbon atoms within the molecule while the third is filled by a lone pair of electrons and a p_z orbital which forms part of the delocalised π system. This non-bonding pair of electrons is located in the plane of the aromatic ring and will be the main interacting part of the molecule with the surface. In contrast, the oxygen atom of THF can be viewed as being sp^3 hybridised. It has four equivalent orbitals of sp^3 character, two of which are involved in bonding within the molecule and two filled with lone pair electrons.

In an attempt to rationalise the role and significance of the number of lone pairs and the orbital characteristics of the oxygen on bonding we compare the current NIXSW data with that obtained from studies of acetone [13] and methanol [14] on Cu(111), carried out in the lab previously. Table 5 compares the current data with that from the previous studies.

	Cu-O / Å	T_{\max} monolayer / K	Oxygen hybridisation	No. of lone pairs
THF	2.39	173	sp^3	2
Acetone	2.73	157	sp^2	2
Methanol	2.89	163	sp^3	2
Furan	3.08	156	sp^2	1

Table 5. A comparison is made of the results of the current TPD and NIXSW study of furan and THF with those from previous work on acetone [13] and methanol [14].

Like furan, the oxygen in acetone is sp^2 hybridised, however it has two rather than one lone pair of electrons that could interact with the surface. The oxygen atom in methanol is similar to that of THF, being sp^3 hybridised and with two oxygen lone pairs that are available for bonding with the surface. The data in the table above shows that the fact the oxygen atom of THF is sp^3 hybridised compared to the sp^2 hybridised oxygen of furan is not enough to account for the significant differences observed in bond strength between the two molecules. If the hybridisation scheme of the oxygen was the cause of the stronger bond observed for THF then a similar effect would be expected for methanol. However, within experimental error, these two molecules have identical Cu-O separations. Considering the number of lone pairs available for bonding to the surface also throws no light on why the THF is significantly more strongly bound than furan. Although both methanol and acetone both have two lone pairs available to interact with the surface, neither is significantly more strongly bound than furan. Hence, we must consider other possibilities to explain the unexpected strength of the THF interaction with Cu(111).

Clearly there is an alternative interaction which is not associated with the nature of the oxygen lone pairs of electrons, that operates in the case of THF to enhance its bonding to Cu(111). With the present data we can only speculate on the origin of this alternative interaction, however, we believe that the likeliest candidate is a C-H...Cu interaction between the axial hydrogens of the THF ring and the surface.

Unlike furan, that is planar and aromatic, the saturated THF molecule has three possible conformations [15]. Firstly, the molecule can be planar. This form is the most strained and is hence the least stable conformation. Secondly, an envelope geometry can be adopted (figure 6a) where the oxygen atom is no longer in the plane of the ring but tilts away from it at the attached carbons (2 and 5). The final conformation, the twist form (figure 6b), consists of two planes. The first plane is made up of the oxygen atom and the two attached carbons (2 and 5), with the second plane perpendicular to the first, consisting of the remaining two carbons (3 and 4).

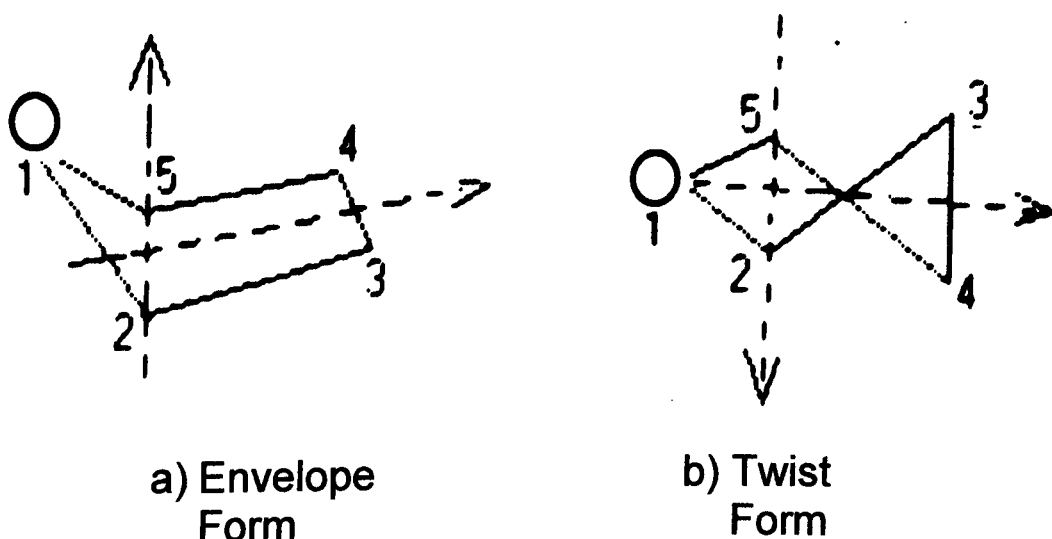


Figure 6. The two most stable conformations of THF in the gas phase are shown. Adapted from ref. 15.

Based on experimental and theoretical work on closely related molecules [15], it is anticipated that in the gas phase the twist and envelope forms would have very similar stabilities, and that both are significantly more stable than the planar conformation. Consequently, if the relative stability of the conformations are not significantly different to that in the gas phase it would be reasonable to assume that within the adsorbed overlayer the twist and envelope forms will be adopted. Both the twist and envelope forms of THF have "axial" C-H bonds that are perpendicular to the plane containing the carbon atoms of the ring. Previous experimental [16] and theoretical [17] studies have shown that axial C-H bonds in other saturated ring compounds, such as cyclohexane, interact with the Cu(111) substrate producing a

C-H...Cu bond. This interaction involves a transfer of charge from the substrate to the molecule and is analogous to hydrogen bonding, with the strength of the interaction shown to be strongly dependent on the distance of the hydrogen atoms from the surface. So, the presence of axial C-H bonds in the most stable conformations of THF would allow the C-H...Cu bond to be formed, which would produce the observed enhancement in bonding compared to the other oxygen containing molecules.

4.4 Conclusions

We have performed the first ever structural study of the adsorption of THF and furan on Cu(111). TPD data from THF shows that it desorbs in two steps. Multilayer desorption at 136 K followed by monolayer at 173 K. NIXSW data of THF shows it adsorbs in an atop adsorption site with a Cu-O separation of 2.39 ± 0.04 Å.

The TPD data for furan shows the molecule desorbs in three steps. Desorption of a first layer (designated α -state at 156 K), which we suggest is likely to be in a flat lying geometry with the aromatic ring parallel to the surface, followed by a second layer (designated β -state at 140 K) resulting from either bilayer formation or a coverage driven phase transition. The data available does not allow us to determine which possibility is correct in the present case. Multilayer desorption then follows at 132 K. Furan is determined to also adopt an atop adsorption site. However, a low $(\bar{1}11) f_{co}$ value indicates a distribution of D values which we attribute to the effects of both static and dynamic disorder. These effects in turn, originate from the extremely weak furan to copper bond strength, resulting in a displacement from an ideal atop adsorption site and a greater amplitude of vibration parallel to the Cu(111) surface.

Finally, we have examined the differences observed in the bonding of furan and THF to Cu(111). We conclude that, although the molecules differ significantly in several ways, the main cause of the much stronger adsorption of THF compared to furan is caused by the effects of the interaction of axial C-H bonds with the surface forming a C-H...Cu bond. This type of interaction has been observed in the bonding of other cyclic hydrocarbons and would account for the significantly stronger bonding of THF compared to furan.

4.5 References

- [1] E. Furimsky, Appl. Catal. 6 (1983) 159
- [2] A. Tsumura, L. Tossi, H.E. Katz, Science 268 (1995) 270
- [3] P.K. Milligan, B. Murphy, D. Lennon, B.C.C. Cowie, M. Kadodwala, J. Phys. Chem. B 105 (2001) 140
- [4] B.A. Sexton Surf.Sci. 163 (1985) 99
- [5] J.L. Solomon, R.J. Madix and J. Stohr. J.Chem. Phys. 1991. 94 (5). 4012
- [6] J. T. Roberts and C. M. Friend J. Am. Chem. Soc. 108 (1986) 7204
- [7] K Wang and P.N Ross. Surf Sci. 365 (1996) 753
- [8] A. Sotiropoulos, P. Milligan, B.C.C. Cowie, M. Kadaodwala, Surf. Sci. 444 (2000) 52
- [9] S. M. Johnston, G. Rousseau, V. Dhanak and M. Kadodwala, Surf. Sci. 550 (2003) 111
- [10] S. M. Johnston, G. B. D. Rousseau, V. Dhanak, M. Kadodwala, Surf. Sci. 447 (2001) 163
- [11] P.K. Milligan, B. Murphy, D. Lennon, B.C.C. Cowie, M. Kadodwala, J. Phys. Chem. B 105 (2001) 140
- [12] J. A. Rodriguez, Surf. Sci. 234(1990) 5231
- [13] S. M. Johnston, A. Mulligan, V. Dhanak and M. Kadodwala, Surf. Sci. 548 (2004) 5
- [14] S. M. Johnston, A. Mulligan, V. Dhanak and M. Kadodwala, Surf. Sci. 530 (2003) 111
- [15] T.M. El-Gogary, Spectrochimica Acta Part A 57 (2001) 1405
- [16] R. Raval, S.F. Parker, M.A. Chesters, Surf. Sci. 289 (1993) 22
- [17] K.A. Fossler, R.G. Nuzzo, P.S. Bagus, Wöll, Angew. Chem. Int. Ed. 41 No. 10 (2002) 1735

Chapter 5: Adsorption of Sulphur and Dimethyl Disulphide on Cu(111)

5.1 Introduction

The interaction of sulphur with transition metal surfaces has been the subject of long term interest in surface science. This arises from both fundamental interest in the wide range of adsorbate-induced rearrangements and reconstructions of metal surfaces it induces and from applications in heterogeneous catalysis where sulphur is seen as an archetypal catalyst poison. Due to this, the S/Cu(111) system as well as the interaction of methyl thiolate with Cu(111) have been the subject of extensive interest and are generally well understood. In this chapter, we repeat a selection of these measurements as an initial characterisation to our model catalytic study reported in chapter 6. However, in addition to this we also present new results measuring work function changes induced by sulphur and methyl thiolate adsorption on Cu(111), as well as the first TPD measurements of the desorption of DMS.

5.1.1 Sulphur

The first study examining the interaction of sulphur on Cu(111) was performed in 1968 by Domange and Oudar [1]. This study identified three room temperature structures formed upon sulphur adsorption. The first of these was identified as a $(\sqrt{3}\times\sqrt{3})R30^\circ$, followed by a transitory, complex phase, and finally a $(\sqrt{7}\times\sqrt{7})R19.1^\circ$ phase upon sulphur saturation. Observation of the $(\sqrt{3}\times\sqrt{3})R30^\circ$ has only been reported once since this initial study, which may be due to either an experimental artefact or the structure may only fall within a narrow temperature and coverage range. Both the other structures have been observed in many subsequent studies. One of the key results in this study was the first measurement of sulphur coverage incorporated into the $(\sqrt{7}\times\sqrt{7})R19.1^\circ$ structure, measured using radioactive ^{35}S tracer. This concluded a sulphur coverage of 0.43 ML. Both this and a number of subsequent studies have suggested that the S/Cu(111) system may be the surface analogy of bulk copper sulphide (CuS).

Since the completion of this first study, a number of additional studies have been performed examining the effects of both temperature and coverage. The complex phase has been observed a number of times at room temperature and has been studied using a variety of techniques. STM measurements [2,3] have shown the

complex structure to develop at a sulphur coverage of *ca.* 0.35 ML. The structure appears with characteristic zigzag lines in STM images and for this reason is also often called the zigzag phase. This structure has no simple Woods notation but is described as $\begin{pmatrix} 4 & 1 \\ -1 & 4 \end{pmatrix}$ in matrix notation. At sulphur coverages below $\theta_s=0.25$ ML no structures have been reported at room temperature. However, in the first low temperature study of the S/Cu(111) surface using STM, Wahlström et. al. [4] observed the development of sulphur structures at low surface coverage ($\theta_s=0.05$ ML). They report at low coverages observing islands formed by protrusions organised in a honeycomblike structure. They identify this structure as a $(\sqrt{43}\times\sqrt{43})R\pm 7.5^\circ$ and determine an order-disorder transition takes place at 150 K. They attribute the appearance of the honeycomb structure to condensation of atoms or clusters when the crystal is cooled that are otherwise mobile at room temperature. Further to this work, in a second study by the same authors [5], they also observe the formation of a further three structures below 230 K and in the coverage range $0.25 < \theta < 0.35$. These structures have been labelled by the authors I, II and III, with their full matrix notation given in table 1, along with full descriptions of all the other structures mentioned in this review.

Turning our attention to the final structure formed on Cu(111), the $(\sqrt{7}\times\sqrt{7})R19.1^\circ$ we find this the topic of extensive interest. The most recent structural study on this system was performed by Jackson and co-workers using NIXSW [6] and compares the results of this study with previously proposed structural models from a number of other studies [7,8,9,10]. After consideration of their own data with that of the previously proposed model systems, the authors find closest agreement with the model proposed by Foss et. al. [10]. In this study the authors examined both the structure of the zigzag phase and the $(\sqrt{7}\times\sqrt{7})R19.1^\circ$ phase. Previous STM work [2] has suggested a link between both these structures, with a tip induced phase transition observed from the zigzag to $(\sqrt{7}\times\sqrt{7})R19.1^\circ$ phases during STM experiments, and the authors hoped to gain additional insight into the $(\sqrt{7}\times\sqrt{7})R19.1^\circ$ structure by firstly examining that of the zigzag phase. In their paper the authors use X-ray diffraction to study both structures and conclude that both consist of Cu_4S units with a S atom being adsorbed in the fourfold hollow site of the Cu tetramer. The zigzag structure is considered to consist of two such units with the $(\sqrt{7}\times\sqrt{7})R19.1^\circ$ being constructed from only one. A diagram of the structure proposed by Foss et. al. is shown in figure 1.

Structure	Matrix Notation	Coverage θ_s / ML	Temperature / K
$(\sqrt{43} \times \sqrt{43})R\pm 7.5^\circ$ (Honeycomb)	$\begin{vmatrix} 6 & -1 \\ 1 & 7 \end{vmatrix}$	0.05 to 0.25	<170
Structure I	$\begin{vmatrix} 4 & 0 \\ -3 & 6 \end{vmatrix}$	0.25 to 0.35	<230
Structure II	$\begin{vmatrix} 5 & -1 \\ -3 & 8 \end{vmatrix}$	0.25 to 0.35	<230
Structure III	$\begin{vmatrix} 3 & 3 \\ -9 & 16 \end{vmatrix}$	0.25 to 0.35	<230
$(\sqrt{3} \times \sqrt{3})R30^\circ$	$\begin{vmatrix} 1 & -1 \\ 1 & 2 \end{vmatrix}$	0.33	300
Zigzag (Complex)	$\begin{vmatrix} 4 & 1 \\ -1 & 4 \end{vmatrix}$	0.33 to 0.43	300
$(\sqrt{7} \times \sqrt{7})R19.1^\circ$	$\begin{vmatrix} 3 & 2 \\ 1 & 3 \end{vmatrix}$	0.43	300
Pseudo-(100)c(2×2)-S (By electron induced decomposition)	$\begin{vmatrix} 1 & -1 \\ 1 & 1 \end{vmatrix}$	—	300

Table 1. Summary of ordered S structures formed on the Cu(111) surface.

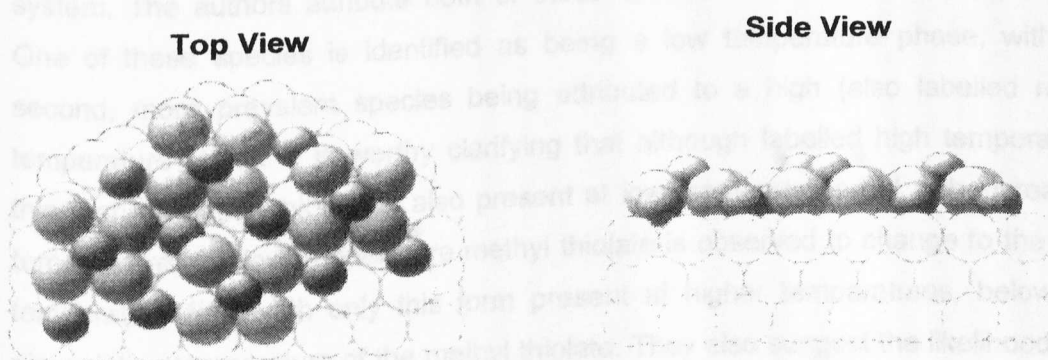


Figure 1. Schematic top and side views of the surface model of the $(\sqrt{7} \times \sqrt{7})R19.1^\circ$ structure first proposed by Foss et. al. [10] from XRD data and later supported by Jackson et. al. [6] in their NIXSW study. Cu substrate atoms are drawn unshaded, with the outermost Cu atoms lightly shaded. S atoms are represented by the darkly shaded spheres. Taken from reference 7.

5.1.2 Dimethyl Disulphide

The adsorption of DMS on Cu(111) has been the subject of extensive study in several publications by Woodruff and co-workers [12-16]. The first of these studies used angle-resolved photoemission to probe both room temperature adsorption and also the effects of temperature on DMS adsorbed at cryogenic temperatures. This study concluded DMS adsorbs molecularly at low temperature and reacts upon heating to give adsorbed methyl thiolate. This observation was clarified in a latter study where the authors noted that a small amount of DMS cracks to methyl thiolate immediately upon adsorption even at low temperatures. They attribute this to the effects of reactive sites (e.g. defects) on the Cu(111) surface. The study also concluded the same methyl thiolate species is formed regardless of whether DMS is dosed at room temperature or at cryogenic temperatures and then heated. In addition to this, angle resolved measurements suggested the S-C bond lies close to perpendicular to the copper surface.

In a later study [13], the system was probed further using soft XPS. The results of this study began to suggest the system to be far more complicated than suggested by the initial UPS experiments. This data showed the presence of four types of sulphur in the adsorption process during heating of the Cu(111) surface. Two of these were easily assigned. The first was attributed to adsorbed molecular DMS at cryogenic temperatures, with a second peak attributed to atomic S after dissociation of adsorbed methyl thiolate. This left two S species to account for in the adsorption system. The authors attribute both of these species to adsorbed methyl thiolate. One of these species is identified as being a low temperature phase, with the second, more prevalent species being attributed to a high (also labelled room) temperature phase. It is worthy clarifying that although labelled high temperature, this form of methyl thiolate is also present at low temperatures but with increasing temperature, the low temperature methyl thiolate is observed to change to the high temperature form with only this form present at higher temperatures, below the dissociation temperature of the methyl thiolate. They also suggest the likelihood of a reconstructed surface related to the formation of two methyl thiolate species, with high temperature methyl thiolate assigned to adsorption on reconstructed areas of the surface, while the low temperature form is adsorbed on unreconstructed areas of the crystal. This supposition was investigated further in two studies using NIXSW [14] and STM [15]. The results of these studies confirmed that methyl thiolate does indeed induce a reconstruction of the Cu(111) surface. This is identified as being a

pseudo-square surface reconstruction of the Cu(111) surface induced by the high temperature methyl thiolate species. This methyl thiolate-induced pseudo-(100) reconstruction is considered to correspond to a commensurate structure (figure 2). Two further structures are also identified in the STM study. One of these is a $\begin{vmatrix} 5 & 0 \\ 1 & 3 \end{vmatrix}$ hexagonal honeycomb like structure that is attributed to the low temperature form of methyl thiolate adsorbed on the unreconstructed surface. The final structure has hexagonal symmetry, had not been observed before and is attributed to an alternative end point to the pseudo-square phase, attributed to high adsorbate coverages.

In the most recent study of DMS adsorption on the Cu(111) surface Driver and Woodruff study the effects of electron beam induced decomposition of adsorbed methyl thiolate on the Cu(111) surface. Methyl thiolate overlayers are known to be unstable under an electron beam cracking to leave adsorbed atomic S. This process is extremely fast and hence using LEED has proved difficult in determining the periodicity of the overlayer. However, in this study the authors report observing the expected square symmetry diffraction pattern immediately after switching on the LEED. This pattern is reported to quickly transform into a poor-quality $(\sqrt{7} \times \sqrt{7})R19.1^\circ$. The authors then use STM to further probe the structure remaining after electron beam exposure. This confirms the presence of the $(\sqrt{7} \times \sqrt{7})R19.1^\circ$ structure observed by LEED but in addition to this the authors also find co-existing regions of both the zigzag phase, described previously, and the new pseudo-square S structure. The new S structure is assigned to S atoms occupying alternate fourfold hollow sites in a $c(2 \times 2)$ arrangement, on the reconstructed Cu surface with a distorted (100)-like geometry.

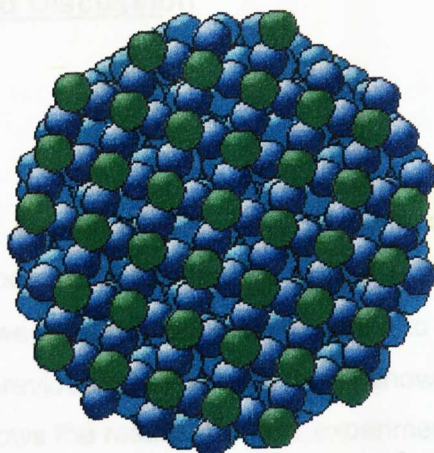


Figure 2. Schematic diagram of the pseudo-(100)c(2x2)-S surface formed by high temperature methyl thiolate on Cu(111) proposed in ref. 16. Cu atoms are drawn in blue, with S in green.

In this chapter we have used the techniques of LEED, TPD, UPS and XPS to study the interaction of sulphur and DMS with the Cu(111) surface. Both XPS measurements of sulphur uptake and UPS recorded at various sulphur coverages are consistent with the results of previous work. In LEED experiments we observe two ordered structures during the adsorption process at sulphur coverages of ~ 0.29 ML and 0.43 ML, which we have identified as the previously observed zigzag structure and the $(\sqrt{7}\times\sqrt{7})R19.1^\circ$ respectively. Finally, we measure work function changes during increased sulphur uptake. We observe a linear increase in work function with increasing sulphur coverage followed by a more sudden increase associated with $(\sqrt{7}\times\sqrt{7})R19.1^\circ$ formation.

In the case of adsorption of DMS on the Cu(111) surface we observe desorption of DMS multilayers at 154 K followed by dissociation of the remaining methyl thiolate moiety observed between 325-475 K. UPS and XPS measurements are again consistent with the results of previous studies. Finally, we make measurements of work function with increasing methyl thiolate coverage. The results we obtain here show a linear decrease in work function with increasing methyl thiolate coverage. We attribute this to a strong molecular dipole anti-parallel to that of the surface dipole, which is consistent with theory.

5.2 Results and Discussion

5.2.1 Sulphur

The initial uptake of sulphur on the Cu(111) surface was measured using XPS during increasing exposure of the surface to H₂S followed by annealing to 573 K. Absolute coverages were calculated with reference to the $(\sqrt{7}\times\sqrt{7})R19.1^\circ$ structure, which as described previously has already been shown to represent a coverage of 0.43 ML. Figure 3 shows the results of these experiments as a plot of H₂S exposure against absolute coverage. As can be seen from the figure, rapid H₂S uptake occurs up to 20L suggesting a linear sticking probability up to this point. After this point uptake slows considerably until saturation and formation of the $(\sqrt{7}\times\sqrt{7})R19.1^\circ$ structure. This uptake curve is consistent with both the original work of Campbell and Koel [17] on this system and also with a more extensive study of uptake carried out in our lab previously [18]. These studies concluded H₂S adsorption to be dissociative above 200 K, leaving atomic S after desorption of H₂.

Figure 4 shows nested normal emission UPS spectra recorded for the clean Cu(111) surface and 4 sulphur coverages determined by XPS to be 0.11 ± 0.03 , 0.16 ± 0.01 , 0.29 ± 0.02 , and 0.43 ML recorded at ca. 110 K. Characteristic bands associated with both the clean and sulphur covered surface are discussed in detail elsewhere [19,20,21,22]. Briefly, the most prominent features of the clean surface between 2-4.5 eV are attributed to emission from the Cu d-orbitals. With increasing sulphur coverage we observe a general attenuation of these orbital features. Additionally, the feature at around 0.4 eV on the clean surface has been identified as being characteristic of a Shockley type surface state [21]. However, the feature at 1 eV below the E_F, labelled Cu ?, is more difficult to assign. Previous work has attributed this to being either as a result of another Cu surface state [21] or as a satellite peak [22]. The current study can add no further information regarding the origin of this state. Upon sulphur adsorption, both the Cu surface state and the state labelled Cu ?, are attenuated.

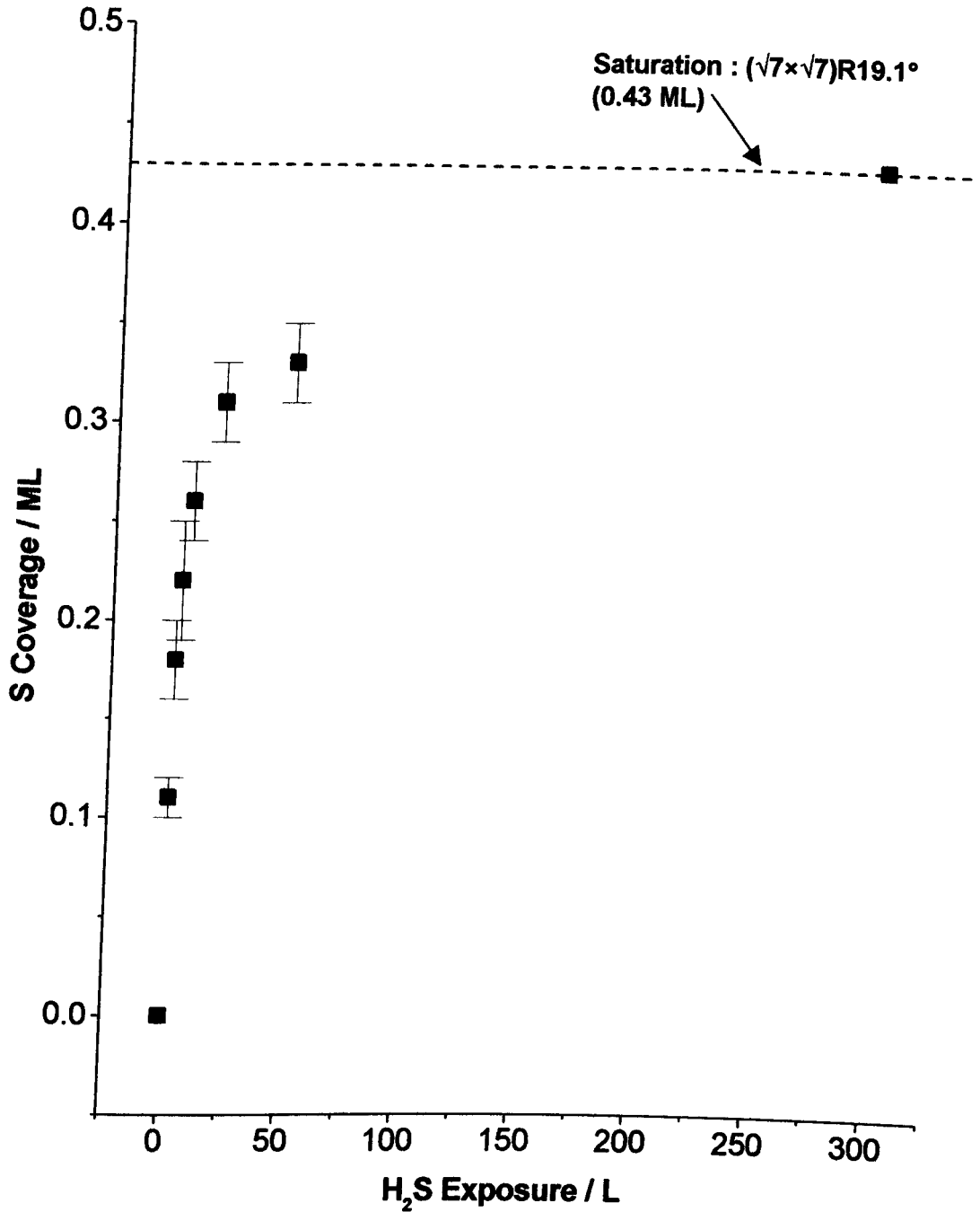


Figure 3. Sulphur uptake on Cu(111) exposed to H₂S and flashed to 573 K. Sulphur uptake was monitored using S2s XPS, with absolute coverage calculated with reference to the saturated surface.

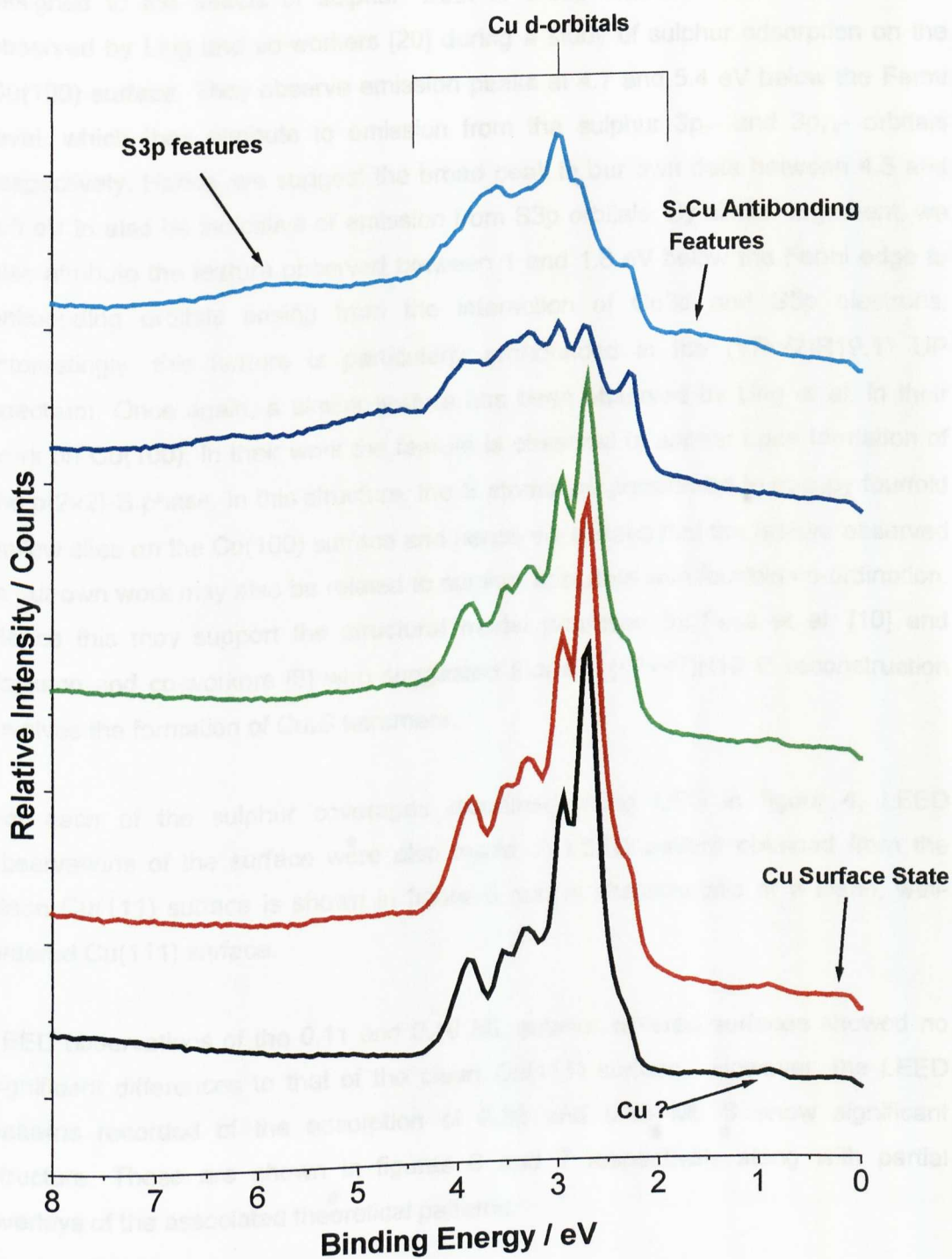


Figure 4. Normal emission UP spectra of clean copper surface (black), $\theta_s=0.11\pm0.03$ (red), 0.16 ± 0.01 (green), 0.29 ± 0.01 (blue), and 0.43 ML (cyan) adsorbed sulphur. Sulphur coverages were determined using XPS. UP spectra were recorded at ca. 110 K.

In addition to these observations we also observe the growth of two new features assigned to the effects of sulphur. Both of these features are similar to those observed by Ling and co-workers [20] during a study of sulphur adsorption on the Cu(100) surface. They observe emission peaks at 4.7 and 5.4 eV below the Fermi level, which they attribute to emission from the sulphur $3p_z$ - and $3p_{x,y}$ - orbitals respectively. Hence, we suggest the broad peak in our own data between 4.5 and 6.5 eV to also be indicative of emission from S3p orbitals. By similar argument, we also attribute the feature observed between 1 and 1.8 eV below the Fermi edge to antibonding orbitals arising from the interaction of Cu3d and S3p electrons. Interestingly, this feature is particularly pronounced in the $(\sqrt{7}\times\sqrt{7})R19.1^\circ$ UP spectrum. Once again, a similar feature has been observed by Ling et al. in their work on Cu(100). In their work the feature is observed to appear upon formation of the $p(2\times 2)$ -S phase. In this structure, the S atoms are considered to occupy fourfold hollow sites on the Cu(100) surface and hence we believe that the feature observed in our own work may also be related to sulphur adsorbed with fourfold co-ordination. Hence this may support the structural model proposed by Foss et al. [10] and Jackson and co-workers [6] who suggested that the $(\sqrt{7}\times\sqrt{7})R19.1^\circ$ reconstruction involves the formation of Cu_4S tetramers.

For each of the sulphur coverages examined using UPS in figure 4, LEED observations of the surface were also made. A LEED pattern obtained from the clean Cu(111) surface is shown in figure 5 and is characteristic of a clean, well-ordered Cu(111) surface.

LEED observations of the 0.11 and 0.16 ML sulphur covered surfaces showed no significant differences to that of the clean Cu(111) surface. However, the LEED patterns recorded of the adsorption of 0.29 and 0.43 ML S show significant structure. These are shown in figures 6 and 7 respectively along with partial overlays of the associated theoretical patterns.

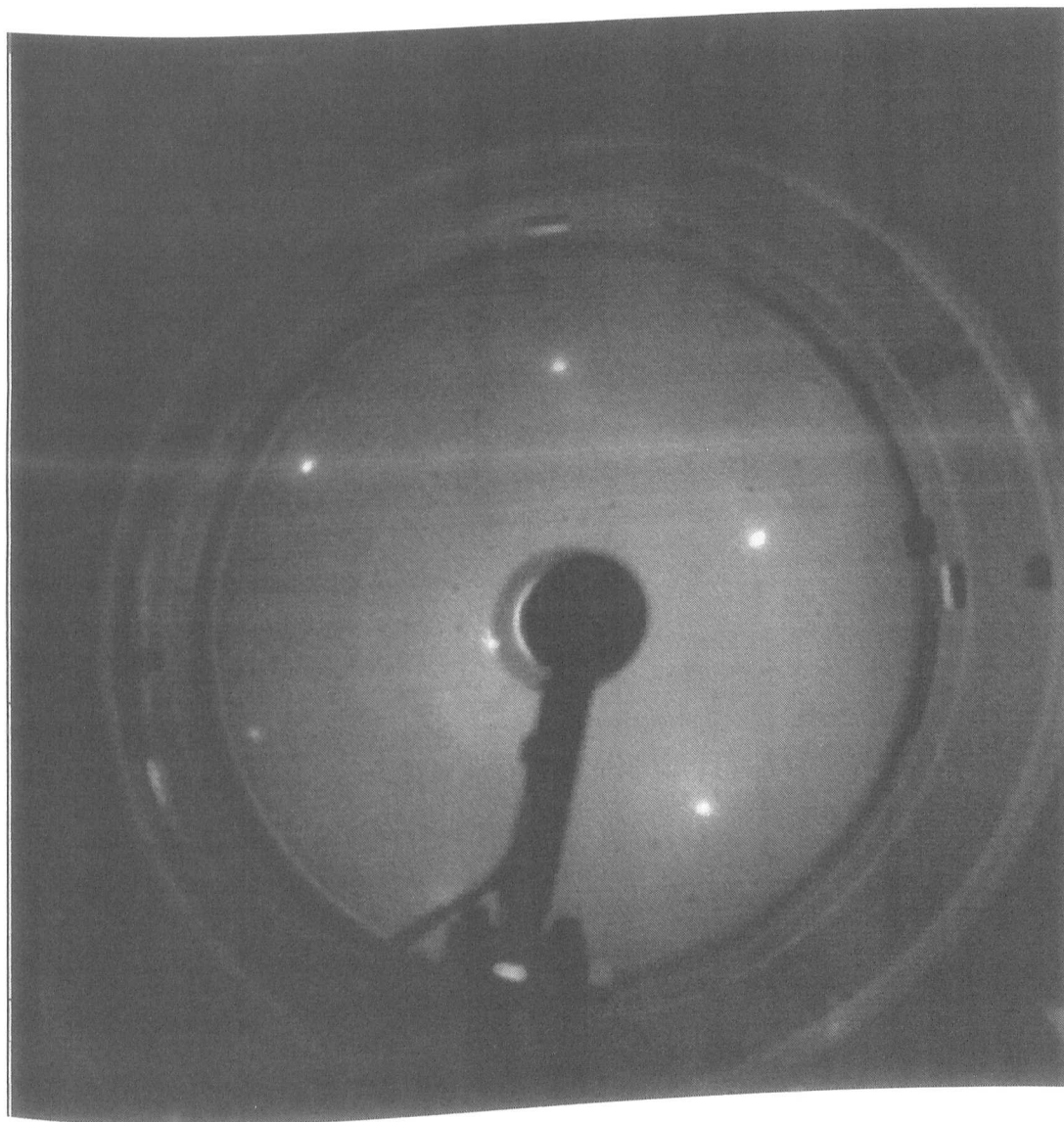


Figure 5. LEED pattern showing the clean Cu(111) (1×1) surface taken at $T=307$ K and $E_b=110$ eV.

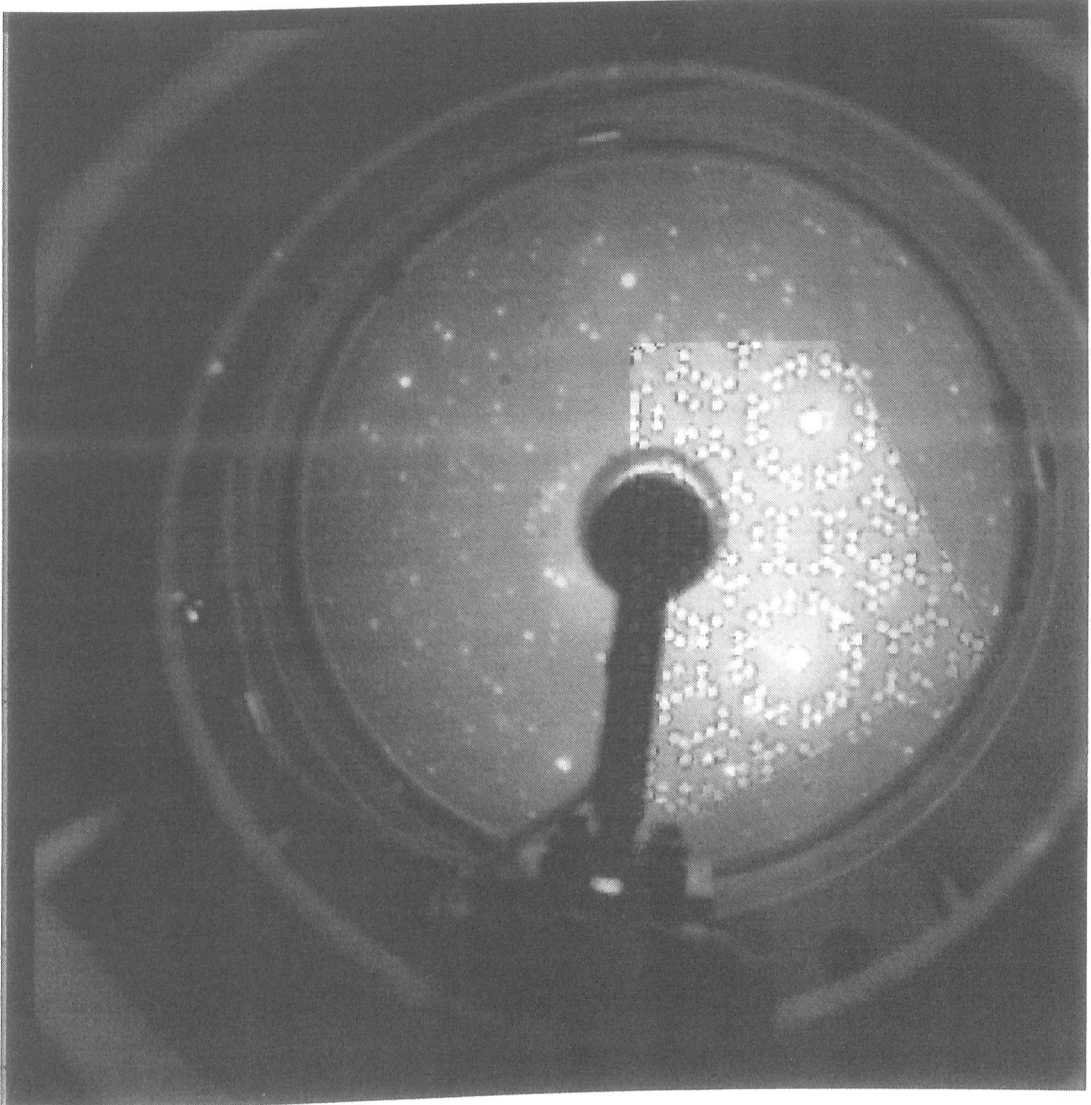


Figure 6. LEED pattern showing 0.29 ML S covered surface. $T= 293$ K. $E_b= 110$ eV. Partial overlay of theoretical zigzag LEED pattern obtained from ref. 23.

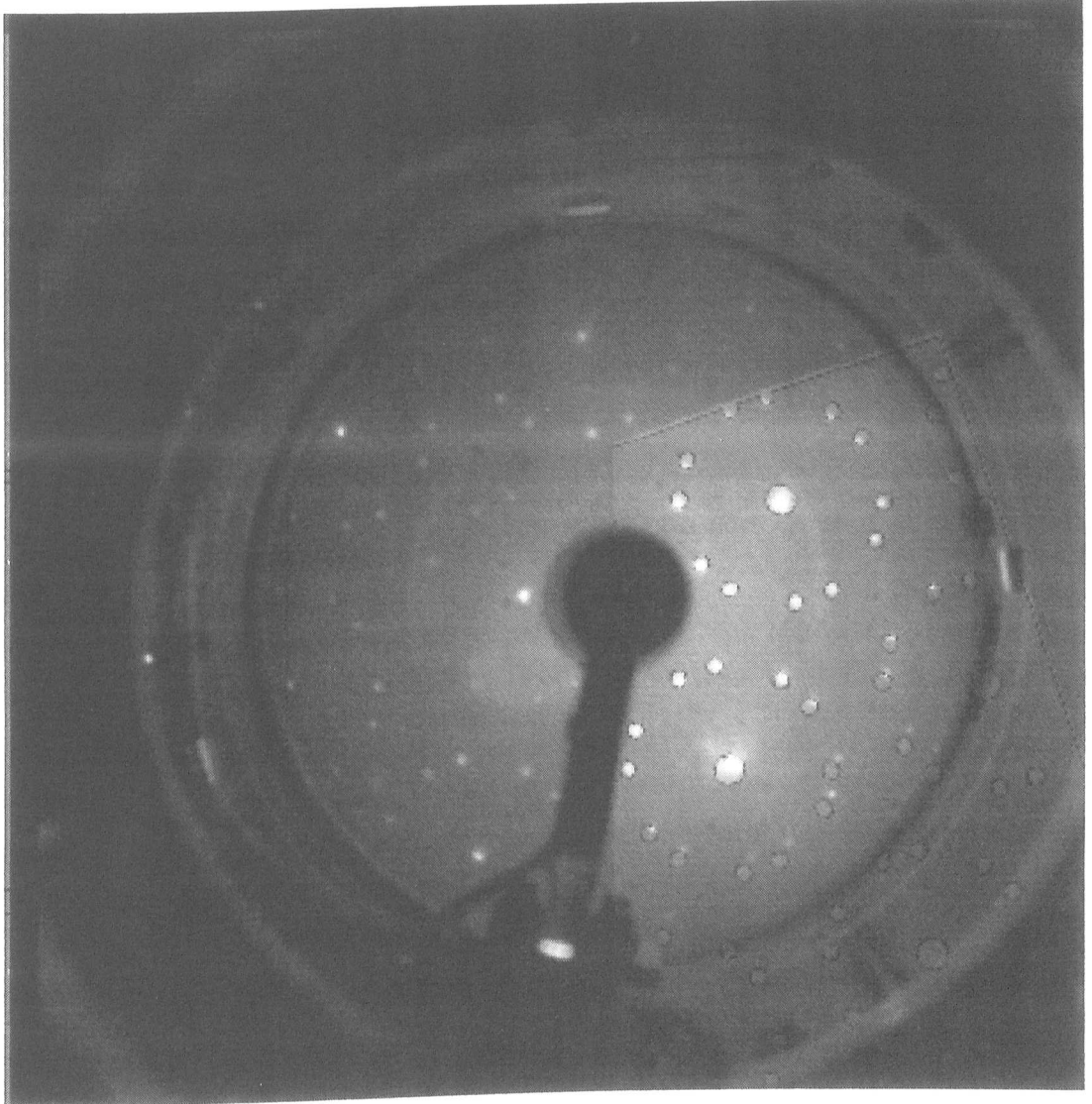


Figure 7. LEED pattern showing 0.43 ML S covered surface. $T= 273$ K. $E_b= 110$ eV. Partial overlay of theoretical $(\sqrt{7}\times\sqrt{7})R19.1^\circ$ LEED pattern obtained from ref. 23.

Figure 6 shows the LEED pattern recorded with a sulphur coverage of 0.29 ML. Within experimental error this coverage is consistent with the expected coverage (0.33 ML) at which the zigzag (or complex) phase has been observed previously. The theoretical pattern associated with this phase is also shown in figure 6 and displays a close match to the experimental pattern. However, there are some small discrepancies between the experimental and theoretical patterns. Firstly, the curvature of the LEED optics means that the flat theoretical overlay cannot be matched perfectly over large areas of the screen. However, more importantly, we observe some spots missing from the experimental data that are found in the theoretical pattern. This is particularly clear in the ring of spots surrounding the substrate spots of the copper. We would suggest that this may have been observed previously and may be part of the reason why the pattern has proved difficult to identify in the past. Hence, the reason for its initial name of the complex phase. Additionally, many of the structures observed after sulphur adsorption on Cu(111) have been shown to be sensitive to both temperature and sulphur coverage. Hence, we believe the missing spots may be the result of a narrow range of temperature and/or S coverage.

The LEED pattern recorded in figure 7 is entirely consistent with that expected for a saturation coverage of S on Cu(111), namely the $(\sqrt{7}\times\sqrt{7})R19.1^\circ$ structure. The overlay of the theoretical $(\sqrt{7}\times\sqrt{7})R19.1^\circ$ is a good match for the observed LEED pattern, although as before we observe a small degree of discrepancy associated with the curvature of the LEED screen.

Finally, as a last part of our characterisation measurements of the interaction of S with the Cu(111) surface we studied the effects of increasing sulphur adsorption on the work function of the surface. The work function of a solid is defined as the minimum energy required to remove an electron. It can be considered to be a measurement arising from a combination of two contributions. Firstly, one associated with the bulk electronic properties of the solid and secondly a contribution from a surface dipole layer. The surface dipole layer is caused by electron overspill generated from electron wavefunctions penetrating outside the surface. This causes a positive charge at the solid surface to preserve electronic neutrality and hence, generates a dipole layer at the surface. Adsorption on the surface, particularly when significant charge transfer is involved causes changes to this dipole layer and can therefore be measured by work function. In the case of sulphur adsorption we expect charge transfer from the metal to the adsorbate

creating a dipole layer with negative charge outermost, in the same manner as the surface dipole layer. Hence, we expect a net increase in the surface dipole layer and therefore an increase in work function. Our experimental measurements of the change in work function induced on Cu(111) with increasing sulphur coverage are shown in figure 8.

Within experimental error, we observe a gradual increase in work function of 0.15 eV up to a sulphur coverage of 4.0 ML S. At saturation coverages above this where we expect formation of the $(\sqrt{7}\times\sqrt{7})R19.1^\circ$ we observe a sudden increase in work function of 0.13 eV. This data is consistent with previous work function measurements of S adsorption on transition metals. On the Ni(100) [24] surface, sulphur adsorption results in a general increase in work function with increasing sulphur exposure. On the Pt(111) surface [25] however the authors observe an initial increase in work function but a drop upon formation of the ordered $p(2\times 2)$ structure and then a further subsequent increase upon formation of the $(\sqrt{3}\times\sqrt{3})R30^\circ$ structure. Hence, our own data reflects the results of these studies in that we observe a general increase in work function upon adsorption and a sudden change upon the formation of a well ordered structure involving a significant reconstruction.

The observations made here using work function may also provide some information regarding the structures formed in the S/Cu(111) system. Up until onset of the $(\sqrt{7}\times\sqrt{7})R19.1^\circ$ structure we observe essentially linear increases in work function with increasing sulphur coverage. We believe this observation may suggest that up until onset of the $(\sqrt{7}\times\sqrt{7})R19.1^\circ$ structure, there are no significant structural changes on the copper surface. This initially would seem to contradict the idea that a number of different structures are formed on Cu(111) prior to $(\sqrt{7}\times\sqrt{7})R19.1^\circ$ formation. However, it may suggest that all the structures formed prior to the $(\sqrt{7}\times\sqrt{7})R19.1^\circ$ may be closely related and possibly formed from the same basic building blocks. This hypothesis has been confirmed in NIXSW measurements performed previously by our lab on increasing sulphur coverage on Cu(111) [26]. The results of these measurements showed that sulphur adsorption results in identical NIXSW profiles at all sulphur coverages below that of $(\sqrt{7}\times\sqrt{7})R19.1^\circ$ formation. The authors also conclude that the structure is analogous to that of bulk covallite (CuS). As described in the introduction this has been suggested as a possible structure formed during S adsorption on Cu(111) previously. Their own

NIXSW measurements of the $(\sqrt{7}\times\sqrt{7})R19.1^\circ$ structure are consistent with previous work.

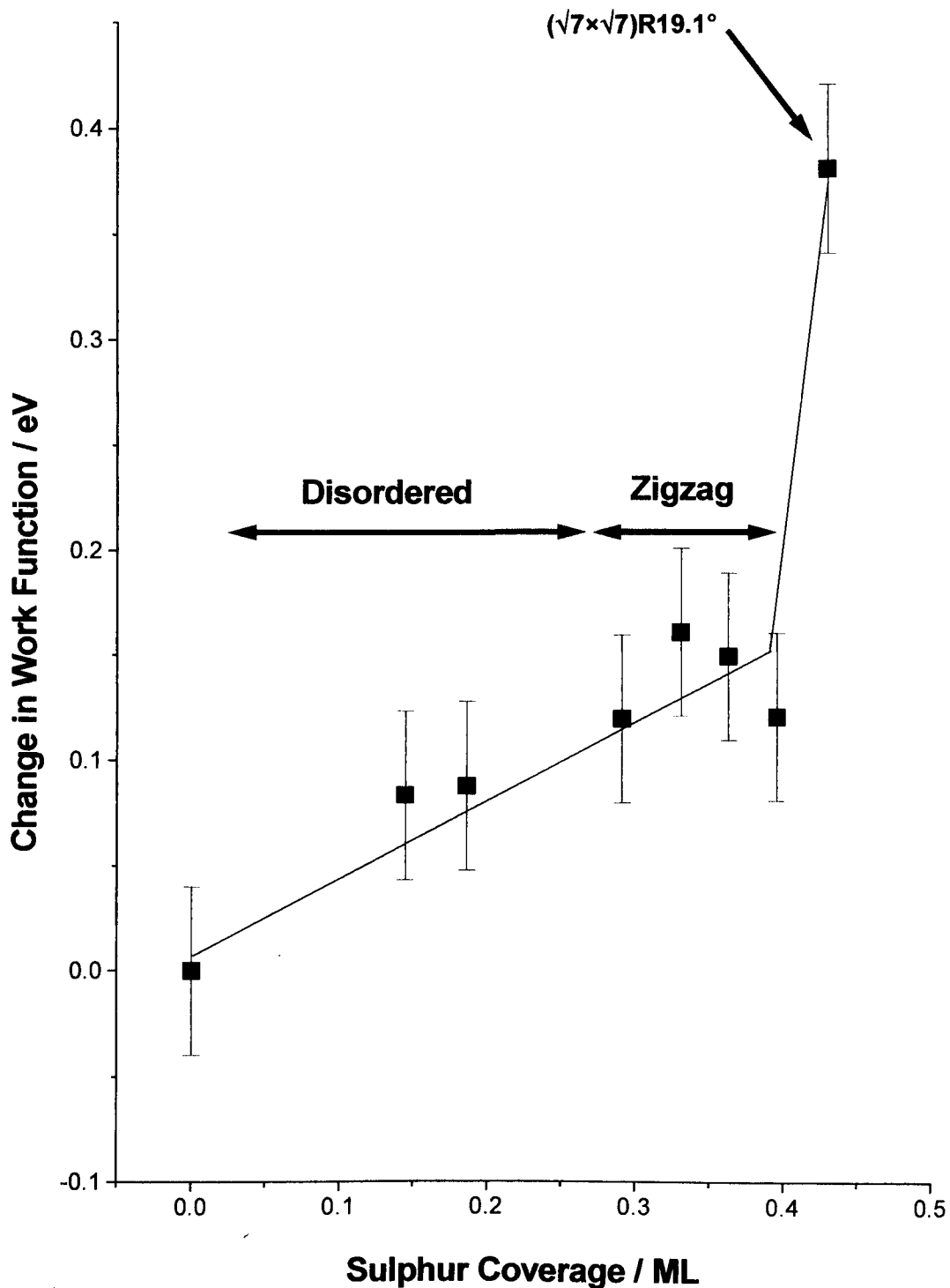


Figure 8. Changes in work function induced by increasing S on Cu(111).

5.2.2 Dimethyl Disulphide

Initial characterisation of the adsorption of DMS on Cu(111) took place using TPD. Figure 9 shows nested TPD spectra of the desorption of DMS and subsequent dissociation of methyl thiolate from Cu(111). In figure 9a the Cu(111) surface was exposed to 5L DMS, which is sufficient to obtain DMS multilayers, at ca. 100 K and the TPD spectrum was then recorded by monitoring the evolution of its parent ion (94 amu). Only one peak is observed in the TPD spectra, with a $T_{\max}=154$ K, which we attribute to desorption of DMS multilayers. No further DMS desorption is observed in our studies up to temperatures of 800 K. Hence, this would suggest complete dissociation of the chemisorbed layer.

Due to the limitations of our experimental set up we were unable to perform experiments involving heating continuously from 100 to 800 K. Hence, we first heated from 100 K to room temperature, then allowed the liquid nitrogen in the sample re-entrant to boil off before continuing the experiment. We found that the disadvantage of this method is exposing the crystal to further DMS desorption from the glass re-entrant. Hence, we also performed experiments where the surface was exposed to DMS at room temperature (ca. 298 K). These experiments were found to be in qualitative agreement with those at lower temperature and are shown in figures 9b, 9c and 9d.

Figures 9b, 9c and 9d show desorption from dissociation products of increasing coverages of DMS (which previous work has shown dissociates to methyl thiolate at room temperature) by monitoring desorption at 16, 30 and 2 amu for 9b, 9c and 9d respectively. Due to the dissociation, the sample was cleaned between each dose. In the 16 amu spectra we observe a broad desorption feature, beginning almost immediately upon heating of the surface from 325-475 K. Desorption extends to slightly higher temperatures still in the 2L exposure. Desorption in the 30 amu spectra is somewhat narrower and extends from 375 K to 450 K. Finally, we observe no significant desorption in the 2 amu spectra, within experimental error, except in the 0.5L and 2L spectrum. In these spectra we observe a very small amount of H_2 desorption with a maximum at 430 K. In both the 16 and 30 amu data we observe unusual changes with different exposures of DMS. The spectra vary to some degree in shape, magnitude and the relative positions of T_{\max} . These changes appear to show no clear pattern with respect to coverage. However, we speculate dissociation may be affected by changes to the surface due to cleaning between experiments

e.g. slightly differing defect concentrations. Also, as previously observed we detect the presence of sulphur using AES after completion of TPD experiments, however, we observe no dissociated carbon. This was investigated further using XPS.

As described earlier, dissociation of DMS to methyl thiolate and the subsequent dissociation of methyl thiolate have been observed on a number of occasions. However, no previous TPD measurements of the system have been made and therefore no mechanism has been proposed previously for the molecules dissociation. We propose here based on our own measurements that the desorption masses just described are associated with methane (16 amu), ethane (30 amu) and hydrogen (2 amu). Hence, from our observations we believe that dissociation proceeds via two routes. Firstly, breaking of the S-C bond followed by addition of a hydrogen to the methyl group, resulting in methane desorption. Secondly, breaking of the S-C bond followed by recombination of two methyl groups to form ethane. The first of these mechanisms does raise the question of the source of hydrogen from which methane forms from the dissociated methyl group. We believe there are two possibilities for this. Methane forms from the dissociated methyl group and adsorbed hydrogen present on the surface. Alternatively, we believe there could be some formation of ethene. This would proceed by the combination of two methyl groups and loss of two hydrogen atoms. This hydrogen could then be involved in methane formation. Unfortunately, we did not detect at 28 amu during experiments and cannot confirm this mechanism. In either process, hydrogen would be involved in methane formation and hence, we would not expect to observe significant desorption of H₂ from the surface, consistent with our observations.

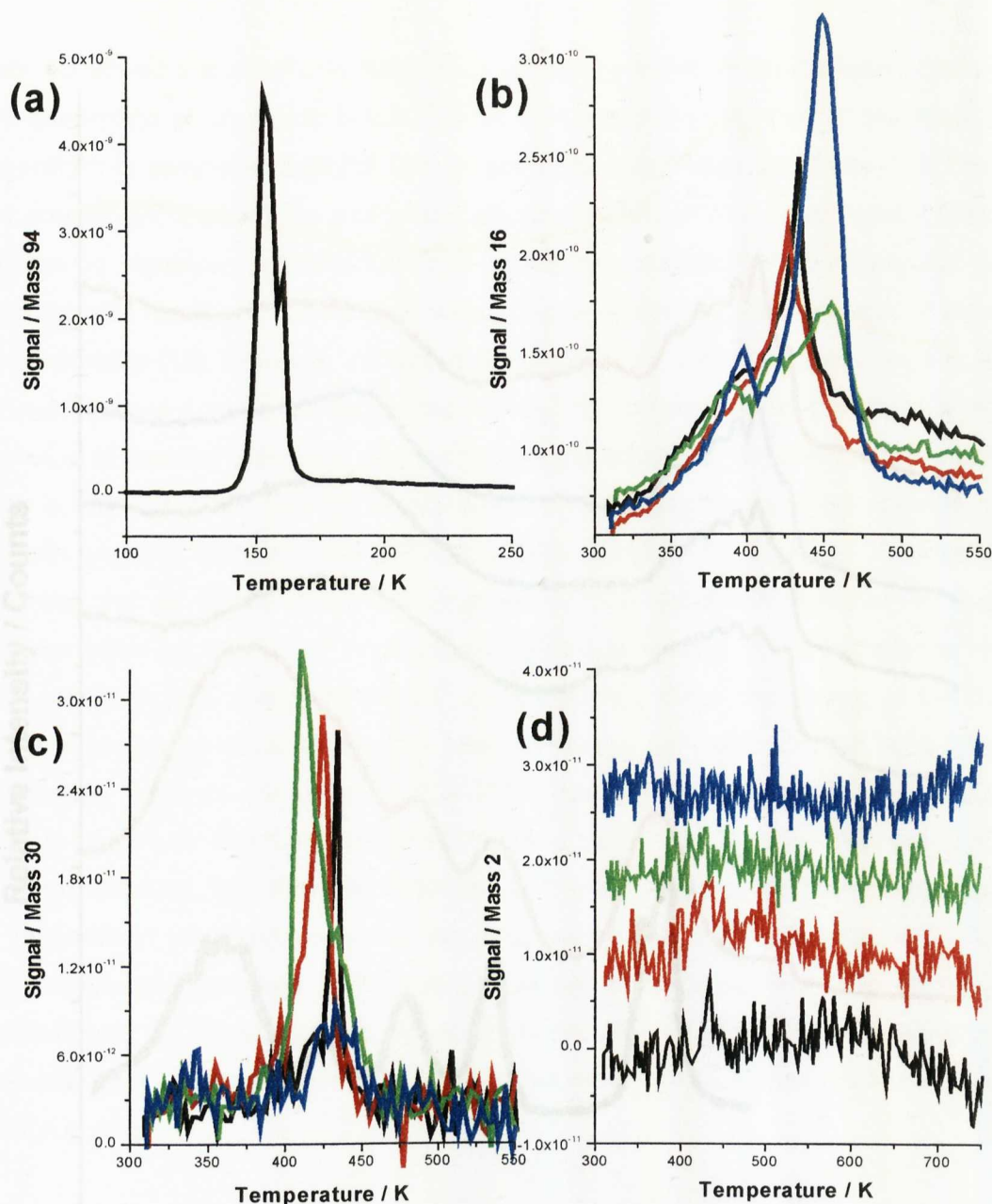


Figure 9a. TPD spectra showing the desorption of DMS (parent ion 94 amu) from Cu(111). Desorption is observed from DMS multilayers at 154 K.

Figure 9b. TPD spectra showing desorption of methane (16 amu) from Cu(111) exposed to 0.1 (blue), 0.25 (green), 0.5 (red) and 2 (black) L DMS. Desorption is observed between 325 to 475 K.

Figure 9c. TPD spectra showing desorption of ethane (30 amu) from Cu(111) exposed to 0.1 (blue), 0.25 (green), 0.5 (red) and 2 (black) L DMS. Desorption is observed between 375 to 450 K.

Figure 9d. TPD spectra showing desorption of hydrogen (2 amu) from Cu(111) exposed to 0.1 (blue), 0.25 (green), 0.5 (red) and 2 (black) L DMS. Desorption is observed at 430 K in 0.5 and 2L spectra.

All spectra were collected with a heating rate of 0.5 Ks⁻¹.

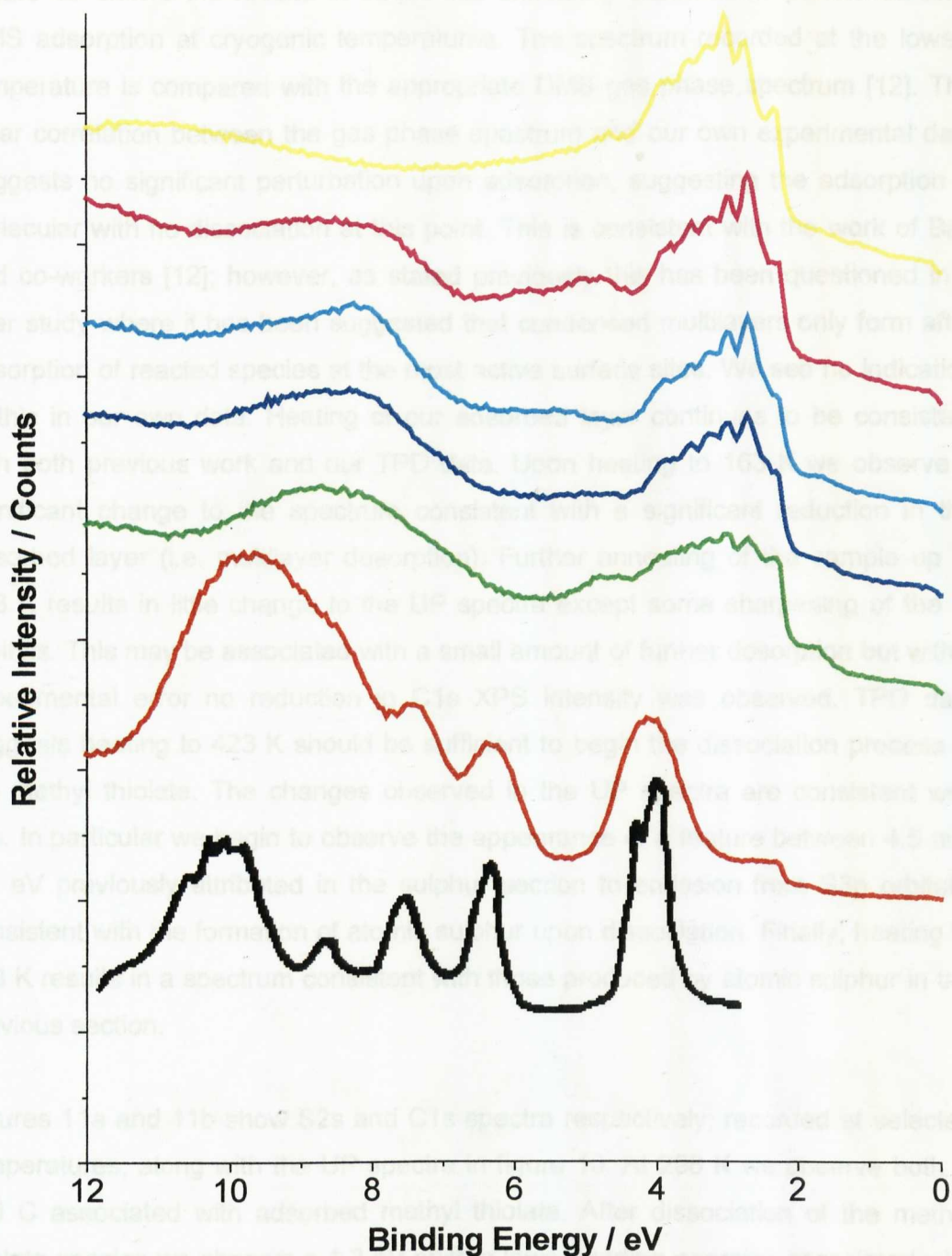


Figure 10. Normal emission UP spectra of DMS (and methyl thiolate) adsorbed on Cu(111) at 108 K (red), heated to 163 K (green), 222 K (blue), 298 K (cyan), 423 K (magenta) and 823 K (yellow). The gas phase DMS UP spectrum (black) is also shown for comparison [12].

Figure 10 shows the results of sequential annealing experiments performed after DMS adsorption at cryogenic temperatures. The spectrum recorded at the lowest temperature is compared with the appropriate DMS gas phase spectrum [12]. The clear correlation between the gas phase spectrum and our own experimental data suggests no significant perturbation upon adsorption, suggesting the adsorption is molecular with no dissociation at this point. This is consistent with the work of Bao and co-workers [12]; however, as stated previously this has been questioned in a later study where it has been suggested that condensed multilayers only form after adsorption of reacted species at the most active surface sites. We see no indication of this in our own data. Heating of our adsorbed layer continues to be consistent with both previous work and our TPD data. Upon heating to 163 K we observe a significant change to the spectrum consistent with a significant reduction in the adsorbed layer (i.e. multilayer desorption). Further annealing of the sample up to 298 K results in little change to the UP spectra except some sharpening of the d-orbitals. This may be associated with a small amount of further desorption but within experimental error no reduction in C1s XPS intensity was observed. TPD data suggests heating to 423 K should be sufficient to begin the dissociation process of the methyl thiolate. The changes observed in the UP spectra are consistent with this. In particular we begin to observe the appearance of a feature between 4.5 and 6.5 eV previously attributed in the sulphur section to emission from S3p orbitals, consistent with the formation of atomic sulphur upon dissociation. Finally, heating to 523 K results in a spectrum consistent with those produced by atomic sulphur in the previous section.

Figures 11a and 11b show S2s and C1s spectra respectively, recorded at selected temperatures, along with the UP spectra in figure 10. At 298 K we observe both S and C associated with adsorbed methyl thiolate. After dissociation of the methyl thiolate species we observe a 1.3 eV shift to lower binding energies associated with the change from molecular S to an atomic S species. The measured S intensity corresponds to a surface coverage of 0.32 ± 0.03 ML. Consistent with our previous AES experiments, we also observe no carbon contamination after methyl thiolate dissociation. Both our UPS and XPS data are consistent with the results of a number of previous studies. Additionally, as discussed in detail in reference 13, the data is in qualitative agreement with the desorption of DMS on both Ni(100) and Cu(100).

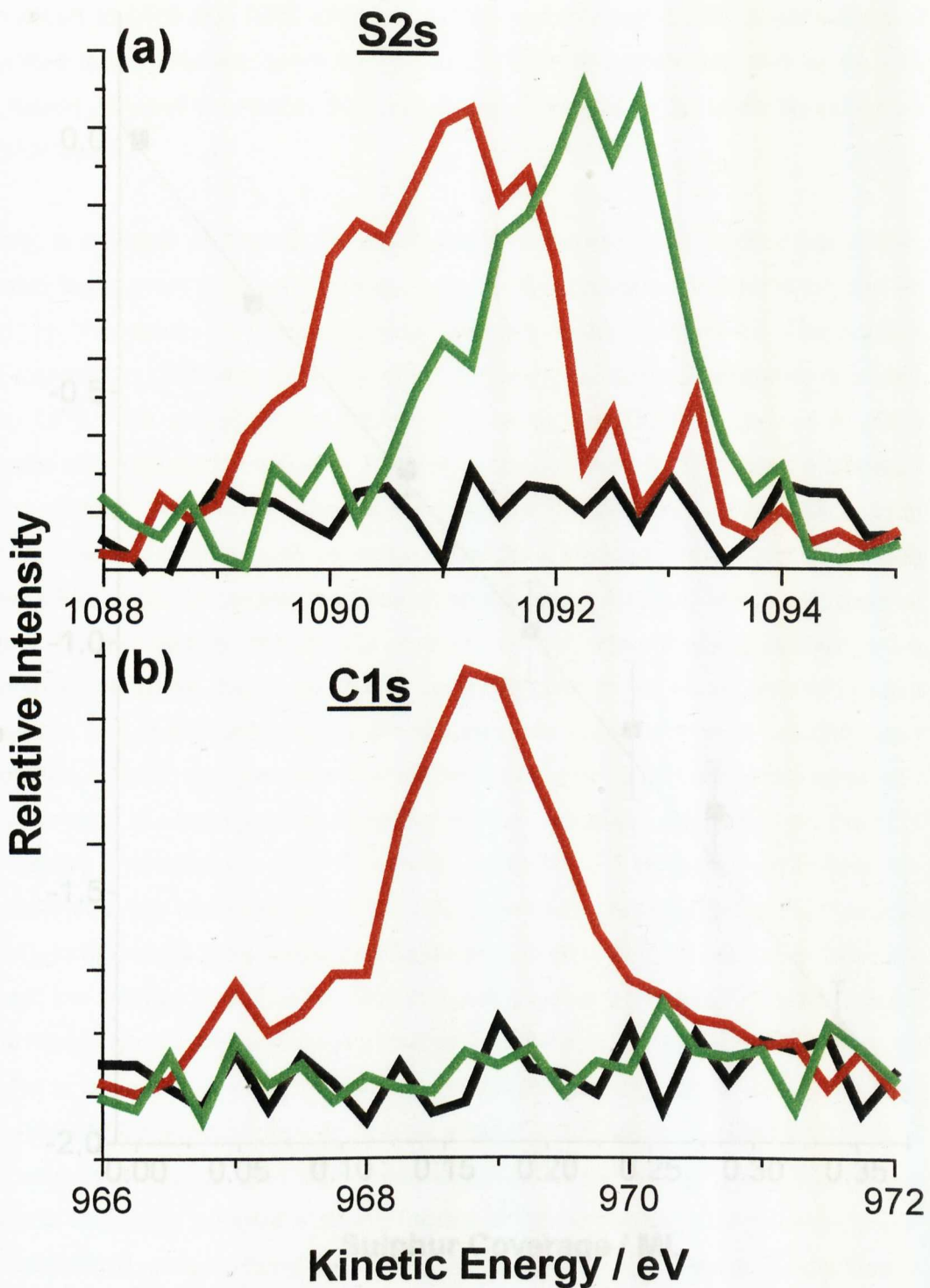


Figure 11a. S2s XP spectra of clean Cu(111) surface (Black), methyl thiolate on Cu(111) heated to 298 K (Red), and 823 K (Green).

Figure 11b. C1s XP spectra of clean Cu(111) surface (Black), methyl thiolate on Cu(111) heated to 298 K (Red), and 823 K (Green).

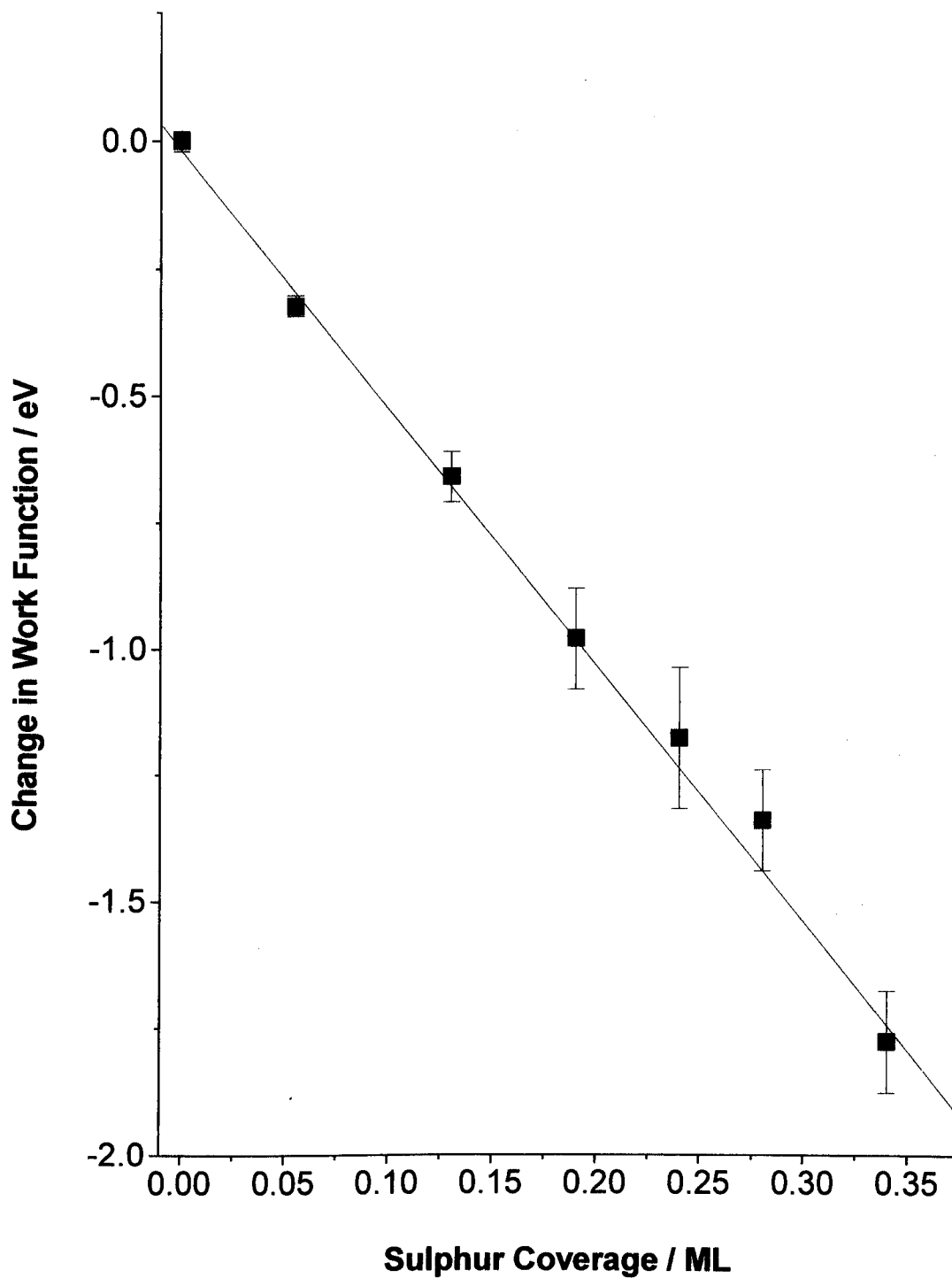


Figure 12. Changes in work function induced by increasing methyl thiolate adsorption on Cu(111).

In addition to UPS and XPS measurements we also made LEED observations of saturated methyl thiolate layers on Cu(111). These measurements also agree with the results of previous studies and show methyl thiolate to be unstable under an electron beam.

Finally, in a similar manner to the experiments performed upon sulphur adsorption, we also made work function measurements of the adsorption of methyl thiolate on Cu(111). The results of these measurements are shown in figure 12. The surface was exposed to DMS at room temperature and work function subsequently recorded using UPS. The adsorption of methyl thiolate on the Cu(111) surface has the opposite effect on work function to that previously observed upon sulphur adsorption on the surface. We observe the work function of the surface to decrease linearly with increasing methyl thiolate coverage. In addition we also observe the magnitude of the effect to be far greater than that observed using sulphur, with a decrease of around 1.8 eV. Initially, the results of these measurements would appear to be unusual in the sense that if we expect methyl thiolate to act as an electronegative adsorbate, like atomic sulphur, we would expect an increase in work function upon adsorption. Indeed, the decrease in work function is more commonly associated with the adsorption of electropositive elements such as Na where adsorption on Cu(111) [27] causes a decrease in work function of up to 2.5 eV. However, we believe we can rationalise our observations by consideration of the theoretical work of Ferral et al. [28]. In this study the authors concluded the bonding of the molecule is primarily through the sulphur p-orbitals but also suggest a lesser interaction with the orbitals of the methyl group. This results in a charge transfer from the metal to the adsorbate causing a depletion of electron density around the primary site of chemisorption, accompanied by accumulation of charge around the S atom. In addition to this a small degree of charge depletion is also observed at the methyl group. Hence the results of this study suggest a strong molecular dipole running along the molecule from the methyl group towards the more electronegative sulphur atom. As discussed already, previous work has shown methyl thiolate adsorbs on Cu(111) with the S-C bond in an orientation close to perpendicular to the surface. Hence, the dipole associated with the molecule will be anti-parallel to that associated with the copper surface. Thus, unlike the situation for atomic sulphur where the direction of charge transfer increases the surface dipole, the anti-parallel dipole associated with methyl thiolate will have the opposite effect, reducing the magnitude of the surface dipole and therefore causing a decrease in work function. This is depicted in figure 13.

5.3.2 Dimethyl Disulphide

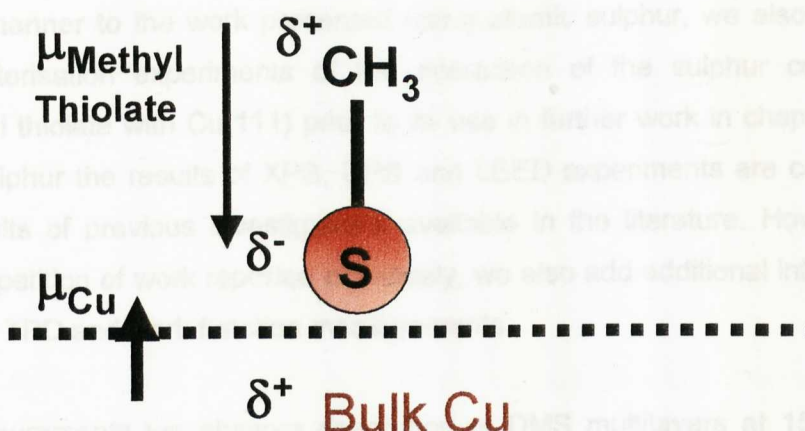


Figure 13. Schematic diagram of interaction of methyl thiolate with the Cu(111) surface.

5.3 Conclusions

5.3.1 Sulphur

We have performed initial characterisation experiments of the interaction of sulphur with Cu(111) as a precursor to the work we present in chapter 6. The results of XPS, UPS and LEED experiments are consistent with the results of previous work both already reported in the literature and performed in our lab. Adding a new dimension to the work reported previously, we have also performed work function measurements during increasing sulphur adsorption on the Cu(111) surface. The results of these measurements show an initial linear increase in work function with exposure to sulphur up until onset of the $(\sqrt{7}\times\sqrt{7})R19.1^\circ$ where we observe a sudden increase. With the aid of NIXSW experiments carried out in our lab previously, we suggest the results point towards the fact that up until the $(\sqrt{7}\times\sqrt{7})R19.1^\circ$, sulphur adsorption results in formation of an essentially CuS like structure. Hence, no significant changes in work function other than linear increase. Upon formation of the $(\sqrt{7}\times\sqrt{7})R19.1^\circ$ structure the work function then increases significantly due to the significant reconstruction of the surface.

5.3.2 Dimethyl Disulphide

In a similar manner to the work presented using atomic sulphur, we also perform initial characterisation experiments of the interaction of the sulphur containing moiety methyl thiolate with Cu(111) prior to its use in further work in chapter 6. As for atomic sulphur the results of XPS, UPS and LEED experiments are consistent with the results of previous investigations available in the literature. However, in addition to repetition of work reported previously, we also add additional information in the form of TPD and work function measurements.

In TPD measurements we observe desorption of DMS multilayers at 154 K. No further desorption is observed until above room temperature, where we observe the dissociation products of methyl thiolate, methanol (16 amu) and ethane (30 amu) to desorb from the surface. For methane this occurs between 325 and 475 K, while for ethane this is observed between 375 and 450 K. We propose a mechanism consistent with our observations where the S-C bond breaks, leading to hydrogen addition to the methyl group resulting in methane desorption and recombination of two methyl groups to form ethane. Following dissociation and desorption we observe only atomic sulphur remaining on the Cu(111) surface, consistent with previous work.

Finally, we have performed work function measurements of adsorbed methyl thiolate on Cu(111). The results of these measurements show methyl thiolate has the opposite effect to that of atomic sulphur on the surface. We observe linear decrease in work function with increasing coverage up until a decrease of 1.8 eV at methyl thiolate saturation. We propose the effect is due to a strong molecular dipole associated with the methyl thiolate molecule orientated anti-parallel to that of the surface dipole causing a reduction in magnitude of the surface dipole and therefore of work function. This hypothesis is consistent with the results of previous theoretical work.

5.4 References

- [1] J.L. Domange and J. Oudar, *Surf. Sci.* 11 (1968) 125
- [2] L.Ruan, I. Stensgaard, F. Besenbacher, and E. Laegsgaard, *Ultramicroscopy*, 498 (1992) 42-44
- [3] K. Motai, T.Hushizume, H. Lu, D. Jeon, and T.Sukurai, *Appl. Surf. Sci.* 246 (1993) 67
- [4] E. Wahlström, I. Ekvall, H. Olin, S. Lindgren and L. Walldén, *Phys. Rev. B*, 60(15) (1999) 10699
- [5] E. Wahlström, I. Ekvall, T. Kihlgren, H. Olin, S. Lindgren and L. Walldén, *Phys. Rev. B*, 64 (2001) 155406
- [6] G.J. Jackson, S.M. Driver, D.P. Woodruff, B.C.C. Cowie and R.G. Jones, *Surf. Sci.* 453 (2000) 183
- [7] N.P. Prince, D.L. Seymour, M.J. Ahwin, C.F. McConville, D.P. Woodruff and R.G. Jones, *Surf. Sci.* 203 (1990) 13
- [8] Y. Kitajima, Y. Yakata, H. Sato, T. Yokoyama, T. Ohta, and H.Kuroda, *Jpn. J. Appl. Phys.* 32 (Suppl. 32-2) (1993) 377
- [9] M. Saidu and K.A..R Mitchell, *Surf. Sci.* 441 (1999) 425
- [10] M. Foss, R. Feidenhans'l, M. Neilsen, E. Findeisen, T. Buslaps, R.L. Johnson, F. Besenbacher, *Surf. Sci.* 388 (1997) 5
- [11] P.J. Feibelman, *Phys. Rev. Lett.* 85 (3) (2000) 606
- [12] S. Bao, C.F. McConville, and D.P. Woodruff, *Surf. Sci.* 187 (1987) 133
- [13] M.S. Kariapper, G.F. Grom, G.J. Jackson, C.F. McConville, and D.P. Woodruff, *J. Phys. Condens. Matter.* 10 (1998) 8661
- [14] G.J. Jackson, D.P. Woodruff, R.G. Jones, N.K. Singh, A.S.Y. Chan, B.C.C. Cowie, and V. Formoso, *Phys. Rev. Lett.* 84 (1) (2000) 119
- [15] S.M. Driver and D.P. Woodruff, *Surf. Sci.* 457 (2000) 11
- [16] S.M. Driver and D.P. Woodruff, *Surf. Sci.* 479 (2001) 1
- [17] C.T. Campbell and B.E. Koel, *Surf. Sci.* 183 (1987) 100
- [18] G. Rousseau, PhD Thesis, (2003)
- [19] D. Westphal and A. Goldmann, *Surf. Sci.* 131 (1983) 13
- [20] D.T. Ling, J.N. Miller, D.L. Weissman, P. Pianetta, P.M. Stefan, I. Lindau, and W.E. Spicer, *Surf. Sci.* 124 (1983) 175
- [21] H. Stör and H. Bross, *Surf. Sci.* 124 (1983) 99
- [22] K.K. Kleinherbers and A. Goldmann, *Surf. Sci.* 154 (1985) 489
- [23] K. Hermann and M. A. Van Hove, LEEDpat Version 2.0
- [24] E. L. Hardegree, Pin HO and J. M. White, *Surf. Sci.* 165 (1986) 488

[25] J. Billy and M. Abon, Surf. Sci. Lett. 171 (1) (1986) L387

[26] G. Rousseau, Unpublished work.

[27] D. Tang, D. McIlroy, X. Shi, C. Su and D. Heskett, Surf. Sci. Lett. 255 (1991) L497

[28] A. Ferral, P. Paredes-Olivera, V. A. Macagno and E. M. Patrito, Surf. Sci. 525 (2003) 85

Chapter 6: A Model Study of Crotonaldehyde Hydrogenation

6.1.1 Introduction

The α - β unsaturated aldehyde group of molecules are particularly interesting due to their importance in the fine chemicals industry. This class of molecules contain both a carbonyl group (C=O) and vinyl group (C=C) and the challenge in their use is to selectively control their hydrogenation to either the saturated aldehyde (by hydrogenation of the C=C), the unsaturated alcohol (by hydrogenation of the C=O) or the saturated alcohol (by hydrogenation of both double bonds). By far the most desirable of these for use in the fine chemicals industry is the unsaturated alcohol. However, this is also the most difficult to obtain during hydrogenation as in general terms the C=C bond is considered to be more easily hydrogenated than the C=O. The most successful methods of production used at present have been focussed on stoichiometric homogeneous hydrogenation techniques. However, selective hydrogenation using heterogeneous catalysts has been the subject of a great deal of interest and it is the results of one of these studies that we are particularly interested in here.

In the study in question, Hutchings and co-workers [1] studied the commonly used α - β unsaturated aldehyde model molecule, crotonaldehyde, and the effects of several sulphur containing moieties upon selectivity during hydrogenation on Cu catalysts. The authors concluded the presence of sulphur in any form resulted in an increased selectivity to crotyl alcohol, although the type of sulphur moiety did have a marked result upon the magnitude of the effect with selectivity changing in the order: $\text{CS}_2 \sim \text{SO}_2 < \text{DMS} \sim \text{thiophane} \sim \text{DMSO} < \text{thiophene}$. The effect was also concluded to be a general one for Cu catalysts and was found not to be dependent upon catalyst support. In addition to this, the authors also explored the effect further by examining the effects produced using thiophene modification of Cu catalysts, shown in the study mentioned above to have the greatest effect, on the hydrogenation of crotonaldehyde, acrolein, and a number of substituted molecules [2]. This study concluded that although blocking of active copper sites by sulphur takes place, the promotional effects are primarily electronic in nature. Finally, Hutchings et al. extended their studies to a number of other catalysts, finding the effect to be similar on Au but not on a number of other more traditional transition metal catalysts [3,4].

The observations of Hutchings are particularly interesting when considered with the fact that sulphur is traditionally seen as being an archetypal catalyst poison [5,6]. Therefore, we believe a more detailed study of the underlying mechanisms involved may prove to be interesting. Hence, in the current study we have attempted to use surface science techniques to rationalise the results obtained during the study of Hutchings and co-workers. To this end we have examined the adsorption of crotonaldehyde and its three hydrogenation products, butaldehyde, crotyl alcohol and 1-butanol on Cu(111) and the effects of co-adsorbed atomic sulphur upon bonding in part 1. In part 2, we then expand this study further by examining the effects of sulphur co-adsorption in the form of methyl thiolate with each of the four molecules.

The crotonaldehyde molecule has been the subject of a great deal of interest in the area of catalytic science [1-4,7,8]. However, there are only two previous occasions using surface science techniques where the adsorption of crotonaldehyde has been studied. Both of these have studied adsorption on the Pt(111) surface [9,10]. TPD measurements showed the dissociation of the molecule with the evolution of both CO and propene, which is not unexpected on the more reactive Pt(111) compared to Cu(111) surface. Both studies also focussed highly on the bond geometry of the molecule and hence the origin of the interaction of the molecule with the surface. Each study reached a generally similar conclusion through the use of RAIRS [9] and XPS [10], concluding the interaction of both the carbonyl and vinyl groups to be important with respect to bonding. A possible rehybridisation of the adjacent C=C and C-C bonds was suggested with the original C=C bonds forming two partial σ bonds with the platinum surface. Despite the C=C being in a roughly parallel geometry to the surface, the authors believe the C-C lie in a more upright orientation. The authors also suggest the reactivity of adsorbed aldehydes may also be strongly dependent upon adsorption geometry. In addition to this, one of these studies [9] also raises a further point of relevance. The authors initially note the trans form of crotonaldehyde to be the most energetically favourable but consider isomerisation to the cis form to be possible. Although, they eventually conclude this mechanism does not take place on Pt(111), it may be worth consideration in this study.

No further literature is available regarding crotonaldehyde adsorption and likewise we have identified no relevant work available on either butaldehyde or crotyl alcohol. The adsorption of 1-butanol, however, has been studied on two previous occasions

by Gellman et al. [11,12]. Both of these focussed on the interaction of a number of straight chain alcohols, including 1-butanol, with the Ag(110) surface. The authors concluded that the molecule adsorbs reversibly on the surface with a monolayer desorption temperature of 225 K. Additionally, a monolayer coverage of 1-butanol results in a reduction in surface work function of 0.88 eV. Finally, they predict adsorption takes place via the oxygen atom but that the alkyl chain is orientated close to parallel to the surface.

Due to the limited amount of previous interest in the four molecules studied here, we now expand our literature search further in an attempt to rationalise the possible interactions we may observe here. With this aim in mind we now consider previous work which may shed light on the differing interactions of C=C, C=O and C-OH groups with metal surfaces.

To examine the interaction of C=C we turn our attention to the interaction of ethene with Cu(111) [13-15]. Experimental studies show that ethene adsorption on Cu(111) is both molecular and reversible, with the molecule adopting a geometry parallel to the surface through a primarily π interaction. This is also confirmed in theoretical studies. Unfortunately, no further studies have been found examining simple organic molecules containing C=C groups on Cu(111). However, there is work examining propene on both Ni(100) [13] and Pt(111) [16], although this is obviously less relevant, it may warrant consideration. These showed a primarily π type interaction with the molecule bonded in a parallel manner to the surface in a similar way to ethene on Cu(111) but a di σ bonded molecule on Pt(111) similar to the crotonaldehyde studies on Pt(111) described earlier. Hence, the results of these studies may suggest that in both crotonaldehyde and crotyl alcohol the C=C group may play a role in the interaction with the copper surface.

In attempting to examine the possible effects of C=O and -OH groups to adsorption we now consider the results of previous work on acetone (C=O) and methanol (OH). Some of the results of these studies have already been alluded to in chapter 4 when the bonding of these molecules was considered along with that of THF and furan. Acetone has been the subject of study on both the (100) [17] and (110) [18] faces of copper, but prior to our own, no previous structural studies of acetone adsorption on Cu(111) had been performed. Both studies concluded acetone adsorption to be in an upright geometry via the oxygen lone pair. Our own study of acetone adsorption on Cu(111) [19] concluded the adsorption to be molecular and reversible. Both UPS

and NIXSW showed the molecule weakly interacts with the Cu(111) surface. An atop adsorption site is occupied with an O-Cu distance of 2.73 Å.

Methanol adsorption has been studied a number of times on the three low index faces of copper [20-28]. These studies concluded the adsorption of methanol to be molecular and reversible and although no previous structural studies had been performed, spectroscopic techniques had been used to infer adsorption takes place via the oxygen lone pair with the O-H and O-CH₃ tilted with respect to the surface normal on Cu(100). However, a theoretical investigation [28] of methanol adsorption on Cu(111) suggested the interaction to be through the hydroxyl proton. The results of our own study [29] confirm methanol adsorption to be molecular and reversible, adsorbing in an atop adsorption site with a O-Cu distance of 2.89 Å. Within experimental error this is the same distance as that observed in our acetone data, which we believe suggests the interaction to be through the oxygen lone pairs and not the hydroxyl proton.

Consideration of this work on acetone and methanol would lead us to expect the primary interaction between all four of the molecules in the current study to be through the oxygen atom. Additionally, it suggests we are only likely to observe a weak interaction between the molecules and the surface and that this interaction is not significantly affected by orbital character. Finally, the results of previous work suggest that all four of our molecules are likely to adsorb with an orientation significantly inclined towards or even parallel to the surface. In addition, for both crotonaldehyde and crotyl alcohol there may be an interaction between the C=C group and the surface.

In the current study we perform the first ever work on the adsorption of crotonaldehyde, butaldehyde, crotyl alcohol and 1-butanol on Cu(111) and then subsequently examine the effects of sulphur co-adsorption in the form of atomic sulphur and the sulphur containing moiety methyl thiolate. In TPD data we observe the stabilisation of the bonding of all four molecules in the presence of atomic sulphur at any coverage compared to the clean surface. However, we observe the effect to be more pronounced for both of the aldehydes where we observe an increase in desorption temperature of around 20-35 K more than for the alcohols. Additionally, sulphur is seen to inhibit the dissociation of both the alcohols, which was observed on the clean Cu(111) surface. Finally, we also observe sulphur to

induce orientation changes in the adsorbed layers of all four molecules, resulting in increased surface coverage.

In the presence of co-adsorbed methyl thiolate, we observe significantly different results in comparison to adsorption in the presence of atomic sulphur. TPD and UPS measurements show no significant effect on the adsorption of either of the aldehydes in terms of adsorption stability. However, we do observe a significant reduction in material in the adsorbed layer, which we attribute to steric effects caused by methyl thiolate blocking available adsorption sites. The adsorption of both of the alcohols is significantly different to that of either of the aldehydes. In the presence of methyl thiolate the adsorption of both alcohols is almost completely destabilised, with preferential adsorption of the alcohols believed to be on the CH_3 group of the methyl thiolate.

Based on these observations we propose an electrostatic model to account for the adsorption of the four molecules in the presence of atomic sulphur and methyl thiolate. In this model, the presence of atomic sulphur increases the magnitude of the surface dipole. This therefore generates a stronger interaction between the surface dipole and the anti-parallel dipole associated with each of the molecules. This interaction is enhanced further by orientation changes of the adsorbed molecules resulting in maximum dipole interaction. In the presence of methyl thiolate, our electrostatic model continues to apply. However, instead of increasing the magnitude of the surface dipole, methyl thiolate has a molecular dipole moment pointing towards the surface, reducing the magnitude of the surface dipole. Hence, upon co-adsorption of our four molecules we have two parallel dipoles, which is unfavourable and hence we see no stabilisation effects. In addition to this, we propose the effects of hydrogen bonding to be significant in the adsorption of the two alcohols. This causes preferential adsorption on the methyl group of the methyl thiolate and subsequent nucleation, again involving hydrogen bonding, resulting in almost complete destabilisation of the chemisorbed layer.

Finally, based on the results obtained here and the electrostatic mechanism just described we propose a mechanism to rationalise catalytic observations made during the hydrogenation of crotonaldehyde.

Part 1: The Adsorption of Crotonaldehyde and Related Molecules on Cu(111) and the Effects of Sulphur Co-adsorption

6.1.2 Results

6.1.2.1 Adsorption on Clean Cu(111) - TPD

Figures 1-4 show nested TPD spectra from surfaces exposed to sequentially higher doses of crotonaldehyde, butaldehyde, crotyl alcohol, and 1-butanol respectively, obtained by monitoring their parent ions (70, 72 and 72 amu) for crotonaldehyde, butaldehyde, and crotyl alcohol and the largest cracking fraction (56 amu) for 1-butanol. Monitoring 1-butanol's parent ion produces TPD spectra with poor signal to noise as the parent ion is a relatively small fraction of the cracking pattern. Exposures are quoted in units of mbar.s, with pressures being measured by an ion gauge with no correction for sensitivity.

Crotonaldehyde adsorbs reversibly on the Cu(111) surface. This is confirmed by AES taken after desorption showing no carbon remaining on the surface and the lack of any other desorption products such as H₂ being evolved during TPD experiments. There are three desorption features visible at 150 K, 163 K and 182 K. The features at 163 K and 182 K saturate with increasing coverage and are assigned to desorption from chemisorbed crotonaldehyde. The peak at 150 K does not saturate with increasing exposure and is attributed to desorption from condensed multilayers.

The TPD spectra for butaldehyde adsorbed on clean Cu(111) are shown in figure 2. Adsorption of butaldehyde is molecular and reversible, confirmed by the same observations as for crotonaldehyde. Desorption of butaldehyde multilayers takes place at 141 K followed by one saturated chemisorbed layer at 176 K.

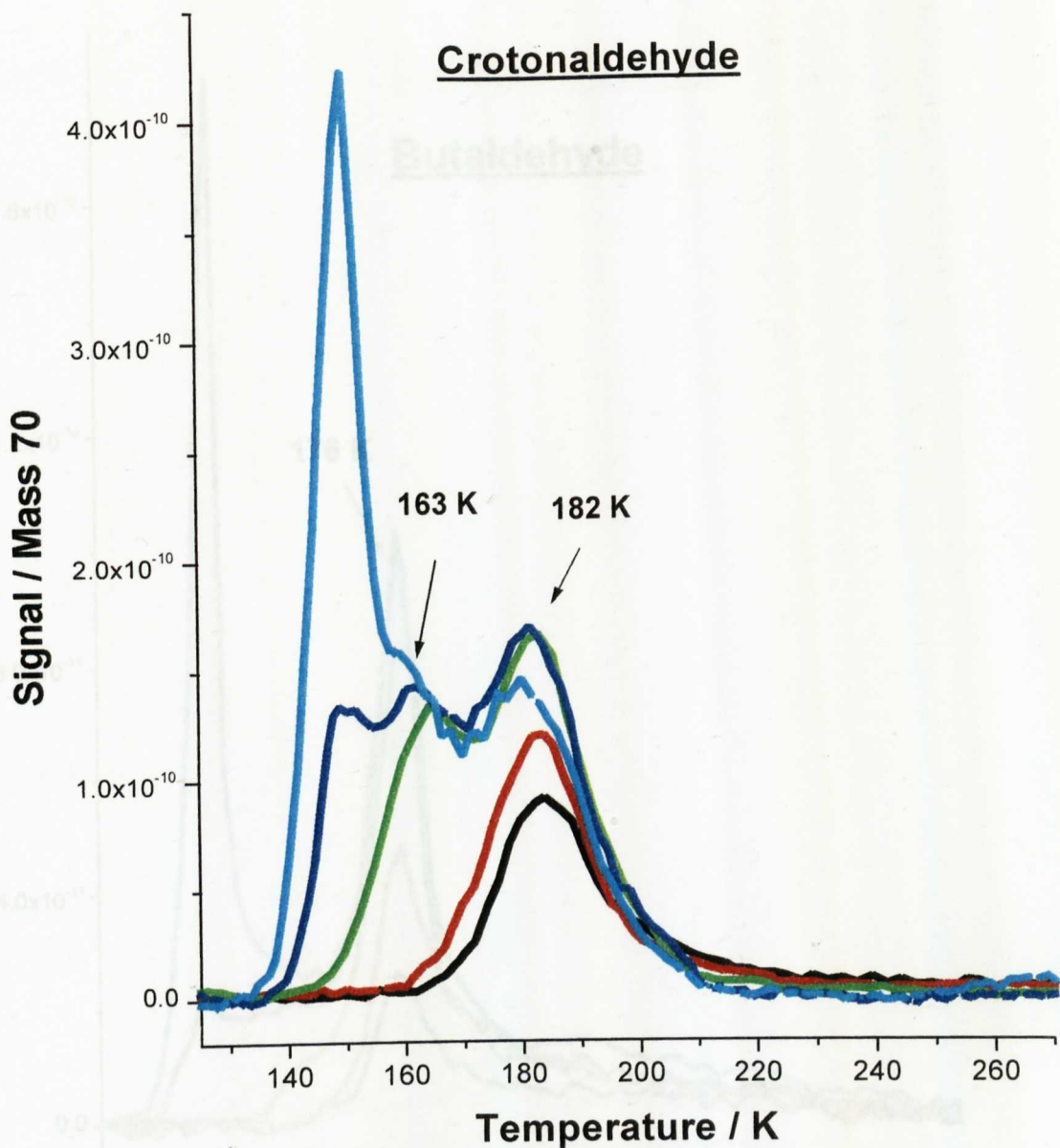


Figure 1. TPD spectra showing desorption of crotonaldehyde (parent ion 70 amu) from surfaces that had been dosed with sequentially higher exposures (0.5 (black), 1 (red), 2 (green), 3 (blue), 4 (cyan) $\times 10^{-6}$ mbar.s) at ca. 100 K are displayed. All spectra were collected with a heating rate of 0.5 K s^{-1} . Desorption is observed from chemisorbed (163 K and 182 K) and multilayer (150 K) states.

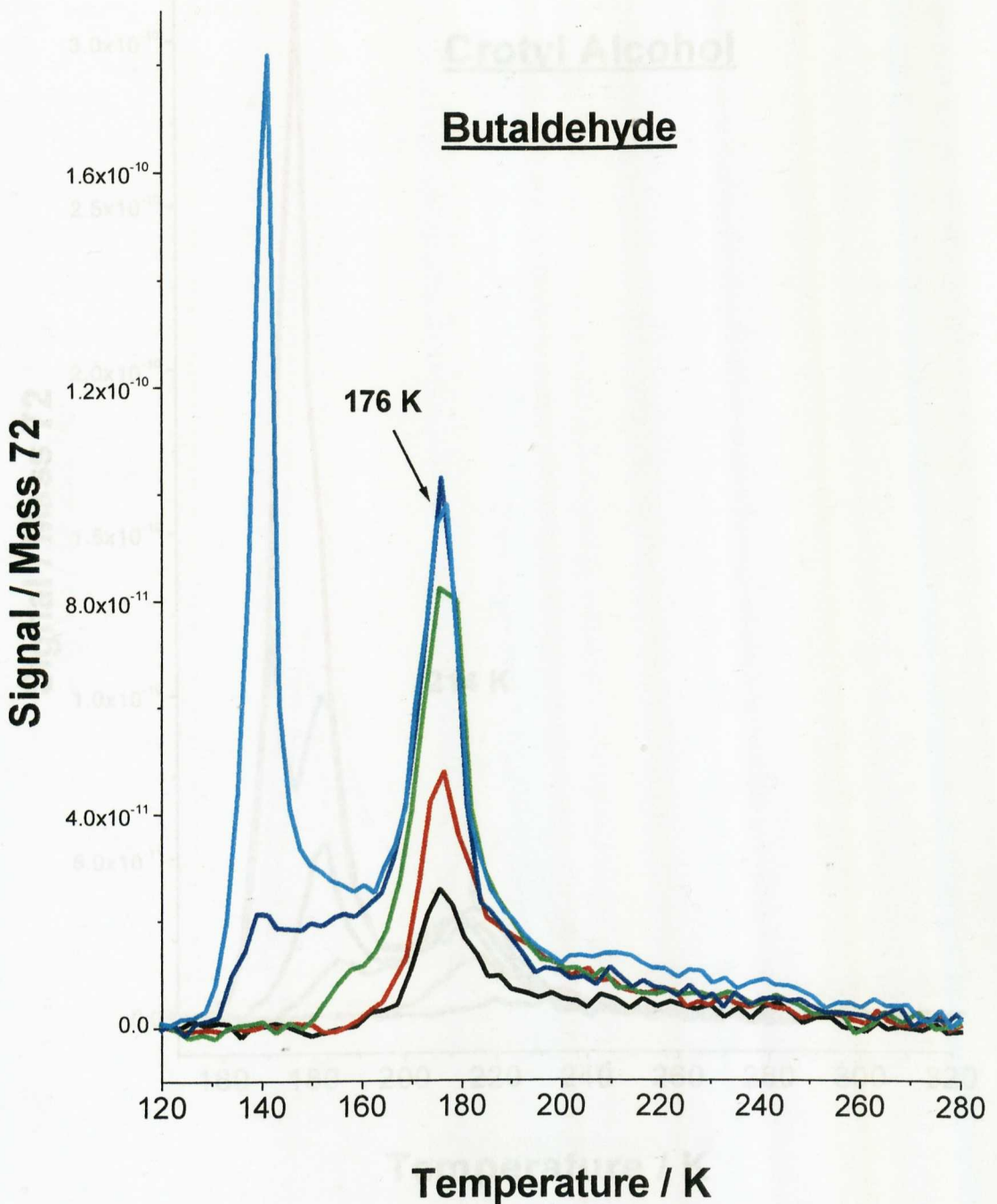


Figure 3. TPD spectra showing desorption of crotyl alcohol (parent ion 72 amu)

Figure 2. TPD spectra showing desorption of butaldehyde (parent ion 72 amu) from surfaces that had been dosed with sequentially higher exposures (1 (black), 2 (red), 3 (green), 4 (blue), 5 (cyan) $\times 10^{-6}$ mbar.s) at ca. 100 K are displayed. Experimental conditions were identical to those in figure 1. Desorption is observed from a chemisorbed state at 176 K and condensed multilayers at 141 K.

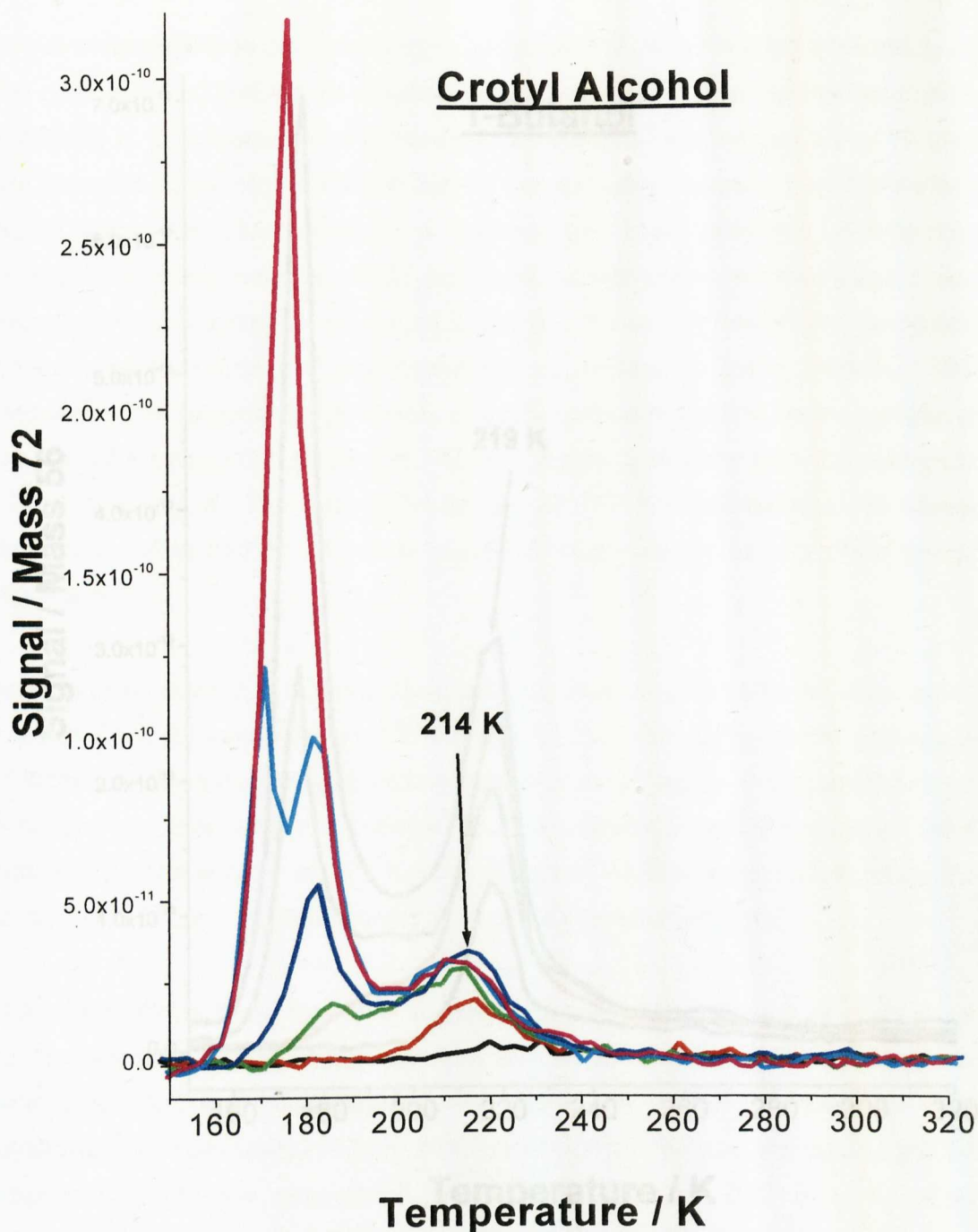


Figure 3. TPD spectra showing desorption of crotyl alcohol (parent ion 72 amu) from surfaces that had been dosed with sequentially higher exposures (0.1 (black), 0.25 (red), 1 (green), 2 (blue), 4 (cyan), 6 (magenta) $\times 10^{-6}$ mbar.s) at ca. 100 K are displayed. Experimental conditions were identical to those in figure 1. Desorption is observed from a chemisorbed state at 214 K and condensed multilayers at 177 K.

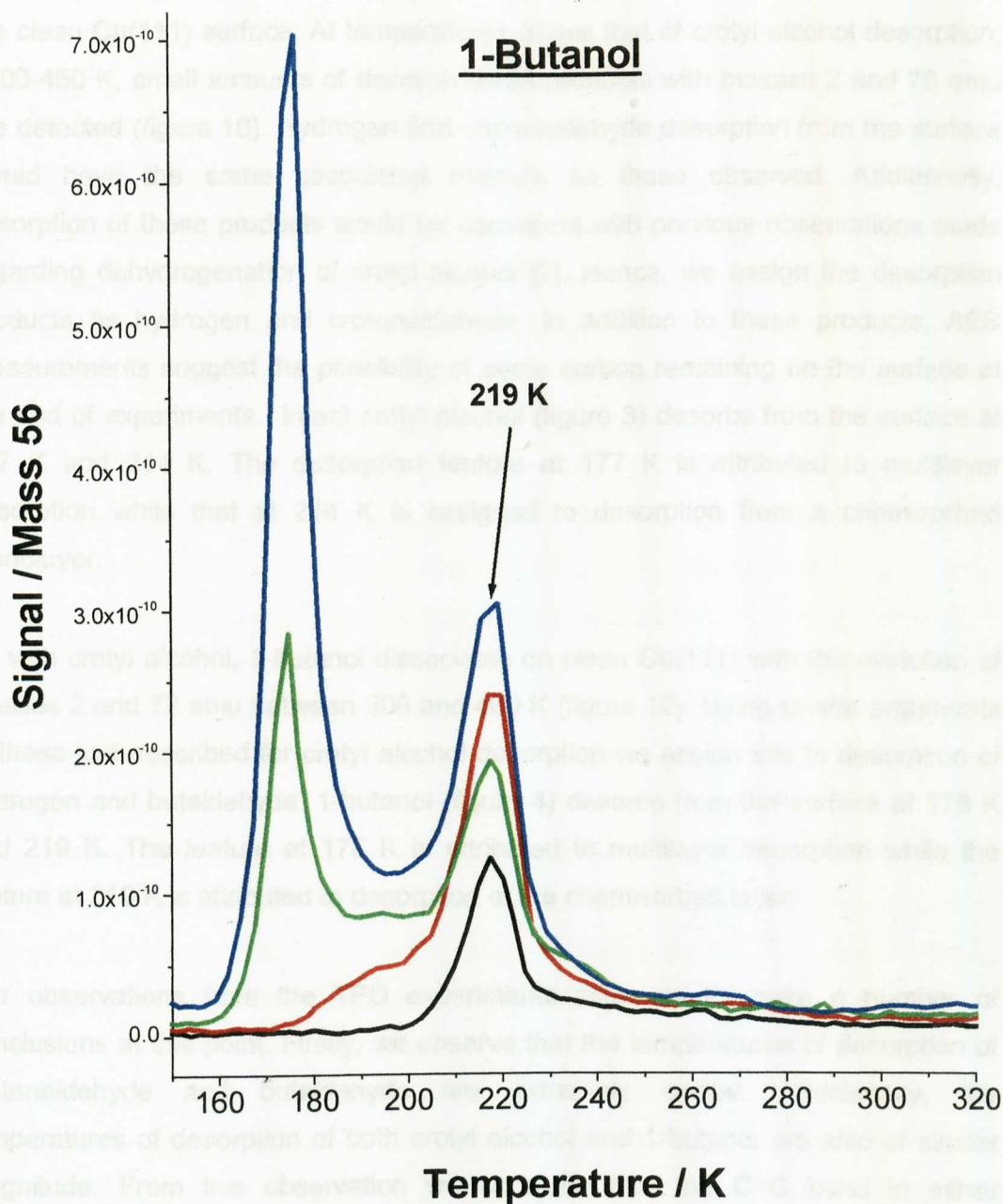


Figure 4. TPD spectra showing desorption of 1-butanol (cracking fraction at 56 amu) from surfaces that had been dosed with sequentially higher exposures (1 (black), 3 (red), 5 (green), 7 (blue), $\times 10^{-6}$ mbar.s) at ca. 100 K are displayed. Experimental conditions were identical to those in figure 1. Desorption is observed from a chemisorbed state at 219 K and condensed multilayers at 176 K.

Unlike crotonaldehyde and butaldehyde, crotyl alcohol does not adsorb reversibly on the clean Cu(111) surface. At temperatures above that of crotyl alcohol desorption, ~300-450 K, small amounts of decomposition products with masses 2 and 70 amu are detected (figure 10). Hydrogen and crotonaldehyde desorption from the surface would have the same associated masses as those observed. Additionally, desorption of these products would be consistent with previous observations made regarding dehydrogenation of crotyl alcohol [2]. Hence, we assign the desorption products as hydrogen and crotonaldehyde. In addition to these products, AES measurements suggest the possibility of some carbon remaining on the surface at the end of experiments. Intact crotyl alcohol (figure 3) desorbs from the surface at 177 K and 214 K. The desorption feature at 177 K is attributed to multilayer desorption while that at 214 K is assigned to desorption from a chemisorbed monolayer.

As with crotyl alcohol, 1-butanol dissociates on clean Cu(111) with the evolution of masses 2 and 72 amu between 300 and 400 K (figure 12). Using similar arguments to those just described for crotyl alcohol desorption we assign this to desorption of hydrogen and butaldehyde. 1-butanol (figure 4) desorbs from the surface at 176 K and 219 K. The feature at 176 K is attributed to multilayer desorption while the feature at 219 K is attributed to desorption of the chemisorbed layer.

Our observations from the TPD experiments allow us to make a number of conclusions at this point. Firstly, we observe that the temperatures of desorption of crotonaldehyde and butaldehyde are extremely similar. Additionally, the temperatures of desorption of both crotyl alcohol and 1-butanol are also of similar magnitude. From this observation we conclude that the C=C bond in either crotonaldehyde or crotyl alcohol does not significantly interact with the Cu(111) surface as we do not observe an increased temperature of desorption for either of these molecules relative to butaldehyde or 1-butanol respectively. Hence, we conclude the main interaction of the molecules to be through the oxygen lone pair in a similar manner to that of either acetone or methanol although for both alcohols we observe an increased desorption temperature compared to either of the aldehydes. We attribute this to the effects of hydrogen bonding in the alcohol layers, which we would expect to be more significant for the two alcohol molecules in comparison to the aldehydes. Finally, the small level of dissociation of both alcohols we observe is

consistent with only a limited amount of reaction and we suggest is likely to be due to reaction at only the more reactive defect sites.

6.1.2.2 UPS and XPS

The adsorption of the four molecules, crotonaldehyde, butaldehyde, crotyl alcohol and 1-butanol, on the clean Cu(111) surface was characterised further using XPS and UPS. UP spectra of each molecule were recorded after adsorption of condensed multilayers and then after subsequent annealing of the layer to temperatures appropriate to produce a monolayer coverage. These are shown in figure 5. Upon adsorption of each molecule we observe the same effects with regard to the clean surface (The UP spectrum from clean Cu(111) has been discussed previously). Adsorption of each molecule at ca. 110 K results in attenuation of the d-band and the appearance of adsorbate induced bands in the spectrum (multilayers in figure 5). Upon annealing to temperatures appropriate to produce a monolayer coverage we observe re-appearance of emission from the d-band but the sharp structure and surface state consistent with the clean Cu(111) surface remain absent. These observations are consistent with those of previous studies [27].

In figure 5, the spectra labelled (a) correspond to spectra recorded from both multilayer and monolayer coverages of crotonaldehyde. Both of these spectra consist of a very broad band from 7-12 eV with a peak maximum at around 8.9 eV. In the multilayer spectrum this broad feature also shows the presence of a shoulder at 7.7 eV although this component is not clearly resolved in the monolayer spectrum. In addition to this broad feature we also observe another broad band at 5.0 eV in the multilayer spectrum from crotonaldehyde. Upon annealing, this feature splits and can clearly be seen to contain two components. To identify the origin of these components and indeed the rest of the components of the spectra we would ideally like to compare our results with those of gas phase UP spectra. However, we have found no previous work in the available literature of this type. Hence, we must look further afield in an attempt to interpret our results. The feature at 5.0 eV consists of 2 components which, we believe are consistent with emission from both the O lone pair orbitals and the C=C π -orbital component. These assignments are based on a number of pieces of previous work. Firstly, our own work carried out on acetone and methanol produced a single feature in UPS data with similar binding energy to the feature we observe here. This feature was also present in the work of

Sexton et al. [17] and was assigned to emission from O lone pair orbitals. Additionally, however, Kleyna et al. [16] also made observations of a single feature in their work on propene on Ni(100) that would also be consistent with the current work. In these experiments this was assigned as being a feature of emission from the π -orbital associated with the C=C bond of this molecule. Hence, we believe the similar features we observe in our own data to be due to emission from both the lone pair oxygen orbitals and the π -orbital associated with the C=C bond. Significantly, we observe no relative shift in the positions of the adsorbate-induced bands of the monolayer with respect to the multilayer features, including those of the oxygen lone pair and the C=C bond, suggesting only a weak interaction with the Cu(111) surface.

The spectra labelled (b) in figure 5 correspond to multilayer and monolayer butaldehyde coverages. Emission is observed from molecular orbitals at 10.1, 8.9 and 7.2 eV, as well as emission from the oxygen lone pair orbitals at 4.5 eV on the multilayer and monolayer spectra. Note that the band at 4.5 eV contains only one component and is significantly narrower than that associated with crotonaldehyde, consistent with no C=C group. As for crotonaldehyde we observe no shift in the relative positions of emission bands between the monolayer and multilayer, again suggesting only a weak adsorbate-surface interaction.

Figure 5 (c) shows the multilayer and monolayer UP spectrum recorded from crotyl alcohol. After adsorption we observe emission from 4 adsorbate bands, at 10.0, 8.8, 7.0 and the centre of a broad band at 5.0 eV. This final band appears to be made up of two components, which would be consistent with emission from both the O lone pair orbitals and the C=C π -orbital component. No significant shifts are observed in the monolayer spectrum compared to that of the multilayer.

Figure 5(d) shows the multilayer and monolayer UPS data recorded from 1-butanol overlayers. Adsorbate induced emission is observed from a peak at 9.5 eV followed by a broad band with a maximum around 6.1 eV and finally O lone pair orbital emission around 4.9 eV in the multilayer spectrum. This band is narrower than the corresponding bands in the crotonaldehyde and crotyl alcohol spectra, in a similar manner to that obtained for butaldehyde, consistent with no C=C group in the molecule. No significant shifts of the bands already identified are observed upon annealing although a new band appears at 10.5 eV, not previously visible in the multilayer spectrum.

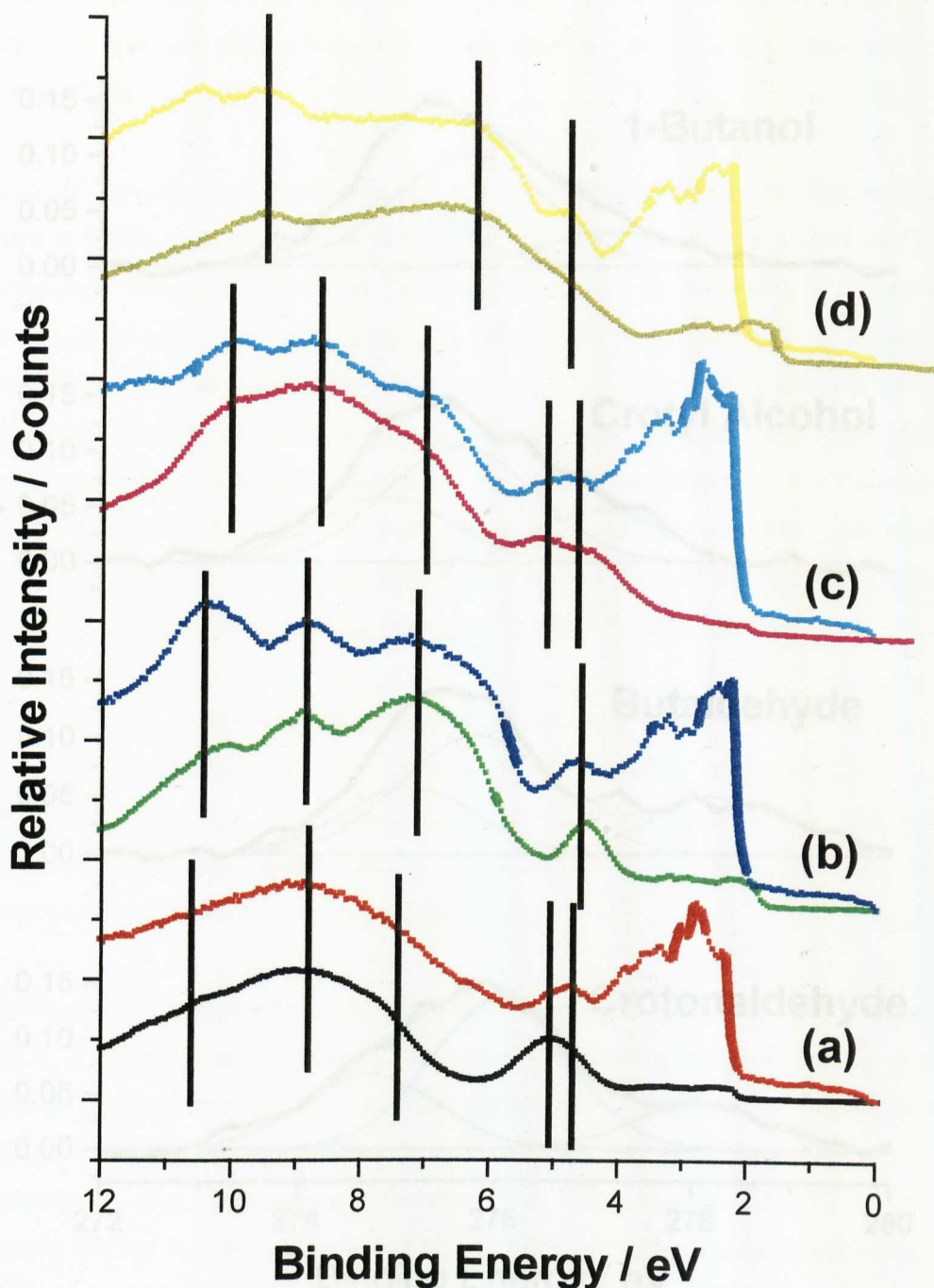


Figure 5. Normal emission UP spectra of (a) crotonaldehyde multilayers ($\times 0.55$, black) and monolayer (red), (b) butaldehyde multilayers ($\times 0.33$, green) and monolayer (blue), (c) crotyl alcohol multilayers ($\times 0.50$, magenta) and monolayer (cyan) and (d) 1-butanol multilayers ($\times 0.50$, dark yellow) and monolayer (yellow) adsorbed on Cu(111). Binding energies are relative to E_F . Lines have been added to facilitate comparison of peak positions.

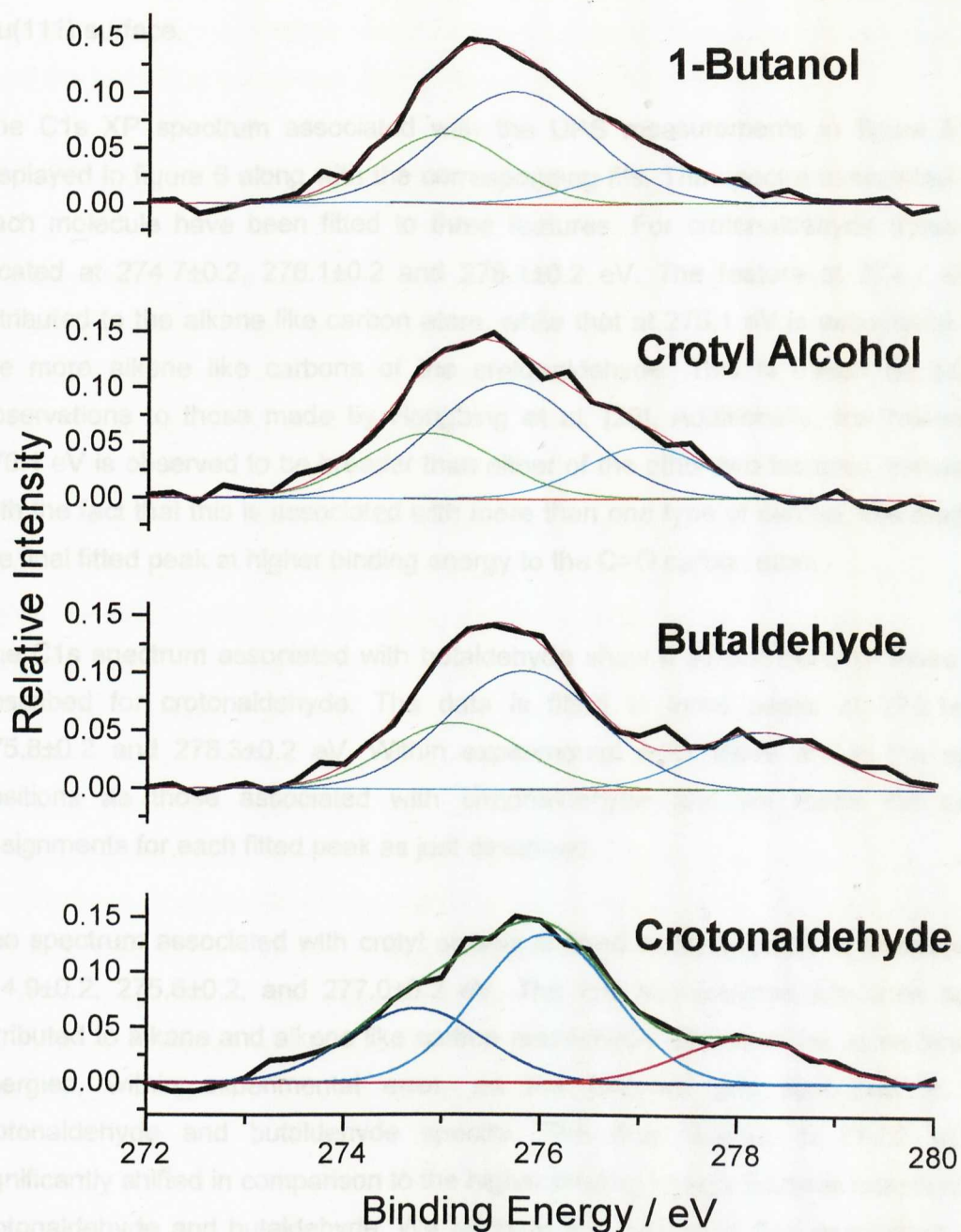


Figure 6. C1s spectra of crotonaldehyde, butaldehyde, crotyl alcohol and 1-butanol monolayers adsorbed on clean Cu(111). The corresponding fits are also shown.

The UPS observations we have made at this stage are consistent with those of the TPD data in that we observe a weak interaction of all four molecules with the Cu(111) surface.

The C1s XP spectrum associated with the UPS measurements in figure 5 are displayed in figure 6 along with the corresponding fits. The spectra associated with each molecule have been fitted to three features. For crotonaldehyde these are located at 274.7 ± 0.2 , 276.1 ± 0.2 and 278.1 ± 0.2 eV. The feature at 274.7 eV is attributed to the alkane like carbon atom, while that at 276.1 eV is associated with the more alkene like carbons of the crotonaldehyde. This is based on similar observations to those made by Hongbing et al. [28]. Additionally, the feature at 276.1 eV is observed to be broader than either of the other two features, consistent with the fact that this is associated with more than one type of carbon. We attribute the final fitted peak at higher binding energy to the C=O carbon atom.

The C1s spectrum associated with butaldehyde show a similar trend to those just described for crotonaldehyde. The data is fitted to three peaks at 275.1 ± 0.2 , 275.8 ± 0.2 and 278.3 ± 0.2 eV. Within experimental error these are in the same positions as those associated with crotonaldehyde and we make the same assignments for each fitted peak as just described.

The spectrum associated with crotyl alcohol is fitted to three peaks at positions of 274.9 ± 0.2 , 275.6 ± 0.2 , and 277.0 ± 0.2 eV. The first two features are once again attributed to alkane and alkene like carbon respectively and have the same binding energies, within experimental error, as the features just described in the crotonaldehyde and butaldehyde spectra. The final feature at 277.0 eV is significantly shifted in comparison to the higher binding energy features observed for crotonaldehyde and butaldehyde. We attribute this feature to that associated with the C-OH group.

Finally, we turn our attention to the C1s spectrum associated with 1-butanol. The data is fitted to peaks at 275.0 ± 0.2 , 275.7 ± 0.2 , and 277.2 ± 0.2 eV. In a similar manner to crotyl alcohol we attribute these features to being associated with alkane like carbon, alkene like carbon and the C-OH group respectively.

Due to the methods of sample preparation (i.e. heating condensed multilayers to produce monolayer or sub-monolayer coverages), we believe use of XPS to compare surface coverages would be inappropriate. Hence, we will not attempt to use the technique in this way during the course of this chapter.

6.1.2.3 Adsorption on S/Cu(111) Surfaces – TPD

Having characterised the adsorption on the clean surface, we then repeated TPD experiments with increasing amounts of pre-adsorbed atomic sulphur present on the crystal. Sulphur coverages were measured using AES and were calculated with reference to the $(\sqrt{7}\times\sqrt{7})R19.1^\circ$ structure.

TPD spectra of crotonaldehyde adsorption from surfaces pre-dosed with increasing amounts of sulphur are shown in figure 7. Crotonaldehyde continues to adsorb reversibly in the presence of atomic sulphur with no signs of dissociation. For all sulphur coverages, the crotonaldehyde desorption spectra becomes significantly more complicated than that observed from the clean Cu(111) surface. At all coverages of sulphur we observe both increases in desorption temperature and in material in the adsorbed layer. The increase in desorption temperature is observed both by an increase in temperature of the maximum rate of desorption (T_{max}) and in an increase in desorption temperature of the trailing edge of the main desorption peak. In addition to this, the increased area under the monolayer peak in the TPD spectra also reflects an increase in the amount of adsorbed material in the monolayer, as discussed in chapter 2. The changes to T_{max} , monolayer packing density and maximum temperature of the trailing edge are summarised in table 1.

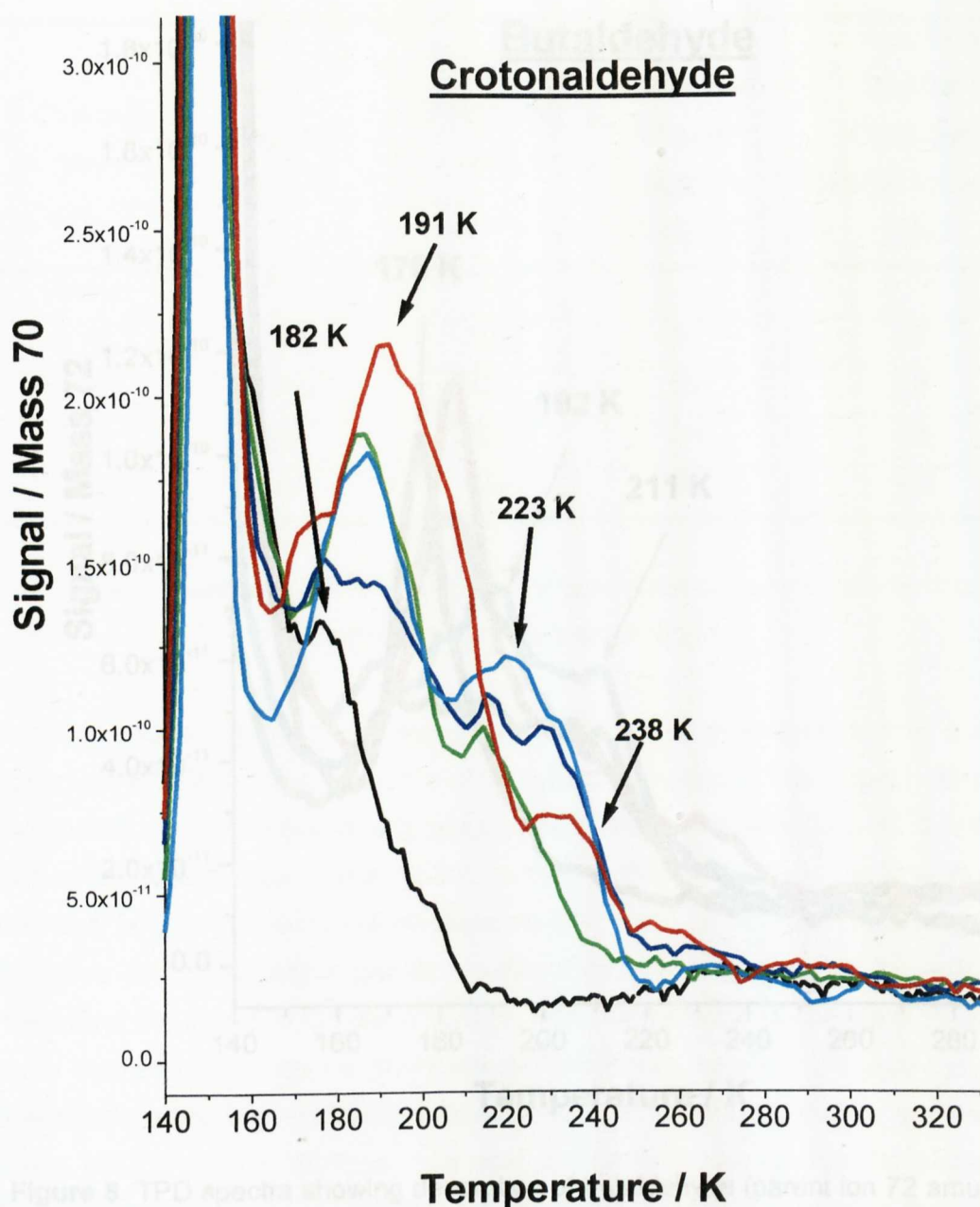


Figure 7. TPD spectra showing desorption of crotonaldehyde (parent ion 70 amu) from surfaces which had been pre-dosed with 0.10 ± 0.04 (blue), 0.15 ± 0.04 (green), 0.27 ± 0.01 (cyan) and 0.43 ML (red) sulphur. A spectrum obtained from a clean surface (black) is also shown for comparison. Experimental conditions were identical to those in figure 1.

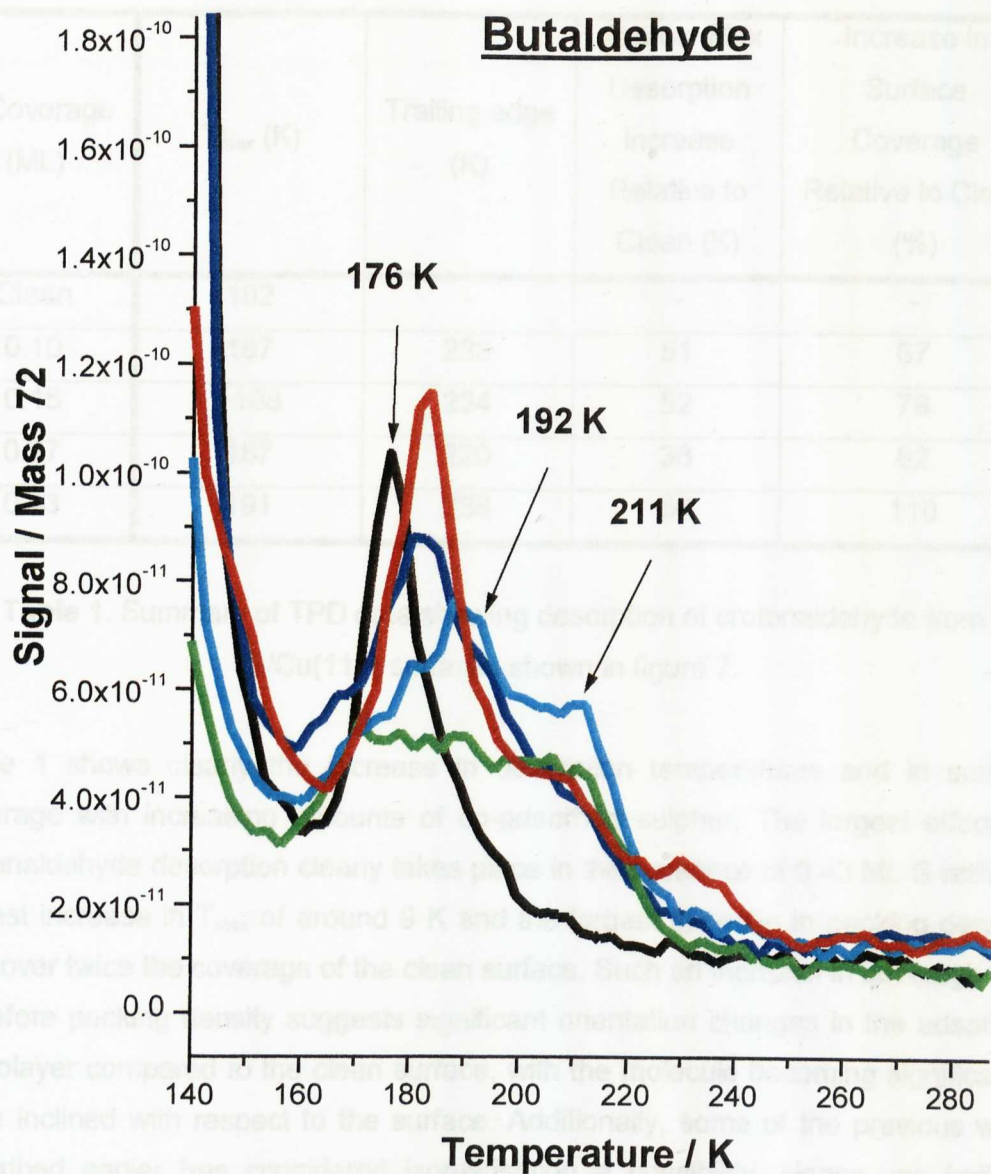


Figure 8. TPD spectra showing desorption of butaldehyde (parent ion 72 amu) from surfaces which had been pre-dosed with 0.10 ± 0.04 (blue), 0.15 ± 0.04 (green), 0.27 ± 0.01 (cyan) and 0.43 ML (red) sulphur. A spectrum obtained from a clean surface (black) is also shown for comparison. Experimental conditions were identical to those in figure 1.

S Coverage (ML)	T_{\max} (K)	Trailing edge (K)	Approx. Max Desorption Increase Relative to Clean (K)	Increase in Surface Coverage Relative to Clean (%)
Clean	182	-	-	-
0.10	187	233	51	67
0.15	~188	234	52	78
0.27	187	220	38	82
0.43	191	238	56	118

Table 1. Summary of TPD data showing desorption of crotonaldehyde from S/Cu(111) surfaces shown in figure 7.

Table 1 shows clearly the increase in desorption temperatures and in surface coverage with increasing amounts of co-adsorbed sulphur. The largest effect on crotonaldehyde desorption clearly takes place in the presence of 0.43 ML S with the largest increase in T_{\max} of around 9 K and the largest increase in packing density, with over twice the coverage of the clean surface. Such an increase in coverage and therefore packing density suggests significant orientation changes in the adsorbed monolayer compared to the clean surface, with the molecule becoming significantly more inclined with respect to the surface. Additionally, some of the previous work described earlier has considered isomerisation a possibility. Hence, we believe some conformational changes may also be partially responsible for increased packing density. Finally, we observe the temperature of the trailing edge to increase by ca. 56 K.

The corresponding butaldehyde TPD spectra are shown in figure 8. Similarly to crotonaldehyde, butaldehyde continues to adsorb reversibly in the presence of atomic sulphur. Also, for all sulphur coverages, T_{\max} , trailing edge and surface coverage all increase in a similar manner to crotonaldehyde, although the observed effects for crotonaldehyde are somewhat larger than for butaldehyde. These effects are summarised in table 2.

S Coverage (ML)	T_{max} (K)	Trailing edge (K)	Approx. Max Desorption Increase Relative to Clean (K)	Increase in Surface Coverage Relative to Clean (%)
Clean	176	-	-	-
0.10	182	194	18	46
0.15	Broad	211	35	22
0.27	191	211	35	53
0.43	184	226	50	56

Table 2. Summary of TPD data showing desorption of butaldehyde from S/Cu(111) surfaces shown in figure 8.

In this instance, the largest increase in T_{max} occurs on the 0.27 ML surface with a temperature increase of 15 K. However, the largest increase in trailing edge temperature is observed on the saturated surface once again, with an increase in temperature of desorption of *ca.* 50 K. The increase in surface coverage is of a similar magnitude for both of these surfaces and represents an increase of *ca.* 54 % that of the clean surface.

Figure 9 shows TPD spectra of the desorption of crotyl alcohol in the presence of pre-adsorbed atomic sulphur. Significantly, the dissociation of crotyl alcohol at higher temperatures is inhibited by the presence of sulphur, indicated by the lack of dissociation products, previously observed on the clean Cu(111) surface (figure 10). As is the case for the previous two molecules, crotonaldehyde and butaldehyde, we observe significant increases in T_{max} , trailing edge and packing density of the crotyl alcohol molecules. These effects are summarised in table 3.

S Coverage (ML)	T_{max} (K)	Trailing edge (K)	Approx. Max Desorption Increase Relative to Clean (K)	Increase in Surface Coverage Relative to Clean (%)
Clean	214	-	-	-
0.10	230	231	17	86
0.15	230	234	20	88
0.27	233	234	20	124
0.43	221	240	26	82

Table 3. Summary of TPD data showing desorption of crotyl alcohol from S/Cu(111) surfaces shown in figure 9.

The most pronounced effect on T_{max} and surface coverage is observed on the 0.27 ML covered surface with a T_{max} increase of 19 K and an increase in surface coverage of 124%. Again this suggests significant orientation and possibly conformational changes to accommodate the large increase in packing density. Like crotonaldehyde, crotyl alcohol also has cis and trans conformations. However, the largest increase in trailing edge is observed to take place on the 0.43 ML surface, and represents an increase of ca. 26 K.

Finally, the desorption of 1-butanol is shown in figure 11. As is the case for the other alcohol, the dissociation of 1-butanol is inhibited by the presence of sulphur on the copper surface (figure 12) and like the previous three molecules we observe increases in T_{max} , trailing edge and surface coverage. These results are summarised in table 4.

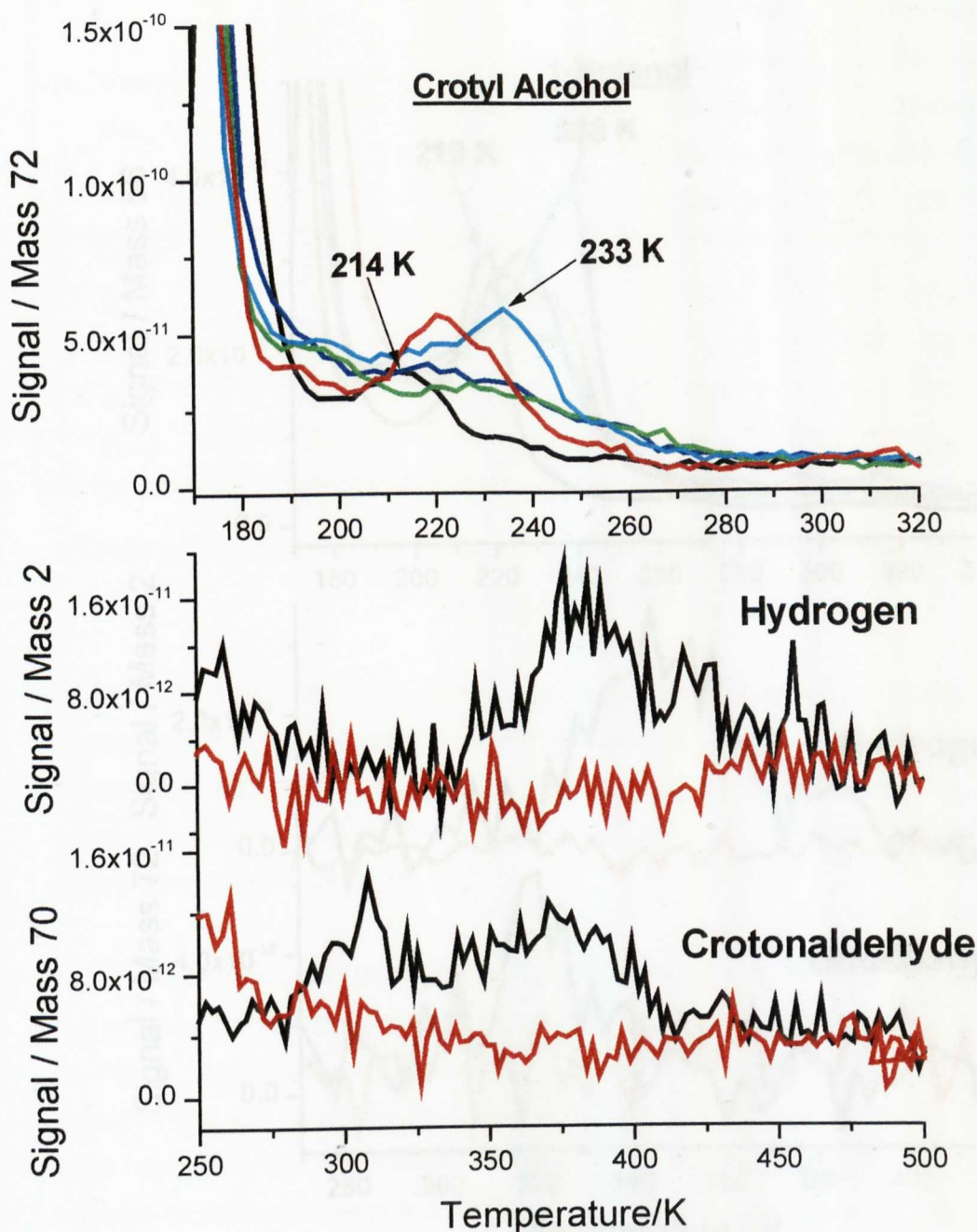


Figure 9. TPD spectra showing desorption of crotyl alcohol (parent ion 72 amu) from surfaces which had been pre-dosed with 0.10 ± 0.04 (blue), 0.15 ± 0.04 (green), 0.27 ± 0.01 (cyan) and 0.43 ML (red) sulphur. A spectrum obtained from a clean surface (black) is also shown for comparison. Experimental conditions were identical to those in figure 1.

Figure 10. Comparison spectra of the dissociation of crotyl alcohol (parent ion 72 amu) to give crotonaldehyde (parent ion 70 amu) and hydrogen (2 amu) on clean surface (black) with spectra indicating the reaction is inhibited in the presence of sulphur (red).

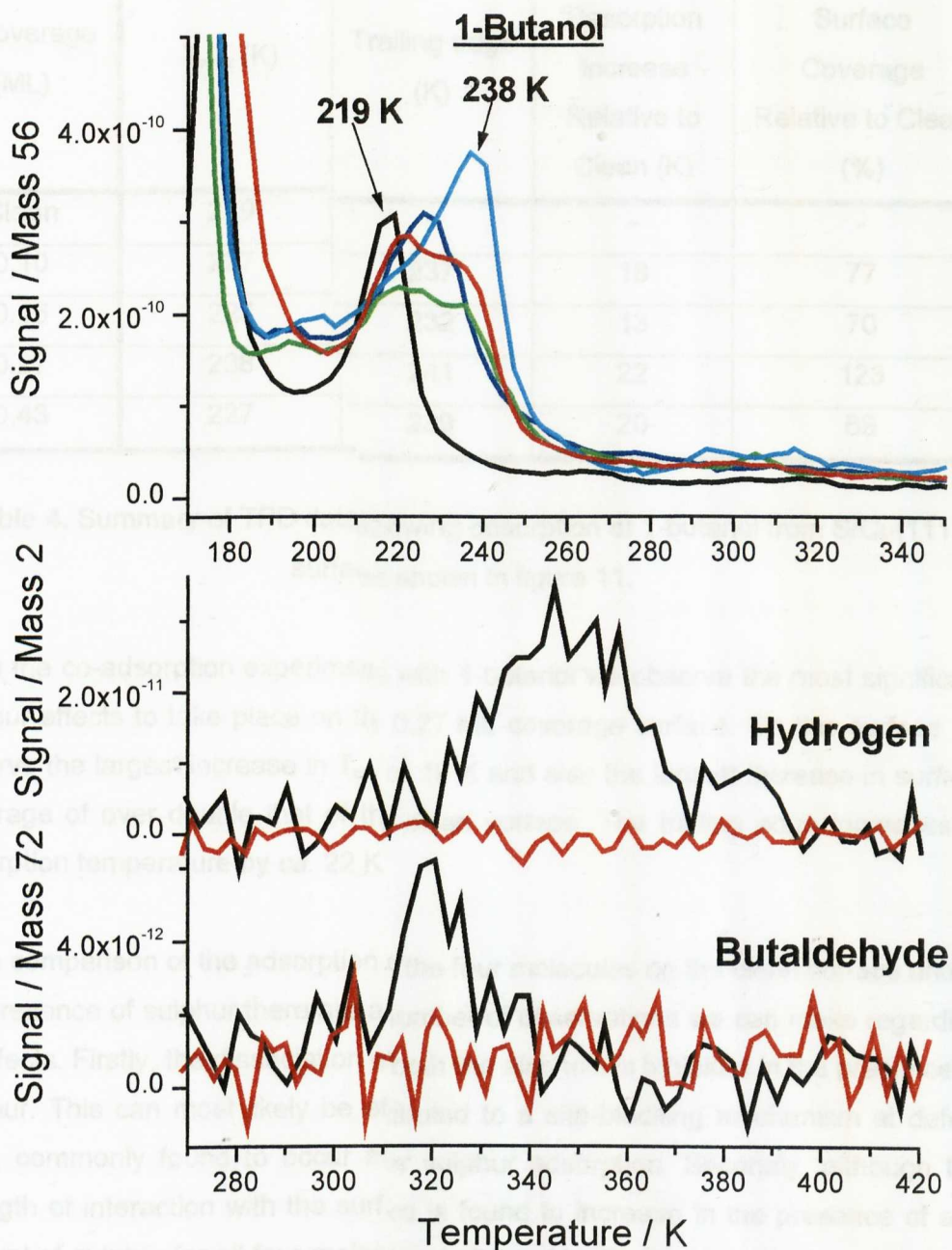


Figure 11. TPD spectra showing desorption of 1-butanol (parent ion 72 amu) from surfaces which had been pre-dosed with 0.10 ± 0.04 (blue), 0.15 ± 0.04 (green), 0.27 ± 0.01 (cyan) and 0.43 ML (red) sulphur. A spectrum obtained from a clean surface (black) is also shown for comparison. Experimental conditions were identical to those in figure 1.

Figure 12. Comparison spectra of the dissociation of 1-butanol (parent ion 72 amu) to give butaldehyde (parent ion 70 amu) and hydrogen (2 amu) on clean surface (black) with spectra indicating the reaction is inhibited in the presence of sulphur (red).

S Coverage (ML)	T_{\max} (K)	Trailing edge (K)	Approx. Max Desorption Increase Relative to Clean (K)	Increase in Surface Coverage Relative to Clean (%)
Clean	219	-	-	-
0.10	227	237	18	77
0.15	227	232	13	70
0.27	238	241	22	123
0.43	227	239	20	69

Table 4. Summary of TPD data showing desorption of 1-butanol from S/Cu(111) surfaces shown in figure 11.

From the co-adsorption experiments with 1-butanol we observe the most significant sulphur effects to take place on the 0.27 ML coverage surface. On this surface we observe the largest increase in T_{\max} of 19 K and also the largest increase in surface coverage of over double that of the clean surface. The trailing edge increases in desorption temperature by *ca.* 22 K.

From comparison of the adsorption of the four molecules on the clean surface and in the presence of sulphur there are a number of observations we can make regarding its effects. Firstly, the dissociation of both the alcohols is inhibited in the presence of sulphur. This can most likely be attributed to a site-blocking mechanism at defect sites, commonly found to occur after sulphur adsorption. Secondly, although the strength of interaction with the surface is found to increase in the presence of any amount of sulphur for all four molecules, indicated by the increase in T_{\max} and of the temperature of the trailing edge, the effects are most pronounced for the crotonaldehyde molecule. After this, butaldehyde generally shows the next most pronounced, followed by the two alcohols which are generally less stabilised than the two aldehydes overall. For all four molecules and all coverages of sulphur we observe a significant increase in packing density of the molecules on the Cu(111) surface suggesting sulphur induces orientation changes in the adsorbed layers of all four molecules.

6.1.2.4 UPS and XPS

Following TPD experiments, the adsorption of each of the four molecules co-adsorbed with sulphur was studied using the techniques of XPS and UPS. Figure 13 shows UP spectra recorded from a monolayer of crotonaldehyde adsorbed on each of four sulphur covered surfaces. Additionally, spectra recorded from crotonaldehyde adsorbed on a clean Cu(111) surface is also shown along with a UP spectrum from condensed crotonaldehyde multilayers. Each of the sulphur covered surfaces is similar to that of the clean surface and multilayer spectra in that they consist of two broad prominent features. The first of these is from 7-12 eV with the second having a maximum at 5.0 eV. The second feature is in fact a combination of emission due to the O lone pair orbitals and π -orbital as discussed earlier and significantly, is not shifted on the S covered surfaces. This fact would suggest that S does not have any significant electronic effect on the interaction of either the O lone pair orbitals or the π -orbitals with the surface. The broad feature from 7-12 eV is more interesting. On the clean Cu(111) surface this feature shows a peak at 8.9 eV but no other components can be clearly resolved. In the presence of S however, this feature changes considerably. The position of the main peak remains at 8.9 eV for all of the S coverages. However, two new features either side of the main feature become more resolved at 7.4 and 10.7 eV in the presence of S. Additionally, the relative intensities of the three features making up the broad band from 7-12 eV can be seen to change depending upon the amount of S present on the surface. This observation would be consistent with the results of TPD experiments as the change in surface coverage observed in TPD data would suggest orientation changes in the adsorbed layer dependent upon sulphur coverage. Changes such as this would manifest themselves in UPS experiments as small changes in the UPS spectrum such as changes to the relative intensity of adsorbate bands. Hence, in agreement with TPD experiments, we attribute the changes in relative intensity of adsorbate bands in UP spectra to be due to orientation changes in the adsorbed layer.

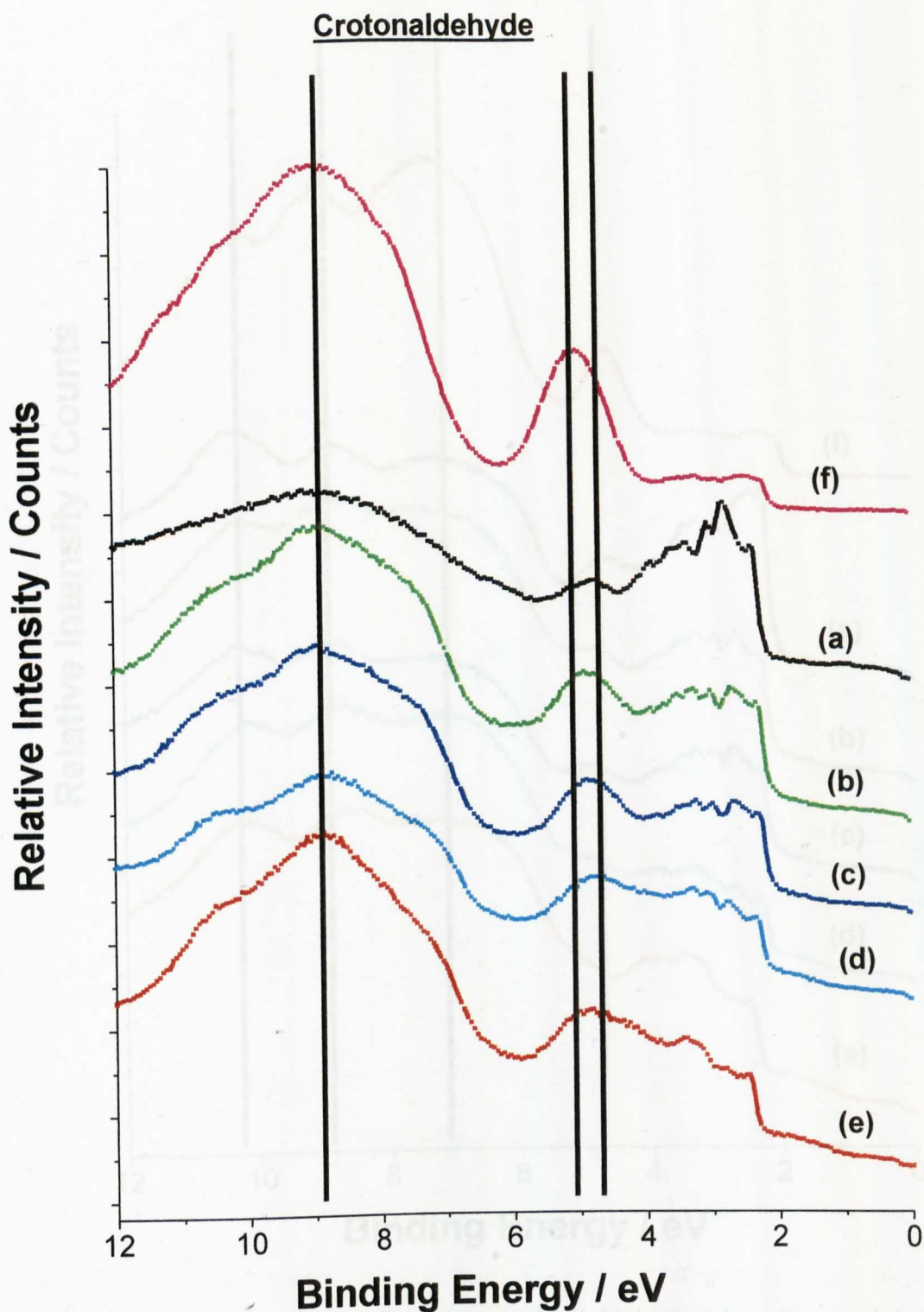


Figure 13. Normal emission UP spectrum of crotonaldehyde adsorption on (a) clean Cu(111) (black) and (b) 0.11 ± 0.03 (green), (c) 0.16 ± 0.01 (blue), (d) 0.29 ± 0.01 (cyan), and (e) 0.43 ML (red) pre-adsorbed sulphur. A multilayer spectrum (f) (magenta) is also shown for comparison. Binding energies are relative to E_F . Lines have been added to facilitate comparison of peak positions.

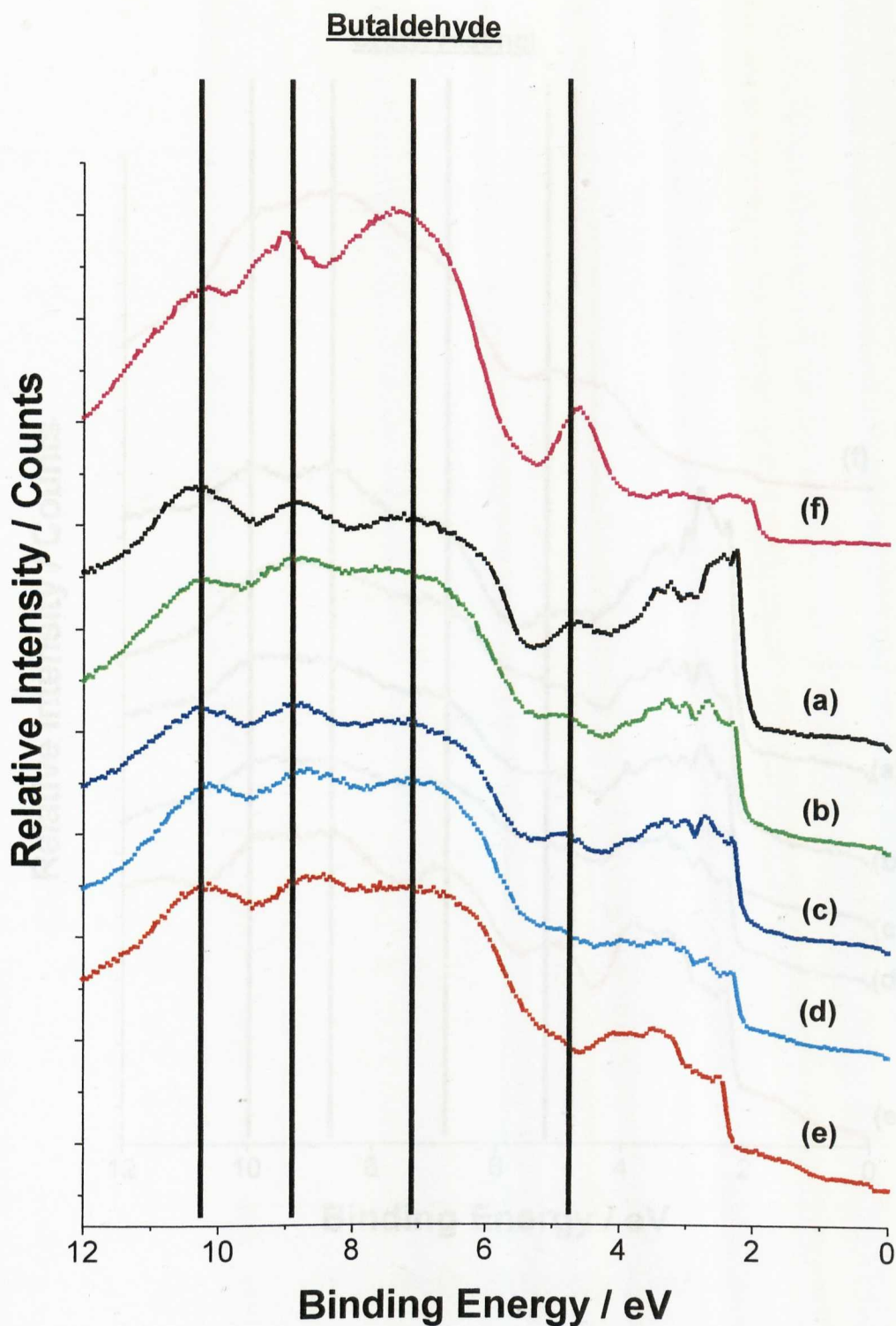


Figure 14. Normal emission UP spectrum of butaldehyde adsorption on (a) clean

Figure 14. Normal emission UP spectrum of butaldehyde adsorption on (a) clean Cu(111) (black) and (b) 0.11 ± 0.03 (green), (c) 0.16 ± 0.01 (blue), (d) 0.29 ± 0.01 (cyan), and (e) 0.43 ML (red) pre-adsorbed sulphur. A multilayer spectrum (f) (magenta) is also shown for comparison. Binding energies are relative to E_F . Lines have been added to facilitate comparison of peak positions.

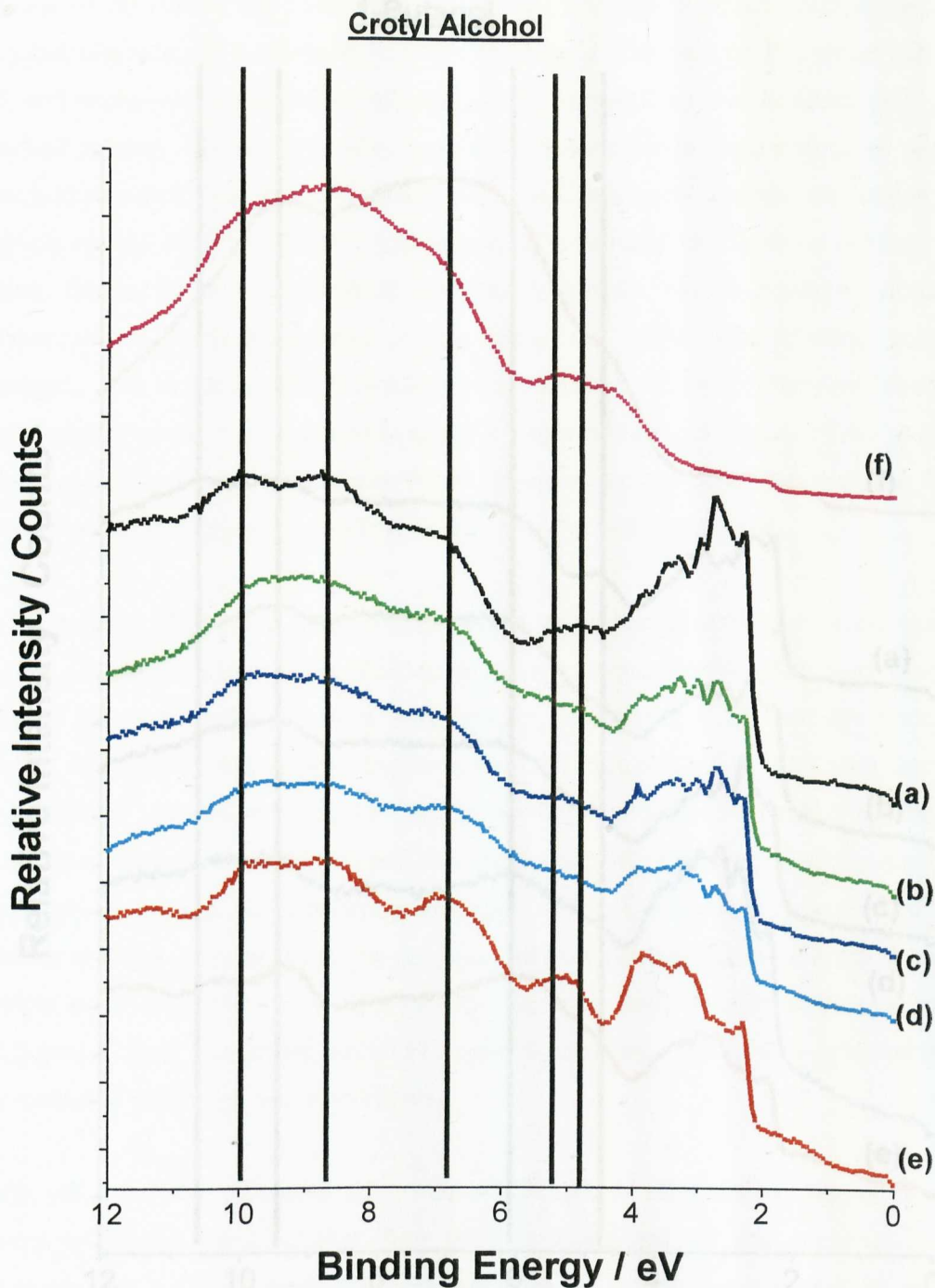


Figure 15. Normal emission UP spectrum of crotyl alcohol adsorption on (a) clean Cu(111) (black) and (b) 0.11 ± 0.03 (green), (c) 0.16 ± 0.01 (blue), (d) 0.29 ± 0.01 (cyan), and (e) 0.43 ML (red) pre-adsorbed sulphur. A multilayer spectrum (f) (magenta) is also shown for comparison. Binding energies are relative to E_F . Lines have been added to facilitate comparison of peak positions.

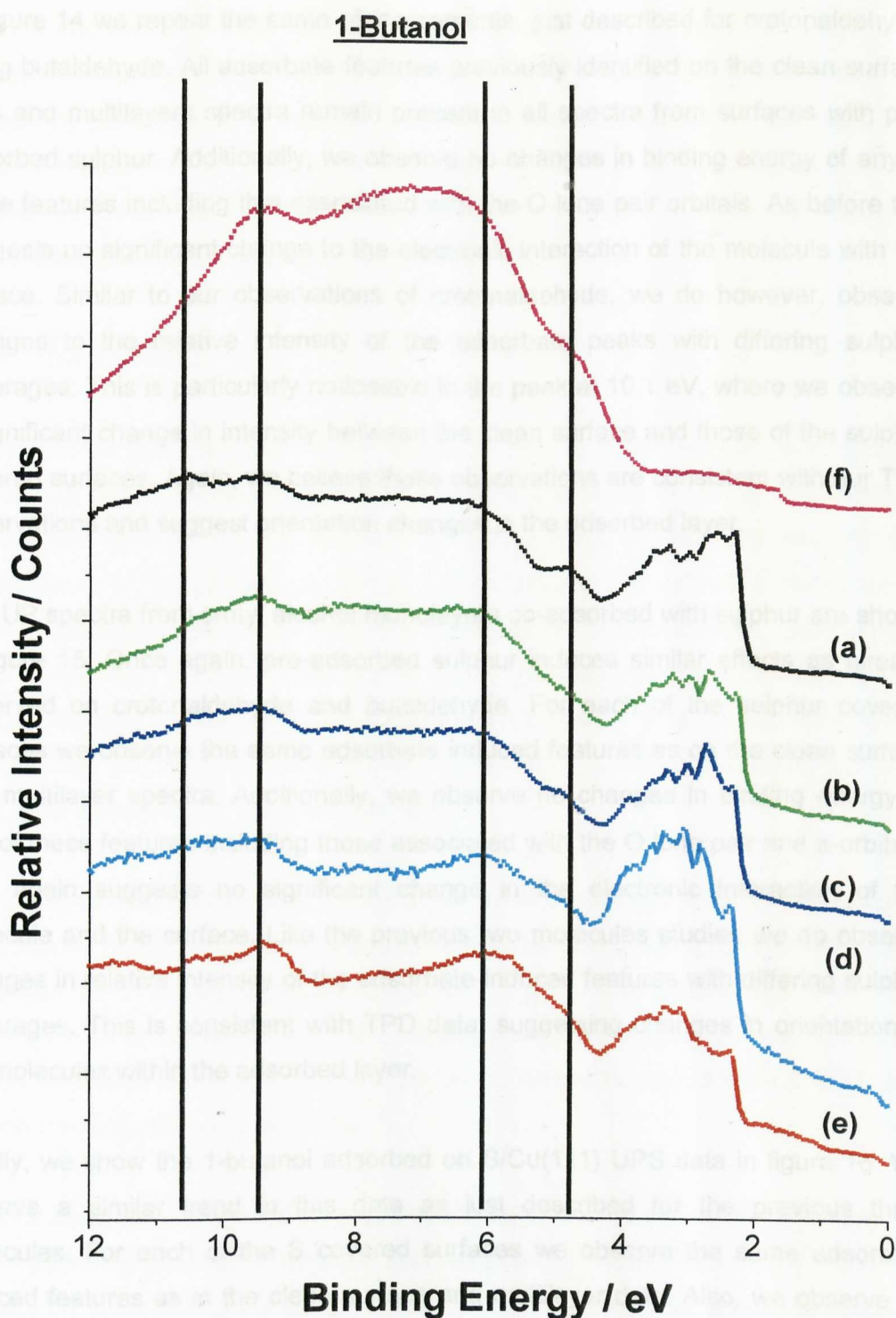


Figure 16. Normal-emission UPS spectrum of 1-butanol adsorption on (a) clean Cu(111) (black) and (b) 0.11 ± 0.03 (green), (c) 0.16 ± 0.01 (blue), (d) 0.29 ± 0.01 (cyan), and (e) 0.43 ML (red) pre-adsorbed sulphur. A multilayer spectrum (f) (magenta) is also shown for comparison. Binding energies are relative to E_F . Lines have been added to facilitate comparison of peak positions.

In figure 14 we repeat the same measurements, just described for crotonaldehyde, using butaldehyde. All adsorbate features previously identified on the clean surface UPS and multilayers spectra remain present in all spectra from surfaces with pre-adsorbed sulphur. Additionally, we observe no changes in binding energy of any of these features including that associated with the O lone pair orbitals. As before this suggests no significant change to the electronic interaction of the molecule with the surface. Similar to our observations of crotonaldehyde, we do however, observe changes to the relative intensity of the adsorbate peaks with differing sulphur coverages. This is particularly noticeable in the peak at 10.1 eV, where we observe a significant change in intensity between the clean surface and those of the sulphur covered surfaces. Again, we believe these observations are consistent with our TPD observations and suggest orientation changes in the adsorbed layer.

The UP spectra from crotyl alcohol monolayers co-adsorbed with sulphur are shown in figure 15. Once again, pre-adsorbed sulphur induces similar effects as already observed on crotonaldehyde and butaldehyde. For each of the sulphur covered surfaces we observe the same adsorbate induced features as on the clean surface and multilayer spectra. Additionally, we observe no changes in binding energy of any of these features including those associated with the O lone pair and π -orbitals. This again suggests no significant change in the electronic interaction of the molecule and the surface. Like the previous two molecules studied we do observe changes in relative intensity of the adsorbate-induced features with differing sulphur coverages. This is consistent with TPD data, suggesting changes in orientation of the molecules within the adsorbed layer.

Finally, we show the 1-butanol adsorbed on S/Cu(111) UPS data in figure 16. We observe a similar trend in this data as just described for the previous three molecules. For each of the S covered surfaces we observe the same adsorbate induced features as in the clean surface and multilayer data. Also, we observe no significant shifts in binding energy, including of the feature associated with the O lone pair orbital. Once again, this suggests no significant electronic interaction induced by S pre-adsorption. However, we do observe changes in the relative intensity of the adsorbate features and we attribute this to changes in orientation of the molecules in the layer induced by S.

In summary, the UPS data allows us to make two main conclusions. Firstly, UP spectra confirm that the molecules' orientation on the Cu(111) surface is strongly affected by the presence of sulphur. However, the measurements do not suggest a significant effect on the interaction between any of the four molecules and the surface, evidenced by the lack of any relative shifts in the spectra, particularly of peaks associated with the O lone pair or π -orbitals.

6.1.3 Discussion

At the start of this study we set ourselves the task of developing a mechanism to account for both our observations in this section and those in part 2. In addition to this we also wish to use this mechanism to rationalise our observations with the catalytic work of Hutchings et al. Hence, although at this point we will concentrate on the work presented here examining the adsorption of crotonaldehyde, butaldehyde, crotyl alcohol and 1-butanol with atomic sulphur, we will also show this mechanism can be extended to account for our observations in part 2. The question of whether this can then be used to address the work of Hutchings will be discussed at a later point, after discussion of the results in part 2.

In any model we propose here we have two main observations that must be taken into account. Firstly, why does the presence of sulphur stabilise adsorption of all four molecules in TPD experiments? Secondly, why is this stabilisation effect not observed in UPS measurements? We believe the answer to both of these questions can be answered using a mechanism based on an electrostatic model, based on a variation of models used previously.

The first study to examine electrostatic interactions studied the effects of Cl and Cs on the selective oxidation of ethylene and subsequent combustion of ethylene oxide on Ag(111) [31]. This study demonstrated that the presence of an electronegative element such as Cl could result in stabilisation of co-adsorbed molecules. Additionally, the opposite effects are observed in the presence of the electropositive Cs molecule. These effects were attributed to an electronic perturbation of the system and charge transfer from the adsorbate to the metal. In subsequent studies the role of Cl in the promotional effects of benzene on copper were examined [32,33]. The effect was first observed in TPD experiments [32] and was subsequently examined theoretically in a latter study [33]. The results of the

theoretical study concluded that the presence of Cl on the surface induces an electrostatic effect, where the adsorbed Cl⁻ anions on the surface lower the Fermi level and create increased charge donation from the benzene to the copper. This overcompensates for the expected reduction in copper to benzene charge donation and results in an increased stability in bonding. In addition to this, investigation of the effects of sulphur on transition metals was examined by Rodriguez and Hrbek [34]. Using UPS measurements Rodriguez and co-worker showed that the presence of sulphur reduces the density of states of Pt, Pd and Rh at the Fermi level by withdrawing charge from the metal d-band. In the case of these transition metal surfaces, adsorbates bonding to the surface do so primarily through an interaction involving charge transfer from the metal d-band into the molecular anti-bonding levels of the adsorbate. Hence, sulphur poisons the interaction between the surface and any adsorbed molecules. On the coinage metal surfaces however, the primary charge transfer is usually from the molecules to the metal surface and as such is not adversely affected by the reduction in density of states at the Fermi level as back donation from the metal is less important on these surfaces. The results of these studies show that the presence of electronegative elements can have a significant effect on the bonding of co-adsorbed elements. Additionally, they have highlighted that the observations can be rationalised using electronic arguments. However, in this work, charge transfer plays an important role in the process. In our own work we believe that charge transfer does not play a role in the process. We will discuss this further shortly.

A variation on the electrostatic models described above has been used to interpret the ordering effects of CO co-adsorbed with sodium, benzene, fluorobenzene and ethylidyne on the Rh(111) surface [35]. The authors examined the effects of dipoles by measuring changes in the work function of the surface. They propose that for the examined systems, CO induced ordering is observed for all systems where the adsorbate has a positive dipole moment in comparison to the negative dipole induced by the adsorbed CO. They conclude that anti-parallel dipole moments interact attractively and induce ordering of the system, while the opposite effect is observed for parallel dipoles.

An electrostatic model has been used in previous work carried out in our lab to interpret the interaction of S with co-adsorbates [36]. In this study, the effects of sulphur co-adsorption with benzene, thiophene and cyclohexene was examined on the Cu(111) surface. The observations made in this particular study show a number

of differences in comparison with the current work. The presence of S was shown to stabilise the adsorption of thiophene and benzene on the Cu(111) surface but only at sulphur coverages up to 0.33 ML. At coverages above this amount the adsorption of the molecules is destabilised. Cyclohexene however, is stabilised at all sulphur coverages. These observations were made in both TPD and UPS experiments. In TPD experiments stabilisation/destabilisation could obviously be identified by changes in desorption temperature in a similar manner to the observations made in the present study. However, unlike in the current study, UPS experiments also signalled the stabilisation of the molecules by significant shifts to higher binding energies of the π -level in UP spectra. The author concluded that the mechanism of the stabilisation effects observed is as follows: Adsorption of the electronegative sulphur species on the surface increases the magnitude of the surface dipole. The direction of the molecular dipole is anti-parallel to that of the surface and hence acts attractively. As a result of this increased interaction, charge donation from the π species to the Cu(111) substrate also increases, increasing the size of the molecules associated dipole and further contributing to the stabilisation of the molecule. The destabilisation of thiophene and benzene at higher S coverages was suggested to be a steric effect. The adsorption of thiophene and benzene is through the delocalised π system of the ring. This requires a large area of exposed copper compared to cyclohexene, whose π electrons are localised on the olefinic portion of the molecule, and hence at higher sulphur coverages the lack of S free Cu adsorption sites results in destabilisation of the molecules adsorption on the surface.

If we now turn our attention to the results of our own work we believe an electrostatic model can also be used to describe the results. As discussed in the previous chapter, a surface dipole layer exists even on the clean Cu(111) surface. A measurement related to the layer is made in work function measurements and it can be affected by the adsorption of sulphur. Likewise, a molecular dipole will be associated with each of the four molecules of interest. We suggest this will be generated due to a centring of a large electron density on the O atom, resulting in a dipole moment pointing along the molecule towards the oxygen. Indeed, the work of Gellman et al. [11,12] on 1-butanol is consistent with this hypothesis, showing a reduction in work function, consistent with the effects of a dipole anti-parallel to that of the copper surface. The interaction between these two dipole moments will obviously depend on their relative directions to each other. This in turn will depend heavily on the interaction and orientation of the molecules with respect to the

surface. As stated previously, we believe the interaction of all four molecules to be primarily through the interaction of the oxygen atoms and does not significantly involve the C=C bond. This is based on both our previous work on furan, THF, acetone and methanol (chapter 4) which suggested interactions through only the O lone pair electrons and from the TPD data in this current study where we observe similar desorption temperatures of both the two aldehydes and the two alcohols suggesting no significant interaction of the C=C bond. The orientation of the four molecules is somewhat more difficult to determine. None of the measurements made in this study allow us to infer adsorption geometry, so we must turn to studies of similar molecules. Using previous studies of acetone [37] and formaldehyde [38] as examples of C=O containing molecules and of studies of a number of straight chain alcohols [11,12] to infer the orientation of our two alcohols we propose all four molecules would be significantly inclined away from the surface normal. Hence on the clean surface, the dipole interaction is unlikely to be maximised. This model is shown schematically in figure 17.

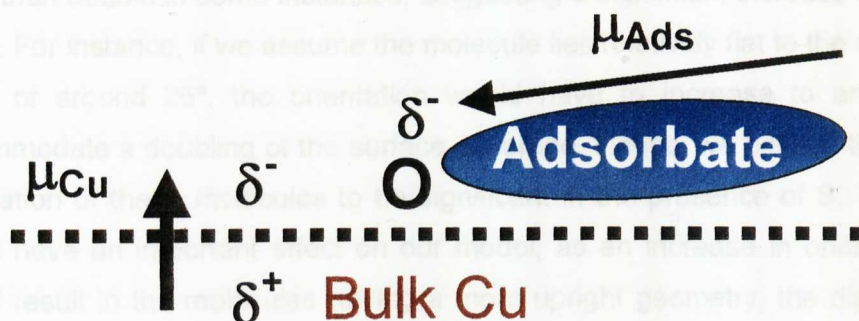


Figure 17. Diagram showing the interaction of crotonaldehyde, butaldehyde, crotyl alcohol and 1-butanol with the Cu(111) surface. μ_{Cu} and μ_{Ads} interact attractively.

From our current study, we believe we can make one further observation regarding the electrostatic interaction of the four molecules with the Cu(111) surface. Unlike in the work carried out in our lab previously on benzene and thiophene we observe no dipole facilitated charge transfer in the current study. We make this observation primarily on the basis that we observe no shifts in our UPS data that would support the suggestion that there is no significant charge transfer. Additionally, previous work on THF, furan, acetone and methanol showed all four molecules to be extremely weakly adsorbed on the Cu(111) surface. O-Cu values from NIXSW measurements were consistent with a weak van der Waals interaction, consistent with no charge transfer. Indeed UPS work on methanol and acetone also showed no

shifts upon adsorption. Hence we interpret the dipole interaction to be purely electrostatic in nature, without facilitating charge transfer.

In our experiments using pre-adsorbed sulphur we clearly observe significant effects upon the interaction of the four molecules with the surface. Hence, we obviously expect sulphur adsorption to have a significant impact on our electrostatic model. In chapter 5, we have shown that the presence of S on the Cu(111) surface induces an increase in work function. This is consistent with charge transfer from the metal to the S atoms and an increase in the magnitude of the surface dipole. Hence upon co-adsorption of our four molecules of interest we expect a stronger interaction between the increased surface dipole and the molecular dipole in the presence of sulphur. In addition to this we expect a second mechanism to play a role in the stabilisation of the four molecules. TPD and UPS measurements suggest an increase in packing density of the adsorbed layers of all four molecules. This would be consistent with potentially some conformational changes and certainly orientation changes in the adsorbed layer. Indeed, TPD data suggests the surface coverage to more than double in some instances, suggesting a significant increase in orientation angle. For instance, if we assume the molecule lies relatively flat to the surface at an angle of around 25° , the orientation would have to increase to around 63° to accommodate a doubling of the surface coverage. Hence, we believe the change in orientation of these molecules to be significant in the presence of S. This, in turn, would have an important effect on our model, as an increase in orientation angle would result in the molecules having a more upright geometry, the dipole moment changing to a more upright direction and therefore a greater level of interaction with the surface dipole. This is depicted in figure 18.

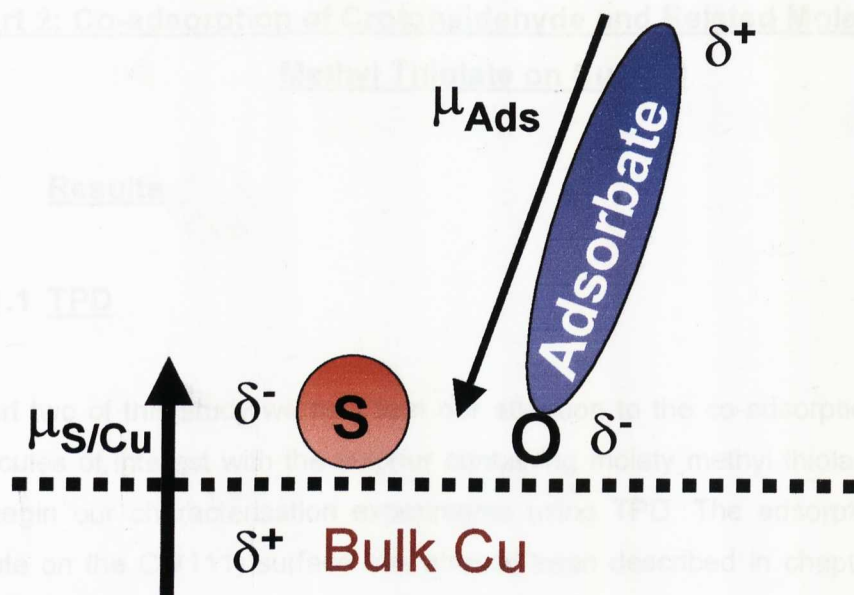


Figure 18. Diagram showing the interaction of crotonaldehyde, butaldehyde, crotyl alcohol and 1-butanol with the S/Cu(111) surface. $\mu_{S/Cu} > \mu_{Cu}$ and the interaction with μ_{Ads} increases.

Using this model we can also rationalise one further observation made in this study. In TPD data we observe a slightly greater stabilisation effect on the two aldehydes in the presence of S compared to that of the two alcohols. If we consider the dipole moments of crotonaldehyde (3.67 D) and 1-butanol (1.66 D) [39], we can see that in our electrostatic model we would expect a larger effect on the adsorption of aldehydes since they have a larger dipole moment. Hence, this fits our observations. The UPS data on the sulphur pre-covered surfaces is similar to the clean surface in that we observe no significant shifts in the relative positions of the adsorbate features. In the same manner as for the clean surface, we interpret this as evidence of no dipole facilitated charge transfer such as that seen in the adsorption of benzene and thiophene. This is also corroborated by the observation that all four molecules are stabilised even when adsorbed on a saturated sulphur layer. In the experiments performed on thiophene and benzene where charge transfer was proposed to take place, destabilisation of the adsorption was observed on saturated sulphur surfaces. This is not observed in the current experiments and again suggests a purely electrostatic effect with no charge transfer.

Part 2: Co-adsorption of Crotonaldehyde and Related Molecules with Methyl Thiolate on Cu(111)

6.2.1 Results

6.2.1.1 TPD

In part two of this study we now turn our attention to the co-adsorption of our four molecules of interest with the sulphur containing moiety methyl thiolate. As before, we begin our characterisation experiments using TPD. The adsorption of methyl thiolate on the Cu(111) surface has already been described in chapter 5, with the adsorption of crotonaldehyde, butaldehyde, crotyl alcohol and 1-butanol on clean Cu(111) described in part 1. Hence, we will not repeat these descriptions here and concentrate on co-adsorption experiments with methyl thiolate instead.

In all experiments reported here methyl thiolate was adsorbed at room temperature, before cooling of the sample followed by adsorption of the four molecules of interest. Reproducibly adsorbing the same amount of methyl thiolate on the surface proved to be extremely difficult, partly due to the dosing characteristics of the molecule itself and also due to the fact that the only means of measuring sulphur coverage available was AES. Since methyl thiolate dissociates during exposure to an electron beam, sulphur coverages could only be recorded after completion of TPD experiments and subsequent dissociation of the methyl thiolate. Due to these difficulties we performed experiments using two methodologies in an attempt to make accurate comparison between molecules possible. Firstly, each of the four molecules was co-adsorbed with a freshly prepared methyl thiolate surface; the methyl thiolate was subsequently dissociated to leave atomic sulphur and TPD experiments repeated from that surface. This allowed for accurate comparison of identical sulphur coverages in both molecular and atomic forms. Secondly, we wished to ensure each molecule was adsorbed with equivalent amounts of methyl thiolate. To achieve this aim we prepared one methyl thiolate layer and recorded TPD spectra of the desorption of each molecule in turn.

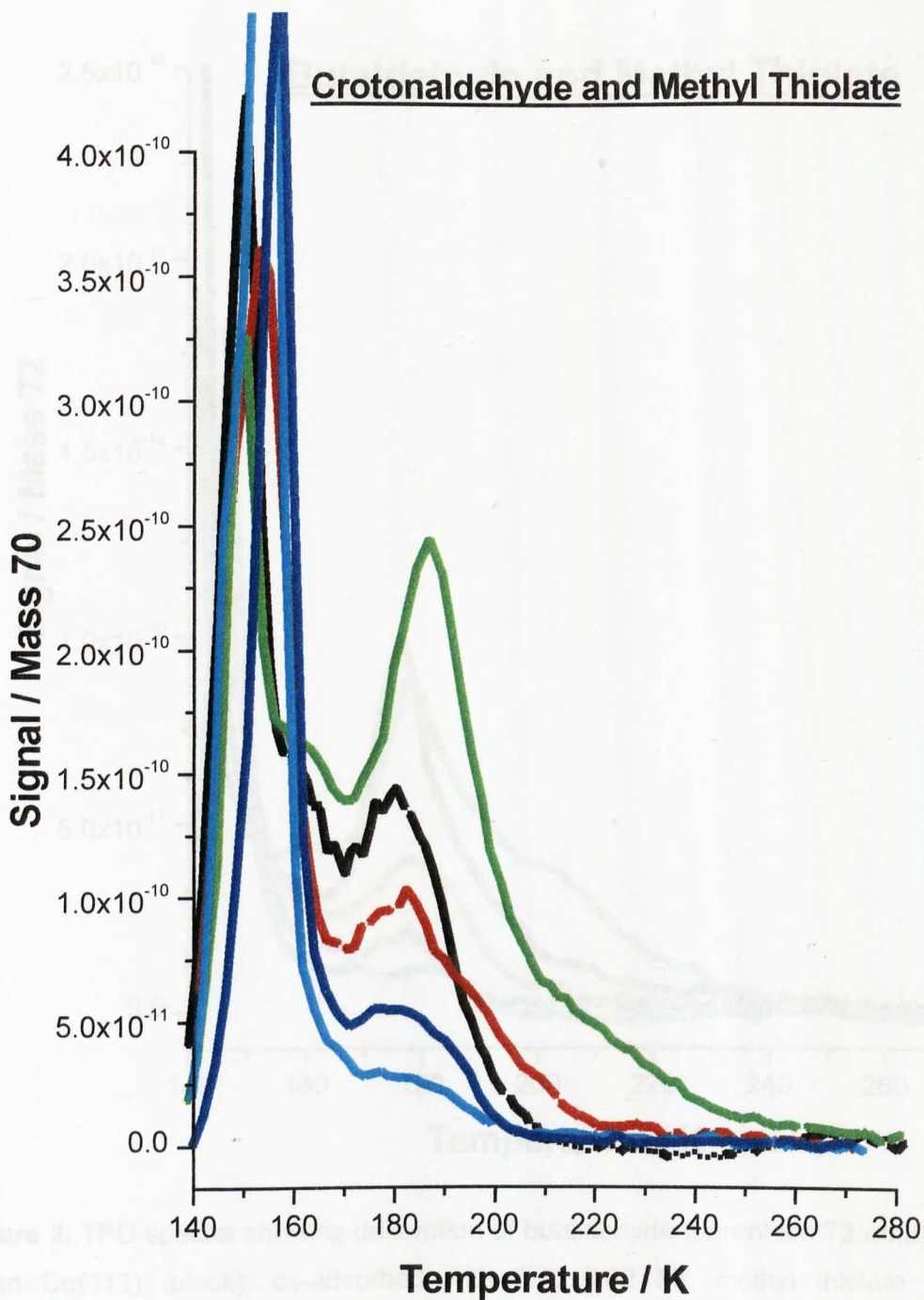


Figure 1. TPD spectra showing desorption of crotonaldehyde (parent ion 70 amu) from clean Cu(111) (black), co-adsorbed with 0.08±0.01 ML methyl thiolate (red), 0.08±0.01 ML atomic sulphur (green), 0.15±0.03 ML methyl thiolate (blue) and 0.21±0.02 ML methyl thiolate (cyan). All methyl thiolate surfaces were freshly prepared. All spectra were collected with a heating rate of 0.5 Ks⁻¹.

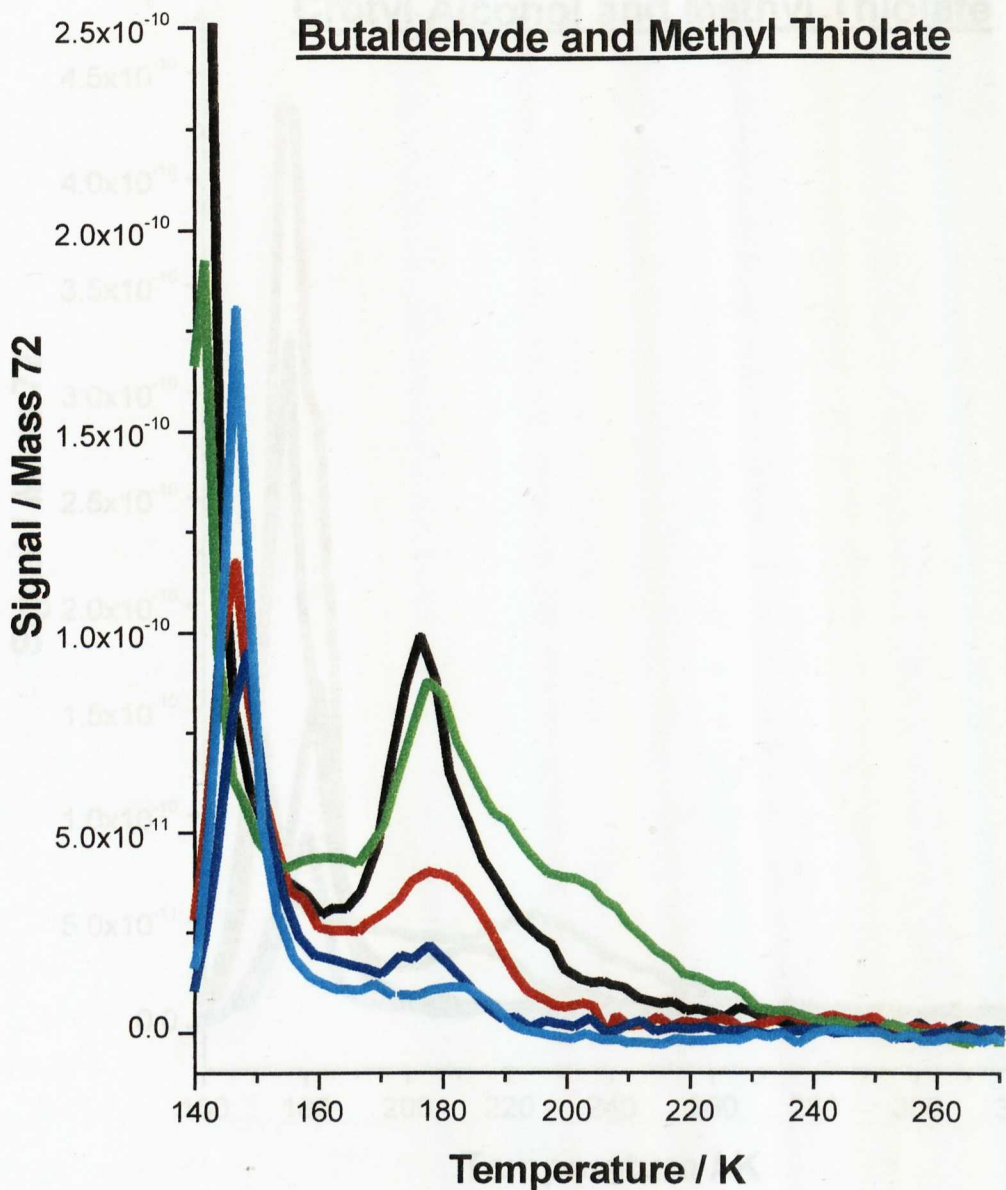


Figure 2. TPD spectra showing desorption of butaldehyde (parent ion 72 amu) from clean Cu(111) (black), co-adsorbed with 0.13 ± 0.02 ML methyl thiolate (red), 0.13 ± 0.02 ML atomic sulphur (green), 0.15 ± 0.03 ML methyl thiolate (blue) and 0.21 ± 0.02 ML methyl thiolate (cyan). Crotonaldehyde experiments performed previously on 0.15 (blue) and 0.21 ML (cyan) methyl thiolate surfaces. Experimental conditions were identical to those in figure 1.

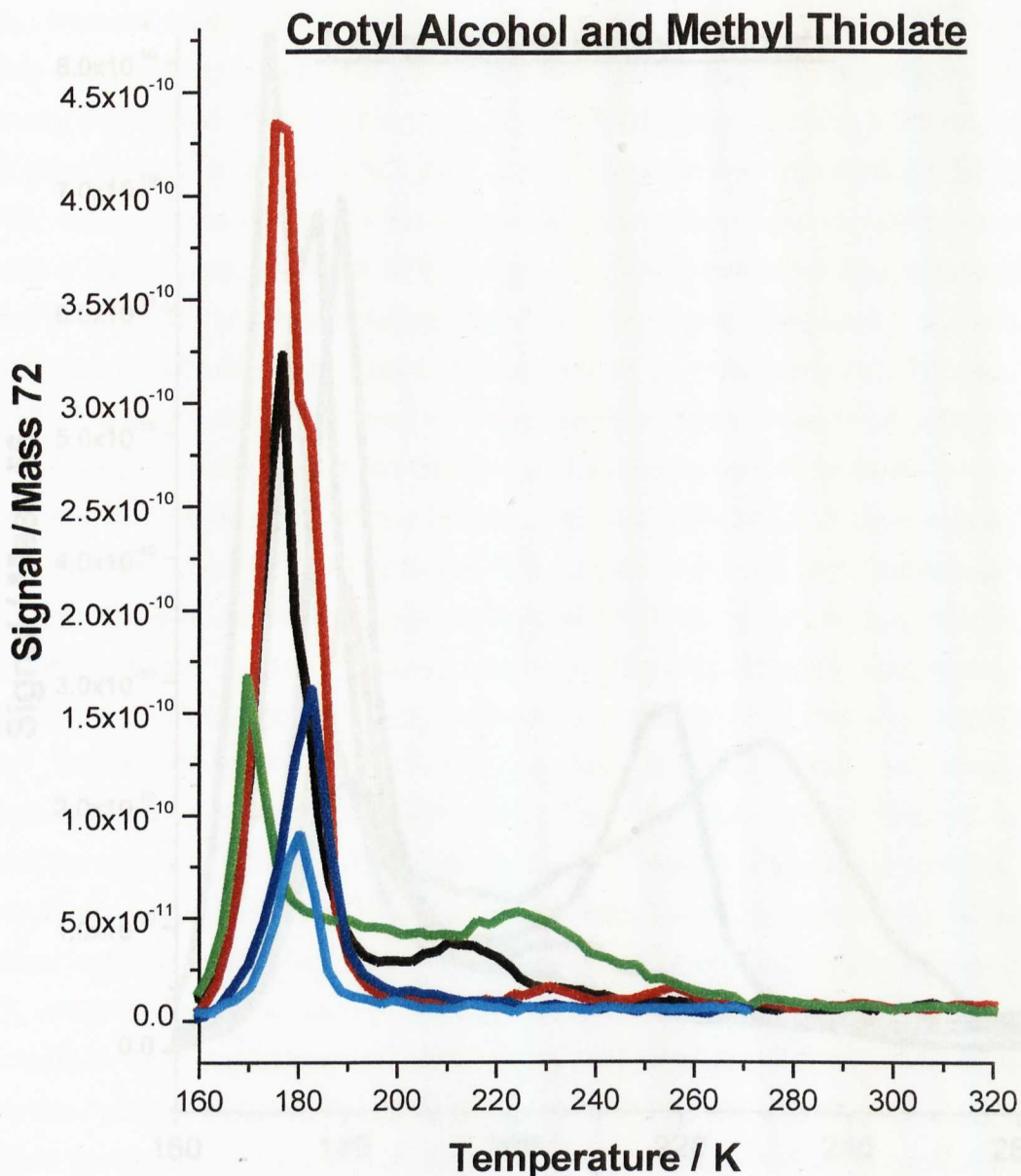


Figure 3. TPD spectra showing desorption of crotyl alcohol (parent ion 72 amu) from clean Cu(111) (black), co-adsorbed with 0.21 ± 0.01 ML methyl thiolate (red), 0.21 ± 0.01 ML atomic sulphur (green), 0.15 ± 0.03 ML methyl thiolate (blue) and 0.21 ± 0.02 ML methyl thiolate (cyan). Crotonaldehyde and butaldehyde experiments performed previously on 0.15 (blue) and 0.21 (cyan) ML methyl thiolate surfaces. Experimental conditions were identical to those in figure 1.

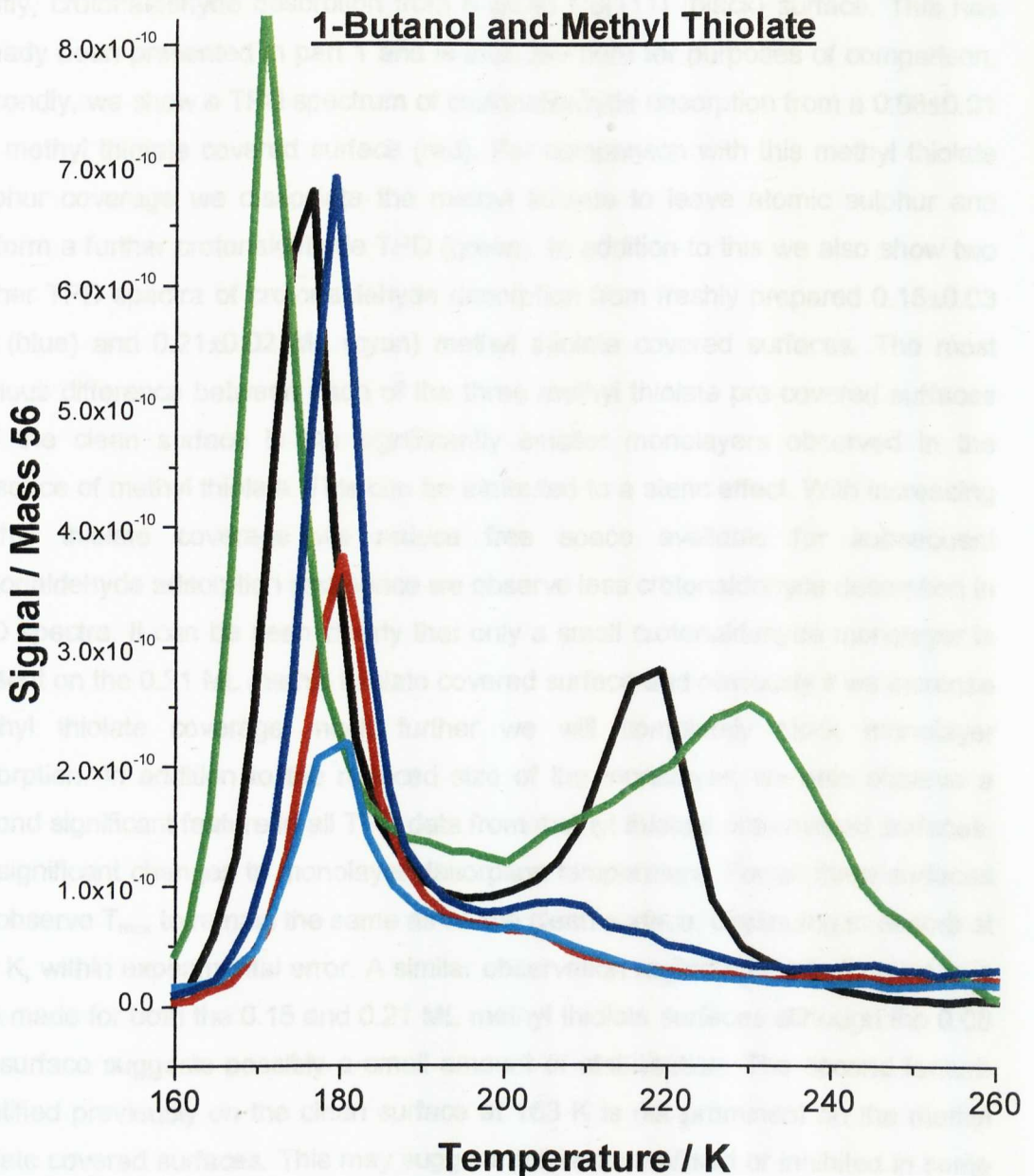


Figure 4. TPD spectra showing desorption of 1-butanol (fraction 56 amu) from clean Cu(111) (black), co-adsorbed with 0.20 ± 0.05 ML methyl thiolate (red), 0.20 ± 0.05 ML atomic sulphur (green), 0.15 ± 0.03 ML methyl thiolate (blue) and 0.21 ± 0.02 ML methyl thiolate (cyan). Crotonaldehyde, butanaldehyde and crotyl alcohol experiments performed previously on 0.15 (blue) and 0.21 (cyan) ML methyl thiolate surfaces. Experimental conditions were identical to those in figure 1.

Figure 1 shows TPD spectra of crotonaldehyde recorded from 5 different surfaces. Firstly, crotonaldehyde desorption from a clean Cu(111) (black) surface. This has already been presented in part 1 and is included here for purposes of comparison. Secondly, we show a TPD spectrum of crotonaldehyde desorption from a 0.08 ± 0.01 ML methyl thiolate covered surface (red). For comparison with this methyl thiolate sulphur coverage we dissociate the methyl thiolate to leave atomic sulphur and perform a further crotonaldehyde TPD (green). In addition to this we also show two further TPD spectra of crotonaldehyde desorption from freshly prepared 0.15 ± 0.03 ML (blue) and 0.21 ± 0.02 ML (cyan) methyl thiolate covered surfaces. The most obvious difference between each of the three methyl thiolate pre-covered surfaces and the clean surface is the significantly smaller monolayers observed in the presence of methyl thiolate. This can be attributed to a steric effect. With increasing methyl thiolate coverage we reduce free space available for subsequent crotonaldehyde adsorption and hence we observe less crotonaldehyde desorption in TPD spectra. It can be seen clearly that only a small crotonaldehyde monolayer is present on the 0.21 ML methyl thiolate covered surface and obviously if we increase methyl thiolate coverage much further we will completely block monolayer adsorption. In addition to the reduced size of the monolayer, we also observe a second significant feature in all TPD data from methyl thiolate pre-covered surfaces. No significant changes to monolayer desorption temperature. For all three surfaces we observe T_{max} to remain the same as on the clean surface, continuing to desorb at 182 K, within experimental error. A similar observation regarding the trailing edge is also made for both the 0.15 and 0.21 ML methyl thiolate surfaces although the 0.08 ML surface suggests possibly a small amount of stabilisation. The second feature identified previously on the clean surface at 163 K is not prominent on the methyl thiolate covered surfaces. This may suggest this is destabilised or inhibited in some way by the presence of methyl thiolate. As mentioned previously, the 0.08 ML methyl thiolate coverage was subsequently dissociated and experiments were repeated from the 0.08 ML atomic S coverage. The results from this surface are comparable with those in the previous chapter on S covered surfaces prepared using H_2S . We observe the presence of atomic sulphur to induce an increase in the T_{max} to 188 K, along with increases in trailing edge and surface coverage. Additionally, this spectrum highlights the significant differences induced by atomic S in comparison to methyl thiolate.

Figure 2 shows the corresponding spectra for butaldehyde, desorption from clean Cu(111) (black), a 0.13 ± 0.02 ML methyl thiolate coverage (red), the atomic sulphur

left from dissociation of that layer (green) and from two further methyl thiolate coverages, 0.15 ± 0.03 ML (blue) and 0.21 ± 0.02 ML (cyan). Both of these surfaces had previously been used in the experiments presented in figure 1 using crotonaldehyde, as discussed earlier. The observations made here for butaldehyde are similar to those just described for crotonaldehyde. Butaldehyde desorption from surfaces pre-dosed with increasing amounts of methyl thiolate show reduced monolayer desorption, with the smallest monolayer observed from the largest dose of methyl thiolate. These observations are reconciled using the same arguments described above for crotonaldehyde. Once again, we observe no significant shifts in T_{\max} , with the maximum remaining at ca. 176 K. Likewise we observe no significant increase in trailing edge temperature in the presence of methyl thiolate. Butaldehyde desorption from the atomic S covered surface is consistent with the results presented in part 1. We observe a slight increase in T_{\max} , as well as increases in the maximum temperature of the trailing edge and in packing density. Once again, the significant differences between this surface and that exposed to methyl thiolate are highlighted.

TPD spectra showing crotyl alcohol desorption from 5 surfaces is shown in figure 3. Desorption from a clean Cu(111) surface (black), a 0.21 ± 0.01 ML methyl thiolate coverage (red), the atomic sulphur left from dissociation of that layer (green) and from two further methyl thiolate coverages, 0.15 ± 0.03 ML (blue) and 0.21 ± 0.02 ML (cyan) are shown. Both of these surfaces had previously been used in the experiments presented in figures 1 and 2 using crotonaldehyde and butaldehyde in the manner discussed earlier. Our observations of crotyl alcohol desorption from each of the methyl thiolate pre-covered surfaces are significantly different to those made previously for crotonaldehyde and butaldehyde desorption. The presence of methyl thiolate on the Cu(111) surface completely destabilises the adsorption of a crotyl alcohol monolayer, resulting in the observation of only condensed multilayers in TPD spectra. This observation would suggest that crotyl alcohol preferentially adsorbs on the methyl thiolate rather than the copper surface. The atomic sulphur data is once again consistent with the work presented in part 1, with an observed increase in T_{\max} , temperature of trailing edge and in surface coverage.

Finally, we present the results of TPD measurements of 1-butanol adsorption in the presence of methyl thiolate. As for the other three molecules we present desorption from clean Cu(111) (black), a 0.20 ± 0.05 ML methyl thiolate coverage (red), the atomic sulphur left from dissociation of that layer (green) and from two further methyl

thiolate coverages, 0.15 ± 0.03 ML (blue) and 0.21 ± 0.02 ML (cyan) are shown. Both of these surfaces had previously been used in the experiments presented in figures 1, 2 and 3 using crotonaldehyde, butaldehyde and crotyl alcohol in the manner discussed earlier. The 1-butanol desorption data from methyl thiolate covered surfaces shows similar behaviour to that of crotyl alcohol in that we observe significant destabilisation of the adsorbed layer, signalled by the almost complete disappearance of the chemisorbed layer. However, unlike crotyl alcohol we observe an additional feature apart from the multilayer. This feature has a maximum around 209 K on the 0.15 ML surface and slightly lower at 204 K on the 0.20 and 0.21 ML methyl thiolate covered surfaces. We attribute this feature to a small amount of chemisorbed 1-butanol. Despite this small amount of chemisorbed state, this data suggests preferential adsorption on the methyl thiolate rather than on the Cu(111) surface in a similar manner to crotyl alcohol. The atomic sulphur data is once again consistent with the work presented in part 1 with an observed increase in T_{\max} , trailing edge and in surface coverage.

The effects of co-adsorbed methyl thiolate on the adsorption of crotonaldehyde, butaldehyde, crotyl alcohol and 1-butanol are both significant and extreme. While co-adsorption of methyl thiolate with both crotonaldehyde and butaldehyde has no significant effect other than reducing the observed surface coverage, the adsorption of crotyl alcohol and 1-butanol is significantly destabilised. This suggests a preferential adsorption of both these molecules on the CH_3 group of the methyl thiolate as opposed to the Cu(111) surface. Significantly, the magnitude of the destabilisation is considerably larger than for any stabilisation effects observed in the presence of atomic sulphur in the previous set of experiments.

6.2.1.2 UPS and XPS

As we did for the atomic sulphur experiments reported in the previous section, we performed further characterisation of the methyl thiolate experiments using the techniques of XPS and UPS.

Figures 5 and 6 show UP and C1s spectra recorded from a 0.18 ± 0.01 ML coverage of methyl thiolate and from that layer co-adsorbed with crotonaldehyde. The adsorbed methyl thiolate UP spectrum has already been discussed fully in chapter 5 and will not be discussed further here. The spectrum labelled (b) is recorded from crotonaldehyde multilayers co-adsorbed with methyl thiolate. This spectrum is

consistent with that of spectrum (e) recorded from a clean surface and displays two broad features as described in the previous chapter. The absolute intensity of the two spectra differ slightly but this would be consistent with different surface coverages. Condensed crotonaldehyde multilayers co-adsorbed with methyl thiolate are subsequently annealed to produce a monolayer coverage of crotonaldehyde co-adsorbed with methyl thiolate. This is labelled spectrum (c). The equivalent spectrum (f) from a clean surface is also shown. Firstly, we note that the co-adsorbed spectrum is significantly less intense than that from the clean surface (spectrum has been multiplied by 2 to aid comparison). This would again be consistent with the reduced crotonaldehyde coverage as indicated in TPD data. Secondly, we observe a slight change in the shape of the co-adsorbed spectrum compared to that from the clean surface. The spectrum continues to contain two broad features. However, the first stretching from a 7-12 eV usually has a maximum at 8.9 eV but this is shifted to slightly lower binding energy in the co-adsorbed spectrum. We believe this observation can be accounted for by the fact that the crotonaldehyde UPS components are superimposed on that of the methyl thiolate components. We believe this causes the small differences we observe between this and the clean surface spectrum. The position of the second feature already attributed to the O lone pair and π -orbitals shows no relative change in position. Finally, we show spectrum (d) obtained after crotonaldehyde desorption, which is consistent with our original methyl thiolate layer, as expected.

Figure 6 shows the C1s XP spectra recorded along with the UPS data just described. From this data we observe two important facts. Firstly, XPS confirms a significant reduction in the adsorbed layer of crotonaldehyde co-adsorbed with methyl thiolate consistent with both the UP spectrum and TPD measurements. Also, within experimental error, we observe no carbon left on the surface, apart from that related to methyl thiolate, after desorption of the crotonaldehyde layer.

The same procedure as that just applied to crotonaldehyde was once again applied to the other three molecules. The UPS results from butaldehyde and 0.18±0.01 ML S coverage of methyl thiolate are shown in figure 7. Similar observations are made here as for the adsorption of crotonaldehyde. Butaldehyde multilayers from both the methyl thiolate covered surface (b) and the clean surface (e) are identical. The two monolayer coverage surfaces do, however, show some small differences. The overall spectrum from the methyl thiolate surface (c) is significantly reduced (spectrum is multiplied by 2 for comparison purposes) but this is once again

consistent with a reduced butaldehyde coverage. The relative positions of all the adsorbate peaks remain the same in the co-adsorbed spectrum with respect to the clean surface. This includes the position of the feature associated with emission from the O lone pair orbital. However, we do observe changes in the relative intensities of adsorbate peaks. Particularly, the intensity of the feature at 7.2 eV is significantly reduced. Once again, as we suggested for crotonaldehyde this may be a result of the butaldehyde spectrum being effectively superimposed on top of that from the methyl thiolate. As before, annealing of the layer results in butaldehyde desorption and a UP spectrum consistent with that of the original methyl thiolate layer.

The C1s spectra in figure 8 also show similar behaviour to that observed for crotonaldehyde. We can see again that the adsorbed butaldehyde layer on the clean surface is significantly greater than that on the co-adsorbed surface and also that, within experimental error, no extra carbon is left on the surface after butaldehyde desorption.

Crotyl alcohol UPS co-adsorption data (figure 9) is significantly different to that observed for either crotonaldehyde or butaldehyde but is consistent with the TPD data presented earlier. The condensed multilayer of crotyl alcohol co-adsorbed with 0.21 ± 0.03 ML methyl thiolate (b) shows a number of differences in relative intensity of the adsorbate features compared to that of the clean surface (f). In particular, the feature at around 7.0 eV is significantly reduced compared to the rest of the spectrum. Despite this we observe no shifts in the relative positions of adsorbate peaks, including the feature associated with the O lone pair and π -orbitals. Upon heating of the condensed multilayers to temperatures usually appropriate to produce a monolayer, we observe the complete disappearance of any orbitals usually associated with crotyl alcohol and a return to a spectrum essentially consistent with the adsorbed methyl thiolate. However, we do observe an exception to this in that the d-band section of the spectrum does not reappear fully at this stage, being slightly less resolved and intense than the original methyl thiolate surface. This observation would be consistent with the presence of a small amount of crotyl alcohol adsorbed on the Cu(111) surface. Further heating of the layer to temperatures past that usually sufficient to desorb molecular crotyl alcohol results in the d-band becoming sharper and more intense but still less so than that of the methyl thiolate surface suggesting some dissociated crotyl alcohol remains.

The C1s data in figure 10 is consistent with the corresponding UPS data in figure 9. Small amounts of carbon are observed to remain on the surface after initial heating. Again, in a similar manner to the UPS data this suggests the possibility of a small amount of chemisorbed crotyl alcohol may be present. Further heating results in a reduction in the amount of carbon remaining but a small amount still remains not associated with the methyl thiolate molecules. Again this would be consistent with some dissociated crotyl alcohol remaining on the surface. A monolayer coverage of crotyl alcohol from a clean surface is also shown for comparison.

Finally, we compare the co-adsorption of 1-butanol (figure 11) with 0.19 ± 0.02 ML methyl thiolate. Like crotyl alcohol, 1-butanol produces significantly different UP spectra from either crotonaldehyde or butaldehyde. The co-adsorbed multilayer spectrum (b), like crotyl alcohol, shows a change in the relative intensities of the adsorbate peaks. In particular, the peak at 9.5 eV becomes significantly enlarged with respect to the other features. Despite this we still observe no changes in the relative positions of the adsorbate features, including the peak associated with the O lone pair orbitals. Upon heating, all adsorbate bands disappear and the d-band associated with the copper surface re-appears. However, as for crotyl alcohol, the d-band is not as intense or as well resolved as those on the initial methyl thiolate UPS. Further heating results in an increase in d-band intensity but even after heating past temperatures usually appropriate to desorb a 1-butanol monolayer we still do not observe a return to the original spectrum suggesting some possible dissociation.

Figure 12 shows the XP spectra corresponding to the UPS data of co-adsorbed 1-butanol and methyl thiolate. Initial heating of the condensed multilayers results in a XP spectrum showing a small amount of carbon present over and above that of the methyl thiolate layer. This is similar to our observations just made regarding crotyl alcohol and is also in agreement with the 1-butanol TPD data which suggested the presence of a small amount of adsorption on the metal surface. Further heating results in a reduction of this amount of carbon, leaving a spectrum, which within experimental error, suggests no carbon remaining except that of the methyl thiolate. This observation is in contrast to that of the UPS but could be due to only a small amount of carbon remaining out with the detection threshold of the XPS.

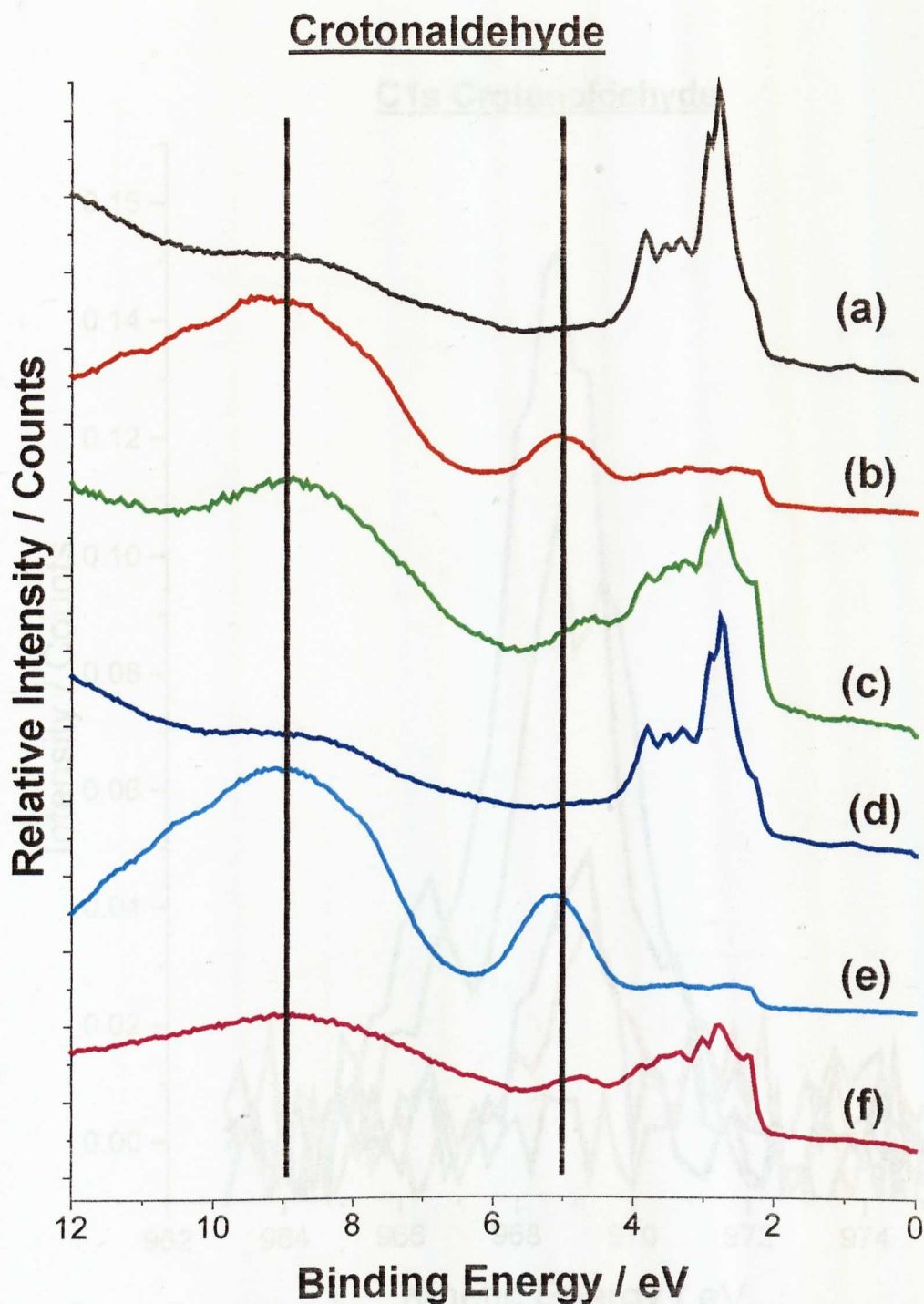


Figure 5. Normal emission UP spectrum of (a) 0.18 ± 0.01 ML methyl thiolate (black), (b) co-adsorbed crotonaldehyde multilayers (red) and (c) a co-adsorbed crotonaldehyde monolayer ($\times 2$, green). (d) shows methyl thiolate spectrum after crotonaldehyde desorption (blue) and (e) multilayer (cyan) and (f) monolayer (magenta) coverages of crotonaldehyde on clean Cu(111) are also shown for comparison. Binding energies are relative to E_F . Lines have been added to facilitate comparison of peak positions.

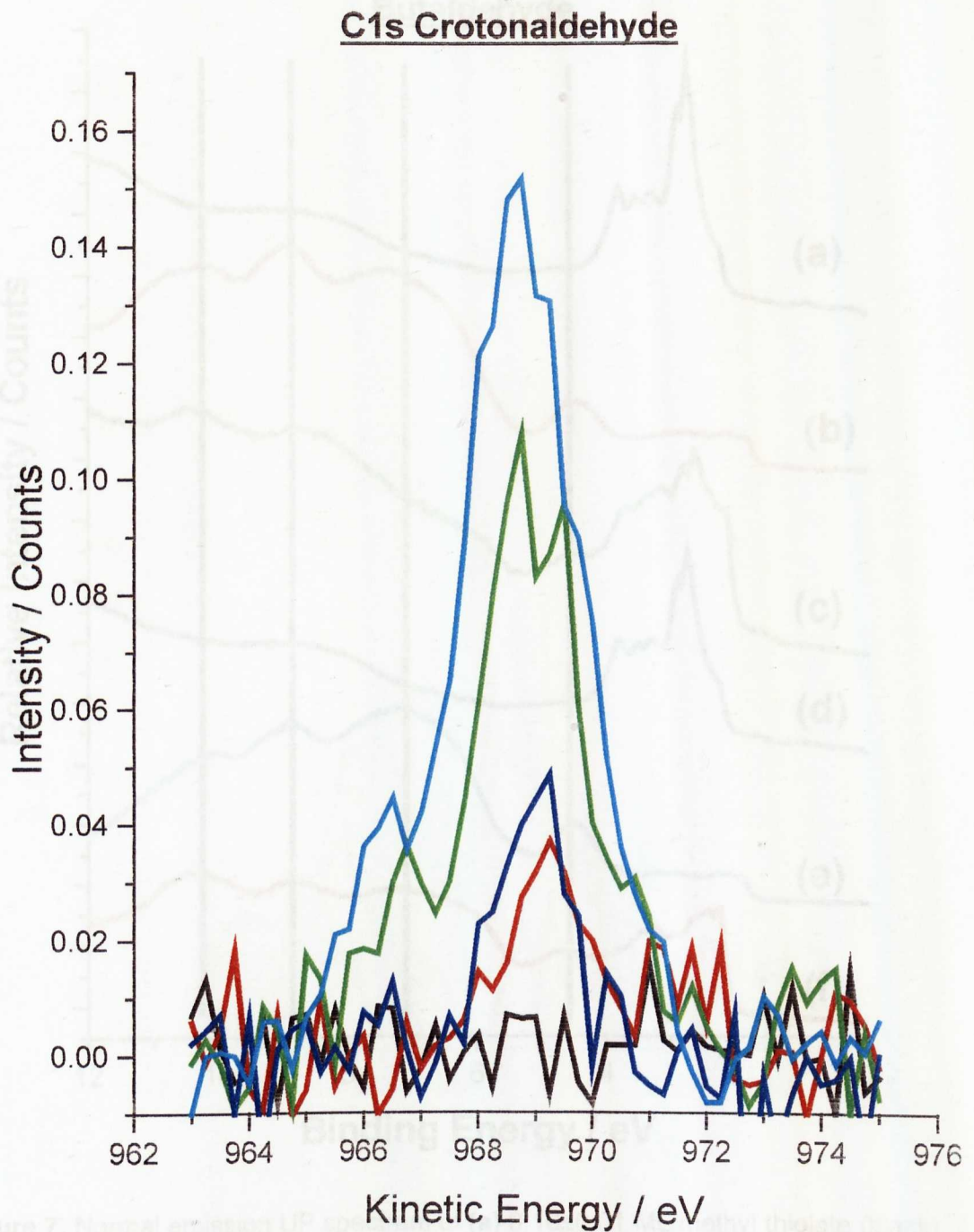


Figure 6. XP spectra of clean Cu(111) surface, 0.18 ± 0.01 ML methyl thiolate (red), co-adsorbed crotonaldehyde (green) and XP spectrum of surface after crotonaldehyde desorption (blue). A crotonaldehyde monolayer from a clean surface (cyan) is also shown for comparison.

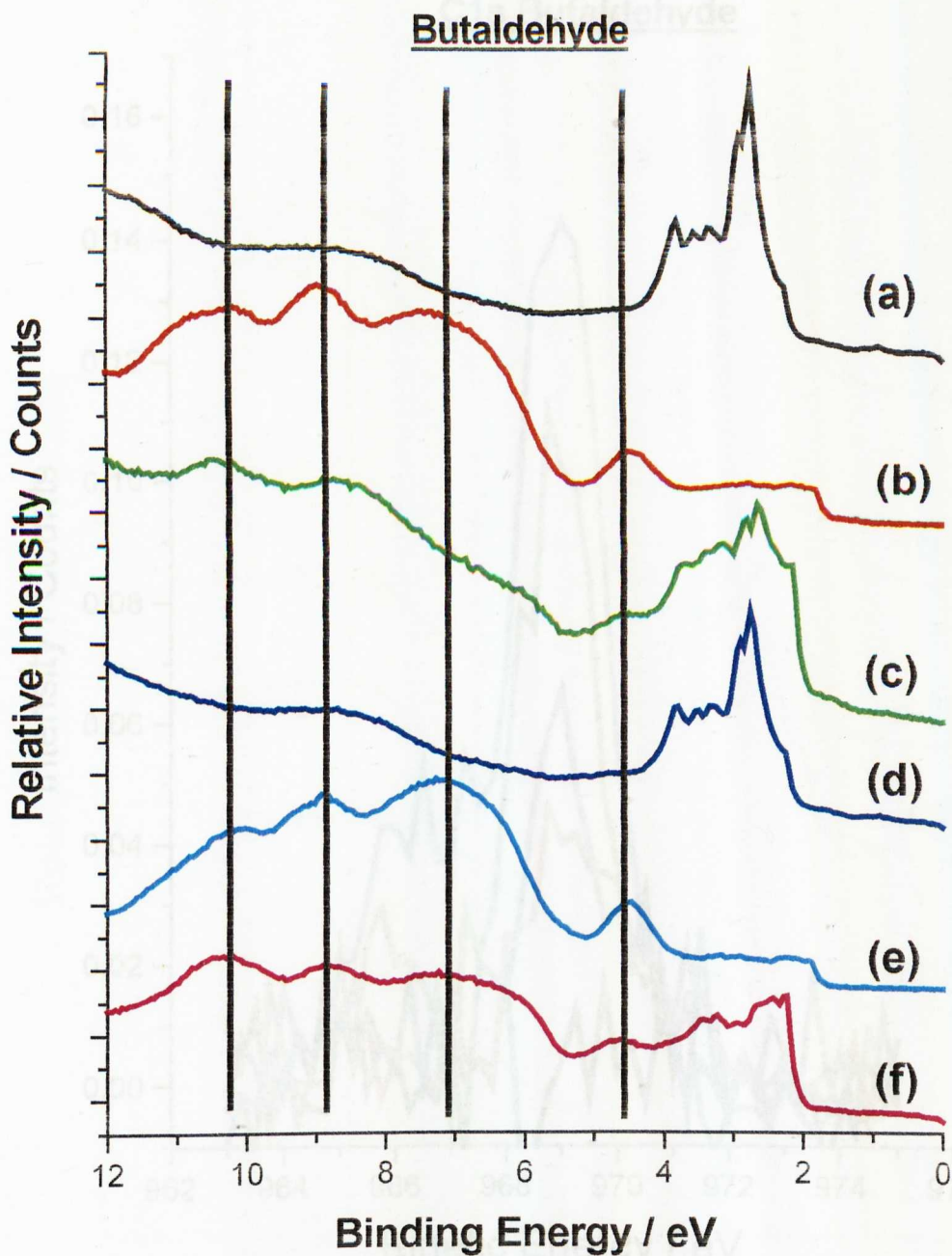


Figure 7. Normal emission UP spectrum of (a) 0.18 ± 0.01 ML methyl thiolate (black), (b) co-adsorbed butaldehyde multilayers (red) and (c) a co-adsorbed butaldehyde monolayer ($\times 2$, green). (d) shows methyl thiolate spectrum after butaldehyde desorption (blue) and (e) multilayer (cyan) and (f) monolayer (magenta) coverages of butaldehyde on clean Cu(111) are also shown for comparison. Binding energies are relative to E_F . Lines have been added to facilitate comparison of peak positions.

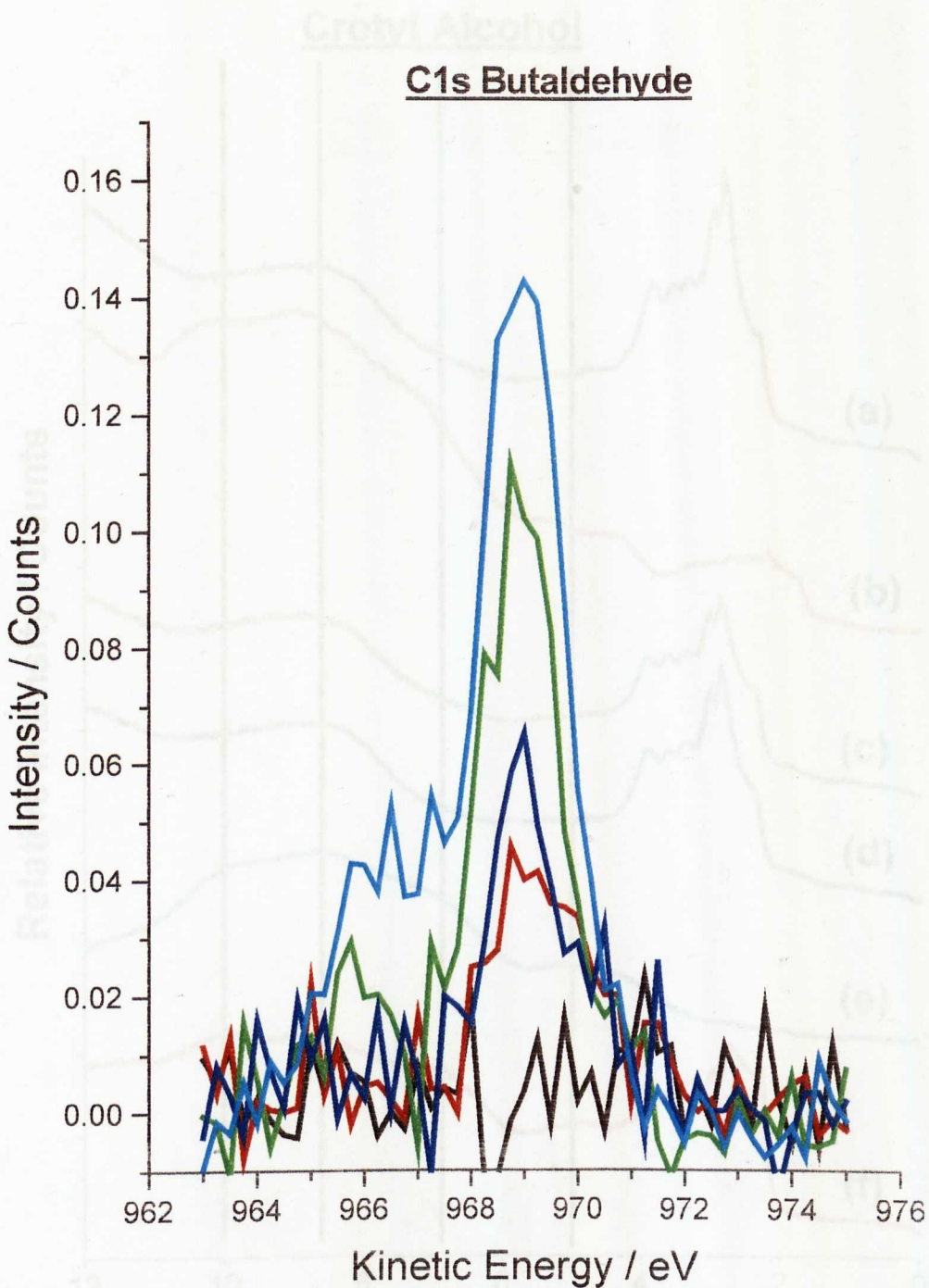


Figure 8. XP spectra of clean Cu(111) surface, 0.18 ± 0.01 ML methyl thiolate (red), co-adsorbed butaldehyde (green) and XP spectrum of surface after butaldehyde desorption (blue). A butaldehyde monolayer from a clean surface (cyan) is also shown for comparison.

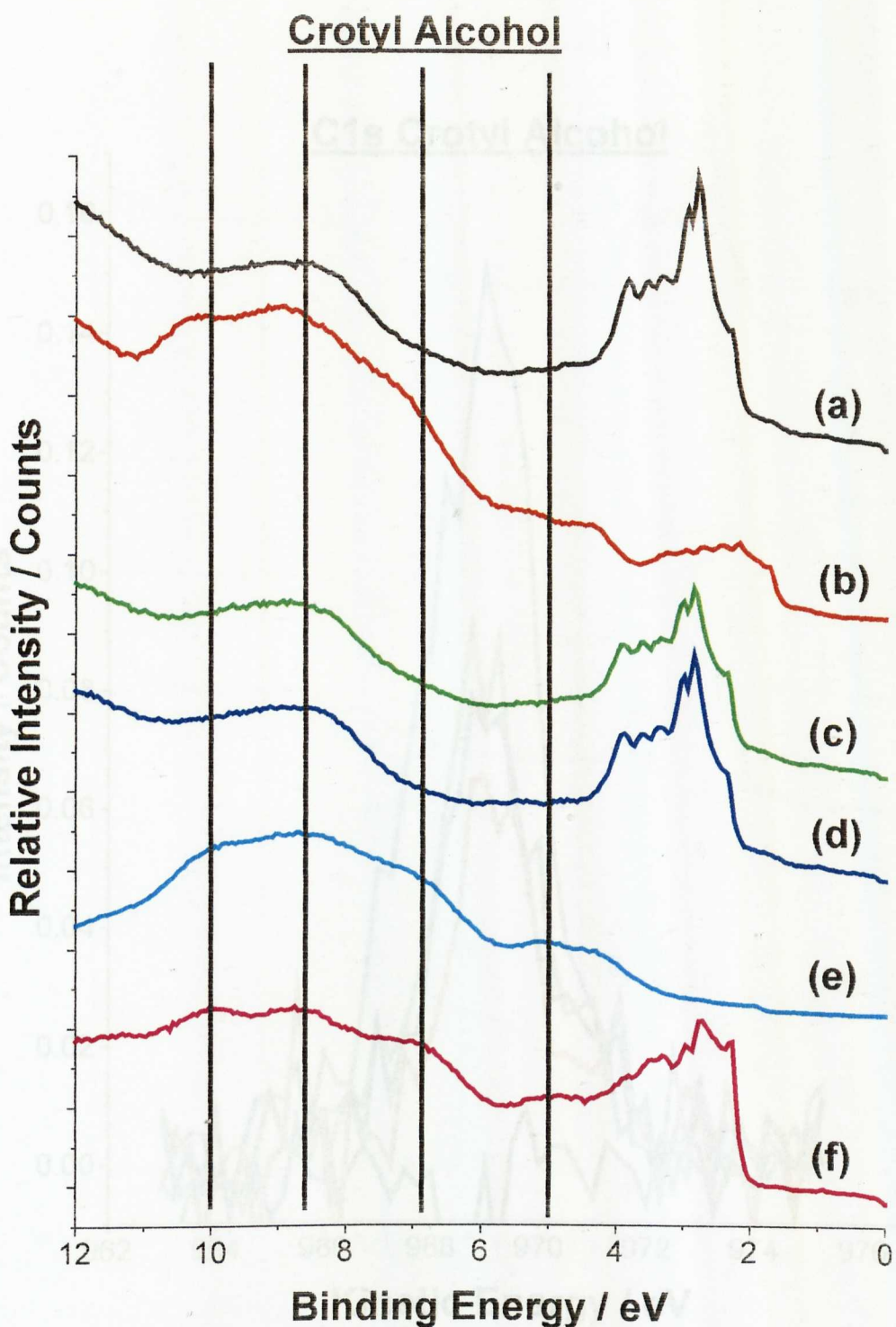


Figure 9. Normal emission UP spectrum of (a) 0.21 ± 0.03 ML methyl thiolate (black), (b) co-adsorbed butaldehyde multilayers (red) and (c) annealed to a temperature normally appropriate to produce a co-adsorbed crotyl alcohol monolayer (green). (d) shows methyl thiolate spectrum after crotyl alcohol desorption (blue) and (e) multilayer (cyan) and (f) monolayer (magenta) coverages of crotyl alcohol on clean Cu(111) are also shown for comparison. Binding energies are relative to E_F . Lines have been added to facilitate comparison of peak positions.

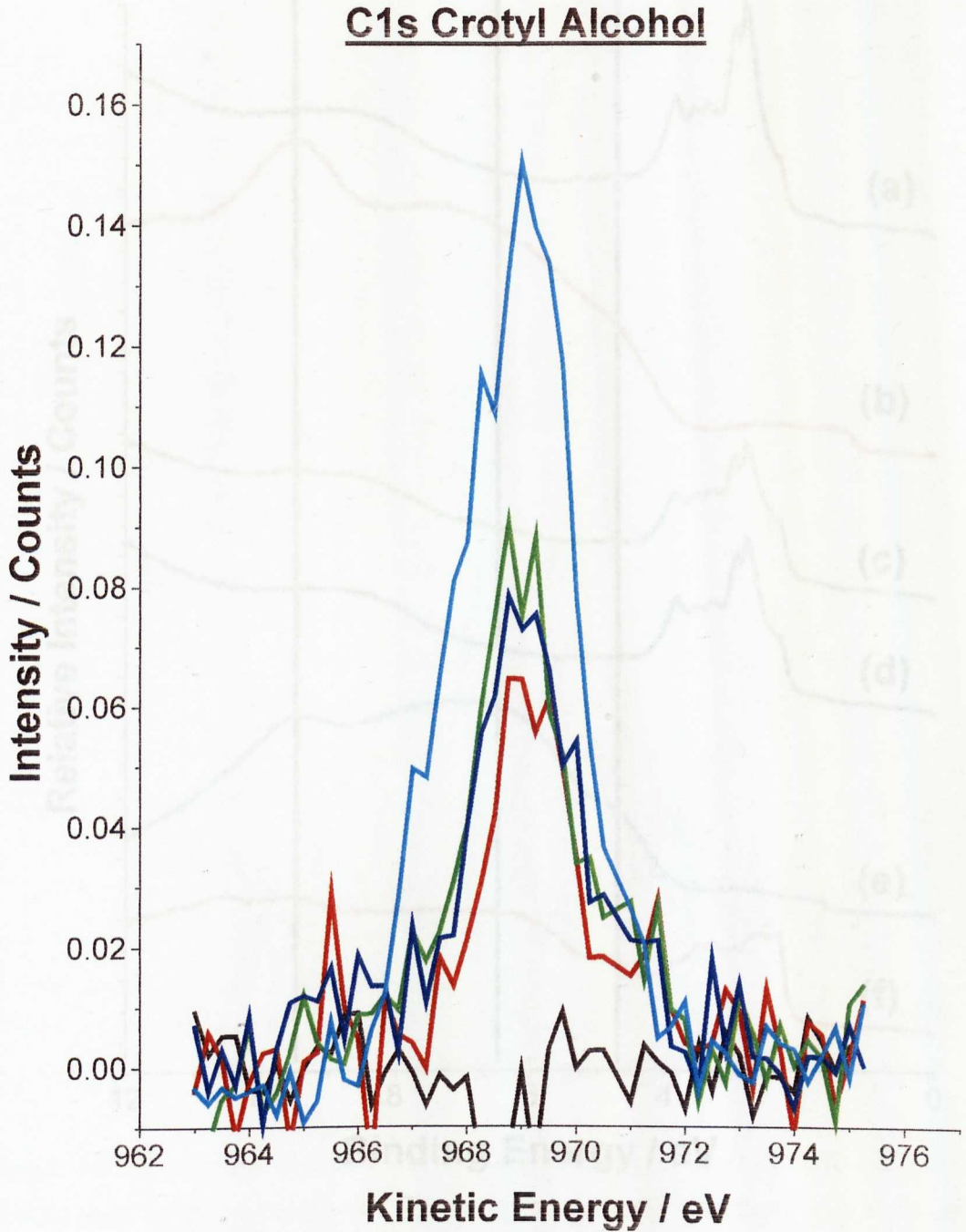


Figure 10. XP spectra of clean Cu(111) surface, adsorbed 0.21 ± 0.03 ML methyl thiolate layer (red), co-adsorbed crotyl alcohol (green) and XP spectrum of surface after crotyl alcohol desorption (blue). A crotyl alcohol monolayer from a clean surface (cyan) is also shown for comparison.

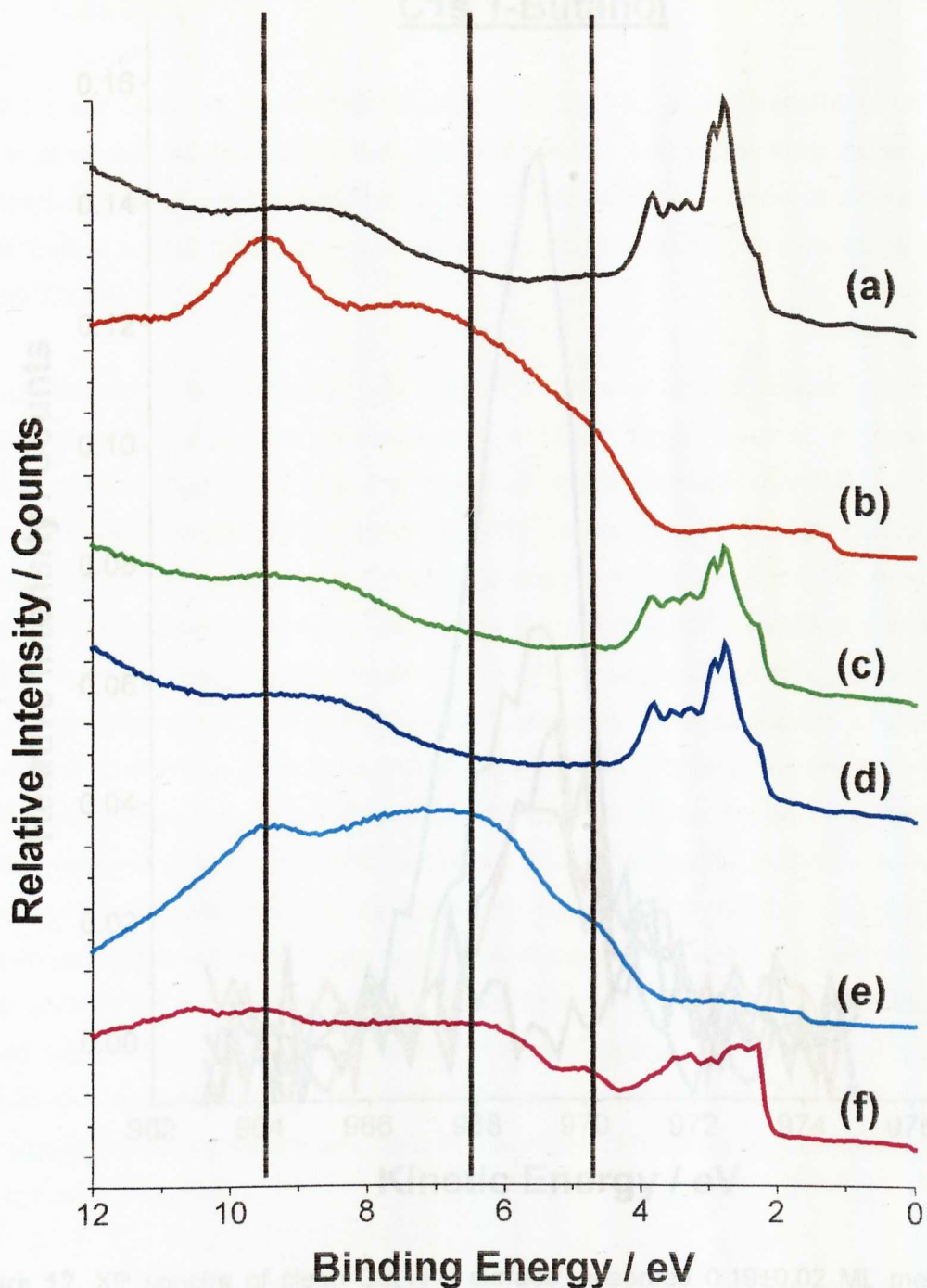
1-Butanol

Figure 9. Normal emission UP spectrum of (a) 0.19 ± 0.02 ML methyl thiolate (black), (b) co-adsorbed 1-butanol multilayers (red) and (c) annealed to a temperature normally appropriate to produce a co-adsorbed 1-butanol monolayer (green). (d) shows methyl thiolate spectrum after 1-butanol desorption (blue) and (e) multilayer (cyan) and (f) monolayer (magenta) coverages of 1-butanol on clean Cu(111) are also shown for comparison. Binding energies are relative to E_F . Lines have been added to facilitate comparison of peak positions.

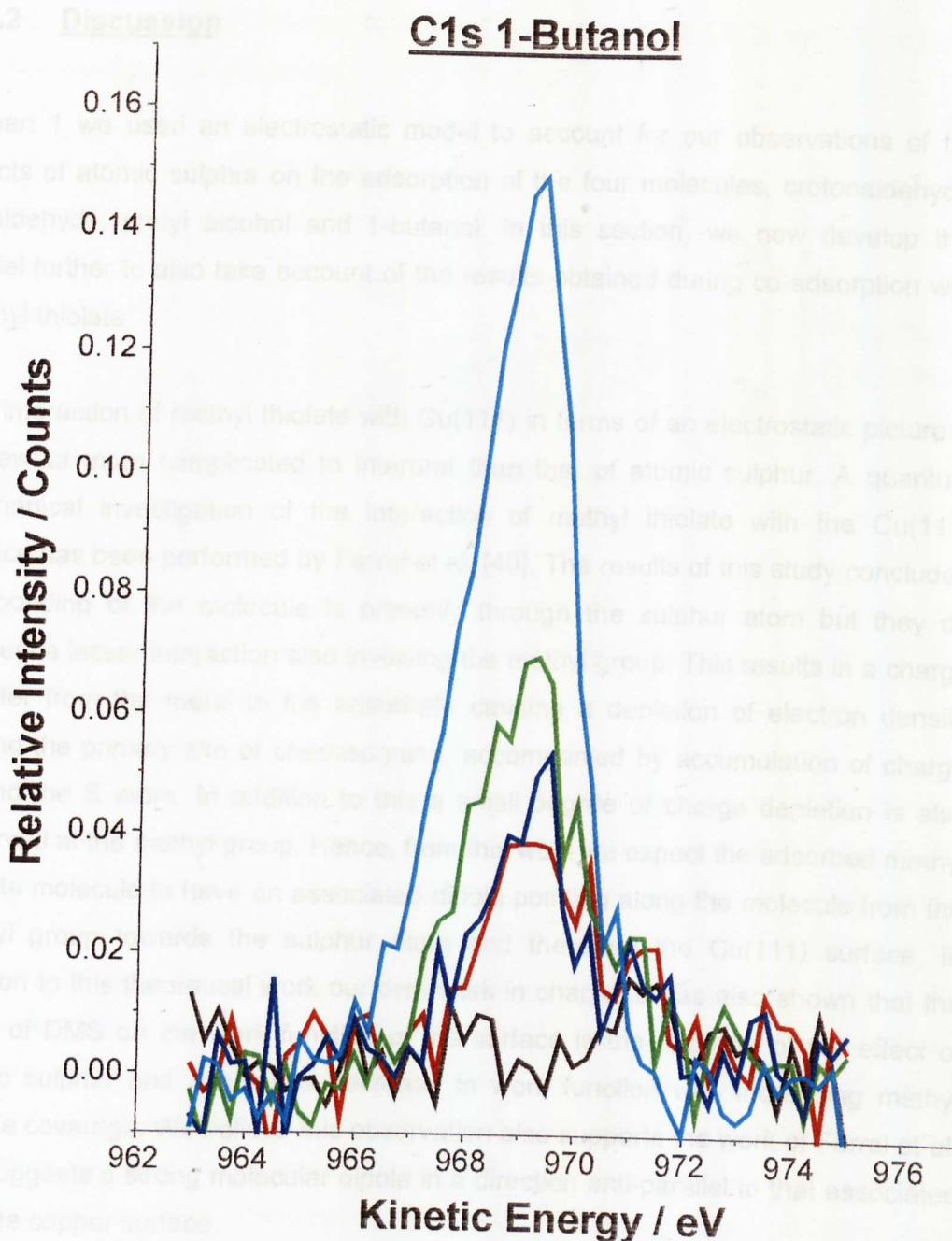


Figure 12. XP spectra of clean Cu(111) surface, adsorbed 0.19 ± 0.02 ML methyl thiolate layer (red), co-adsorbed 1-butanol (green) and XP spectrum of surface after 1-butanol desorption (blue). A 1-butanol monolayer from a clean surface (cyan) is also shown for comparison.

6.2.2 Discussion

In part 1 we used an electrostatic model to account for our observations of the effects of atomic sulphur on the adsorption of the four molecules, crotonaldehyde, butaldehyde, crotyl alcohol and 1-butanol. In this section, we now develop that model further to also take account of the results obtained during co-adsorption with methyl thiolate.

The interaction of methyl thiolate with Cu(111) in terms of an electrostatic picture is somewhat more complicated to interpret than that of atomic sulphur. A quantum mechanical investigation of the interaction of methyl thiolate with the Cu(111) surface has been performed by Ferral et al. [40]. The results of this study concluded the bonding of the molecule is primarily through the sulphur atom but they do suggest a lesser interaction also involving the methyl group. This results in a charge transfer from the metal to the adsorbate causing a depletion of electron density around the primary site of chemisorption, accompanied by accumulation of charge around the S atom. In addition to this a small degree of charge depletion is also observed at the methyl group. Hence, from this work we expect the adsorbed methyl thiolate molecule to have an associated dipole pointing along the molecule from the methyl group towards the sulphur atom and therefore the Cu(111) surface. In addition to this theoretical work our own work in chapter 5 has also shown that the effect of DMS on the work function of the surface is the opposite of the effect of atomic sulphur and induces a decrease in work function with increasing methyl thiolate coverage. We believe this observation also supports the work of Ferral et al. and suggests a strong molecular dipole in a direction anti-parallel to that associated with the copper surface.

Based on this previous work, we propose the following model to explain our observations. In the presence of co-adsorbed methyl thiolate, we have the opposite electrostatic effect to that observed for atomic sulphur. Namely, rather than having the dipoles associated with our four molecules of interest and that of the copper surface being anti-parallel, we have a parallel dipole associated with the adsorbed methyl thiolate. This type of interaction, as has been discussed previously, would be unfavourable and we would therefore not expect to see any stabilisation of any of our four molecules. Hence, this is consistent with our observations made of all four of our molecules in the sense we see no stabilisation effects in TPD data. Therefore,

based on this idea we propose the model depicted in figure 13 for the adsorption of both of the aldehyde molecules.

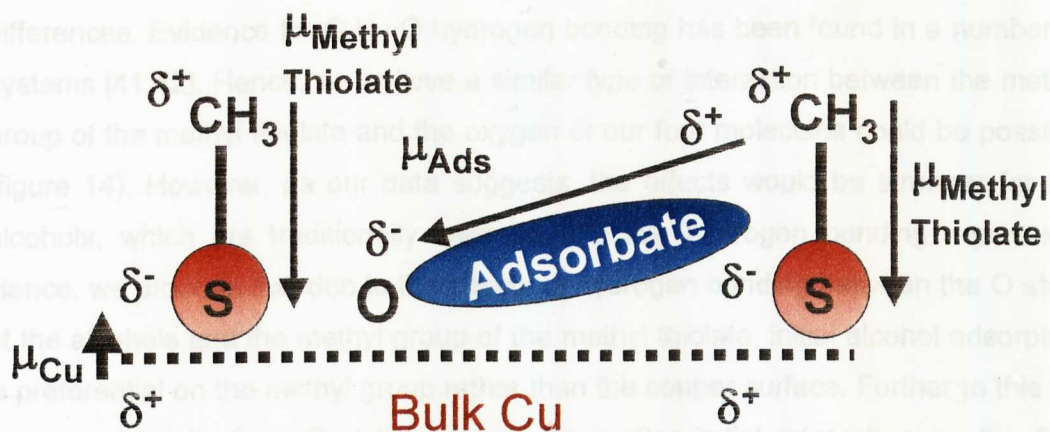


Figure 13. Diagram showing the interaction of crotonaldehyde and butanal with co-adsorbed methyl thiolate on the Cu(111) surface.

We propose adsorption of both of the aldehyde molecules takes place between adsorbed methyl thiolate molecules. The surface dipole is reduced due to the presence of methyl thiolate and in addition to this the dipole associated with the methyl thiolate points towards the surface. Both of these effects contribute to the fact we observe no stabilisation of the aldehydes. Additionally, we propose the aldehydes return to an orientation that is significantly inclined toward the surface. This is based on the fact that we observe the molecules orientation to change in the presence of atomic sulphur to maximise the overlap of anti-parallel dipoles. Hence, we believe the opposite effect to be likely in the presence of methyl thiolate and this would explain the disappearance of the 163 K chemisorbed state in TPD spectra from methyl thiolate covered surfaces.

The situation regarding the adsorption of the two alcohols in the presence of methyl thiolate is clearly not fully described by the mechanism just described for the two aldehydes. Our observations in TPD and UPS suggest a small amount of adsorption on the copper surface continues and we believe this takes place in a similar manner to that just described for the two aldehyde molecules. However, we also observe a second mechanism to take place, which is much more extreme than any of the effects observed in the presence of sulphur described so far. Namely, significant destabilisation of the adsorbate layers. The observed destabilisation immediately suggests that both of the alcohol molecules preferentially adsorb on the methyl

thiolate molecule rather than on the Cu(111) surface. Hence, to fully account for our observations, we must examine the possible mechanisms involved in adsorption on the methyl group. We believe the effects of hydrogen bonding can account for these differences. Evidence for C-H...O hydrogen bonding has been found in a number of systems [41,42]. Hence, we believe a similar type of interaction between the methyl group of the methyl thiolate and the oxygen of our four molecules could be possible (figure 14). However, as our data suggests, the effects would be stronger for the alcohols, which are traditionally seen as effective hydrogen bonding molecules. Hence, we propose that due to the effects of hydrogen bonding between the O atom of the alcohols and the methyl group of the methyl thiolate, initial alcohol adsorption is preferential on the methyl group rather than the copper surface. Further to this we propose a nucleation effect then takes place after initial adsorption on the CH₃ group. The mechanism for this effect would also be as a result of the stronger hydrogen bonding characteristics of the alcohol molecules. We suggest this based on the fact that the OH group of the alcohols would act both as a strong acceptor and donor in the hydrogen bonding process [42]. In the aldehydes, hydrogen bonding is far less favourable and would have to take place between the O atom and a CH group. This would then be an interaction between a strong acceptor and weak donor [42] and less likely. The effects of hydrogen bonding on the interaction between the four molecules is evidenced by the boiling points of the four molecules (crotonaldehyde: 374 K, butaldehyde: 348 K, crotyl alcohol: 395 K and butanol: 391 K). The higher boiling point of the two alcohols is a common indication of hydrogen bonding between the alcohol molecules. The increased boiling point is then also reflected in the higher desorption temperatures in TPD measurements, observed for the two alcohols compared to those of the aldehydes. Hence, we conclude the adsorption on the methyl group and subsequent nucleation effect to be due to the stronger hydrogen bonding of the alcohols compared to that of the aldehydes, where adsorption on the surface remains more favourable.

Part 3: Summary of the Co-adsorption of Crotonaldehyde and Related Molecules with S and Methyl Thiolate on Cu(111)

6.3.1 Summary

In the previous two parts of this chapter, we have presented results and discussion examining the adsorption of crotonaldehyde, butyraldehyde, crotyl alcohol and 1-butanol with both atomic sulfur and methyl thiolate on Cu(111). In this section we now propose a mechanism we propose to account for our observations and results. We also consider the catalytic observations of Hutchings.

In part 1, we showed the interaction of the four molecules with the clean Cu(111) surface. The mechanism for the adsorption of the four molecules is shown and discussed in part 1.

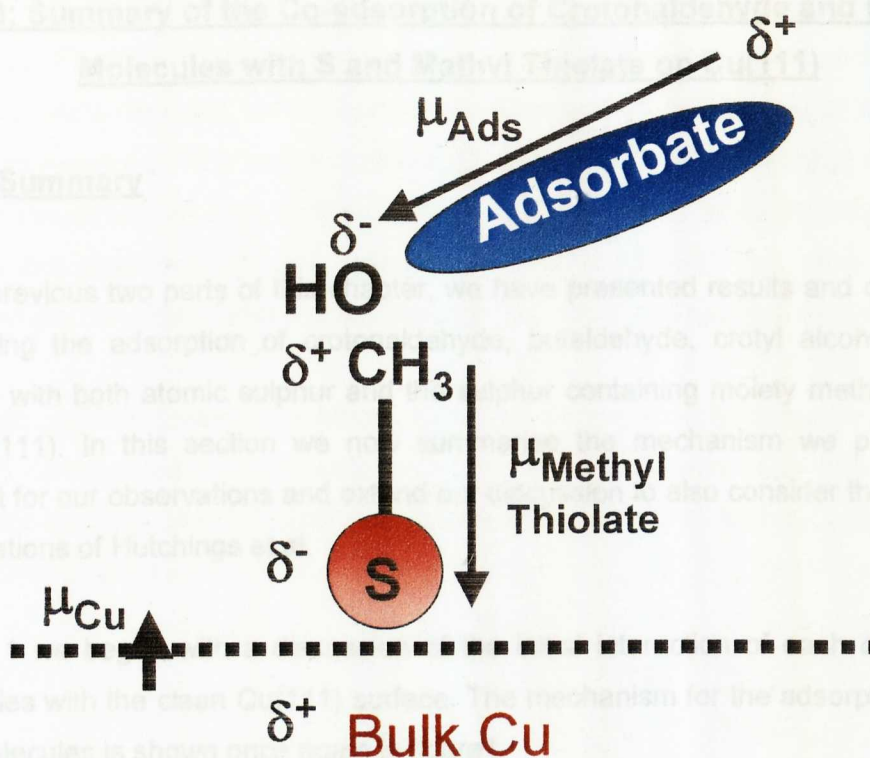


Figure 14. Diagram showing the interaction of crotyl alcohol and 1-butanol with co-adsorbed methyl thiolate on the Cu(111) surface.

Figure 1. Diagram showing the interaction of crotonaldehyde, butyraldehyde, crotyl alcohol and 1-butanol with the Cu(111) surface. μ_{Cu} and μ_{Ads} interact attractively.

We propose the observations we have made in the previous two sections can be explained fully using an electrostatic model. We begin by examining the interaction of each of the molecules with the clean surface in electrostatic terms. The molecular dipoles associated with each of the four molecules pointing along the molecule toward the surface interacts with the surface dipole associated with the copper. Both dipoles are anti-parallel and hence, this is a favourable interaction. The observation of no significant changes in UPS suggests no charge transfer effects in the adsorption process. Additionally, we observe both of the alcohol molecules to have higher temperatures of desorption than either of the aldehyde molecules. We

Part 3: Summary of the Co-adsorption of Crotonaldehyde and Related Molecules with S and Methyl Thiolate on Cu(111)

6.3.1 Summary

In the previous two parts of this chapter, we have presented results and discussion examining the adsorption of crotonaldehyde, butaldehyde, crotyl alcohol and 1-butanol with both atomic sulphur and the sulphur containing moiety methyl thiolate on Cu(111). In this section we now summarise the mechanism we propose to account for our observations and extend our discussion to also consider the catalytic observations of Hutchings et al.

In part 1 we began with a discussion of the initial interaction of each of the four molecules with the clean Cu(111) surface. The mechanism for the adsorption of the four molecules is shown once again in figure 1.

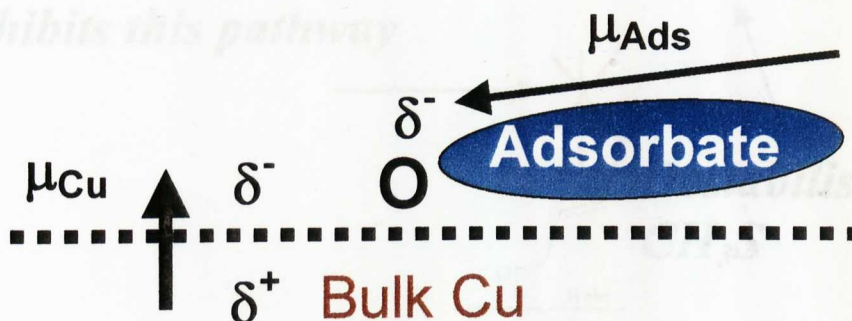


Figure 1. Diagram showing the interaction of crotonaldehyde, butaldehyde, crotyl alcohol and 1-butanol with the Cu(111) surface. μ_{Cu} and μ_{Ads} interact attractively.

We propose the observations we have made in the previous two sections can be explained fully using an electrostatic model. We begin by examining the interaction of each of the molecules with the clean surface in electrostatic terms. The molecular dipole associated with each of the four molecules pointing along the molecule toward the surface interacts with the surface dipole associated with the copper. Both dipoles are anti-parallel and hence, this is a favourable interaction. The observation of no significant changes in UPS suggests no charge transfer effects in the adsorption process. Additionally, we observe both of the alcohol molecules to have higher temperatures of desorption than either of the aldehyde molecules. We

attribute this to the effects of hydrogen bonding between the adsorbate alcohol molecules. Finally, we make a further important observation from the clean surface adsorption data. Namely, we observe a small amount of dissociation of both of the alcohol molecules in TPD measurements. During the desorption of crotyl alcohol we observe desorption of both crotonaldehyde and hydrogen, while for 1-butanol we observe the reaction products butanaldehyde and hydrogen. The small amounts observed are consistent with surface reactions at only more reactive defect sites.

If we now consider these observations alongside the work of Hutchings et al. we can begin to develop the reaction mechanism in figure 2 to rationalise the increased selectivity to crotyl alcohol observed during crotonaldehyde hydrogenation in the presence of sulphur.

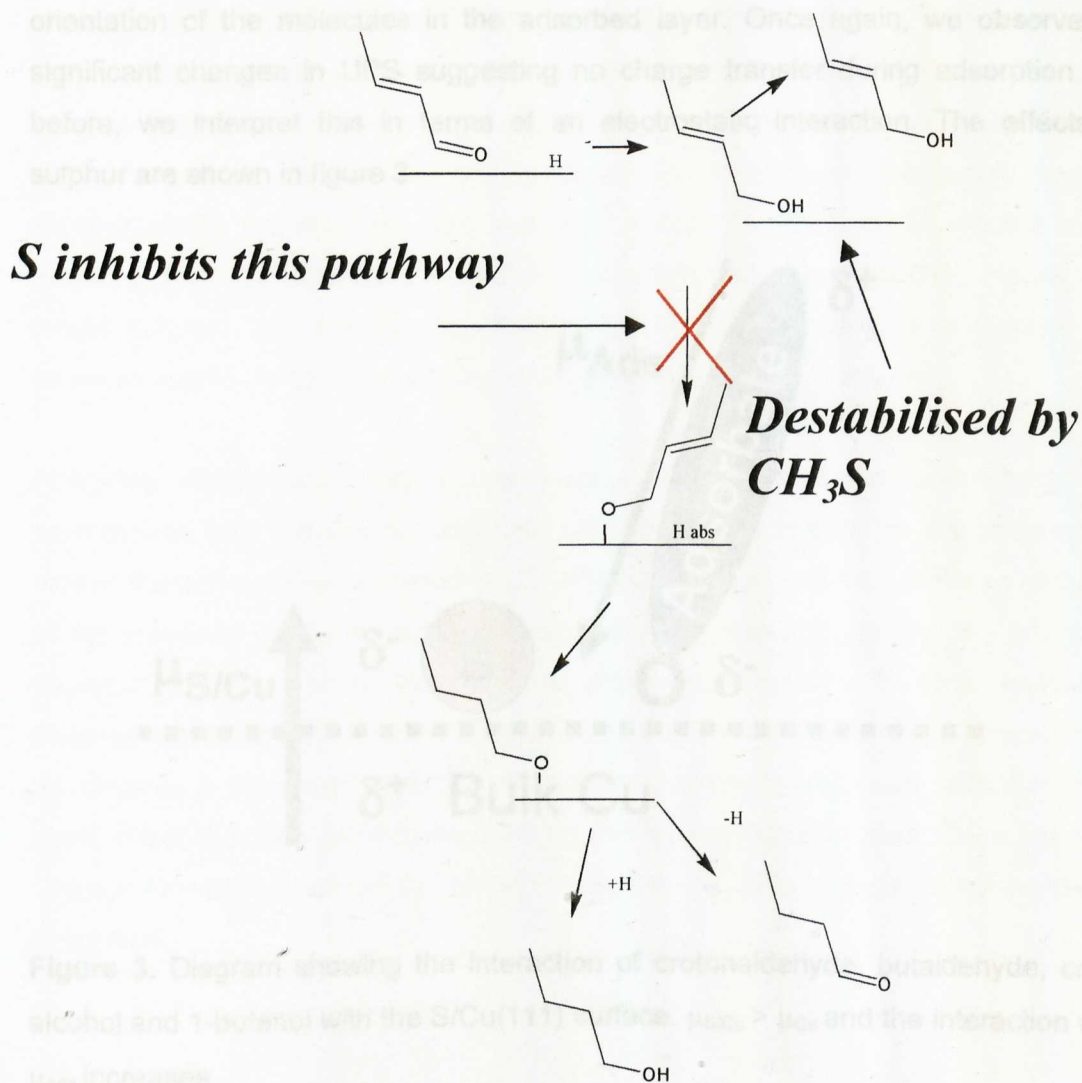


Figure 2. Proposed reaction mechanism for increased selectivity to crotyl alcohol formation during the hydrogenation of crotonaldehyde in the presence of sulphur.

We propose the results of the clean surface experiments may suggest that upon hydrogenation of crotonaldehyde to crotyl alcohol the adsorbed crotyl alcohol species can react further with the copper. In our own work this is suggested by the observed dissociation just described. The result of this is formation of alkoxy species, which then go on to form either 1-butanol or butaldehyde by addition or elimination of hydrogen.

If we now turn our attention to the adsorption of the four molecules of interest with atomic sulphur we observe significant effects on adsorption. In our TPD measurements we observe the adsorption of all four molecules to be stabilised in the presence of sulphur at any coverage. In addition to this we also observe significant increases in surface coverage suggesting significant changes to the orientation of the molecules in the adsorbed layer. Once again, we observe no significant changes in UPS suggesting no charge transfer during adsorption. As before, we interpret this in terms of an electrostatic interaction. The effects of sulphur are shown in figure 3.

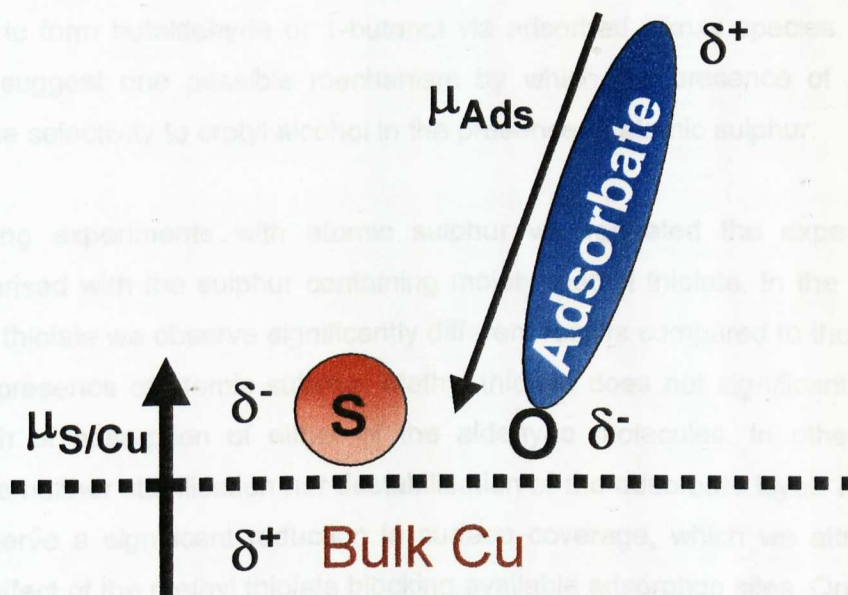


Figure 3. Diagram showing the interaction of crotonaldehyde, butaldehyde, crotyl alcohol and 1-butanol with the S/Cu(111) surface. $\mu_{S/Cu} > \mu_{Cu}$ and the interaction with μ_{Ads} increases.

From our work function measurements in chapter 5 we know that the presence of atomic sulphur results in an increase in magnitude of the surface dipole. We

propose this results in an increased magnitude of interaction with the anti-parallel dipole associated with each of our four molecules. In addition to this we believe the orientation changes we observe in TPD and UPS would also enhance the interaction with the surface by maximising the interaction of the two dipoles. In our TPD data we observe the largest effects of sulphur to be observed during co-adsorption of crotonaldehyde with atomic sulphur, closely followed by butaldehyde. We believe this is observed because of the larger magnitude of the dipole moment associated with the aldehyde molecules. In terms of our reaction mechanism in figure 2, this observation is important. This shows that in the presence of atomic sulphur we would expect our reactant, crotonaldehyde, to be more stabilised than that of the products. Additionally, with relevance to the hydrogenation scheme proposed in figure 2 we make a final observation. In the presence of atomic sulphur we observe the dissociation of both crotyl alcohol and 1-butanol to be inhibited. Again, this would be consistent with dissociation only taking place at the more reactive defect sites of the surface and may indicate site blocking of these sites by sulphur. However, in terms of the hydrogenation mechanism, this would suggest sulphur blocks the reaction path described earlier by which crotyl alcohol reacts further to form butaldehyde or 1-butanol via adsorbed alkoxy species. Hence, this would suggest one possible mechanism by which the presence of sulphur can increase selectivity to crotyl alcohol in the presence of atomic sulphur.

Following experiments with atomic sulphur we repeated the experiments just summarised with the sulphur containing moiety methyl thiolate. In the presence of methyl thiolate we observe significantly different results compared to those recorded in the presence of atomic sulphur. Methyl thiolate does not significantly affect the strength of adsorption of either of the aldehyde molecules. In other words we observe neither stabilisation nor destabilisation of the adsorbate layer. However, we do observe a significant reduction in surface coverage, which we attribute to the steric effect of the methyl thiolate blocking available adsorption sites. Once again we use our electrostatic model to interpret these results. This is depicted schematically in figure 4.

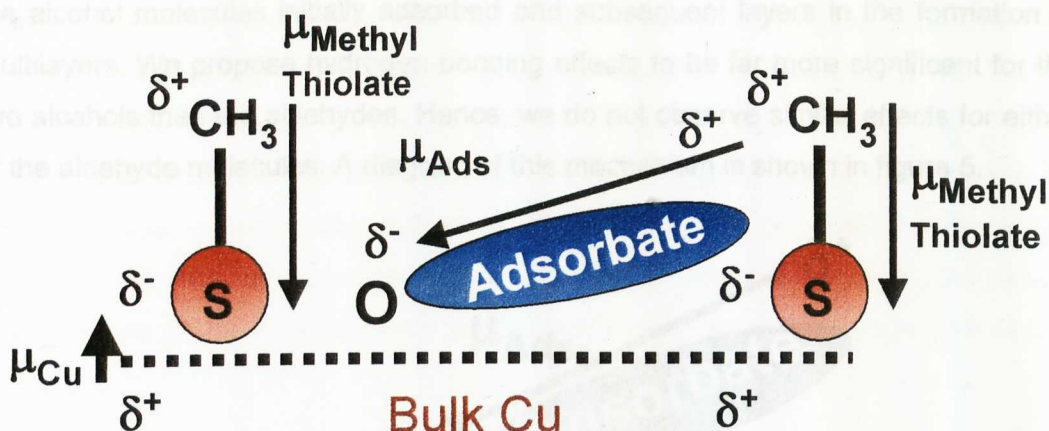


Figure 4. Diagram showing the interaction of crotonaldehyde and butaldehyde with co-adsorbed methyl thiolate on the Cu(111) surface.

Our work function measurements in chapter 5 show that the adsorption of methyl thiolate on the surface has the opposite effect on work function to that of atomic sulphur. Instead of increasing the magnitude of the surface dipole, methyl thiolate causes a reduction in surface dipole due to the dipole of the molecule being in a direction anti-parallel to that of the surface dipole. While this dipole is anti-parallel to that of the surface, it will be in an overall parallel direction to that of the four molecules of interest. This would therefore be an unfavourable interaction. Hence, this would clearly account for the fact that we observe no stabilisation of either of the aldehydes in the presence of methyl thiolate. Each of the aldehyde molecules adsorbs on the copper surface between methyl thiolate molecules, most probably returning to an orientation significantly inclined away from the surface normal, to reduce the effects of the two parallel dipoles. Hence, in terms of our catalytic mechanism we do not expect the presence of methyl thiolate to have a significant effect on the adsorption of the reactant molecule, crotonaldehyde.

The effect of methyl thiolate on the adsorption of the two alcohols is significantly different, although we believe can still be interpreted by use of an electrostatic mechanism. Upon adsorption of either of the alcohols with pre-adsorbed methyl thiolate we observed the almost complete destabilisation of the chemisorbed layer. We believe we can account for this observation by considering the effects of hydrogen bonding. Previous work has supported the possibility of $\text{C-H}\cdots\text{O}$ hydrogen bonds and we propose this mechanism results in preferential adsorption of the alcohol molecules on the methyl group of the methyl thiolate. The effects of hydrogen bonding then play a further role, resulting in a nucleation effect between

the alcohol molecules initially adsorbed and subsequent layers in the formation of multilayers. We propose hydrogen-bonding effects to be far more significant for the two alcohols than the aldehydes. Hence, we do not observe similar effects for either of the aldehyde molecules. A diagram of this mechanism is shown in figure 5.

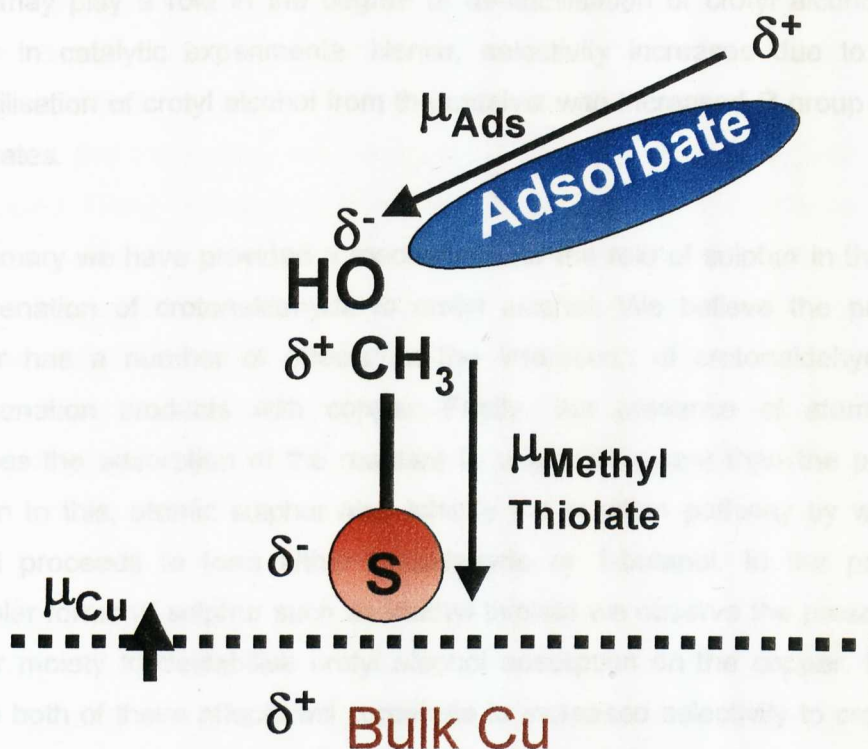


Figure 5. Diagram showing the interaction of crotyl alcohol and 1-butanol with co-adsorbed methyl thiolate on the Cu(111) surface.

The results of these observations are significant with respect to our proposed catalytic model, particularly as the effect of methyl thiolate on the adsorption of the two alcohols is significantly greater than any of the effects described previously. We believe that these observations suggest that the presence of methyl thiolate on a copper catalyst would induce destabilisation of crotyl alcohol from the catalyst, as indicated in figure 2. However, as described already, methyl thiolate would not produce a similar effect on crotonaldehyde. Hence, once again, we would observe the reactant to remain significantly more stable than the product of interest, crotyl alcohol. The destabilisation of crotyl alcohol from the catalyst would then prevent further reactions taking place and therefore formation of either butaldehyde or 1-butanol. Hence, increasing selectivity during hydrogenation of crotonaldehyde towards crotyl alcohol. In addition to this, our observations agree with Hutchings further in that the effects of methyl thiolate in our experiments are significantly

greater than any of the effects that we observe in the presence of atomic sulphur. In their work they observe selectivity to crotyl alcohol to increase in the order $CS_2 \sim SO_2 < DMS \sim \text{thiophane} \sim DMSO < \text{thiophene}$. Hence, we believe our own observations combined with the catalytic work may suggest that the size of the R group may play a role in the degree of destabilisation of crotyl alcohol from the copper in catalytic experiments. Hence, selectivity increases due to increased destabilisation of crotyl alcohol from the catalyst with increased R group size of co-adsorbates.

In summary we have provided a mechanism for the role of sulphur in the selective hydrogenation of crotonaldehyde to crotyl alcohol. We believe the presence of sulphur has a number of effects on the interaction of crotonaldehyde and its hydrogenation products with copper. Firstly, the presence of atomic sulphur stabilises the adsorption of the reactant to a greater extent than the products. In addition to this, atomic sulphur also inhibits the reaction pathway by which crotyl alcohol proceeds to form either butaldehyde or 1-butanol. In the presence of molecular forms of sulphur such as methyl thiolate we observe the presence of the sulphur moiety to destabilise crotyl alcohol adsorption on the copper. Hence, we believe both of these effects will contribute to increased selectivity to crotyl alcohol during hydrogenation. Finally, we have shown that the underlying mechanisms for both our surface science observations and most likely the analogous catalytic experiments are electrostatic in nature and can be explained by consideration of the effects of surface/molecular dipole mechanisms and hydrogen bonding effects.

From the results obtained in this study, we believe we have shown surface science can be used to rationalise catalytic observations, and in particular be useful in studying the underlying mechanisms involved in surface reactions. However, we accept that the catalytic process is clearly more complicated than just the mechanism proposed here. Further insight into the process would be useful, such as performing additional studies on other faces of copper surfaces and investigating the effects of other forms of sulphur such as thiophene in an attempt to gain a more complete picture of the catalytic process.

6.3.2 Conclusions

Contrasting the usual view of sulphur as an archetypal catalyst poison, we have demonstrated the promotional effects of sulphur on the Cu(111) surface. Using

surface science techniques to model the hydrogenation of crotonaldehyde on copper in the presence of sulphur, we have demonstrated that the presence of the electronegative adsorbate results in the stabilisation of crotonaldehyde, butaldehyde, crotyl alcohol and 1-butanol on the Cu(111) surface. Additionally, we observe the presence of sulphur to inhibit the dissociation of crotyl alcohol and 1-butanol. The effects of the sulphur containing moiety methyl thiolate are even more pronounced. While we observe no significant changes to the stability of adsorption of either of the aldehydes, the adsorption of both alcohols is almost completely destabilised. Using our observations made here using surface science techniques and making comparisons with catalytic studies we show that the interaction of each of the molecules with copper in the presence of sulphur can be fully described using an electrostatic model. This model accounts for both our own observations here and can be developed to form a reaction mechanism to explain the increased selectivity to crotyl alcohol observed during crotonaldehyde hydrogenation in the presence of sulphur.

6.3.3 References

- [1] G.J. Hutchings, F. King, I.P. Okoye, M.P. Padley and C.H. Rochester, *J. of Catal.* 148 (1994) 464
- [2] G.J. Hutchings, F. King, I.P. Okoye, M.B. Padley, C.H. Rochester, *J. of Catal.* 148 (1994) 453
- [3] J.E. Bailie and G.J. Hutchings, *J. of Mol. Catal A: Chemical* 177 (2002) 209
- [4] J.E. Bailie, H.A. Abdullah, J.A. Anderson, N.V. Richardson, N. Hodge, J.G. Zhang, A. Burrows, C.J. Kiely and G.J. Hutchings *Phys. Chem. Chem. Phys.* 3 (201) 4113
- [5] D.S. Newsome, *Catalysis Rev.-Sci. Eng.* 21 (1980) 275
- [6] C.T. Campbell and B.E. Koel, *Surf. Sci.* 183 (1987) 100
- [7] F. Coloma, B. Bachiller-Baeza, C.H. Rochester and J.A. Anderson, *Phys. Chem. Chem. Phys.* 3 (2001) 4817
- [8] D.I. Jerdev, A. Olivas and B.E. Koel, *J. of Catal.* 208 (2002) 278
- [9] J.C. de Jesus and F. Zaera, *Surf. Sci.* 430 (1999) 99
- [10] E. Janin, S. Ringler, J. Weissenrieder, T. Akermark, U.O. Karlsson, M. Göthelid, D. Nordlund, H. Ogasawara, *Surf. Sci.* 482 (2001) 83
- [11] R. Zhang and A. J. Gellman, *J. Phys. Chem.* 95 (1991) 7433
- [12] Q. Dai and A.J. Gellman, *Surf. Sci.* 257 (1991) 103

- [13] R. Linke, C. Becker, Th. Pelster, M Tanemura, K. Wandelt, *Surf. Sci.* 377-379 (1997) 655
- [14] S. Turton, R.G. Jones, *Surf. Sci* 344-379 (1997) 719
- [15] G.W. Watson, R.P.K. Wells, D.J. Willock, G.J. Hutchings, *Surf. Sci.* 459 (2000) 93
- [16] R. Kleyana, D. Borgmann, G. Wedler, *Surf. Sci* 402-404 (1998) 131
- [17] A. Valcárcel, J.M. Ricart, A. Clotet, A. Markpvits, C. Minot, F. Illas, *Surf. Sci.* 519 (2002) 250
- [18] B.A. Sexton and A.E. Hughes, *Surf. Sci.* 140 (1984) 227
- [19] K. Prabhakaran and C.N.R. Rao, *Appl. Surf. Sci.* 44 (1990) 205
- [20] B.A. Sexton and A.E. Hughes, *Surf. Sci.* 140 (1984) 227
- [21] J.N. Russell, S.M. Gates and J.T. Yates Jr, *Surf. Sci.* 163 (1985) 516
- [22] S.M. Gates, J.N. Russell and J.T. Yates Jr, *Surf. Sci.* 159 (1985) 233
- [23] M.A. Chesters, E.M. McCash, *Spectrochim. Acta* 43A (1987) 1625
- [24] I.E. Wachs and R.J. Madix, *J. Catal.* 53 (1978) 208
- [25] M. Bowker and R.J. Madix, *Surf. Sci.* 95 (1980) 190
- [26] B.A. Sexton, A.E. Hughes and N.R. Avery, *Surf. Sci.* 155 (1985) 366
- [27] A. Peremans, F. Maseri, J. Darville and J.-M. Gilles, *J Vac. Sci. Technol. A* 8 (1990) 3224
- [28] J.R.B. Gomes and J.A.N.F. Gomes, *Surf. Sci.* 471 (2001) 59
- [29] S.M. Johnston, A. Mulligan, V. Dhanak and M. Kadodwala, *Surf. Sci.* 530 (2003) 111
- [30] L. Hongbing, R. J. Hamers, *Surf. Sci.* 416 (1998) 354
- [31] S.A. Tan, R.B. Grant and R.M. Lambert, *J. of Catal.* 106 (1987) 54
- [32] J.R. Lomas, C.J. Baddeley, M.S. Tikhov, R.M. Lambert, *Langmuir* 11 (1995) 3048
- [33] J.R. Lomas and G. Pacchioni, *Surf. Sci.* 365 (1996) 297
- [34] J.A. Rodriguez and J. Hrbek, *Acc. Chem. Res.* 32 (9) (1999) 719
- [35] C.M. Mate, C-T. Kao and G.A. Somojai, *Surf. Sci.* 206 (1988) 145
- [36] G. Rousseau, PhD Thesis 2003
- [37] D. Syomin and B.E. Koel, *Surf. Sci* 498 (2002) 53
- [38] J.R.B. Gomes, J.A.N.F. Gomes and F. Illias, *J. Mol. Catal.* 170 (2001) 187
- [39] *Handbook of Chemistry and Physics, 1913-1995*, CRC Press
- [40] A. Ferral, P. Paredes-Olivera, V.A. Macagno, and E.M. Patrino, *Surf. Sci.* 525 (2003) 85
- [41] R. Taylor, O. Kennard, *J. Am. Chem. Soc.* 104 (19) (1982) 5063
- [42] F.H. Allen, W. D. S. Motherwell, *Acta. Cryst.* B58 (2002) 407

Chapter 7: Growth of Nanoscale Aluminium Oxide Films on NiAl(110)

7.1 Introduction

The formation of thin oxide films is of a great deal of interest to a wide scientific community due to their important role in a number of fields and applications, ranging from microelectronics to anti-corrosion and coating technologies. In particular, Al_2O_3 is of interest as a possible wide gap insulating material for potential use in nano-electronic devices such as a metal-insulator-metal (M-I-M) electron emitter and in the field of heterogeneous catalysis where it is used commonly as a support material. With this in mind, it is clear why aluminium oxide films have been the subject of extensive study.

From a surface science standpoint the study of Al_2O_3 films can pose a problem. The intrinsically insulating nature of Al_2O_3 films makes them difficult to study with traditional surface science electron spectroscopic techniques. For this reason it is desirable to create a film on a metal support. Although thin films are known to form on Al single crystal surfaces, they have been found to form amorphous oxide layers without a well-ordered geometric structure [1]. However, NiAl(110) has been shown to form well-ordered Al_2O_3 layers, which can be formed by oxidation and annealing of the NiAl(110) crystal. This preparation method has been used extensively in the study of thin aluminium oxide films and particularly in the preparation of films for use as mimics of the Al_2O_3 support material used commonly in heterogeneous catalysis.

In this chapter we report the results of using Al2p photoemission to study for the first time, the entire oxidation process from initial oxygen adsorption on NiAl(110) to the effects of multiple oxidation and annealing cycles. We show that oxidation at room temperature results in the formation of a predominately amorphous aluminium oxide film and a small γ -like Al_2O_3 component. However, oxidation at elevated temperatures results in formation of a γ -like Al_2O_3 film. Annealing of this layer to 1273 K results in significant changes to the structure, with formation of an α -like Al_2O_3 film. This layer is not homogeneous, however, and contains a significant metallic component, therefore making it unsuitable for use as a mimic of catalytic support material or as an insulating material in electronic devices. Further to this work we also show that during multiple oxidation and annealing cycles the layer retains α -like Al_2O_3 character, but that the amount of aluminium in the layer

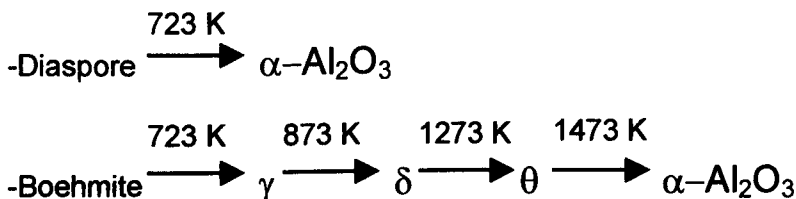
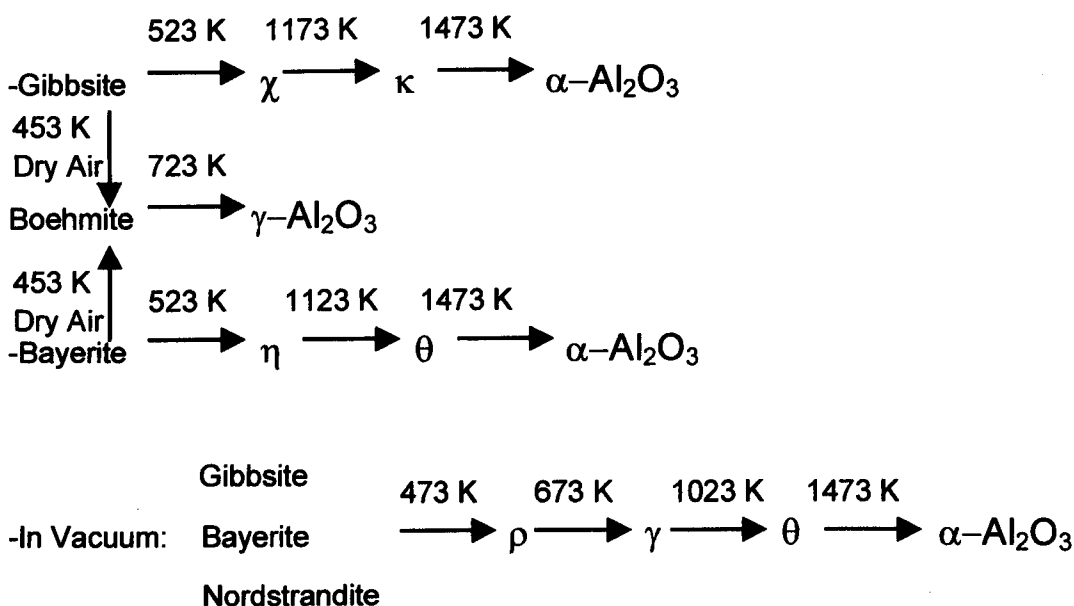
increases with each cycle. This is consistent with the filling of Al^{3+} vacancies in the oxide layer and provides an explanation for LEED observations made previously, which have suggested improved oxide crystallinity with increased oxidation and annealing cycles. However, despite this, the layer continues to retain a significant metallic aluminium component and is therefore non-homogeneous.

The clean NiAl(110) bulk crystal has a CsCl structure but is unique to the other faces of NiAl in that there are equal amounts of both Ni and Al at the surface. In addition, the surface exhibits a rippled effect with the Al atoms displaced by around 0.22 Å from the bulk crystal. Finally, the surface is unusual in that both theory and experiment have shown the termination of the bulk NiAl at the (110) surface results in surface states, which have been suggested may be important in the oxidation process, although this has never been explored [2-4].

The initial oxidation of NiAl(110) has previously been studied by both experimental and theoretical methods. Isern and Castro [5] have used both LEED and AES to study the adsorption and initial oxidation of NiAl at room temperature. They conclude that oxygen adsorption takes place in two stages. Firstly, a constant adsorption rate up to an exposure of 15L followed by a second stage with a slightly decreased adsorption rate up to 90L. Above this exposure oxygen uptake increases slowly until saturation above an exposure of 300L. The authors propose their observations can be explained by initial adsorption of a chemisorbed phase at low exposures followed by a subsurface phase at higher exposures. Oxygen uptake then stops after formation of an Al_2O_3 layer that prevents further oxygen transport into the bulk. No ordered structures are observed by LEED during oxygen adsorption.

In addition to the experimental work of Isern and co-worker, the initial stages of oxidation have been probed by Lozovoi et al. by the application of ab initio-density functional calculations [6,7]. From the results, the authors conclude that the overall driving force for stability of the layer during initial oxidation is the expulsion of Ni. This is achieved by the introduction of point defects at the surface in the form of Al antisites and Ni vacancies, to such a degree that the authors suggest the possibility of the surface being coated by an aluminium layer formed by the Ni depletion at oxygen pressures above that required for dissociation of the NiAl.

The formation of well-ordered crystalline Al_2O_3 oxide films by adsorption and subsequent annealing cycles has received even more attention than the initial oxidation stage with a wide variety of techniques utilised in the process. One of the earliest studies of this system was performed by Jaeger et al. [8] using LEED, EELS, XPS and ARUPS. This study was performed on the oxide layer formed after one cycle of oxygen adsorption followed by annealing. The authors concluded the formation of a well-ordered Al_2O_3 layer by the observation of a well-ordered LEED pattern. Furthermore, they suggest the thickness of the film to be 5 Å, in agreement with a number of other studies, and that the film covers the entire crystal surface, which they conclude due to the inertness of the film to molecular adsorption and additionally due to the results of a STM study [9]. However, in a LEEM study performed by McCarty [10], he showed the presence of un-oxidised portions of NiAl that he attributed to "pin holes" in the oxide layer. In addition to the question of oxide layer homogeneity the actual structure of the aluminium oxide formed also raises some controversy. A number of studies have tended towards assignment of the oxide as being either $\gamma\text{-Al}_2\text{O}_3$ or $\alpha\text{-Al}_2\text{O}_3$ [8,9,11], but more recent work using X-ray diffraction [12] has complicated this issue still further by suggesting a $\kappa\text{-Al}_2\text{O}_3$ layer may be formed. Hence, at this point in time no definitive assignment has been made due to a number of difficulties encountered in assigning the structure of thin film oxide layers formed during the oxidation and annealing process. Firstly, the characterisation of bulk aluminium oxides, from which the thin film structures are determined, are themselves complicated and in some instances not fully understood either. This is understandable given the vast number of aluminium oxide phases that exist and the subtle differences between them. This is illustrated in table 1, which shows the dehydration sequences of some important bulk aluminium hydroxides.

Oxide Hydroxides**Trihydroxides****Table 1.** Dehydration sequences of some important aluminium hydroxides [13-16].

Often the differences between these different phases amount to no more than small variations in octahedral/tetrahedral cation occupation. For instance, the three phases suggested in the literature to be most relevant to this study, $\gamma\text{-Al}_2\text{O}_3$, $\alpha\text{-Al}_2\text{O}_3$ and $\kappa\text{-Al}_2\text{O}_3$ differ as follows: All three structures are based on a hexagonal closely packed array of oxygen atoms with Al^{3+} cations occupying different octahedral and tetrahedral sites in each structure. $\alpha\text{-Al}_2\text{O}_3$ contains only octahedral co-ordinated Al with 2/3 occupation. $\gamma\text{-Al}_2\text{O}_3$ contains both tetrahedral and octahedral Al in the ratio of 3:1 and $\kappa\text{-Al}_2\text{O}_3$ also contains both but in the ratio of 1:1. In addition to these three examples there are obviously many more phases with only minor differences as is shown in table 1. To add to the already complicated nature of this topic, there are further problems encountered when studying thin films. In addition to the many

possible phases that can be formed on a surface, they are particularly difficult to relate back to bulk aluminium oxide structures due to both differences between thin film structures and their bulk counterparts [17] and also due to unreleased strain in thin films [18]. For these reasons, a great deal of ambiguity exists in the assignment of thin film aluminium oxide phases

In an extension of the work carried out by Jaeger and co-workers, Yoshitake et al. have performed two studies examining the effects of both oxygen pressure and sample temperature during the oxidation of NiAl [19,20]. Using LEED and AES they concluded that the crystallinity of the oxide film was improved by introduction of oxygen at lower dosing pressures and at sample temperatures of between 620-670 K. In addition, the authors studied the effects of multiple oxidation cycles. With increasing numbers of oxidation cycles, LEED shows the spots associated with NiAl weakening while the spots characteristic of the Al_2O_3 layer become stronger, suggesting an increase in the thickness of the oxide layer. Using AES, the authors suggest the average maximum thickness of the film to be 13-14 Å. However, they believe the film to be non-homogeneous when its thickness exceeds 5 Å.

In the following sections we now present our own results examining the oxidation of NiAl(110) from the initial stages through to the effects of multiple oxidation and annealing cycles, monitored using Al2p photoemission.

7.2 Results

7.2.1 Room Temperature Adsorption

Figure 1a shows Al2p spectra recorded during increasing exposures of the NiAl(110) surface to oxygen at room temperature. In addition to the recorded spectra we also present the results of fitting each of the spectra. With the exception of the components of the spectra associated with the clean surface (the metallic component), we have fitted each Al2p component to a single Gaussian function rather than to each spin-orbit component. This serves in the first instance to simplify the fitting procedure somewhat but additionally allows for the effects of broadening mechanisms, as discussed by McConville et al. in their work on Al(111). The clean NiAl(110) spectrum in figure 1a is consistent with previous studies and is characterised by two peaks at 73.2 and 73.6 eV corresponding to the $\text{Al}2p_{3/2}$ and

Al $2p_{1/2}$ states respectively. The two spin-orbit components are split by 0.4 eV and are in the expected ratio of 1:2. Upon initial oxidation of the surface we observe the appearance of the first of three fitted peaks which we have identified at higher binding energies than those associated with the clean NiAl. This section of the spectra has been labelled non-metallic and is associated with the aluminium component related to oxide growth. This feature persists throughout increasing oxidation but shifts from its initial position of 74.2 eV in the 1L spectrum to a clear peak at 74.5 eV in the higher coverage spectra. In addition to this feature we also observe the growth of a second feature at exposures of 11L and above. This second peak is observed at a position of 75.7 eV and its position remains unchanged with increasing exposure. Finally, we observe a third fitted peak associated with the oxide. This is observed initially in the 51L spectrum and grows with increasing oxygen exposure. The position of the peak remains constant throughout at a binding energy of 76.4 eV. Concurrently with the growth of the three non-metallic features we also observe a reduction in the size of the metallic component of the spectra, suggesting a layer forming over the entire surface. A summary of all the components identified by peak fitting is given in table 2. At this point, we will adopt the labels of chemisorbed, tetrahedral and octahedral for the three non-metallic aluminium states we have identified at 74.2-74.5, 75.7 and 76.4 eV respectively. These are based on the assignment of three types of aluminium in the layer. Firstly, aluminium associated with chemisorbed oxygen. Secondly, aluminium associated with oxide formation occupying tetrahedral sites and finally, aluminium with octahedral coordination in the oxide layer. We will discuss the basis of these assignments fully in the discussion section after presentation of all our data. However, we feel adopting these labels at this point will aid clarity and we will use them throughout the rest of this chapter for consistency.

Chemical State	Position [eV]
Metallic Al $2p_{3/2}$	73.2
Metallic Al $2p_{1/2}$	73.6
Chemisorbed	74.2 -74.5 (with increasing coverage)
Tetrahedral	75.7
Octahedral	76.4

Table 2. Chemical states and corresponding positions identified in figure 1a.

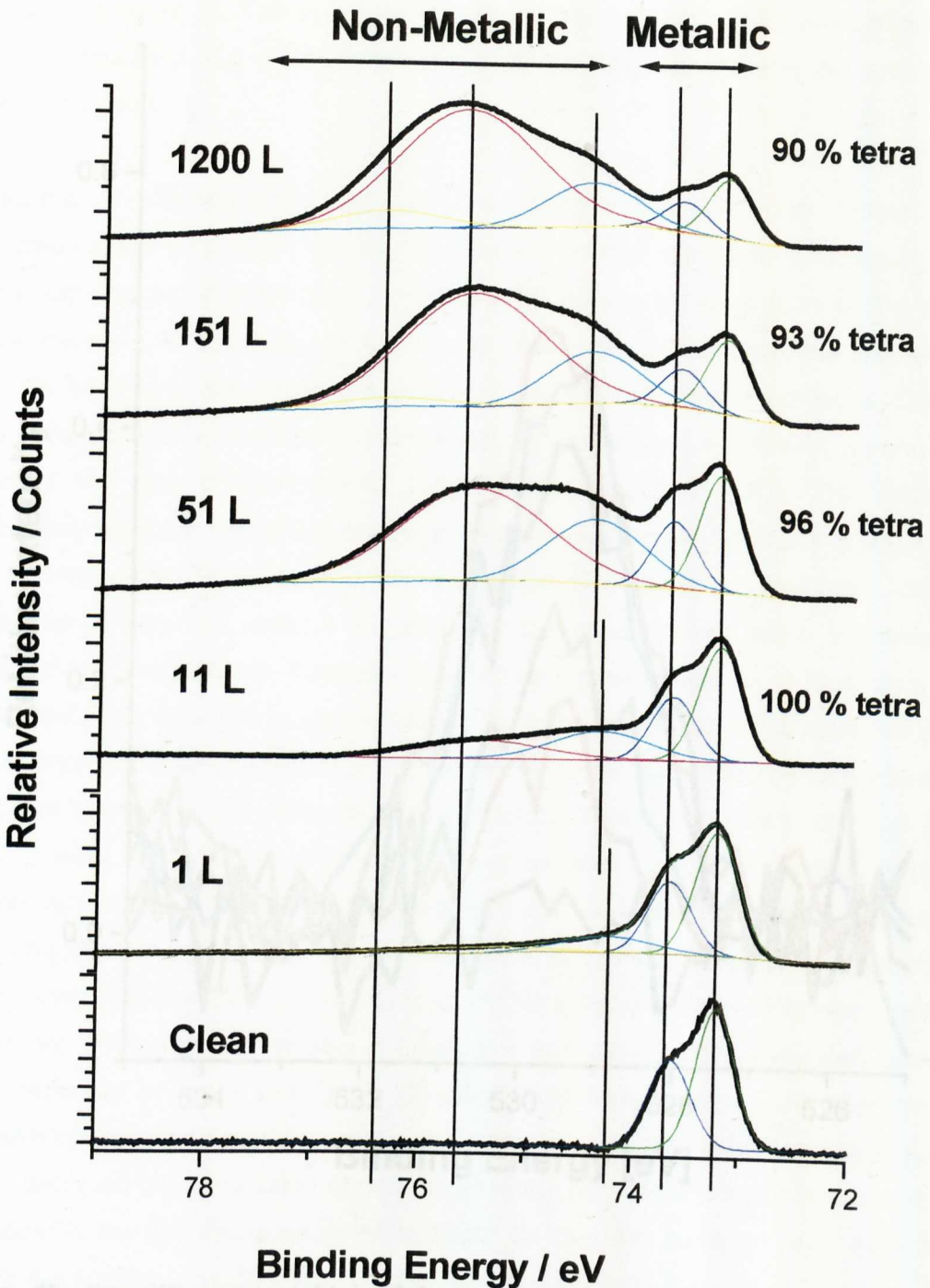


Figure 1a. Al₂p XPS spectra obtained from surfaces which had been dosed with sequentially higher exposures (Clean NiAl(110), 1L, 11L, 51L, 151L, 1200L) at ca. 300 K along with the associated fits are displayed. All spectra were collected with $h\nu = 120$ eV. Vertical lines have been added to aid the eye and metallic and non-metallic areas of the spectra have been identified for clarity. The relative tetrahedral occupation of the oxide layer is also shown for reference.

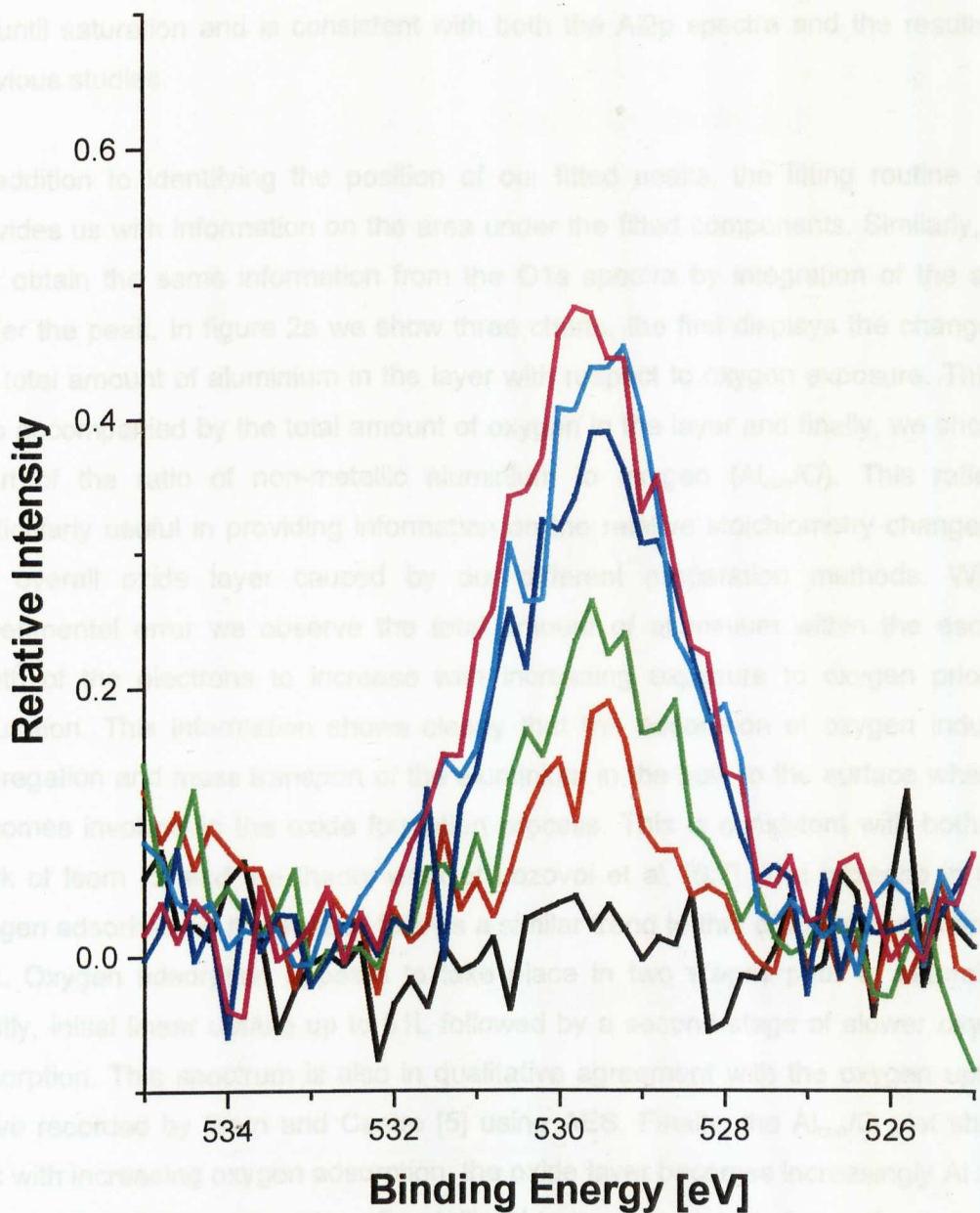


Figure 1b. O1s XP spectra obtained from surfaces which had been dosed with sequentially higher exposures (Clean NiAl(110) (black), 1 (red), 11 (green), 51 (blue), 151 (cyan), 1200 (magenta) L) at ca. 300 K are displayed. All spectra were collected with $h\nu = 1256.6$ eV.

Figure 1b shows the corresponding O1s spectra associated with the Al2p spectra displayed in figure 1a. This shows increasing oxygen adsorption with each exposure up until saturation and is consistent with both the Al2p spectra and the results of previous studies.

In addition to identifying the position of our fitted peaks, the fitting routine also provides us with information on the area under the fitted components. Similarly, we can obtain the same information from the O1s spectra by integration of the area under the peak. In figure 2a we show three charts, the first displays the change in the total amount of aluminium in the layer with respect to oxygen exposure. This is also accompanied by the total amount of oxygen in the layer and finally, we show a chart of the ratio of non-metallic aluminium to oxygen (Al_{non}/O). This ratio is particularly useful in providing information on the relative stoichiometry changes in the overall oxide layer caused by our different preparation methods. Within experimental error we observe the total amount of aluminium within the escape depth of the electrons to increase with increasing exposure to oxygen prior to saturation. This information shows clearly that the adsorption of oxygen induces segregation and mass transport of the aluminium in the bulk to the surface where it becomes involved in the oxide formation process. This is consistent with both the work of Isern [5] and the theory work of Lozovoi et al. [6,7]. The increase in total oxygen adsorbed on the surface follows a similar trend to that of the total aluminium plot. Oxygen adsorption appears to take place in two stages prior to saturation. Firstly, initial linear uptake up to 51L followed by a second stage of slower oxygen adsorption. This spectrum is also in qualitative agreement with the oxygen uptake curve recorded by Isern and Castro [5] using AES. Finally, the Al_{non}/O plot shows that with increasing oxygen adsorption, the oxide layer becomes increasingly Al rich, in line with both the conversion of metallic Al to the non-metallic form, shown by the reduction in the metallic component in figure 1a, and the transport of Al from the bulk to the surface. The final Al_{non}/O ratio upon saturation is 4.33.

Figure 2b shows the area of each of our three fitted peaks identified in figure 1a (chemisorbed, tetrahedral oxide and octahedral oxide) with respect to oxygen exposure.

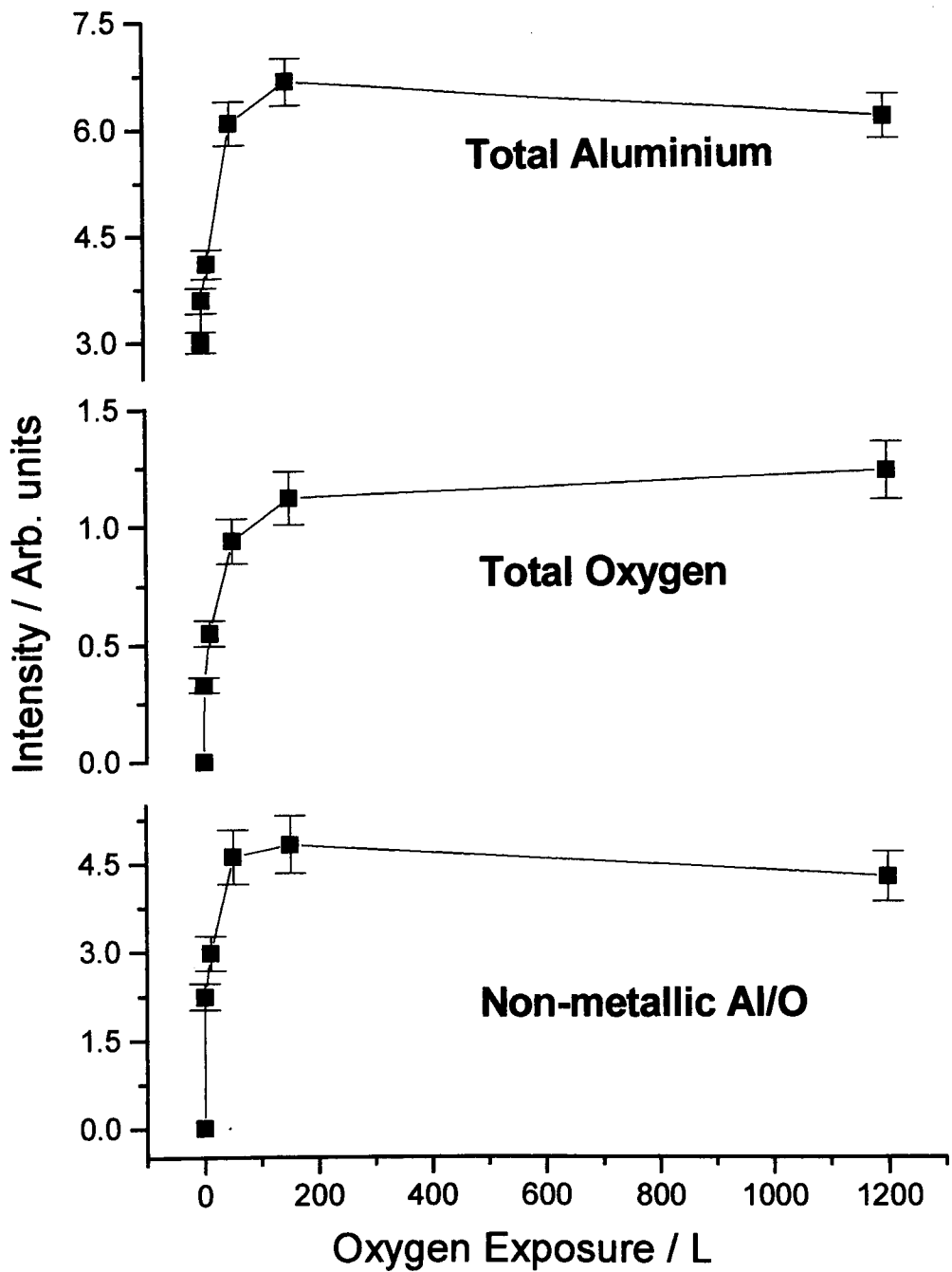


Figure 2a. Total aluminium intensity from figure 1a. Total oxygen intensity from figure 1b and ratio of non-metallic aluminium to oxygen plotted against oxygen exposure.

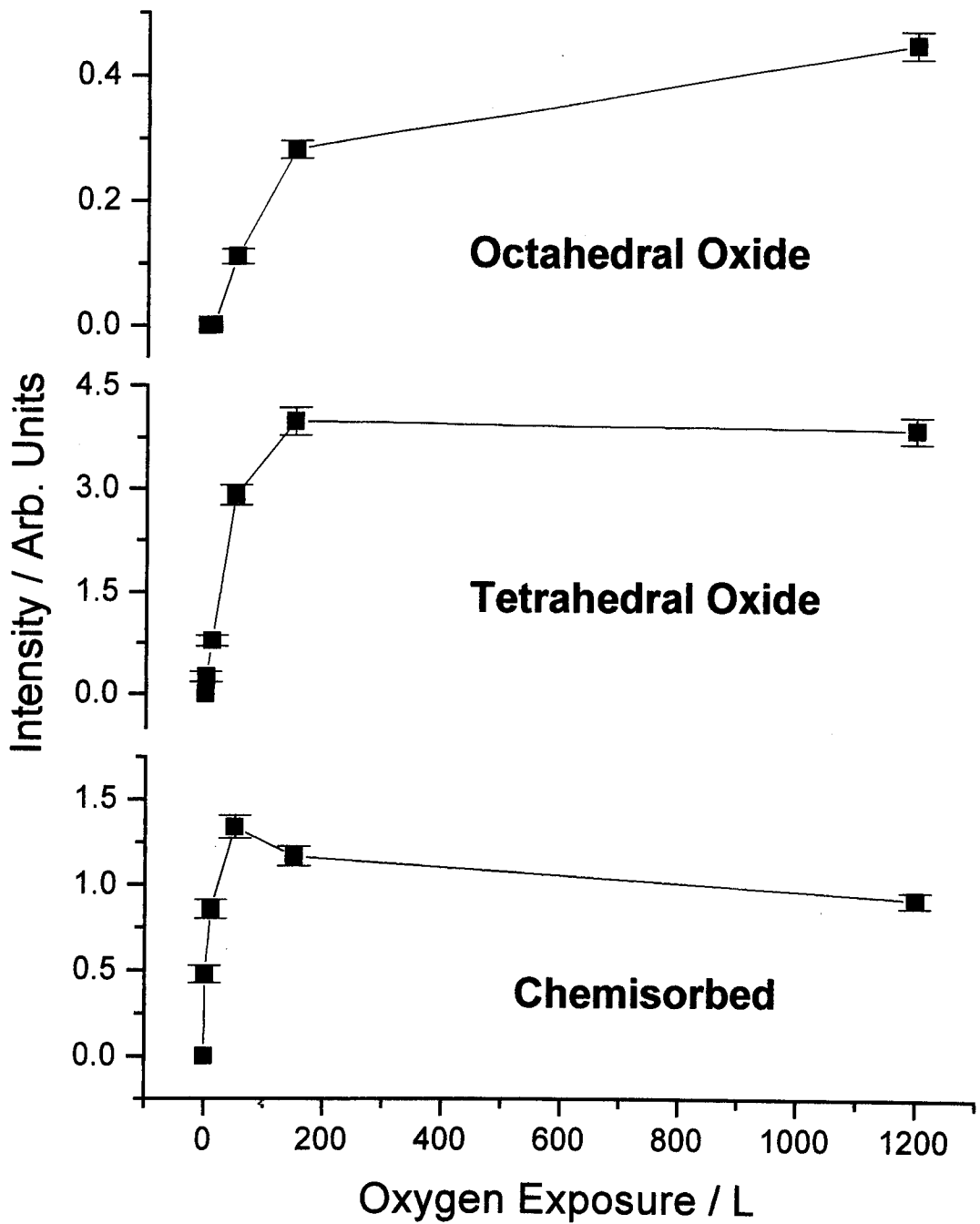


Figure 2b. Chemisorbed, tetrahedral oxide and octahedral oxide intensity from figure 1a plotted against oxygen exposure.

The three plots in figure 2b show initial oxidation begins with aluminium co-ordinated to chemisorbed oxygen. At 11L oxidation then proceeds with oxide formation involving aluminium with tetrahedral co-ordination and finally, the octahedral state develops from exposures above 51L. This information is clear in figure 1a. However, figure 2b shows a number of pieces of information more clearly than by consideration of the Al2p spectra alone. Growth of the chemisorbed phase continues from initial oxidation up to a maximum at 51L. For the two exposures recorded above this we then observe a small reduction in the amount of chemisorbed material on the surface. In the case of the tetrahedral phase we observe a slightly different trend. In this case, occupation of the tetrahedral state increases with increasing oxygen exposure from 11L up to saturation at 151L. Oxygen exposures above this amount result in no change in the amount of the tetrahedral phase on the surface within experimental error. Turning to the octahedral phase we can see a distinctly different trend from that of the other two plots. The octahedral state appears initially upon exposure to 51L of oxygen. This state then continues to increase up to 1200L oxygen exposure. From these observations we have two important pieces of information. The observation of a decrease in chemisorbed state while the octahedral state continues to increase may suggest some degree of conversion from the chemisorbed state to the octahedral aluminium form. Additionally, it is interesting to note that the beginning of octahedral oxide formation coincides with the point at which the overall rate of oxide formation slows, as indicated in figure 2a. This information suggests that octahedral oxide formation is more difficult than formation of either the chemisorbed or tetrahedral states, and may possibly be limited by diffusion through the already formed chemisorbed and tetrahedral co-ordinated layer. Hence, this is why we observe the rate to slow during formation of the octahedral phase. Finally, we make one final use of the information obtained from the fitted data represented in figure 2b. We use this information to calculate the relative tetrahedral to octahedral aluminium occupation in the oxide layer. The chemisorbed phase has been excluded from this calculation. This ratio is displayed in figure 1a and is obviously important in determining the overall Al₂O₃ phase of the oxide layer. We will not discuss this further in this section but will consider the relevance of these ratios in the discussion section when attempting to assign phases to the layers produced by different preparation methods.

7.2.2 Effects of Annealing

Figures 4a and 4b display Al2p and O1s spectra respectively showing the effects of sequential annealing on the disordered layer produced in figures 1a and 1b. Initial heating of the crystal up to 1073 K results in no changes in binding energy of any of the peaks already identified. However, we do observe some changes in magnitude of both the states associated with the oxide and the metallic aluminium components. To make these changes clearer we have once again plotted the magnitude of different parts of the spectra in figures 4a and 4b against temperature. These are shown in figures 5a and 5b. As before, we have subsequently used the data in figure 5b to calculate the relative occupation of the octahedral to the tetrahedral state and this is displayed on the left of figure 4a. In both the spectra in figure 4a and the plot in figure 5b we can clearly see the most significant change to the oxide layer induced by increasing temperature is observed to be an increase in the magnitude of the octahedral co-ordination state. Indeed, within experimental error this state increases by three times the amount between 300 K and annealing to 1073 K. Despite this increase, the tetrahedral state remains constant within experimental error up to 1073 K. Finally, we observe the chemisorbed state to behave differently from either of the two other states. Annealing to 573 K results in a small increase in magnitude of the peak. However, heating further to 1073 K, we observe no further increase in magnitude of the state. In addition to these changes to the non-metallic aluminium components of the spectra, we also observe a change to the metallic component of the spectra with increasing temperature. Upon annealing from 300 K to 1073 K we observe a small increase in the magnitude of the metallic components of the spectra. This is clearly visible in figure 5a. Finally, we note that within experimental error in both figures 4b and 5a, we observe no changes to the amount of oxygen in the adsorbed layer up to annealing to 1073 K.

Upon heating of the surface to 1273 K we observe significant changes to both the Al2p and O1s spectra compared to those just described. Upon heating, the most striking change to the Al2p spectrum is the complete disappearance of both the chemisorbed and tetrahedral states. However, despite this we continue to observe the presence of the octahedral component, although this is somewhat reduced from a magnitude of 1.45 to 0.43, as shown in figure 5b. In addition to this we also observe a change in binding energy of the octahedral component, from its previous position of 76.4 eV, to a position of 76.9 eV after annealing to 1273 K.

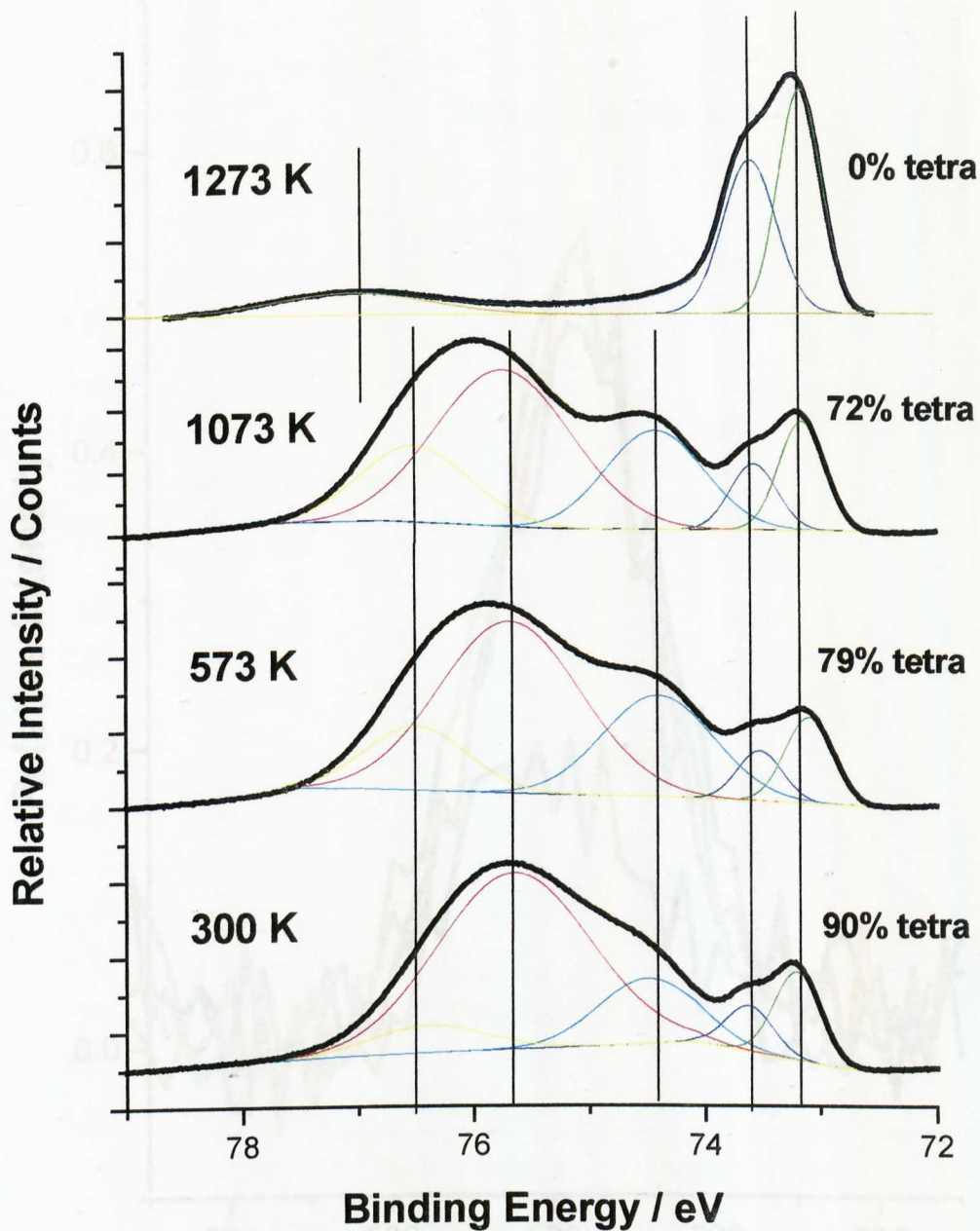


Figure 4a. Al₂p XP spectra obtained from surfaces exposed to 1200L at ca. 300 K and subsequently annealed to 573 K, 1073 K, and 1273 K. The corresponding fits are also shown and the relative tetrahedral occupation of the oxide layer is shown for reference. Experimental conditions were identical to those in figure 1a.

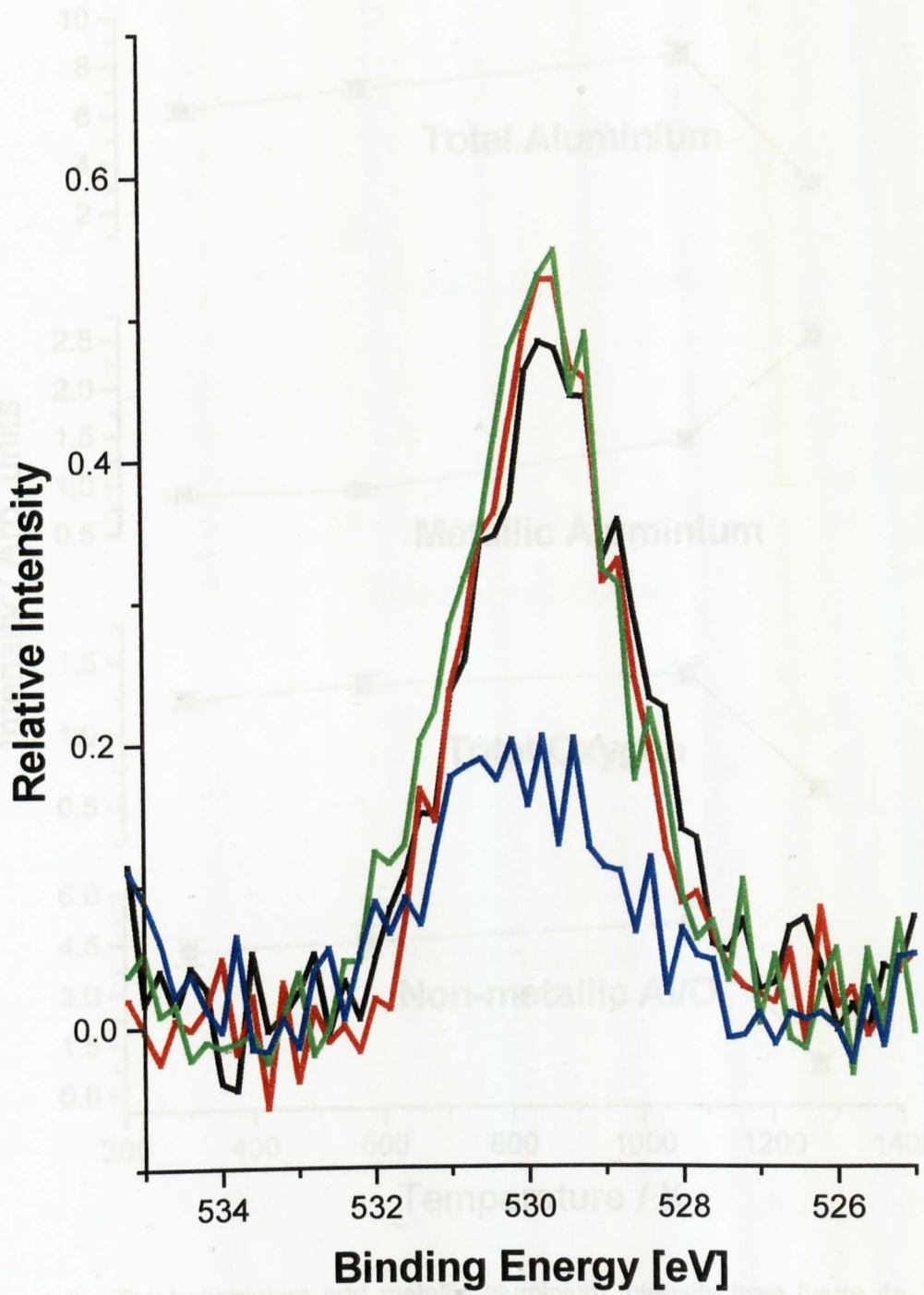


Figure 4b. O1s XP spectra obtained from surfaces exposed to 1200L (black) at ca. 300 K and subsequently annealed to 573 K (red) 1073 K (green) and 1273 K (blue). Experimental conditions were identical to those in figure 1b.

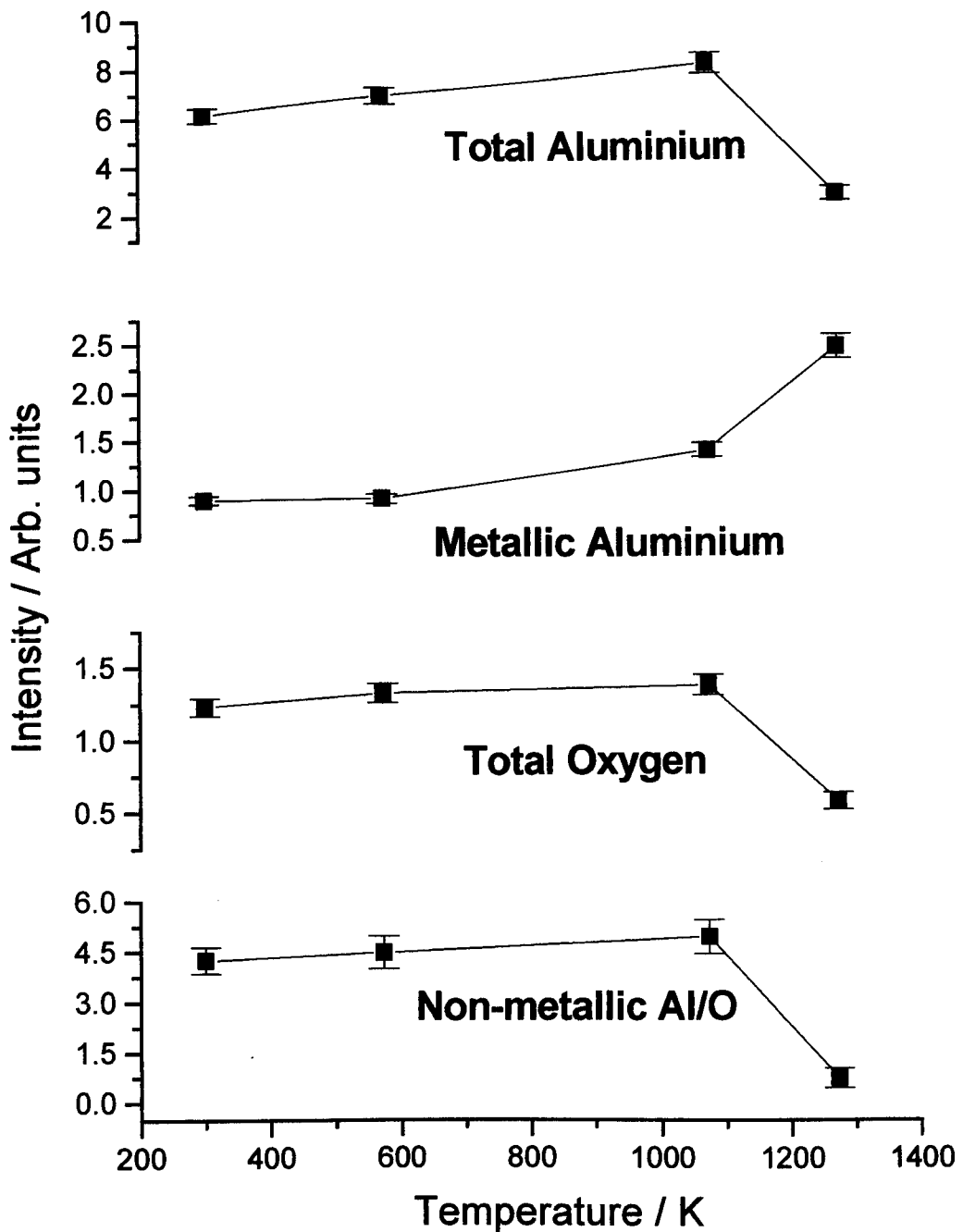


Figure 5a. Total aluminium and metallic aluminium intensity from figure 4a. Total oxygen intensity from figure 5b and ratio of non-metallic aluminium to oxygen plotted against annealing temperature.

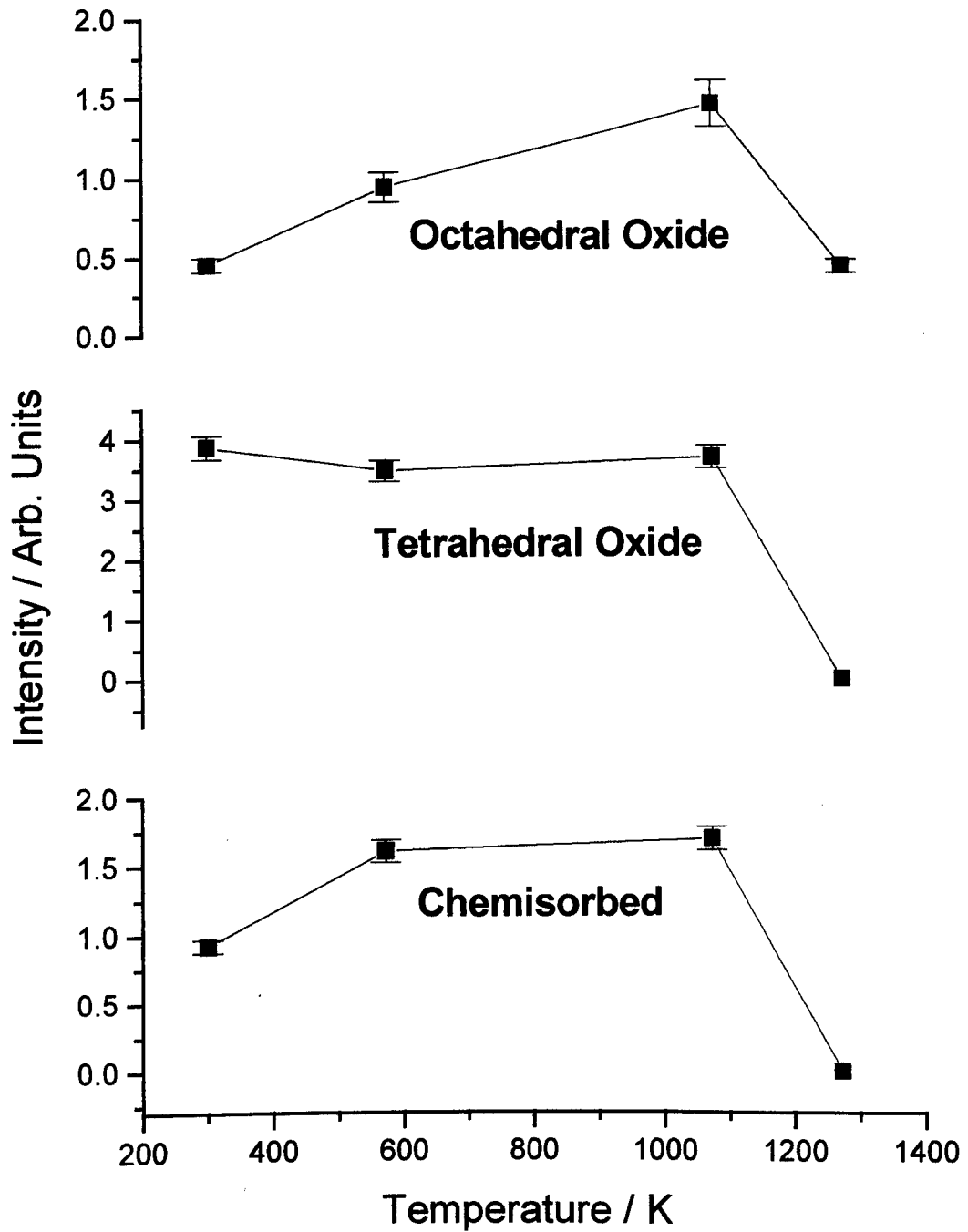


Figure 5b. Chemisorbed, tetrahedral oxide and octahedral oxide intensity from figure 5a plotted against oxygen exposure.

Alongside the changes to the non-metallic components of the layer we also observe a number of other significant changes to our spectra. Firstly, we observe a 60% reduction in the amount of oxygen in the oxide layer. This would be consistent with the large reduction in aluminium and hence the reduction in oxide. Secondly, we also observe a significant increase in magnitude of the metallic component of our Al2p spectra. This increase results in a metallic component of the spectrum with a similar magnitude to that recorded from the clean NiAl surface. Likewise, the binding energy of the metallic components is consistent with that observed on the clean NiAl surface. It is worth noting at this point that despite the large increase in magnitude of the metallic component of the spectrum, the reduction in total aluminium at the surface is significantly greater (figure 5a). Hence, this indicates significant diffusion of aluminium back into the bulk. Finally, as would be expected due to the significant changes to both the amounts of oxygen and aluminium in the oxide we observe a significant change to the Al_{non}/O ratio. This represents a change from 4.33 to 0.74 and as suggested by our previous observations, this again suggests significant changes to both oxide structure and stoichiometry.

LEED observations in previous studies [8] are consistent with the results obtained in the present study upon heating. No LEED patterns are observed after adsorption, while upon initial heating a ring like structure forms followed by the emergence of some bright spots upon heating to 1273 K. However, the patterns still have relatively little structure.

7.2.3 Multiple Adsorption and Annealing Cycles

In this section we perform repeated cycles of adsorption of 1200L oxygen at 823 K followed by annealing at 1273 K for 20 minutes. In figures 6a and 6b we show Al2p and O1s spectra respectively, recorded after each cycle of adsorption.

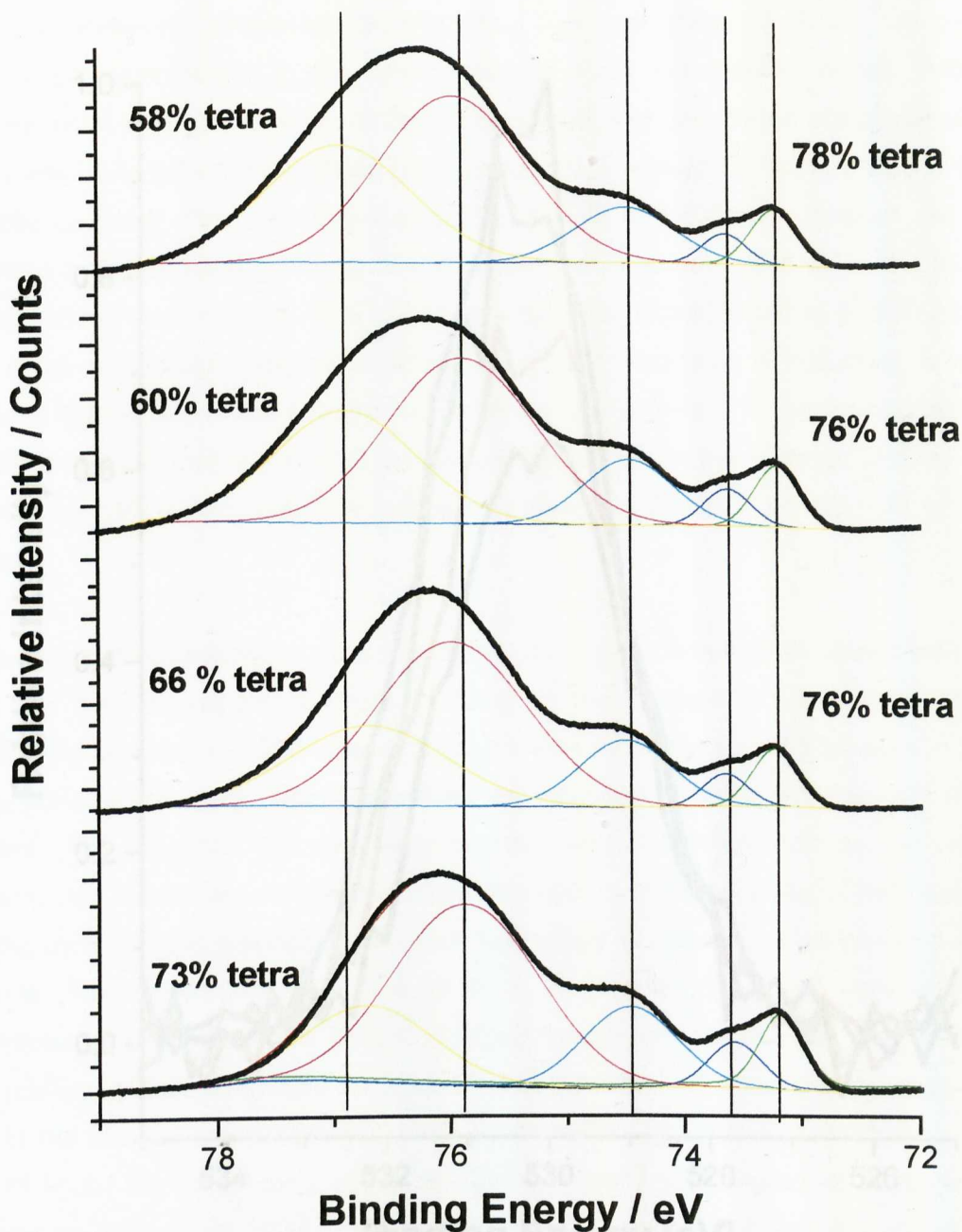


Figure 6a. Al_{2p} XP spectra obtained from a clean NiAl(110) surface, a surface exposed to 1200L at ca. 823 K, surfaces annealed and exposed to 1200L at ca. 823 K a 2nd, 3rd and 4th time along with the associated fits and the relative tetrahedral occupation of the oxide layer is also shown for reference. Experimental conditions were identical to those in figure 1a.

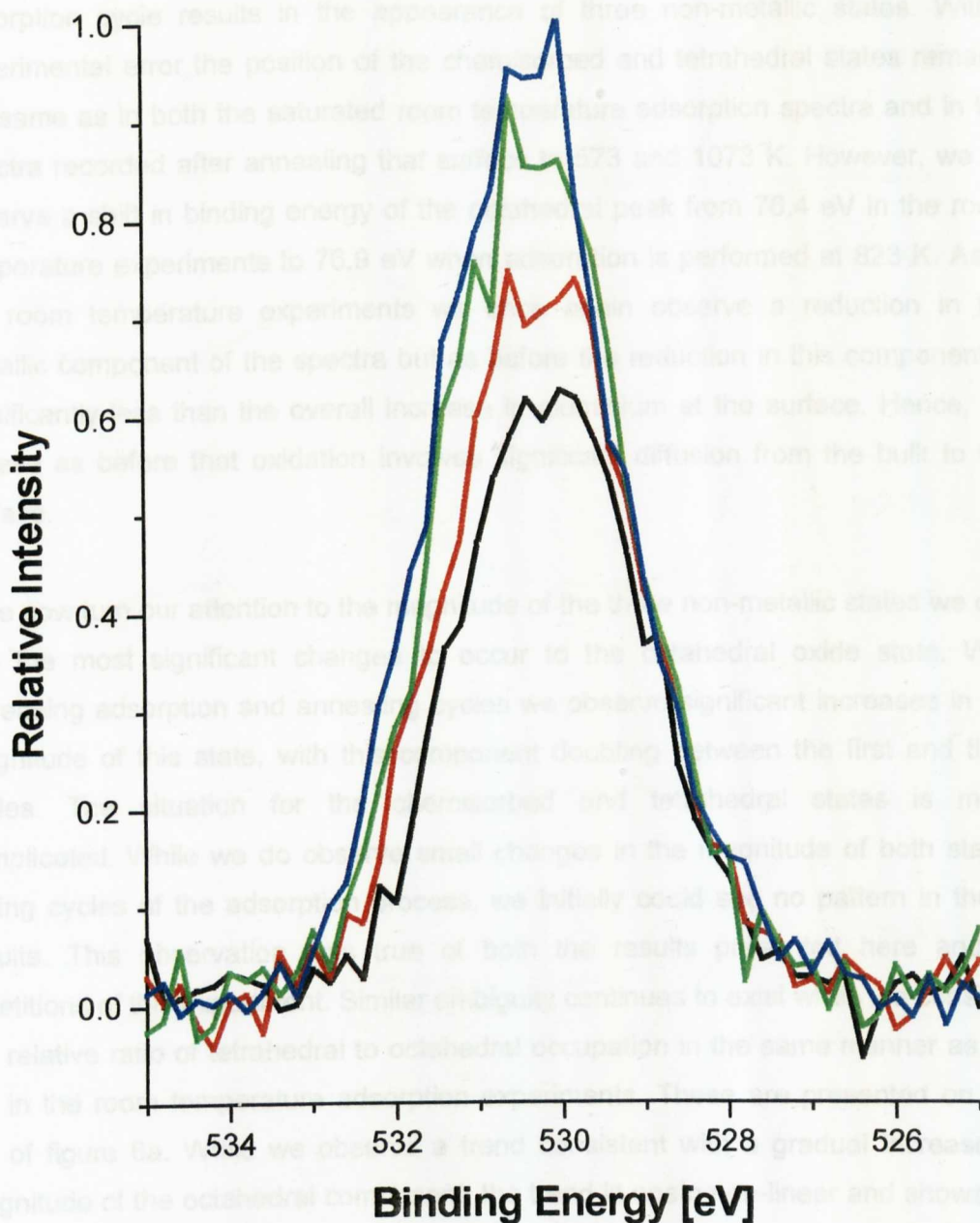


Figure 6b. O1s XPS spectra obtained from a surface exposed to 1200 (black) L at ca. 823 K, surfaces annealed and exposed to 1200L at ca. 823 K, a 2nd (red), 3rd (green) and 4th (blue) time. Experimental conditions were identical to those in figure 1b.

In figure 6a we see a similar trend in the Al2p adsorption spectra as we see in the room temperature adsorption experiments. The adsorption of 1200L in each adsorption cycle results in the appearance of three non-metallic states. Within experimental error the position of the chemisorbed and tetrahedral states remains the same as in both the saturated room temperature adsorption spectra and in the spectra recorded after annealing that surface to 573 and 1073 K. However, we do observe a shift in binding energy of the octahedral peak from 76.4 eV in the room temperature experiments to 76.9 eV when adsorption is performed at 823 K. As in the room temperature experiments we once again observe a reduction in the metallic component of the spectra but as before the reduction in this component is significantly less than the overall increase in aluminium at the surface. Hence, we believe as before that oxidation involves significant diffusion from the bulk to the surface.

If we now turn our attention to the magnitude of the three non-metallic states we can see the most significant changes to occur to the octahedral oxide state. With increasing adsorption and annealing cycles we observe significant increases in the magnitude of this state, with this component doubling between the first and third cycles. The situation for the chemisorbed and tetrahedral states is more complicated. While we do observe small changes in the magnitude of both states during cycles of the adsorption process, we initially could see no pattern in these results. This observation was true of both the results presented here and in repetitions of this experiment. Similar ambiguity continues to exist when we consider the relative ratio of tetrahedral to octahedral occupation in the same manner as we did in the room temperature adsorption experiments. These are presented on the left of figure 6a. While we observe a trend consistent with a gradual increase in magnitude of the octahedral component, the trend is again non-linear and shows no immediately obvious pattern. To fully rationalise these results we must first consider the results of annealing these adsorbed layers.

Figures 7a and 7b show the results of annealing the respective spectra displayed in figures 6a and 6b to 1273 K.

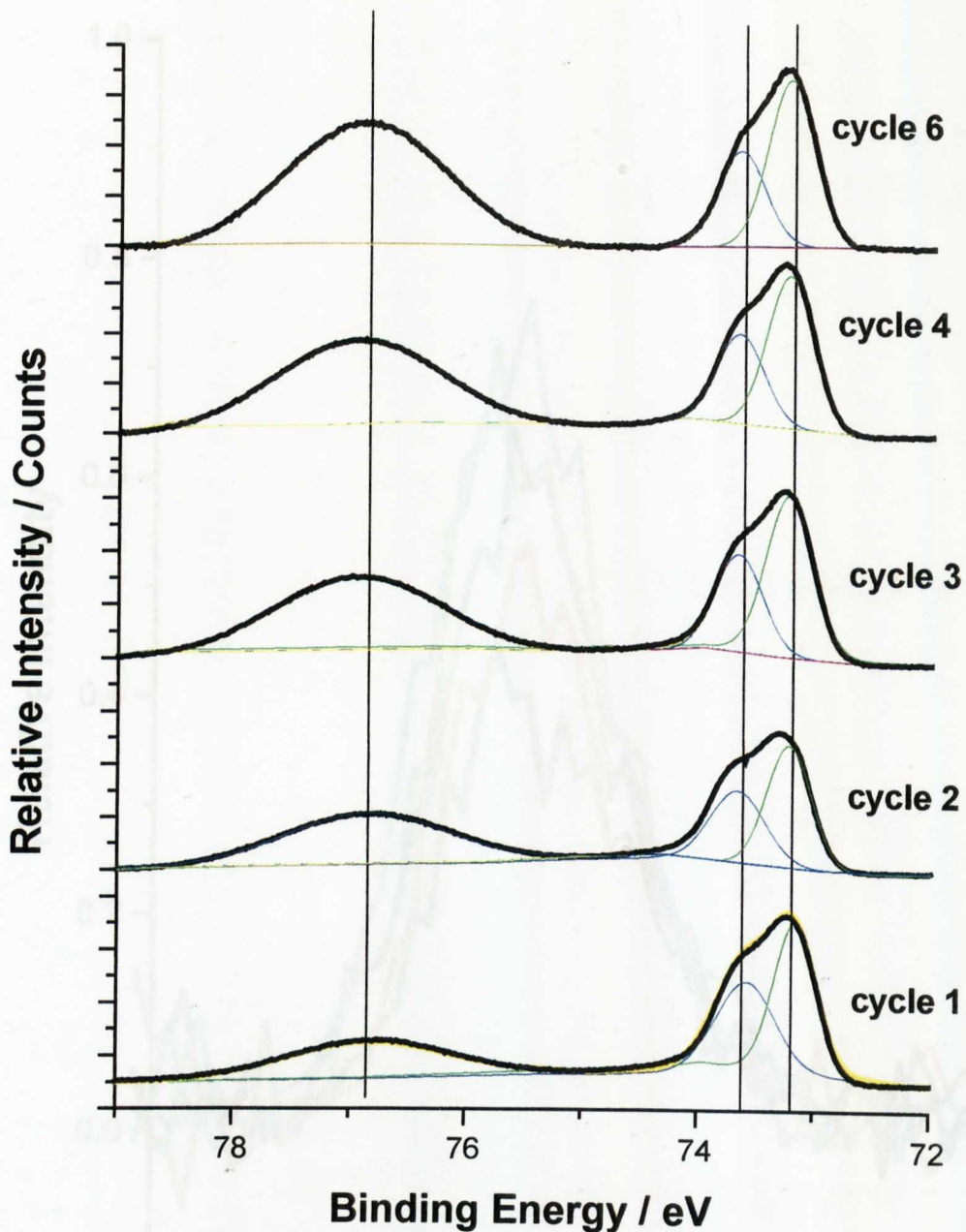


Figure 7a. Al_{2p} XP spectra obtained from a clean NiAl(110) surface, a surface exposed to 1200L at ca. 823 K and annealed to 1273 K, surfaces exposed to 1200L at ca. 823 K and annealed a 2nd, 3rd, 4th and 6th time. Experimental conditions were identical to those in figure 1a.

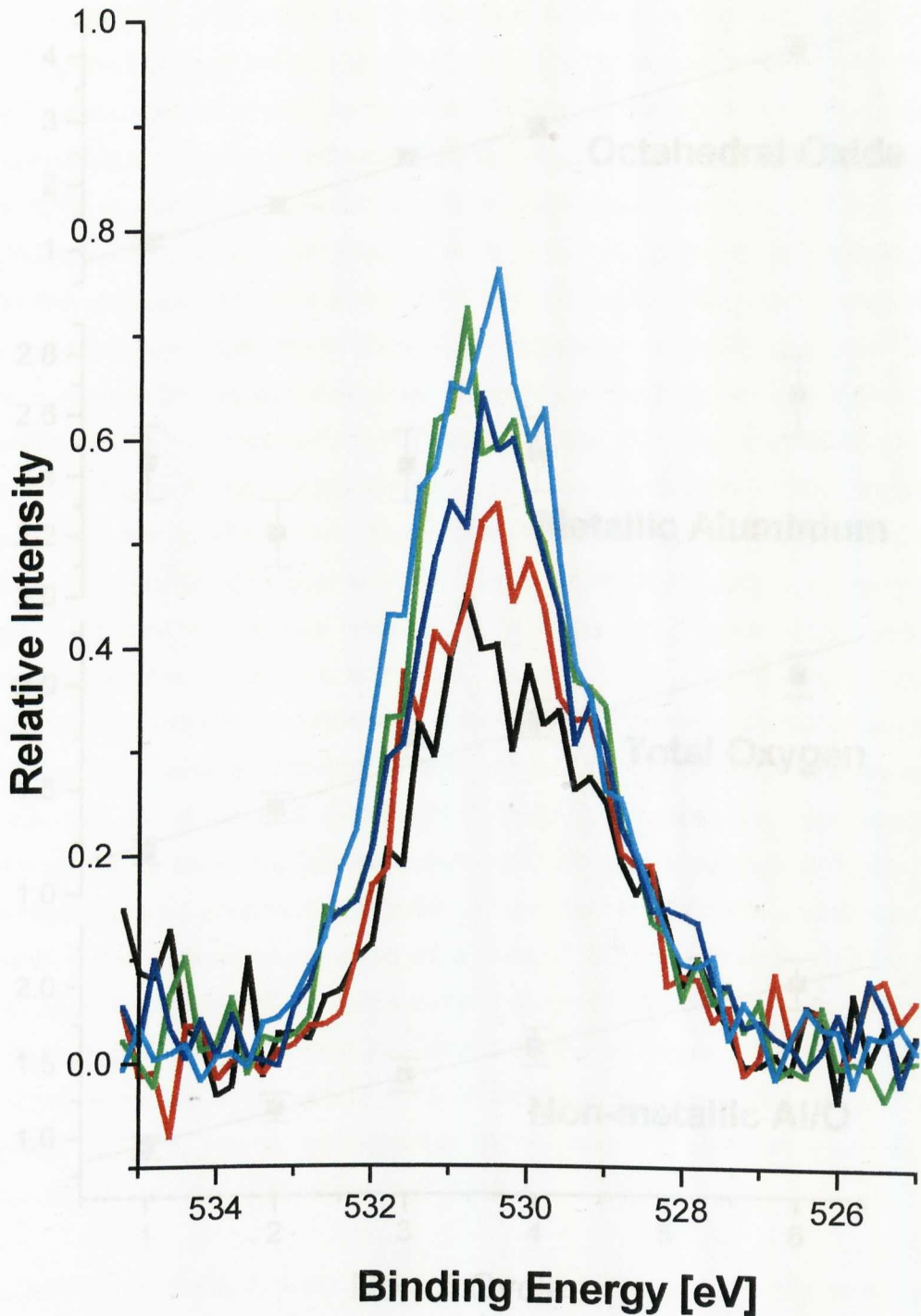


Figure 7b. O1s XP spectra obtained from a surface exposed to 1200L at ca. 823 K and annealed to 1273 K (black), exposed to 1200L at ca. 823 K and annealed to 1273 K a further 2nd (red), 3rd (green), 4th (blue) and 6th (cyan) time. Experimental conditions were identical to those in figure 1b.

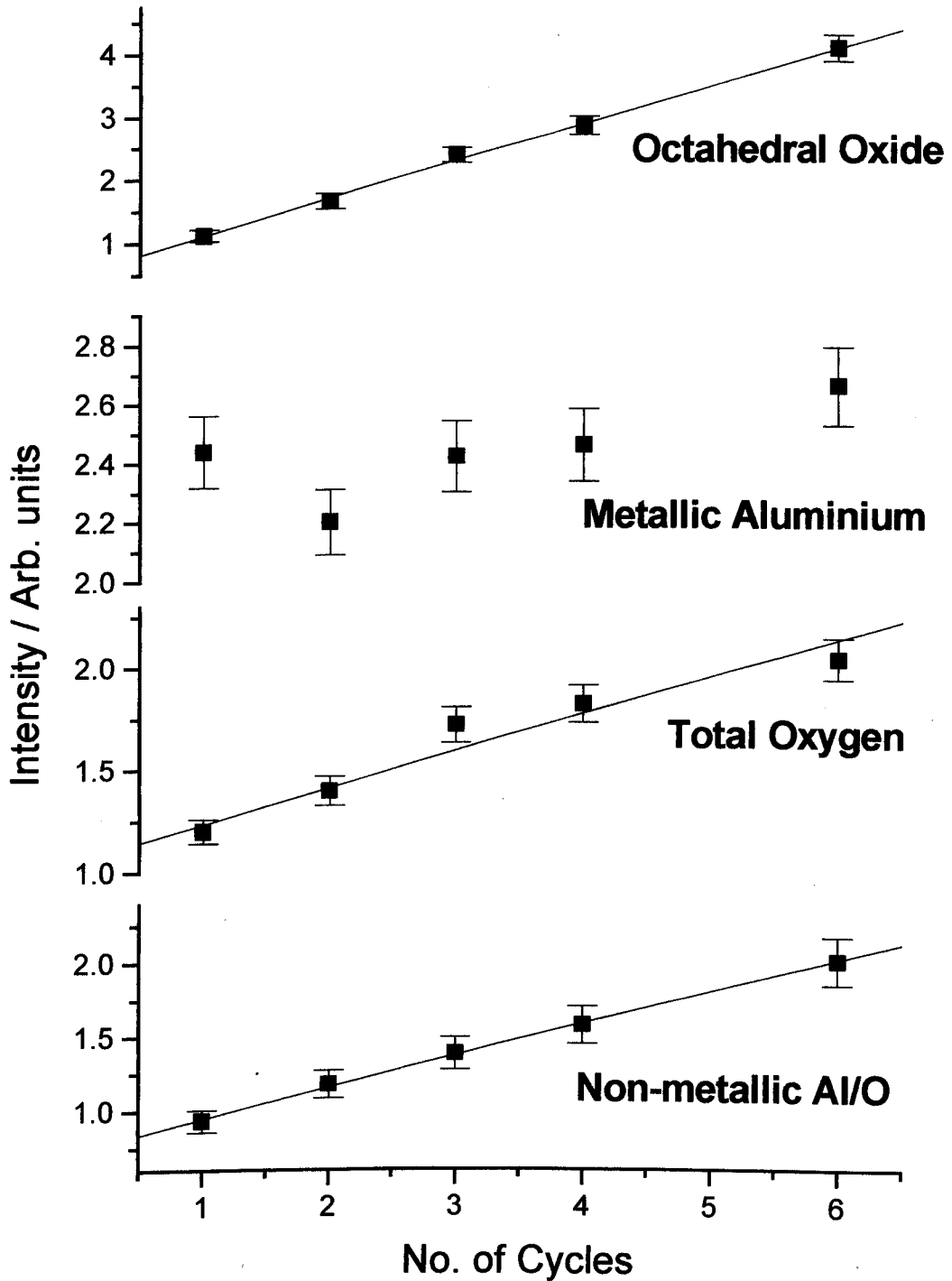


Figure 8. Octahedral oxide and metallic aluminium intensity from figure 7a. Total oxygen intensity from figure 7b and ratio of non-metallic aluminium to oxygen plotted against number of adsorption and annealing cycles.

Following annealing of the surfaces prepared at 823 K, we observe significant changes to both the Al2p and O1s spectra upon annealing. If we initially begin by considering the first cycle we can see that, as before, annealing of the layer results in a significant reduction of both the amount of oxygen and aluminium at the surface. This represents a reduction in adsorbed oxygen and non-metallic aluminium of 67% and of 65% respectively between the first adsorption spectrum and the first annealed spectrum. Once again, this comes about by the complete disappearance of both the chemisorbed state and the tetrahedral oxide state, leaving only the octahedral state present on the surface. This is located at a binding energy of 76.9 eV, the same position as observed after annealing of the layer produced at room temperature to 1273 K. However, in the Al2p spectrum, the large decrease in non-metallic aluminium is also accompanied by a large increase in the metallic component of the spectrum. As observed earlier however, the increase in the metallic component is not equal to the decrease of the non-metallic component, suggesting diffusion into the bulk once again. As before, the position of the metallic component remains consistent with that on the clean NiAl surface. These observations are entirely consistent with those observed previously after annealing to 1273 K of the surfaces prepared by adsorption of oxygen at room temperature. However, we do observe a significant difference between the two sets of experiments. In the annealing experiments performed after adsorption of oxygen at room temperature we observe the formation of octahedral oxide with an intensity of 0.43, while in the surfaces prepared by adsorption at 823 K we observe an intensity of 1.12. Likewise, these differences are also reflected in the Al_{non}/O ratio obtained from the two different preparation methods. For the surfaces prepared at room temperature we observe a ratio of 0.74 in comparison with a ratio of 0.93 for preparation at 823 K. Hence, adsorption at 823 K results in an oxide layer that is more aluminium rich than that prepared at 300 K.

In considering the effects of multiple adsorption and annealing cycles, we have once again integrated the areas of several components of interest and these are displayed in figure 8. In both figures 7a and 8 we can see that with increasing oxidation and annealing cycles the most major effect is once again observed to take place in the octahedral component of the spectra. While we observe no change in binding energy of the octahedral component we do observe changes in magnitude. From figure 8 we can see a linear increase, within experimental error, of the octahedral component with increasing cycles. However, the corresponding O1s data shows a slightly different trend. While we do observe a general increase in oxygen

in the oxide layer with increasing numbers of adsorption cycles we observe the largest increases to take place in the first three cycles. Following this we observe only a small increase between the third and 6th cycles. If we combine the results of the magnitude of the octahedral oxide and the oxygen components we can calculate the Al_{non}/O ratio for each cycle (figure 8). We observe a linear increase in the Al_{non}/O ratio with increasing numbers of cycles from 0.93 after one cycle to 2.00 following six. This observation suggests that while the character of the aluminium in the oxide layer remains the same, the binding energy of the octahedral component remains constant, the oxide layer is becoming increasingly aluminium rich with each adsorption and annealing cycle. Finally, we can see in figure 8 a final significant result. While the non-metallic component of the layer changes significantly with multiple oxidation and annealing cycles, the metallic component of the spectra does not change, within experimental error, in binding energy or magnitude. This observation suggests that despite the increases in oxygen and non-metallic oxide, a significant metallic component remains on the surface as part of the oxide layer.

As discussed earlier, without first considering the effects of annealing we were unable to determine any clear trend in the adsorption spectra recorded during multiple cycles. Hence, having presented the annealing spectra we will now return to the results obtained in the adsorption section of the experiment. Following annealing of each of the adsorption spectra we are left with an increasing octahedral component, as well as an associated O1s component. Hence, we subtracted this octahedral component from each of the subsequent adsorption spectra to obtain information on purely what is produced during each adsorption cycle. After doing this we recalculated the relative octahedral/tetrahedral ratio and these are shown on the right of figure 6a. Within experimental error we observe a ratio of ca. 75% for each adsorption cycle. Hence, despite multiple cycles, the layer produced by adsorption at 823 K always contains a 3:1 occupation of tetrahedral compared to octahedral co-ordinated aluminium in the oxide. Despite the ratio remaining constant we do still observe some variation in the absolute magnitude of aluminium involved in the layer. This forms no pattern as described earlier and we propose may be due to small variations in sample temperature and oxygen pressure. Both these factors have been shown previously to induce significant changes during the oxide formation process [19,20].

7.3 Discussion

There are two overriding questions that have dominated previous studies of this system and which are also of major interest to the current study. Firstly, what is the stoichiometry and phase of the oxide layers being formed and secondly, how homogeneous are these layers? Hence, in this section we will attempt to address both of these issues.

In the results obtained from both the room temperature adsorption and annealing experiments and multiple adsorption and annealing cycles we repeatedly observe the presence of 5 individual states in the Al2p spectra. These have been labelled as chemisorbed, tetrahedral and octahedral oxide and two states associated with metallic aluminium. As described earlier we introduced these labels at an early stage to maintain consistency and clarity throughout the chapter but did not rationalise our assignments. Hence, at this point in the discussion we will now explain the reasons for our assignment of each of the states just described.

In the work of McConville et al. studying the oxidation of Al(111), the authors observe Al2p spectra with a number of similarities to our own work presented here. With increasing exposure to oxygen the authors identify five components in their fitted data. The first of these is easily identified and is assigned as the metallic component associated with the clean Al(111) surface. This is followed by the emergence of three states at higher binding energies than the metallic component, which appear during initial oxidation. These three states are attributed to aluminium co-ordinated to one, two and three chemisorbed oxygen atoms. This is based on the following argument. Oxidation proceeds via the random filling of 3-fold hollow sites on the Al surface. This would mean that each oxygen atom would initially bond locally to three aluminium atoms, but on completion of the layer each surface Al atom has three O atoms bonded to it. Hence, at intermediate points it is reasonable to assume that each aluminium will be bonded to one, two, or three O atoms. Finally, the authors assign the last of the three states to amorphous oxide formation, containing aluminium with both octahedral and tetrahedral co-ordination. A summary of the observations made by McConville et al. is given in table 3 along with comparison with our own results. The binding energy of each feature is also listed and is quoted as the shift relative to the Al2p_{3/2} peak.

Chemical State	Shift (Relative to Al 2p _{3/2}) Al(111) [eV]	Shift (Relative to Al 2p _{3/2}) NiAl(110) [eV]
Chemisorbed: Al co-ordinated to 1 Oxygen	0.49	-
Chemisorbed: Al co-ordinated to 2 Oxygen	0.97	-
Chemisorbed: Al co-ordinated to 3 Oxygen	1.46	1.0-1.3
Oxide: Tetrahedral co-ordination	2.5-2.7	2.5
Oxide: Octahedral co-ordination	-	3.2-3.7

Table 3. Comparison of peak positions during oxidation of NiAl(110) and Al(111).

Comparison of our own data with that of McConville et al. immediately raises the question of why they observe the presence of three chemisorbed states while we observe only one. Firstly, the work of McConville et al. is recorded at better resolution than the current study. In addition to this, the magnitude of the first two chemisorbed features is small relative to the other features in the spectra. Turning to our own work we believe the feature we have identified as the chemisorbed state is in fact a combination of aluminium chemisorbed to one, two and three oxygen atoms. We believe this is the reason for the shift we observe of this particular feature with increasing oxygen exposure. However, despite this shift, we note that our own value for the position of this feature upon oxygen saturation, 1.3 eV with respect to the Al2p_{3/2}, is identical to the position observed by McConville et al. 1.46 eV, within experimental error. Hence, based on these similarities we have made the assignment of this state as aluminium associated with chemisorbed oxygen.

With regard to the first of the oxide states we believe the work of McConville can also help in assigning this peak. The feature they assign in their data as being related to the oxide is found at a position of 2.5-2.7 eV depending upon oxygen exposure and preparation method. The corresponding fitted peak in our own data is found at 2.5 eV, again identical within experimental error to the peak on Al(111). The authors assign this as being an amorphous oxide like phase with possible tetrahedral and octahedral co-ordination. In our own data, we observe only a small octahedral component during adsorption at 300 K. Indeed, without the benefit of being able to anneal the NiAl, we may have fitted both the tetrahedral and octahedral states as one broad feature. Annealing of the Al(111) would not have been possible, as discussed in the introduction. Hence, based on these

observations we also assign this feature to oxide formation but to oxide formation with purely tetrahedral co-ordinated aluminium.

Having accounted for our assignment of the chemisorbed and tetrahedral states we are left with one final state to account for. In some respects assigning the final state as aluminium associated with octahedral co-ordination is an obvious assignment based on previous work on aluminium oxide structures. However, in addition to this we have additional evidence to support this assignment. McConville et al. note in their work that they observe a 0.49 eV increase in binding energy with each increase in aluminium to oxygen co-ordination in the chemisorbed state. The subsequent shift from the chemisorbed state co-ordinated to three oxygen atoms to the oxide state breaks this rule but this would be expected due, most likely, to differing relaxation effects between the chemisorbed and oxide states. However, with subsequent increases in co-ordination of the oxide, we would expect to again follow the trend of 0.49 eV per increase in co-ordination. Hence, going from predominately tetrahedral co-ordinated Al oxide to octahedral co-ordinated Al should result in a shift of 0.98 eV. Indeed in our current data we observe a shift, consistent with this hypothesis between 0.7 and 1.2 eV dependent upon the position of the octahedral peak, which changes with preparation method. Hence, we believe this would suggest assignment of our final feature as aluminium with octahedral co-ordination is appropriate.

Having explained the assignment of each of the states observed during the oxidation and annealing of NiAl we now use this information to examine each of the layers produced, beginning with consideration of the room temperature adsorption experiments. Our observations made during initial oxidation of the surface at room temperature are consistent with the work of Isern and Castro [5] using AES. In addition to this we again note similarities with the work of McConville et al. [1] on Al(111). Our work shows that initial oxidation proceeds in two stages. In the first stages of oxidation we observe the growth of our feature associated with aluminium co-ordinated to chemisorbed oxygen. Further oxygen exposure results in the growth of this state but also the appearance and growth of a second aluminium state associated with aluminium with tetrahedral co-ordination. Following this, we observe the appearance of the octahedral oxide state after 51L oxygen exposure. It is at this point that the oxidation process slows. Additionally, we observe no further growth of the chemisorbed state and indeed a small decrease in magnitude of the chemisorbed state, which may suggest some conversion of the chemisorbed

aluminium to aluminium with octahedral co-ordination. With further exposure, the octahedral state continues to grow, while the tetrahedral saturates at 151L. Isem and co-worker have concluded that initial oxidation takes place by formation of a chemisorbed layer on the top Al atoms followed by a subsurface phase at higher exposures. Oxygen uptake then stops by formation of the thin-film Al_2O_3 layer, which prevents further transport into the bulk. McConville's observations on Al(111) are accounted for by a similar explanation. In the initial stages of oxidation the authors of this study also observe a similar trend to ourselves. At the start of oxidation they observe the growth of their chemisorbed states. However, with increasing coverage they also observe their oxide feature to begin to grow alongside that of the chemisorbed states. They suggest that oxygen firstly adsorbs into 3-fold hollow adsorption sites above the top aluminium atomic layer. However, before completion of the chemisorbed layer, they observe growth of the oxide. They suggest this, based partly on previous work, forms by oxygen penetrating the surface, leading to either local oxide formation or a distinct chemisorbed underlayer phase leading to oxide nucleation. We propose a variation on these studies to fully account for our observations. In agreement with both these studies we observe initial oxidation to proceed by initial chemisorption of oxygen on the surface. This is then followed by further chemisorption of oxygen resulting in growth of the chemisorbed feature in Al2p spectra but by formation of aluminium oxide with tetrahedral Al co-ordination alongside this. Following this we observe formation of octahedral co-ordinated aluminium oxide and we propose that it is formation of this that causes the oxidation process to slow. Hence, this would suggest that formation of the octahedral component is more difficult than either of the other two states. A likely cause of this would be that octahedral oxide formation involves transport of aluminium in the layer, through the already formed tetrahedral oxide and chemisorbed aluminium. Transport in the layer may also be supported by our subsequent experiments where we observe increased amounts of octahedral oxide formed at elevated temperatures. This would be consistent with elevated temperature resulting in greater mobility of aluminium and oxygen at the surface and hence greater amounts of octahedral oxide formation.

If we now turn our attention to the structure of the layer produced by adsorption at room temperature we must consider the relative occupation of octahedral/tetrahedral co-ordinated aluminium in the oxide layer. As discussed already we have calculated these ratios from the data presented already and

displayed the results on the figures concerned. We now summarise this data in table 4.

Room Temperature Adsorption (Figure 1a)		
Dose (Langmuir)	Tetrahedral (%)	Octahedral (%)
Clean	0	0
1	0	0
11	100	0
51	96	4
151	93	7
1200	88	12
Annealing after Room Temperature Adsorption (Figure 4a)		
Temperature (K)	Tetrahedral (%)	Octahedral (%)
300	88	12
573	79	21
1073	72	28
1273	0	100
Multiple Adsorption Experiments (Figure 6a)		
No. of Cycles	Tetrahedral (%)	Octahedral (%)
1	73	27
2	76*	24*
3	76*	24*
4	78*	22*

Table 4. Summary of relative tetrahedral/octahedral occupations of oxide layer.

*Octahedral component from previous annealed spectra has been subtracted.

With increasing oxygen exposure at room temperature we observe a small increase in magnitude of the octahedral component. However, at saturation this component only represents 12% of the oxide layer. Hence, throughout the oxidation we have a layer consisting of predominately tetrahedral co-ordinated aluminium. In the bulk phase, the observation of an Al_2O_3 layer with predominately tetrahedral occupation is associated with amorphous Al_2O_3 [25]. Hence, we believe the layer we formed here by oxidation at room temperature of NiAl is most likely to be associated with an amorphous Al_2O_3 like layer. However, the small amount of octahedral co-ordinated

aluminium present may suggest that in addition to amorphous aluminium oxide we may also have a small amount of a second phase present. This has been suggested previously in HREELS experiments performed on this layer [8,24]. The results of these experiments concluded that adsorption at 300 K results in the formation of both amorphous Al_2O_3 and a γ -like Al_2O_3 phase, which co-exist together. These observations would be consistent with that of our own. Hence, in summary, we believe that the layer consists of a combination of aluminium co-ordinated to chemisorbed oxygen, an amorphous aluminium oxide like phase and a small amount of aluminium with γ -like Al_2O_3 character. Finally, we make one further point of note regarding this layer. Namely, we observe significant attenuation of the metallic component of the Al2p spectra upon adsorption of oxygen. We believe this observation suggests we have a layer covering the whole surface with no exposed surface aluminium or segregated aluminium metal dispersed in the layer.

Upon annealing of this adsorbed layer we observe significant changes in our data which suggest changes to the structure of the oxide layer. Upon heating we observe the amount of aluminium with octahedral co-ordination to increase significantly. Annealing to 573 and 1073 K results in a tetrahedral to octahedral ratio of approximately 75% tetrahedral to 25% octahedral within experimental error. A ratio of 3:1 tetrahedral to octahedral would be consistent with the relative occupation observed in bulk γ - Al_2O_3 . Hence, annealing to these temperatures may be resulting in a change in the adsorbed layer to a structure more consistent with a γ -like Al_2O_3 phase.

The structures formed after annealing the surface prepared at 300 K to 1273 K is very important. Indeed the layer formed by this preparation method and that formed by adsorption at 823 K are clearly similar. Oxide formation by adsorption and annealing has received extensive interest as discussed earlier, particularly due to interest in using this layer as a model of catalytic support and nano-electronic devices. Despite this large-scale interest, the structure of this layer has remained controversial. Generally, the bulk of previous work has determined the structure to be consistent with α - Al_2O_3 , γ - Al_2O_3 or κ - Al_2O_3 [8,9,11,12]. These three assignments have been reached using a number of different techniques, LEED, STM, HREELS, ARUPS, XPS and XRD. Firstly, LEED observations are consistent with either α - Al_2O_3 or γ - Al_2O_3 . Secondly, EELS experiments have shown the presence of three main loss features. Again, these measurements can be resolved to be compatible

with either α -Al₂O₃ or γ -Al₂O₃. STM experiments have favoured γ -Al₂O₃, while α -Al₂O₃ has been favoured by a more recent HREELS study that has attempted to measure the relative Al³⁺ cation occupation of octahedral to tetrahedral sites. In addition to these techniques, α -Al₂O₃ is favoured by a far simpler reasoning. The most thermodynamically stable aluminium oxide phase is that of α -Al₂O₃. The κ -Al₂O₃ structure has been determined by XRD experiments. If we now consider the results of our own study added to this we can see our annealed spectra show the presence of only one type of aluminium involved in the oxide layer. This would tend to suggest that the layer is analogous to an α -Al₂O₃ like phase where there would be only octahedral Al³⁺ cation occupation. Additionally, our annealing experiments shown in figure 4a show that the layer forms only after annealing to 1273 K. This, as has been noted before [21], is below the temperature at which bulk α -Al₂O₃ forms (~1473 K) but is consistent with previous observations of the system. Again, the differences in annealing temperature serve to show that although similar in some respects, thin film oxide layers are not entirely analogous to their bulk oxide counterparts. However, with the available information, we would attribute the structure of our layer to that of an α -like aluminium oxide structure.

With particular importance to the use of this oxide layer in model experiments, as already described, we consider the topic of the homogeneity of the oxide layer formed after adsorption and annealing. Despite significant attenuation of the metallic component of the Al2p spectra during the adsorption process (figures 1a and 6a), upon annealing of the adsorbed layer we see a return of the metallic component of the spectrum. This observation indicates a significant amount of metallic aluminium within the escape depth of the Al2p electrons and hence significant amounts of aluminium near the surface that is not involved in the oxide layer and that retains its metallic character. The most obvious explanation for our observations could be the possibility that we are actually still detecting the Al metal at the crystal surface despite the presence of the oxide layer. However, we reject this as a possible explanation for our observations on the basis that the inelastic mean free path for aluminium oxide is around 5 Å at the kinetic energy of our experiments [22]. In other words, the metallic aluminium signal in our spectra should be attenuated to 37% (1/e) of its initial value over a distance of 5 Å. Although we cannot measure the thickness of our oxide layer using the techniques in this study, a number of previous studies using similar methods of preparation have concluded the thickness to be around 5Å. [8,19,20]. Therefore, if the metallic component of our spectra purely

originated from Al at the crystal surface, we would expect to observe a reduction in that component's intensity by around 63% upon oxide formation. We clearly do not observe this in our experiments, indeed we observe very little reduction in our metallic component upon adsorption and annealing and we therefore discount this as an explanation for our observations. Having eliminated this explanation we are left with the observation that the oxide layer contains a significant metallic aluminium component. As mentioned earlier, McCarty [10] has made a similar observation to this using LEEM. Upon annealing of the adsorbed layer, he observes what he describes as oxide-free regions or "pin holes" to appear in the previously homogeneous layer. This explanation would also be consistent with the observations made in this study. However, an alternative explanation that would also be consistent with both our own observations and those of McCarty would involve segregated aluminium metal dispersed with the oxide layer. Either of these observations would be consistent with the available data. Additionally, either explanation would also be consistent with the results obtained in a LEIS study by Jacobs and co-workers [23] that found more aluminium in the oxide layer than would be consistent with a pure α -Al₂O₃ or γ -Al₂O₃ layer. Regardless of which explanation is correct, either explanation is significant in that it shows that oxide formation is not homogeneous across the entire crystal surface. Additionally, as we discuss shortly, multiple adsorption and annealing cycles do not improve homogeneity. This has serious implications to the use of NiAl(110) in creating model aluminium oxide systems, effectively ruling out its use, as separating the effect of the metal from that of the oxide on experiments would be impractical.

At this point we now turn our attention to the results obtained in our multiple adsorption and annealing experiments. As stated in the results section we initially observed no trend when considering the adsorption experiments. However, by taking account of the octahedral oxide left after annealing we immediately observe a significant trend. This observation is clear in table 4. Each adsorption cycle results in formation of an oxide layer with a tetrahedral to octahedral aluminium ratio of 75% to 25%, within experimental error, in addition to the octahedral component already present on the surface. Based on similar arguments as for the surface prepared by adsorption at 300 K and annealed to 572 or 1073 K, this suggests a γ -like Al₂O₃ layer is always formed by adsorption at 823 K. However, LEED measurements made during multiple adsorption and annealing experiments [19,20] have shown a pattern with no substrate spots visible or any crystalline oxide spots. This would suggest no long-range order in the oxide structure and hence, would suggest we do

not have well-ordered γ -like Al_2O_3 . We believe that two possibilities exist. Firstly, the presence of the chemisorbed phase obscures any long-range order associated with the oxide or alternatively, despite a ratio consistent with γ -like Al_2O_3 , the layer is still relatively disordered but contains both types of aluminium. Either of these explanations could be consistent with our own and previous work. Finally, we note that in each of the adsorption spectra recorded during the multiple cycle experiments we observe significant attenuation of the metallic component of the spectra. Hence, as in the adsorption experiments at 300 K we see no evidence for pin holes or segregated aluminium in the oxide layer formed.

As mentioned previously, the similarities between the layer produced by annealing to 1273 K after adsorption at 300 K and 823 K are clear. The exception to this being that we observe the layer produced after adsorption at 823 K followed by annealing to be more aluminium rich ($\text{Al}_{\text{non}}/\text{O} = 0.93$) than that prepared by adsorption at 300 K ($\text{Al}_{\text{non}}/\text{O} = 0.74$). We will consider this further shortly. Despite this obvious difference, the observation of only octahedral co-ordinated aluminium in the layer and the high annealing temperature (1273 K) is still consistent with an α -like Al_2O_3 phase. This is based on the same arguments already described in assigning the layer formed after adsorption at 300 K and annealing to 1273 K. Also, as described, we believe this layer to contain either pin holes or segregated aluminium metal. Continuing from this point and performing multiple adsorption and annealing cycles results in the oxide layer formed becoming increasingly aluminium rich. This can be seen clearly in the $\text{Al}_{\text{non}}/\text{O}$ ratio, which increases, from 0.93 after one cycle to 2.00 after 6. Despite this increase in aluminium in the oxide layer, the binding energy of the octahedral component remains constant and we continue to observe only one form of aluminium in the oxide layer, octahedral. Hence, this suggests that the overall character of the layer remains constant, i.e. α - Al_2O_3 like. If we do not observe significant changes to the structure, how can we account for incorporation of additional aluminium into the oxide layer? We believe the answer to this may in fact be straightforward. In the bulk α - Al_2O_3 structure 2/3 of octahedral vacancies are filled by Al^{3+} cations [26]. Therefore, we believe in a similar manner that our own α -like Al_2O_3 layer is most likely highly defective with many octahedral vacancies. Hence, with increasing numbers of adsorption and annealing cycles, we propose that aluminium drawn from the bulk is involved in two processes. Firstly, aluminium combines with oxygen adsorbed during the cycles to form new aluminium oxide. Additionally, aluminium fills octahedral vacancies. This mechanism would be

consistent with the enhanced aluminium diffusion compared to oxygen adsorption we observe during multiple adsorption and annealing cycles. Finally, we note that with increasing numbers of cycles, we do not observe any reduction in the magnitude of the metallic component of the Al2p spectra. Hence, despite the formation of additional oxide and the filling of aluminium vacancies, the layer continues to be non-homogeneous, containing segregated aluminium metal or pin holes.

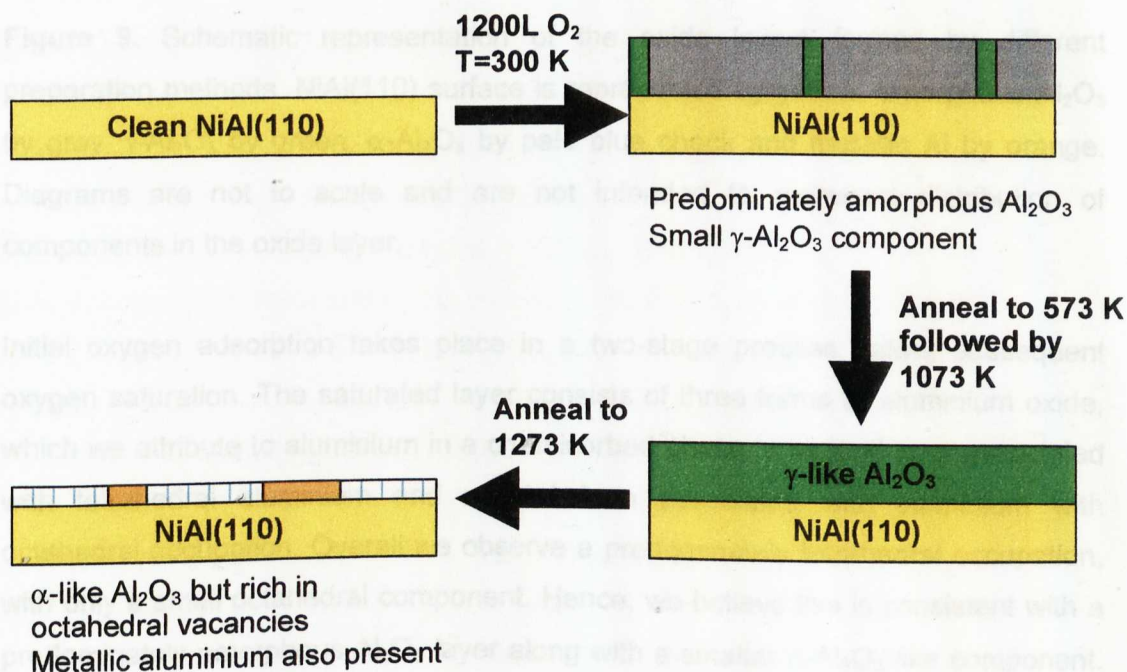
At this point we have one final aspect of our results that is worth considering. As discussed briefly already, although the relative occupations of tetrahedral to octahedral suggest that both the layer produced during room temperature adsorption and annealing to 1073 K and the layer produced during adsorption at 823 K have the same composition, we believe some differences must still exist. We make this observation based on the fact that after annealing of each layer we obtain significantly different amounts of aluminium involved in the oxide. This is in agreement with the work of Lay et al. [19] who have shown using LEED that despite oxygen adsorption at a variety of temperatures producing identical patterns with no long range order, adsorption temperature does have an effect on the resulting pattern after annealing. They observe increasing temperature of adsorption to result in improved oxide crystallinity after annealing. We believe this is consistent with our own data, which suggests increased adsorption temperature results in additional octahedral aluminium present in the annealed oxide layer. To account for these observations we propose the following as a possible mechanism playing a role in the formation of the final α -like Al₂O₃ layer. During the initial adsorption of oxygen we observe a significant attenuation of the metallic component of the Al2p spectra. This would be consistent with adsorption of oxygen onto this metallic component. Since attenuation begins immediately upon oxygen adsorption, this suggests some of the metallic component is involved with chemisorbed oxygen. Further oxidation continues to cause attenuation of the metallic component. Annealing of this layer to 1273 K immediately results in the re-appearance of the metallic component of the spectra, alongside desorption of oxygen associated with the metallic aluminium. Significant oxygen desorption is also observed in O1s spectra. We propose that the dissociation of oxygen from the metallic component may be one of the main driving forces in the oxide formation process. We suggest the elevated temperatures of annealing would result in significantly increased mobility on the surface. This causes the metal component to re-arrange and form either pin holes or segregated aluminium metal, resulting in destabilisation and desorption of chemisorbed and

oxide oxygen. This is consistent with observations made by McCarty, who observes the un-oxidised areas to cluster together with increased temperature. The left over oxide on the surface is that of the most thermodynamically favourable at high temperatures, consistent with the bulk oxide most thermodynamically favourable, α - Al_2O_3 . Hence, we believe that the effects of temperature during the oxygen adsorption phase may also be related to surface mobility. The increased motion on the crystal surface during the adsorption of oxygen at elevated temperatures allows the octahedral component, that which remains after annealing, to become more mobile in the layer. This must result in a distribution of octahedral aluminium in the oxide layer that results in increased conversion to the final state observed after annealing.

7.4 Conclusions

We have performed an Al2p core level photoemission study of aluminium oxide formation on NiAl(110), examining the initial oxidation stages through to the effects of multiple adsorption and annealing cycles on the oxide layers produced. A brief summary of our conclusions is shown schematically in figure 9.

Room Temperature Experiments



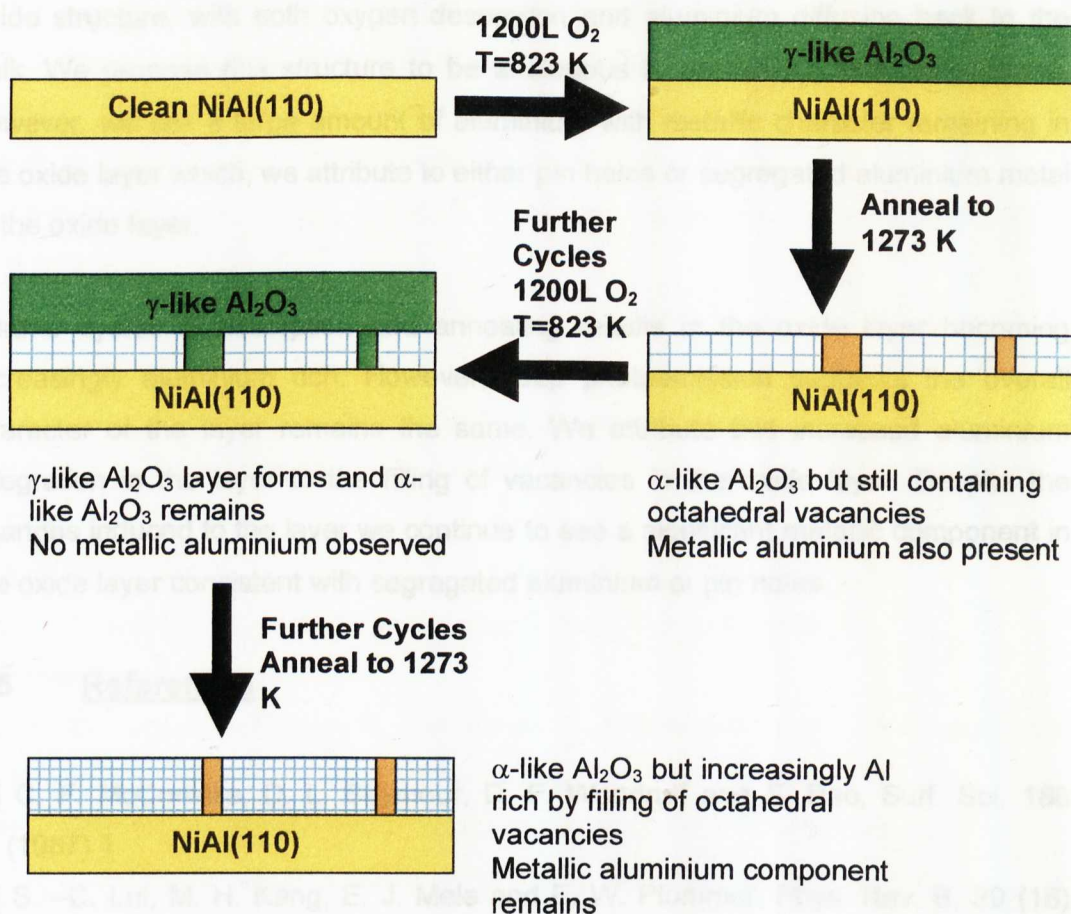
Multiple Adsorption and Annealing Experiments

Figure 9. Schematic representation of the oxide layers formed by different preparation methods. NiAl(110) surface is represented by yellow, amorphous- Al_2O_3 by grey, γ - Al_2O_3 by green, α - Al_2O_3 by pale blue check and metallic Al by orange. Diagrams are not to scale and are not intended to represent distribution of components in the oxide layer.

Initial oxygen adsorption takes place in a two-stage process before subsequent oxygen saturation. The saturated layer consists of three forms of aluminium oxide, which we attribute to aluminium in a chemisorbed phase, a second form associated with tetrahedral aluminium and a third form associated with aluminium with octahedral occupation. Overall we observe a predominately tetrahedral occupation, with only a small octahedral component. Hence, we believe this is consistent with a predominately amorphous Al_2O_3 layer along with a smaller α - Al_2O_3 like component. Annealing of surfaces after room temperature adsorption or adsorption at elevated temperatures results in a layer which also contains three types of aluminium, chemisorbed, tetrahedral co-ordinated and octahedral co-ordinated. In this instance

we observe a tetrahedral/octahedral occupation of 3:1, consistent with a γ -Al₂O₃ like phase. Further annealing of the adsorbed layer causes significant changes to the oxide structure, with both oxygen desorption and aluminium diffusion back to the bulk. We propose this structure to be analogous to an α -Al₂O₃ like oxide phase, however, we see a large amount of aluminium with metallic character remaining in the oxide layer which, we attribute to either pin holes or segregated aluminium metal in the oxide layer.

Further cycles of adsorption and annealing results in the oxide layer becoming increasingly aluminium rich. However, Al2p photoemission suggests the overall character of the layer remains the same. We attribute this increased aluminium integration in the layer to the filling of vacancies in the oxide layer. Despite the changes induced to the layer we continue to see a significant metallic component in the oxide layer consistent with segregated aluminium or pin holes.

7.5 References

- [1] C. F. McConville, D. L. Seymour, D. P. Woodruff and S. Bao, Surf. Sci. 188 (1987) 1
- [2] S. -C. Lui, M. H. Kang, E. J. Mele and E. W. Plummer, Phys. Rev. B, 39 (18) (1989) 13149
- [3] X. Torrelles, F. Wendler, O. Bikondoa, H. Isern, W. Moritz and G. R. Castro, Surf. Sci. 487 (2001) 97
- [4] A. Stierle, C. Tieg, H. Dosch, V. Formoso, E. Lundgre, J. N. Andersen, L. Köhler and G. Kresse, Surf. Sci. Lett. 529 (2003) L263
- [5] H. Isern and G. R. Castro, Surf. Sci. 211/212 (1989) 865
- [6] A. Y. Lozovoi, A. Alavi and M. W. Finnis, Phys. Rev. Lett. 85 (3) (2000) 610
- [7] A. Y. Lozovoi, A. Alavi and M. W. Finnis, Comp. Phy. Comm. 137 (2001) 174
- [8] R. M. Jaeger, H. Kuhlenbeck, H. -J. Freund, M. Wuttig, W. Hoffmann, R. Franchy and H. Ibach, Surf. Sci. 259 (1991) 235
- [9] J. Libuda, F. Winkelmann, M. Bäumer, H. -J. Freund, Th. Bettrams, H. Neddermeyer and K. Müller, Surf. Sci. 318 (1994) 61
- [10] K. F. McCarty, Surf. Sci. 474 (2001) L165
- [11] M. B. Lee, J. H. Lee, B. G. Frederick and N. V. Richardson, Surf. Sci, 448 (2000) L207

- [12] A. Stierle, F. Renner, R. Streitl, H. Dosch, W. Drube and B. C. Cowie, *Science*, 303 (2004) 1652
- [13] P. Gassmann, R. Franchy, and H. Ibach, *Surf. Sci.* 319 (1994) 95
- [14] K. Wefers and G. M. Bell, *ALCOA Technical Papers* 19 (1972)
- [15] H. Saalfeld, *Neues Jahrb. Miner. Abh.* 95 (1960) 1.
- [16] B. C. Lippens and J. J. Steggerda, in: *Physical and Chemical Aspects of Adsorbents and Catalysts*, Ed. B. D. Linsen (Academic Press, New York, 1970) p. 171 ff.
- [17] P. A. Thiry, M. Liehr, J. J. Pireaux, R. Sporken, R. Caudano, J. P. Vigneron, A. A. Lucas, *J. Vac. Sci. Technol. B* 3 (1985) 1118
- [18] M. Liehr, P. A. Thiry, J. J. Pireaux, R. Caudano, *Phys. Rev. B*, 34 (1986) 7471
- [19] T. T. Lay, M. Yoshitake and B. Mebarki, *J. Vac. Sci. Technol. A* 20 (6) (2002) 2027
- [20] M. Yoshitake, B. Mebarki and T. T. Lay, *Surf. Sci.* 511 (2002) L313
- [21] P. Gassmann, R. Franchy and H. Ibach, *Surf. Sci.* 319 (1994) 95
- [22] www.lasurface.com
- [23] J. -P. Jacobs, S. Reijne, R. J. M. Elfrink, S. N. Mikhailov and H. H. Brongersma, *J. Vac. Sci. Technol. A*, 12 (4) (1994) 2308
- [24] R. Franchy, J. Masuch and P. Glassmann, *Appl. Surf. Sci.* 93 (1996) 317
- [25] H. J. van Beek and E. J. Mittemeijer, *Thin Solid Films*, 122 (1984) 131
- [26] A. R. West, *Basic Solid State Chemistry*, 2nd Edition (Wiley, 1999)

**Chapter 8: Enantio-Sensitive Second Harmonic Generation: -
Developing A Unique Probe of Chiral Interfaces**

8.1 Introduction

Chirality has been the subject of a great deal of experimental interest due to the potentially lucrative benefits that can arise from both improved methods of chiral discrimination and of separation and synthesis. This stems from an already huge pharmaceuticals industry producing vast quantities of single enantiomer drugs and from a more general interest from the chemical industry to exploit the differing properties of enantiomers for fragrances and flavourings. As a result, a lot of work has been aimed at producing single enantiomers, but so far the most successful methods to date have been based on homogeneous asymmetric synthesis. However, an alternative method of production, more relevant to this particular study, uses the technique of enantioselective heterogeneous catalysis. The basic idea in enantioselective heterogeneous catalysis is to treat a catalyst with a chiral modifier, usually a single enantiomer of another molecule, which alters the catalyst to produce products of only one handedness. Two of the most successful studies using this method have used tartaric acid to modify Ni/SiO₂ [1] and cinchonidine modification of platinum [2]. However, even these successes have failed to provide much more than a qualitative understanding of the mode of action of modifiers.

In an attempt to improve fundamental understanding of chiral systems a number of surface science studies have been performed, commonly using the technique of STM. In STM experiments of chiral adsorbates, chiral discrimination is achieved by inferring absolute configuration from high resolution STM images, where at low coverage, a discrete small single (immobile) molecule can be imaged and absolute configuration inferred [3], or at high coverages, ordered homochiral domains are observed [4,5]. Unfortunately, this method of chiral discrimination has a number of problems and disadvantages. High-resolution images are difficult to obtain for disordered systems, large molecules and at elevated temperatures, all of which are conditions particularly relevant to catalytic systems and modifiers. Hence, development of a new optical probe of surface chirality would be an ideal compliment to existing STM techniques and is the aim of this study.

A number of conventional spectroscopic chiral probes of the bulk phase already exist. However, bulk phase techniques are generally based on monitoring extremely small asymmetries, which when translated to measuring only the small quantities of adsorbed molecules on surfaces means that the magnitude of the absolute difference in signal is outside the detection limit of systems. However, the technique of second harmonic generation is one possible method that may be useful in addressing these problems. SHG is a second order non-linear optical process, forbidden by the dipole approximation in media with inversion symmetry, making it intrinsically sensitive to symmetry breaking interfaces, such as metal adsorbate systems. Additionally, SHG has already been shown to be an extremely powerful and sensitive probe of chiral systems when applied to liquid-insulator and liquid-liquid interfaces. However, optically active (OA) SHG techniques have never been applied to the problem of chiral adsorbates on metal surfaces.

8.1.1 Enantiomer Sensitive Second Harmonic Generation (ES-SHG)

Despite the SHG technique never having been applied to the study of chiral adsorbates on metal surfaces directly, the technique has been used for a wide variety of studies. Hence, it may be useful here to examine a number of aspects of the SHG technique relating to the current experiments.

A number of studies of adsorbates on metal substrates have been performed previously examining the effects of adsorption on SHG signal. These have focussed on a variety of substrates [6-8] and have also included both Cu(110) [9] and Cu(111) [10-15]. We will concentrate on previous work on Cu, in line with our own choice of substrate. On Cu(110), the authors examined the effects on SHG intensity of incident wavelength, polarisation rotation and sample orientation. In this paper the authors concluded that the effects of surface states on SHG are significant and showed that tuning the fundamental wavelength to 600 nm results in a resonance effect and an intersurface band transition. In addition to this, they also showed that individual elements of the susceptibility tensor can be isolated by careful choice of experimental set-up, particularly choice of polarisation.

The first study of the Cu(111) surface took place in 1986 and was performed by Tom and Aumiller [10]. This paper describes the results of SHG measurements from both the clean Cu(111) surface and during the adsorption of oxygen with particular attention paid to the anisotropy of the surface. The authors find that measurements

of SHG during both polarisation and sample rotation produce SH signals clearly characteristic of the $3m$ symmetry of the (111) face. During oxygen adsorption they observe a significant drop in SH intensity, down to 9% that of the clean surface upon adsorption of a 2000L oxygen saturation dose. Despite the significant drop in intensity, the $3m$ symmetry of the sample remains. Additionally, the authors also showed theoretically that the use of s-polarised fundamental and incident light results in no non-vanishing elements of the electric susceptibility tensor. However, they still detect SH signal, although small, in experiments conducted under these conditions. They concluded that this is due to the fact that the response of the metal cannot be fully predicted by a free electron model and that the electronic response from the metal contains contributions from interband transitions involving d-band electrons, those responsible for the apparent red colour of copper. This is generated by a resonance effect between the second harmonic signal at 532 nm and the interband transition and will result in a significantly enhanced signal generated from the copper surface. This is particularly important in the current work as our own SH wavelength will also coincide with the copper interband transition. Hence, we will also expect to observe an enhanced copper signal significantly larger than that of any adsorbates, which are not in resonance with either the in or out-going radiation.

A number of further studies relating to the Cu(111) surface have been carried out since this initial one focussing on both the electronic properties of the surface and on the effects upon adsorption [11-15]. All of these studies have focussed mainly on considering how surface electronic states of the Cu(111) surface can be probed by SHG and how these are affected by adsorption. All these papers are useful in showing the particular sensitivity of SHG to changes of the surface. In addition, this work has shown SHG from metal surfaces is complex and theoretical interpretation of the results obtained can be difficult. This is due in a large amount to resonance effects between the metal and either the fundamental or harmonic beams. This results in the effects of interband transitions contributing to the generated SH intensity, such as from image-potential state to surface state transitions. Again though, this does show the particular surface sensitivity of SHG. In fact in reference 14, the authors monitor SHG signal with increasing temperature of the Cu(111) surface. They show that the SH signal is particularly sensitive to the number of surface defects at the copper surface. Also, the work of Ishida et al. [15] is particularly interesting as they have used a tuneable laser to perform resonant measurements of the adsorption of both benzene and CO. The resonant nature of the measurements results in an enhancement of the copper signal as described

earlier, allowing the surface electronic structure to be probed during adsorption. Particularly interesting is the observation of a number of new resonances observed, not associated with the already known surface state-image state transition. They also determine one of these to be related to a particular surface site, where benzene is unlikely to adsorb and a second resonance particularly sensitive to a sub-monolayer benzene coverage. The main feature of all the work carried out on the Cu(111) surface and on metal surfaces in general has been to prove the particular sensitivity of SHG to the surface electronic states. Additionally, it has also been shown to be particularly useful in measuring the effects of molecular adsorbates on metal substrates, and it is these effects we will be particularly interested in during the course of this study.

Having considered the applications of SHG in studying metal surfaces we now turn our attention to its use in chiral discrimination experiments. As described, this is the first time chiral discrimination measurements have been performed on an adsorbate-metal interface using SHG. However, SHG has been used previously as a probe of chiral systems and these are obviously relevant to the work we present here. One such technique is circular dichroism-SHG (CD-SHG) [16-20], named due to its similarities to the linear bulk probe circular dichroism (CD). In a CD-SHG experiment, the intensity of the SH beam is measured for both left and right circularly polarised incident beams and intensity differences can be related to the chirality of the adsorbate layer. In addition to CD-SHG, a second technique called linear dichroism-SHG (LD-SHG) [21,22] has been used successfully in chiral discrimination. In this technique the fundamental beam is once again linearly polarised but in this configuration, the SH intensity is measured at $+45^\circ$ and -45° of the linear polarised fundamental beam and chiral effects can be recorded.

The major difference between chiral discrimination work performed previously and the work we report here is the presence of the metal surface. In studies performed on metals such as those described previously, the general aim involved in all experiments is to measure properties of the metal and changes induced by adsorption. This is generally straight forward as the metal signal makes a major contribution to the overall signal or, as is the situation in our experiments, when performing experiments in resonance the metal contribution dominates the SH signal. In the various techniques just described for making chiral measurements, substrates are chosen that do not contribute to the overall SH signal. Hence, it is possible to make chiral measurements of the adsorbate. In the work presented here

we have a potential problem to overcome in making measurements. Namely, the metal signal from the copper, in resonance with the SH radiation, dominates the SH signal recorded for almost all-possible combinations of incident light and detection polarisations. In this situation only chiral changes induced on the metal could be detected. However, by using s-polarised incident radiation (perpendicular to the plane of incidence, hence parallel to the surface) and detecting at, or close to, s-polarisation, such as in the experiments described above, we minimise the metal component allowing the signal from the adsorbate to be measured. The theoretical reasoning for this has already been discussed in chapter 2 and is based on the fact that the electric dipole susceptibility components contributing to the SH signal produced by the surface are reduced. However this in itself poses a potential problem, the electric dipole susceptibility components associated with the chirality of the molecules also vanish. Hence, when we make chiral measurements of the adsorbate we may see no effect if the chiral response is associated with components of the electric dipole susceptibility tensor. In an attempt to address this concern, we now consider further the work of Hache et al. [23-26] already mentioned in chapter 2. The work of these authors has paid particular attention to the origin of chiral effects observed in LD and CD experiments and they have derived expressions for making chiral measurements using both methods. Of particular interest, is the work they have performed on determining the origin of the chiral response observed in SHG measurements from different types of adsorbate molecule [24]. The authors conclude that molecules generally fall into two categories of classical models, Kuhn and Kauzmann. In the first of these, the Kuhn model, chirality stems from the presence of two coupled oscillators, positioned with respect to each other, at an angle that removes any centres of symmetry from the molecule. In reality this model would apply to molecules such as a substituted Tröger base and the authors have synthesised and made measurements from this molecule to test their hypothesis [25]. For this type of molecule, the coupling of the two monomers in interaction generates the chirality of the molecule because the dipole moments of the two monomers are arranged in a non-mirrorsymmetrical configuration. Hence, the resultant SHG signal is also generated as a result due to purely electric terms. More important to the current study is the second type of model system proposed by Hache et al. based on the classical Kauzmann model. In this particular model, optical activity is generated by a single electronic transition with electric and magnetic character. It is modelled by the motion of electrons around a helical path round the molecule imposed by the molecular backbone where the excitation of an electric dipole moment will induce a magnetic dipole moment

and vice versa and hence, optical activity is mainly a magnetic effect. The two molecules we use in this study would most closely be related to the second of these models and we would therefore expect magnetic effects to contribute to the SH signal. However, Hache et al. note that in general it is not possible to describe a molecule entirely by a unique model. Hence, in general, chiral effects from our molecules may come from both electric and magnetic origins. The work of these authors however, is useful, as it suggests we will continue to be able to observe a chiral response when using s-polarised incident radiation.

8.1.2 2-Butanol

Although this chapter is primarily concerned with the results of the SHG experiments we have performed on the two-adsorption systems, we also characterise the adsorption of both molecules using surface science techniques already described and used in earlier sections. Obviously, this process is essential to allow surface preparation for SHG experiments but also to aid in interpretation of SHG results. Hence, we will now consider previous work on both 2-butanol and 1-(1-naphthyl) ethylamine.

As has been discussed earlier in chapter 6, when considering previous work carried out on 1-butanol, there is very little previous work to use for comparison purposes. Hence, once again we have to consider work not directly related to the current study. However, since we have already done this in chapter 6 we will not repeat the review already considered there. Obviously, all the observations made in that chapter apply here to the interaction of both -OH and =O groups made in that literature review and the previous work of our lab on a number of oxygen containing systems and on 1-butanol in chapter 6.

The only previous study found in the literature to involve the adsorption of 2-butanol was carried out by Gellman et al. [27] and involved the adsorption of R and S enantiomers of 2-butanol on the Ag(643) surface. This surface in itself displays chirality due to the position of kink sites and was cut to expose the Ag(643) face described as S and the Ag($\bar{6}$ $\bar{4}$ $\bar{3}$) face which is considered to be equivalent to R. Each combination of both R and S 2-butanol and the R and S surfaces were used during experiments and the spectra were carefully examined for any small changes that may show differing interactions between the left and right handed constituents.

All of these experiments produced identical results and no chiral effects could be observed. The desorption of 2-butanol was shown to be molecular and reversible, following first-order desorption kinetics with T_{max} for monolayer desorption taking place at 225 K. This temperature is similar to that observed in 1-butanol studies on Ag(110) where monolayer desorption is observed at 215 K. Gellman et al. also attempted further experiments with 2-butanol using pre-oxidised surfaces. In these experiments the authors also failed to observe any significant differences between experiments using the different enantiomers. Although the authors make no direct measurements they do discuss the most probable orientation of the molecules on the surface based on previous work [28-32]. They conclude the main interaction between the molecules and the surface to be through the oxygen atom with the C-O bond axis normal to the surface. Although the authors do accept other possible orientations would be possible this hypothesis would be consistent with the work performed on acetone and methanol discussed earlier.

8.1.3 1-(1-Naphthyl) Ethylamine

In a similar manner to 2-butanol, there is only a limited amount of literature concerning the adsorption of 1-(1-naphthyl) ethylamine. However, the molecule has been the subject of some interest by Lambert et al. [33,34,35] with interest in its possible use in enantioselective heterogeneous catalysis.

NEA is a further example of a chiral molecule, which has shown some promise as a chiral modifier during the catalytic hydrogenation of methyl pyruvate to form methyl lactate. The main focus of Lambert's studies have been on the Pt(111) surface, although some other faces of Pt have also been considered including one with R handedness. The results of this work have shown that NEA adsorbs intact on the Pt(111) surface at room temperature (300 K). The authors have also shown that the naphthalene ring of the NEA molecule is inclined at an angle of $46 \pm 5^\circ$ with respect to the metal surface and propose that the molecule is bonded through both an interaction of the naphthalene ring and the lone pair of electrons on the amine nitrogen atom. STM data showed that NEA does not form any long range ordered structures, either adsorbed alone or in the presence of other adsorbates (hydrogen or methyl pyruvate). Upon heating of the sample beyond 320 K (which the authors note has previously been observed as the temperature of enantioselective collapse) dissociation of the ethylamine moiety is observed with H_2 , N_2 , HCN and C_2N_2 all observed as desorption products. From the observations of these studies, the

authors suggest that the results point towards the possibility of a 1:1 interaction model of chiral induction in the enantioselective hydrogenation of alkyl pyruvates.

Although the interaction of NEA has never been studied on Cu(111), cinchonidine, which bears a number of similarities to NEA, has been studied on the Cu(111) surface [36]. In this study the authors propose cinchonidine bonds to the surface predominately through the aromatic ring, which is inclined with respect to the surface in a similar manner to NEA on Pt. Hence, based on these studies we believe the interaction of NEA on Cu(111) will be primarily through the aromatic ring, which will be inclined with respect to the surface. In this adsorption geometry we would expect two of the groups attached to the asymmetric carbon (methyl group, amine group or a hydrogen atom) to also be in close vicinity to the surface and possibly be involved in bonding as suggested by Lambert.

In this chapter we perform the first ever ES-SHG measurements on the model adsorbate-metal systems 2-butanol/Cu(111) and 1-(1-naphthyl)ethylamine/Cu(111). We show that SHG can be used not only for chiral discrimination of adsorbates but can also provide information on the effect of the adsorbates on the metal surface.

8.2 Results

8.2.1 Initial Characterisation - 2-Butanol

Initial characterisation experiments of 2-butanol adsorption on Cu(111) were carried out using both of the UHV systems available in Glasgow. This allowed us to initially characterise the system using TPD, AES, LEED, XPS and UPS, and then use both XPS and UPS to prepare well-defined layers for SHG experiments.

Figure 1 shows nested TPD spectra from surfaces exposed to sequentially higher doses of 2-butanol obtained by monitoring the evolution of the largest cracking fraction of 2-butanol (59 amu). The largest cracking fraction has been used as monitoring the parent ion produces a small signal and poor signal to noise ratio. Exposures are quoted in units of mbar.s, with pressures being measured by an ion gauge with no correction for sensitivity.

2-butanol adsorbs reversibly on the Cu(111) surface. This is confirmed by AES, (and subsequently by XPS and UPS) taken at the end of TPD experiments showing no carbon remaining on the surface and the lack of any other desorption products such as H₂ being evolved during TPD experiments. The TPD spectra of 2-butanol displays two peaks at 170 and 210 K. The peak at 210 K saturates with increasing exposure and is assigned to desorption from a chemisorbed state. The peak at 170 K continues to increase in size with increasing exposure and is attributed to desorption from a condensed multilayer. In addition to TPD and AES, LEED experiments showed no long-range order on the surface induced by the presence of 2-butanol.

After completion of TPD and AES experiments, further characterisation of the system using the techniques of XPS and UPS was carried out. Desorption of multilayer and monolayer states is observed at temperatures consistent with those observed in TPD data and, as stated previously, XPS and UPS also show that desorption is molecular and reversible.

Figure 2 shows UP spectra recorded from monolayer coverages of R, S and racemic 2-butanol obtained after adsorption of condensed multilayers and then subsequent annealing to temperatures appropriate to desorb these, leaving only a monolayer coverage. In addition, a multilayer spectrum of 2-butanol is shown for comparison purposes. The clean Cu(111) UP spectrum has already been presented and discussed in chapter 5. Figure 2 shows that upon adsorption of 2-butanol at ca. 110 K we observe significant attenuation of emission from the copper d-band along with the appearance of adsorbate induced bands. The multilayer spectrum in figure 2 shows the presence of a broad feature between 5.5 and 11.0 eV. This appears to consist of at least two peaks at ca. 9.7 and 7.5 eV although it is difficult to interpret the exact positions due to the poorly resolved nature of the features. In addition to this broad feature, we also observe a second more resolved peak at 4.8 eV. As was the situation for the UPS work carried out in chapter 6, we have been unable to locate a gas phase spectrum of 2-butanol in the literature. Hence, the lone pair assignment is based on the same arguments already made in chapter 6.

Upon annealing to temperatures appropriate to produce a monolayer coverage we observe re-appearance of emission from the d-band but the sharp structure and surface state consistent with the clean Cu(111) surface remain absent. These observations are consistent with those made previously. We observe the broad

feature between 5.5 and 11.0 eV to become more resolved into its constituent parts. This feature appears to be constructed of at least 4 parts with the maxima at 10.5, 8.8, 7.6 and 6.2 eV. More importantly we observe no significant shift of the lone pair orbital peak, relative to the other adsorbate peaks, suggesting only a weak interaction with the Cu(111) surface, as expected from both TPD data and previous work on related molecules.

Of additional interest to the current study is the fact that the UP spectra of the R, S and racemic 2-butanol display peaks with the same relative intensities indicating that the molecules have the same adsorption geometry. This is important in demonstrating that any differences observed in SHG measurements are induced by the chirality of the molecules and not by differences in adsorption behaviour of the two different enantiomers.

Figure 3 shows C1s XP spectra corresponding to the UPS data in figure 2. The important features to note in this data are once again related to the SHG experiments that will be described shortly. Namely, the C1s data shows that the three layers produced in each experiment correspond to identical surface coverages within experimental error. Again, this is important in determining that any differences observed in SHG data are due to chirality and not due to differing adsorbate coverages. In addition to this, we also show a C1s spectrum recorded after desorption of 2-butanol, which is consistent with a clean carbon spectrum, confirming 2-butanol does not dissociate on the Cu(111) surface as described earlier.

The results obtained here during the initial characterisation of 2-butanol on Cu(111) show that the molecule interacts only weakly with the Cu(111) surface. The molecules adsorb intact and show no signs of dissociation. Additionally, this data is useful for comparison purposes during SHG experiments and demonstrates our ability to produce consistent surfaces of R, S and racemic 2-butanol for laser experiments presented in the following sections.

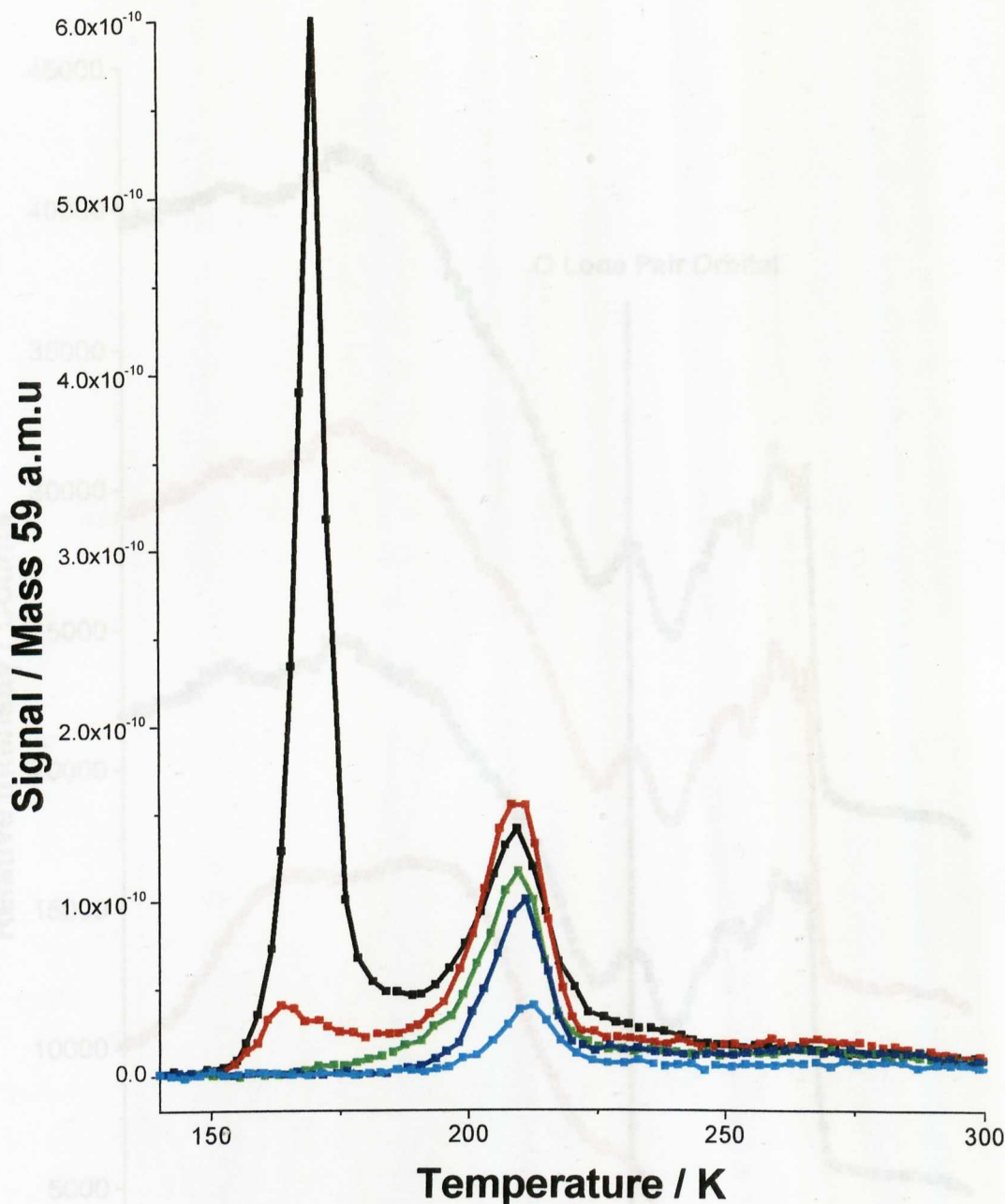


Figure. 1. TPD spectra showing the desorption of 2-butanol (fraction 59 amu) from surfaces which had been dosed with sequentially higher exposures (0.5 (cyan), 1 (blue), 2 (green), 4 (red), 5 (black) $\times 10^{-6}$ mbar.s) at ca. 100 K are displayed. All spectra were collected with a heating rate of 0.5 Ks $^{-1}$. Desorption is observed from chemisorbed (210 K) and multilayer (170 K) states.

Figure 2. Normal emission-UPS spectrum of condensed multilayers (≈ 0.5) (magenta); monolayer racemic (blue), monolayer R (red) and monolayer S (black), 2-butanol adsorbed on Cu(111). All spectra are plotted relative to E_F . Lines have been added to facilitate comparison of peak positions.

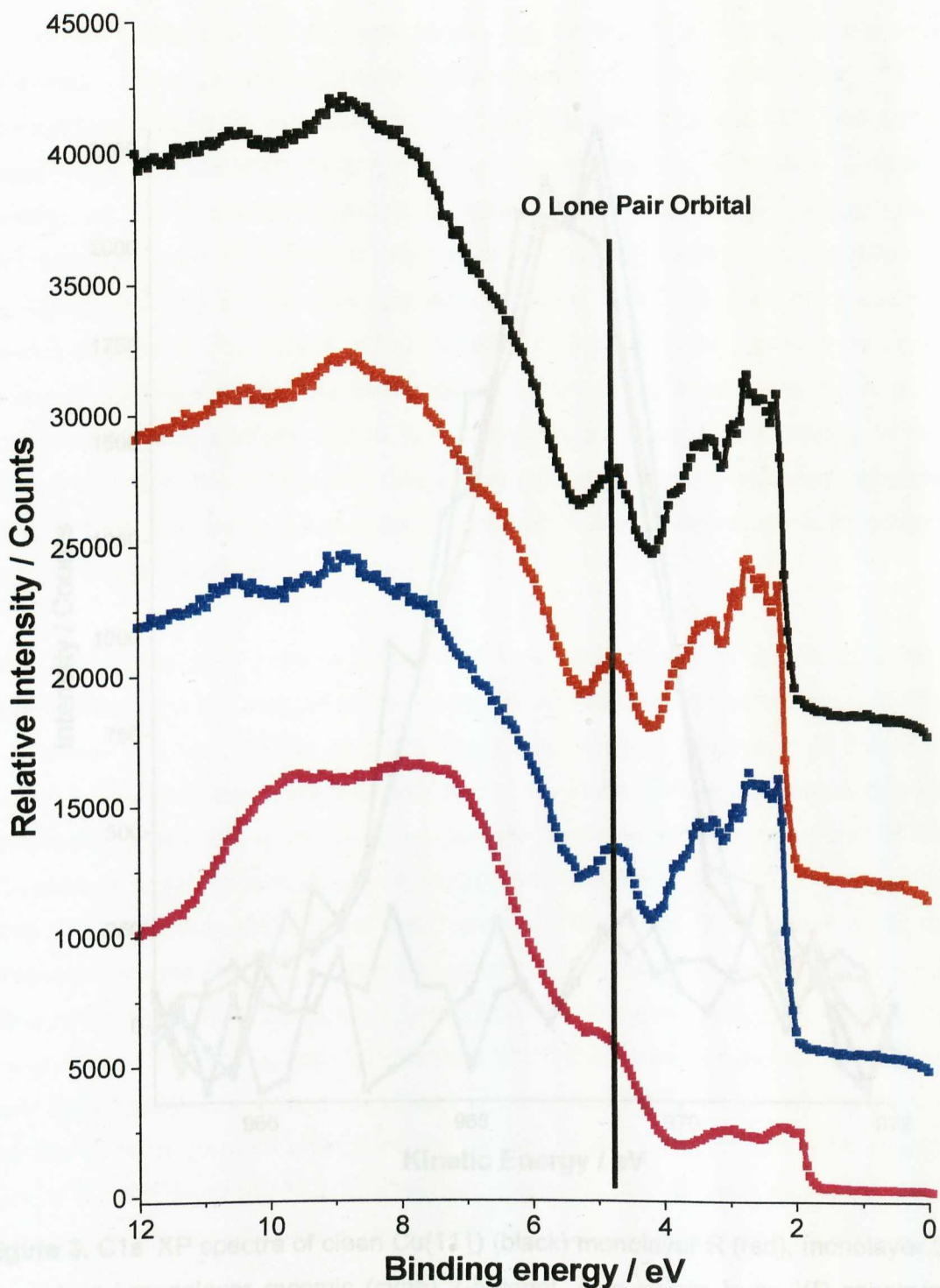


Figure 2. Normal emission UP spectrum of condensed multilayers ($\times 0.5$) (magenta), monolayer racemic (blue), monolayer R (red) and monolayer S (black), 2-butanol adsorbed on Cu(111). All spectra are plotted relative to E_F . Lines have been added to facilitate comparison of peak positions.

8.2.2 1-(1-Naphthyl) Ethylamine

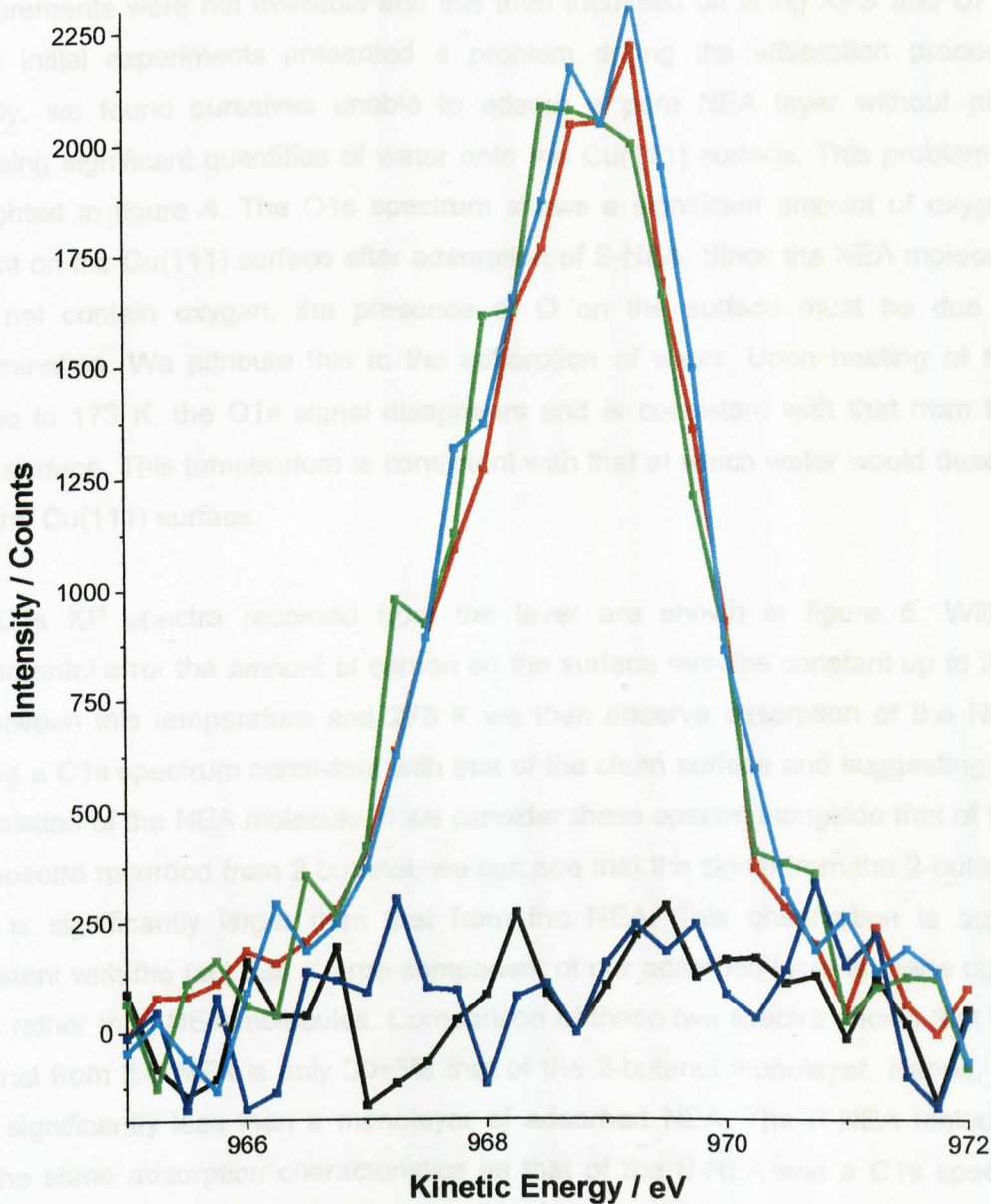


Figure 3. C1s XP spectra of clean Cu(111) (black) monolayer R (red), monolayer S (green) and monolayer racemic (cyan) 2-butanol. Also shown is an XP spectrum recorded after completion of experiments (blue).

8.2.2 1-(1-Naphthyl) Ethylamine

In a similar manner to the characterisation just presented of 2-butanol, we also performed initial characterisation experiments of NEA. However, TPD measurements were not available and this then focussed on using XPS and UPS. These initial experiments presented a problem during the adsorption process. Namely, we found ourselves unable to adsorb a pure NEA layer without also adsorbing significant quantities of water onto the Cu(111) surface. This problem is highlighted in figure 4. The O1s spectrum shows a significant amount of oxygen present on the Cu(111) surface after adsorption of S-NEA. Since the NEA molecule does not contain oxygen, the presence of O on the surface must be due to contamination. We attribute this to the adsorption of water. Upon heating of the surface to 173 K, the O1s signal disappears and is consistent with that from the clean surface. This temperature is consistent with that at which water would desorb from the Cu(111) surface.

The C1s XP spectra recorded from the layer are shown in figure 5. Within experimental error the amount of carbon on the surface remains constant up to 223 K. Between this temperature and 273 K we then observe desorption of the NEA leaving a C1s spectrum consistent with that of the clean surface and suggesting no dissociation of the NEA molecule. If we consider these spectra alongside that of the C1s spectra recorded from 2-butanol, we can see that the signal from the 2-butanol layer is significantly larger than that from the NEA. This observation is again consistent with the fact that a large component of our adsorbed layer is made up of water rather than NEA molecules. Comparison of these two spectra shows that the C signal from the NEA is only $30\pm 5\%$ that of the 2-butanol monolayer. Hence, we have significantly less than a monolayer of adsorbed NEA. The R-NEA molecule has the same adsorption characteristics as that of the S-NEA and a C1s spectra from a R-NEA layer at 173 K is shown alongside the S data for comparison purposes. Within experimental error both the R and S coverages are identical.

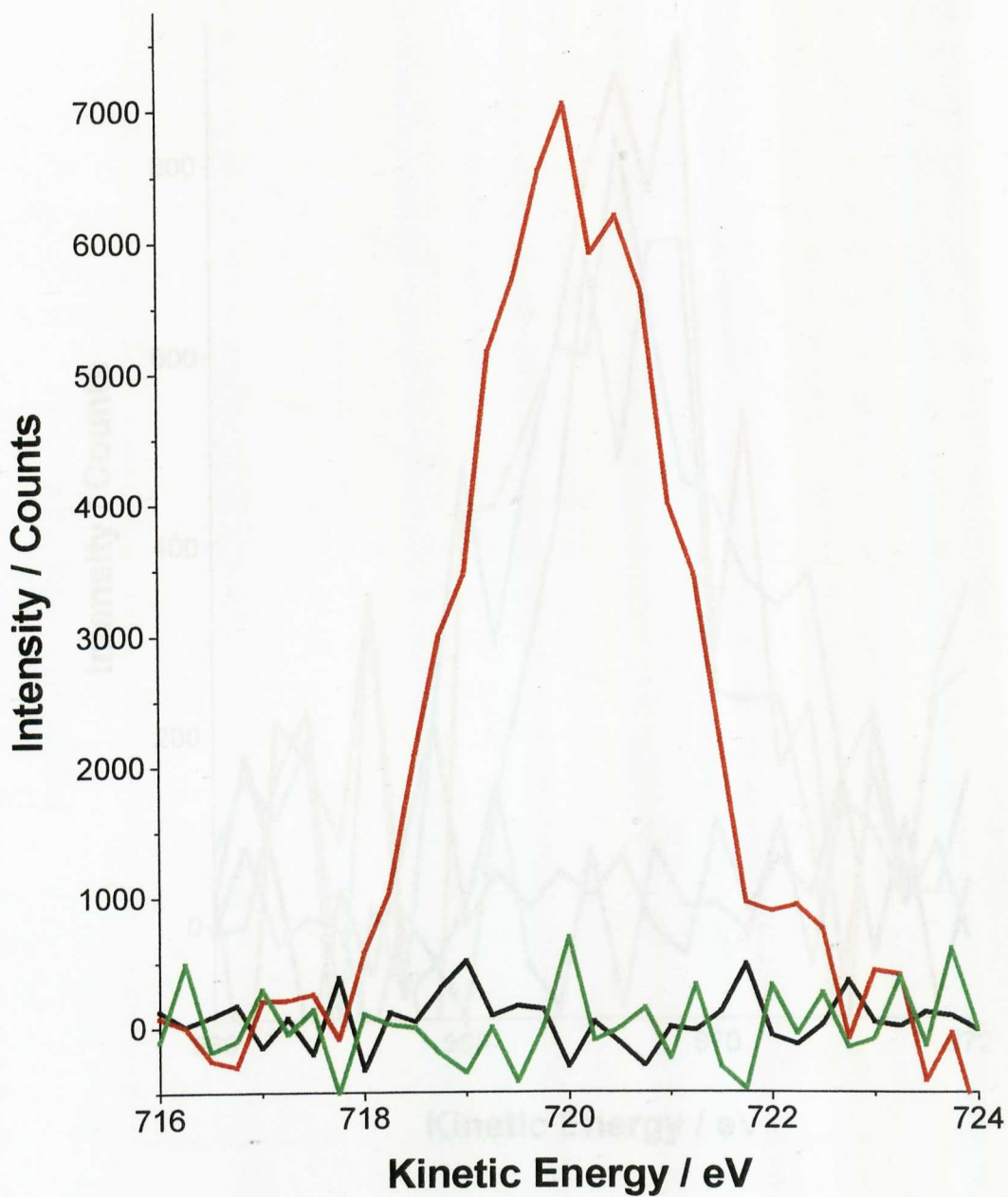


Figure 4. O1s XP spectra of clean Cu(111) (black), after adsorption of S-NEA and annealing to 153 K (red), and after annealing to 173 K (green).

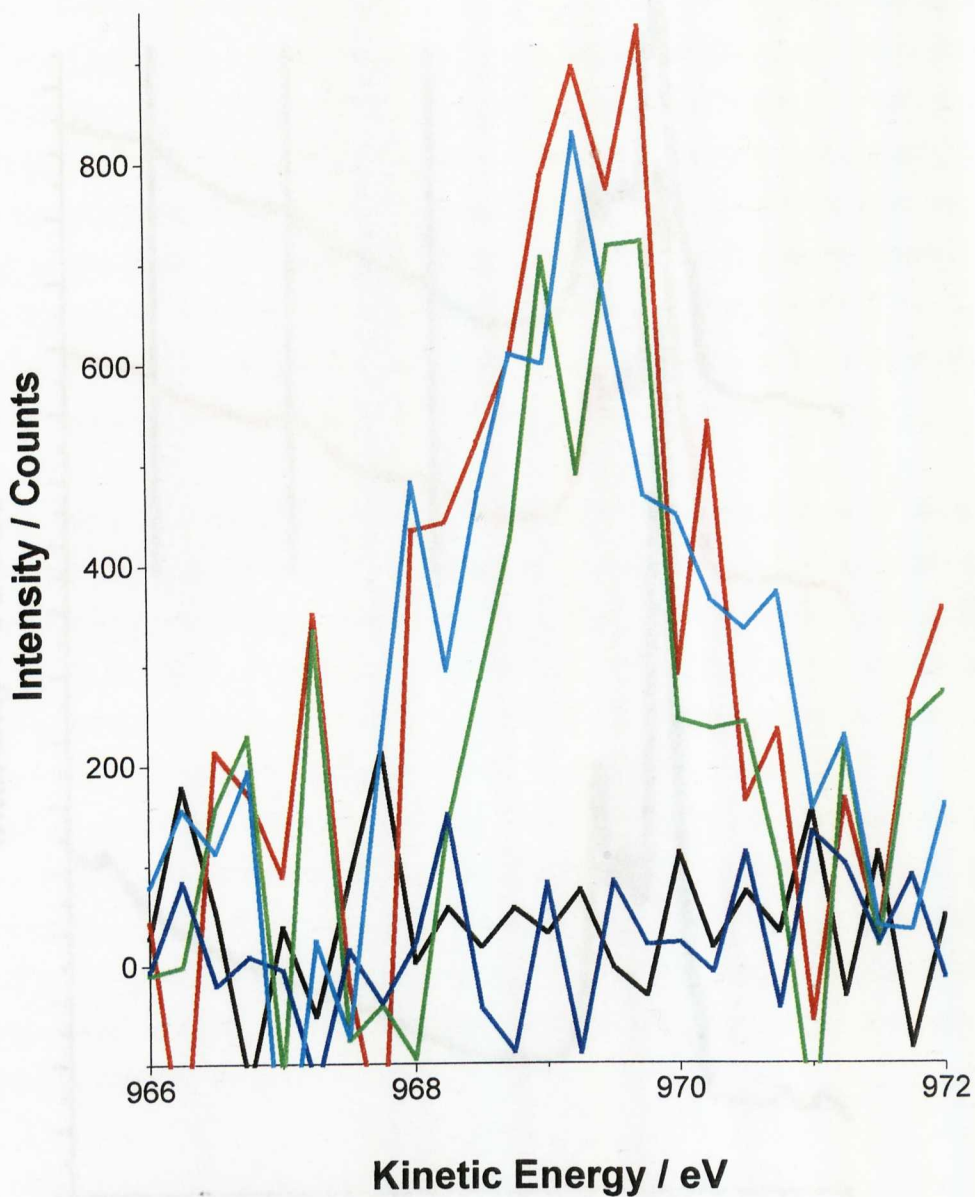


Figure 5. C1s XP spectra of clean Cu(111) (black), after adsorption of S-NEA and annealing to 173 K (red), 223 K (green), 273 K (blue), and the corresponding R-NEA spectrum after adsorption and annealing to 173 K (cyan).

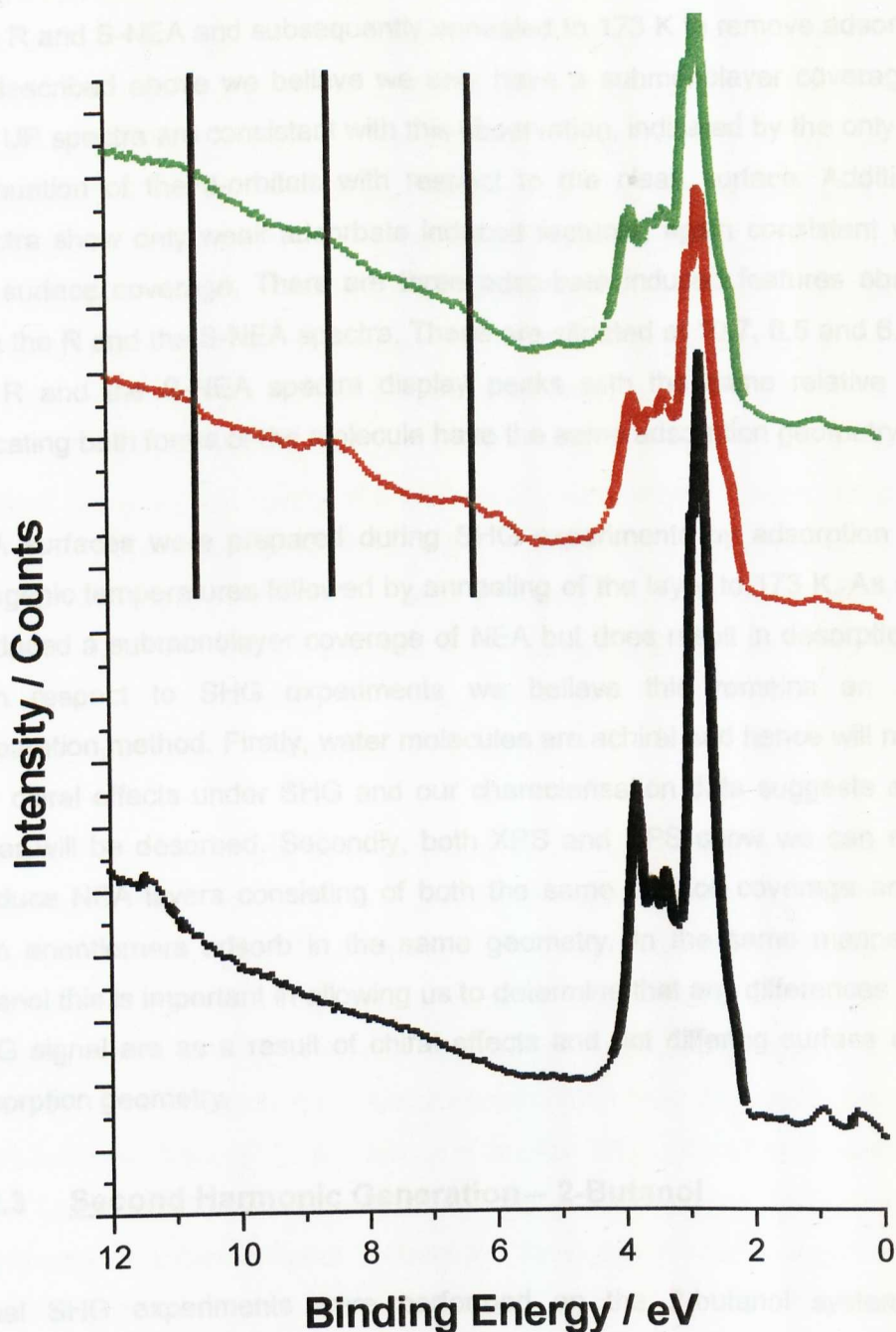


Figure 6. Normal emission UPS spectrum of clean Cu(111) (black), after adsorption of S-NEA (red) and R-NEA (green) and subsequent annealing to 173 K. All spectra are plotted relative to E_F . Lines have been added to aid comparison.

The corresponding UPS data is shown in figure 6 from Cu(111) surfaces exposed to both R and S-NEA and subsequently annealed to 173 K to remove adsorbed water. As described above we believe we only have a submonolayer coverage of NEA. The UP spectra are consistent with this observation, indicated by the only very small attenuation of the d-orbitals with respect to the clean surface. Additionally, the spectra show only weak adsorbate induced features, again consistent with only a low surface coverage. There are three adsorbate induced features observable in both the R and the S-NEA spectra. These are situated at 10.7, 8.5 and 6.3 eV. Both the R and the S-NEA spectra display peaks with the same relative intensities, indicating both forms of the molecule have the same adsorption geometry.

NEA surfaces were prepared during SHG experiments by adsorption of NEA at cryogenic temperatures followed by annealing of the layer to 173 K. As shown, this produced a submonolayer coverage of NEA but does result in desorption of water. With respect to SHG experiments we believe this remains an appropriate preparation method. Firstly, water molecules are achiral and hence will not generate any chiral effects under SHG and our characterisation data suggests at 173 K all water will be desorbed. Secondly, both XPS and UPS show we can reproducibly produce NEA layers consisting of both the same surface coverage and also that both enantiomers adsorb in the same geometry. In the same manner as for 2-butanol this is important in allowing us to determine that any differences observed in SHG signal are as a result of chiral effects and not differing surface coverage or adsorption geometry.

8.2.3 Second Harmonic Generation – 2-Butanol

Initial SHG experiments were performed on the 2-butanol system described previously, with measurements performed on the R, S and racemic overlayers. Linearly polarised light (1064 nm) is incident on the 2-butanol/Cu(111) surface, and changes to the polarisation state of the outgoing SH signal (532 nm) induced by the chirality of the layer are monitored. In the simplest case this is as a result of the polarisation rotation of the light induced by the chiral molecules as discussed earlier. However, in making measurements from metal surfaces the process is complicated by the fact that the observed SH signal has more than one possible contribution. Firstly, a major contribution from the metal-adsorbate interface (SH_{metal}) and a minor contribution from the adsorbate-vacuum interface (SH_{ads}). Both of these contributions can differ in magnitude and phase and reflect different components of

the adsorption system. The SH_{metal} component reflects the electronic structure of the metal, and any changes of SHG signal reflect changes to the electronic structure of the metal induced by adsorbates. Correspondingly, SH_{ads} reflects the adsorbate and changes to it reflect changes of the adsorbate (e.g. chirality). The major problem encountered in these SHG measurements is that for almost all-experimental geometries we observe SH_{metal} is significantly greater than SH_{ads} [6,36]. Under these circumstances changes to the metal dominated signal would only be observed if the electronic structure of the metal had been imbued with chirality by the adsorbate molecules. However, the relative sizes of both contributions to the overall SH signal can be controlled by altering the combinations of the fundamental and reflected light detected. Using a combination of s-polarised fundamental radiation and detecting at or close to s-polarisation, results in a reduction in SH_{metal} signal to such an extent that the contribution from SH_{ads} becomes detectable. However, the use of p-polarised incident radiation (electric field perpendicular to the surface) has the opposite effect, maximising the SH_{metal} component and allowing us to monitor changes to the electronic structure of the surface [11,36, also see chapter 2].

2-butanol chiral overlays were prepared on Cu(111) based on the results in the section described previously. Experiments were performed with s-polarised fundamental radiation and the outgoing SH signal was detected at two polarisations. These have been labelled I_{+35} and I_{-55} representing detection at $+35^\circ$ and -55° with respect to s-polarised light respectively. Based on crystal symmetry arguments the SH signal at $+35^\circ$ should have lower contributions from the metal surface electric dipole susceptibilities (χ^{ooo}), and hence a smaller SH_{metal} than those collected at -55° [39]. This hypothesis is confirmed experimentally by the clean surface measurements shown in figure 7 where the SH signal at $+35^\circ$ is significantly smaller than the signal detected at -55° with a I_{+35}/I_{-55} ratio of 0.088 ± 0.002 . This ratio, and the corresponding ones for both 2-butanol and NEA monolayers, are averages of values obtained from five freshly prepared surfaces with quoted errors corresponding to one standard deviation in ratio.

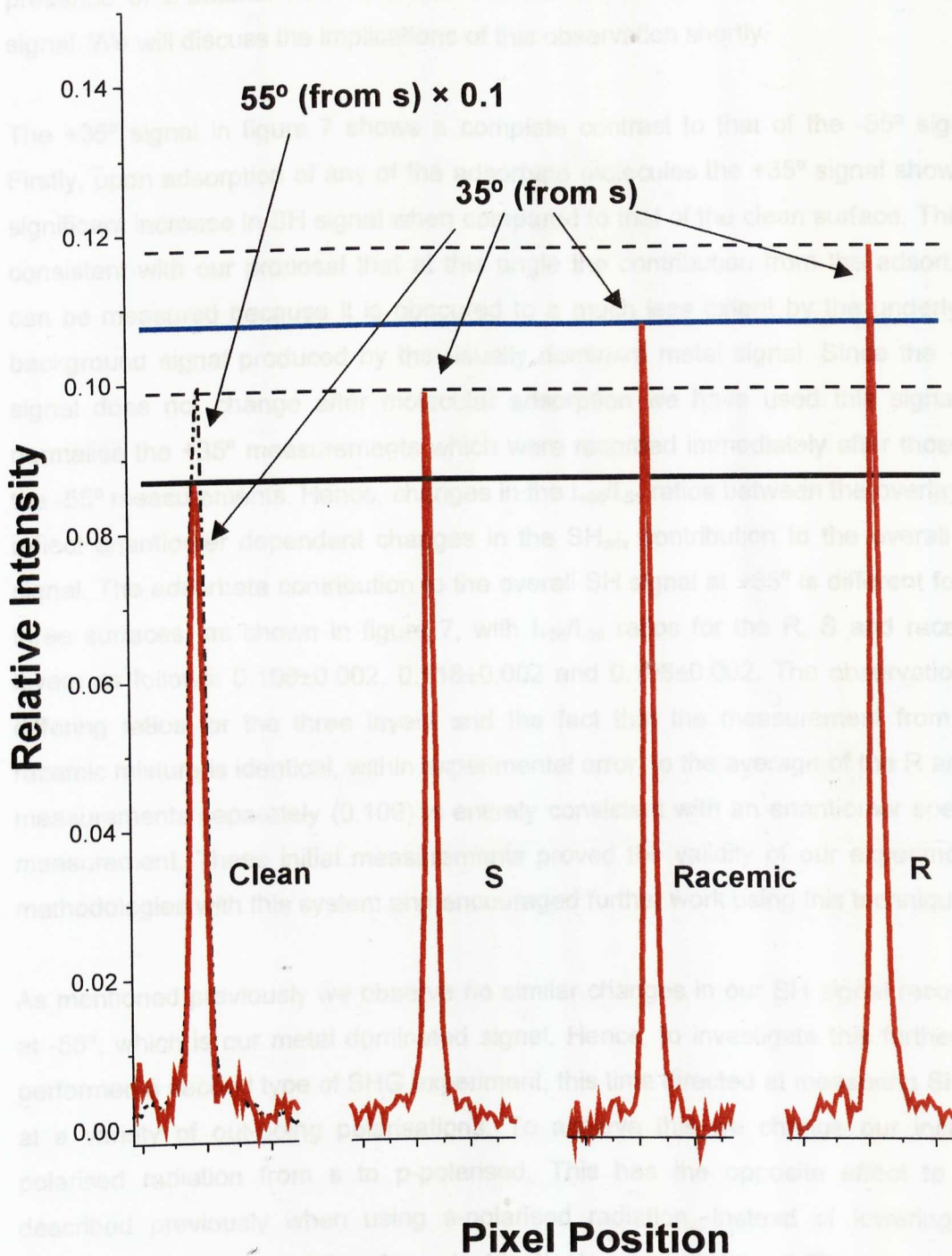


Figure 7. SHG signals monitored at $+35^\circ$ (solid line) and -55° (dashed line $\times 0.1$) for the clean surface and $+35^\circ$ signal for a monolayer of S, R and racemic 2-butanol. All the signals have been normalised against their respective -55° signals. Horizontal lines have been added to aid comparison.

The SH signal recorded for R and S monolayers of 2-butanol at an outgoing polarisation of -55° is identical to that of the clean surface. In other words, the presence of 2-butanol has no effect and makes no contribution to the -55° SH signal. We will discuss the implications of this observation shortly.

The $+35^\circ$ signal in figure 7 shows a complete contrast to that of the -55° signal. Firstly, upon adsorption of any of the adsorbate molecules the $+35^\circ$ signal shows a significant increase in SH signal when compared to that of the clean surface. This is consistent with our proposal that at this angle the contribution from the adsorbate can be measured because it is obscured to a much less extent by the underlying background signal produced by the usually dominant metal signal. Since the -55° signal does not change after molecular adsorption we have used this signal to normalise the $+35^\circ$ measurements which were recorded immediately after those of the -55° measurements. Hence, changes in the I_{+35}/I_{-55} ratios between the overlayers reflect enantiomer dependent changes in the SH_{ads} contribution to the overall SH signal. The adsorbate contribution to the overall SH signal at $+35^\circ$ is different for all three surfaces, as shown in figure 7, with I_{+35}/I_{-55} ratios for the R, S and racemic layers as follows: 0.100 ± 0.002 , 0.118 ± 0.002 and 0.108 ± 0.002 . The observation of differing ratios for the three layers and the fact that the measurement from the racemic mixture is identical, within experimental error, to the average of the R and S measurements separately (0.109) is entirely consistent with an enantiomer specific measurement. These initial measurements proved the validity of our experimental methodologies with this system and encouraged further work using this technique.

As mentioned previously we observe no similar changes in our SH signal recorded at -55° , which is our metal dominated signal. Hence, to investigate this further we performed a second type of SHG experiment, this time directed at measuring SH_{metal} at a variety of out-going polarisations. To achieve this we change our incident polarised radiation from s to p-polarised. This has the opposite effect to that described previously when using s-polarised radiation. Instead of lowering the contribution from the metal surface electric dipole susceptibilities (χ^{eee}) we maximise them using p-polarisation and hence, we have a SH signal dominated by the metal. Using p-polarised incident radiation we then measure the SH signal detected while rotating the polarisation of the out-going radiation in 5° intervals. The results of these measurements on R, and S 2-butanol layers along with that measured from clean Cu(111) are shown in figure 8.

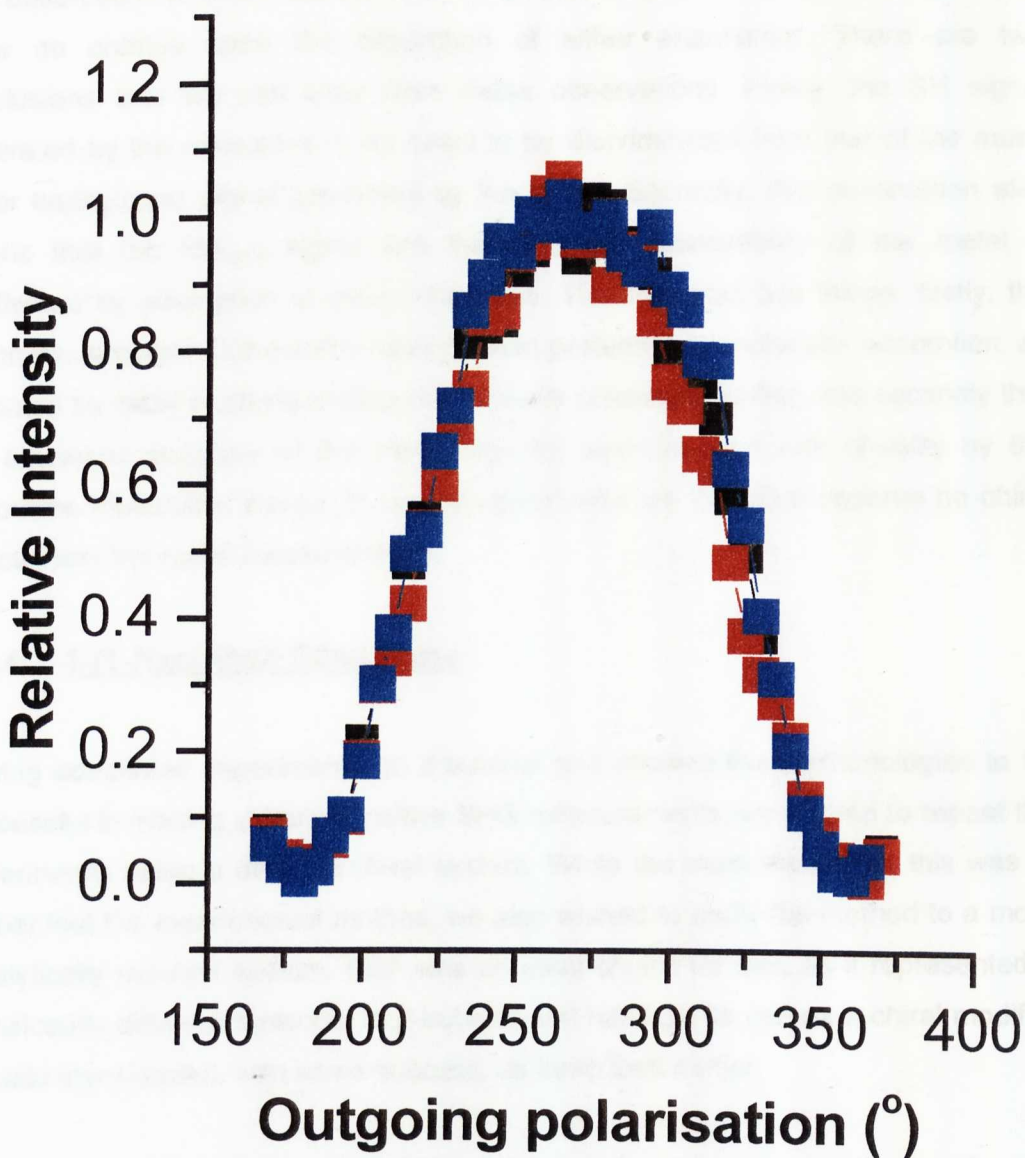


Figure 8. SHG signals monitored during rotation of out-going polarisation using p-polarised fundamental radiation for a monolayer of R (black) and S (red) 2-butanol and clean Cu(111) (blue). All the signals have been normalised with respect to the maximum for p-polarised light.

Within experimental error we observe all three spectra from the R and S 2-butanol and from the clean surface to be identical. In other words we observe no change to the SH signal induced by the adsorption of either the S or R 2-butanol molecules. This observation is consistent with our observations made earlier at -55° , which also show no change upon the adsorption of either enantiomer. There are two conclusions that we can draw from these observations. Firstly, the SH signal generated by the molecules is too small to be discriminated from that of the much larger background signal generated by the metal. Secondly, this observation also means that the SH_{metal} signal and therefore the susceptibility of the metal is unaffected by adsorption of chiral molecules. This indicates two things: firstly, the electronic structure of the metal has not been perturbed by molecular adsorption, as indicated by initial characterisation experiments presented earlier, and secondly that the electronic structure of the metal has not been imbued with chirality by the adsorbate molecules. Hence, in our measurements we therefore observe no chiral effects from the metal measurements.

8.2.4 1-(1-Naphthyl) Ethylamine

Having completed experiments on 2-butanol and showed the methodologies to be successful in making chirally sensitive SHG measurements, we wished to repeat the experiments using a different chiral system. While the main reason for this was to further test the experimental method, we also wished to apply the method to a more catalytically relevant system. NEA was an ideal choice for this, as it represented a significantly different molecule to 2-butanol and has had its use as a chiral modifier already investigated, with some success, as described earlier.

The same experiments just described on 2-butanol overlayers were then performed on NEA layers. As before, we used s-polarised fundamental radiation and detected the outgoing light at angles of $+35^\circ$ and -55° from s-polarised light. The results of these measurements are shown in figure 9.

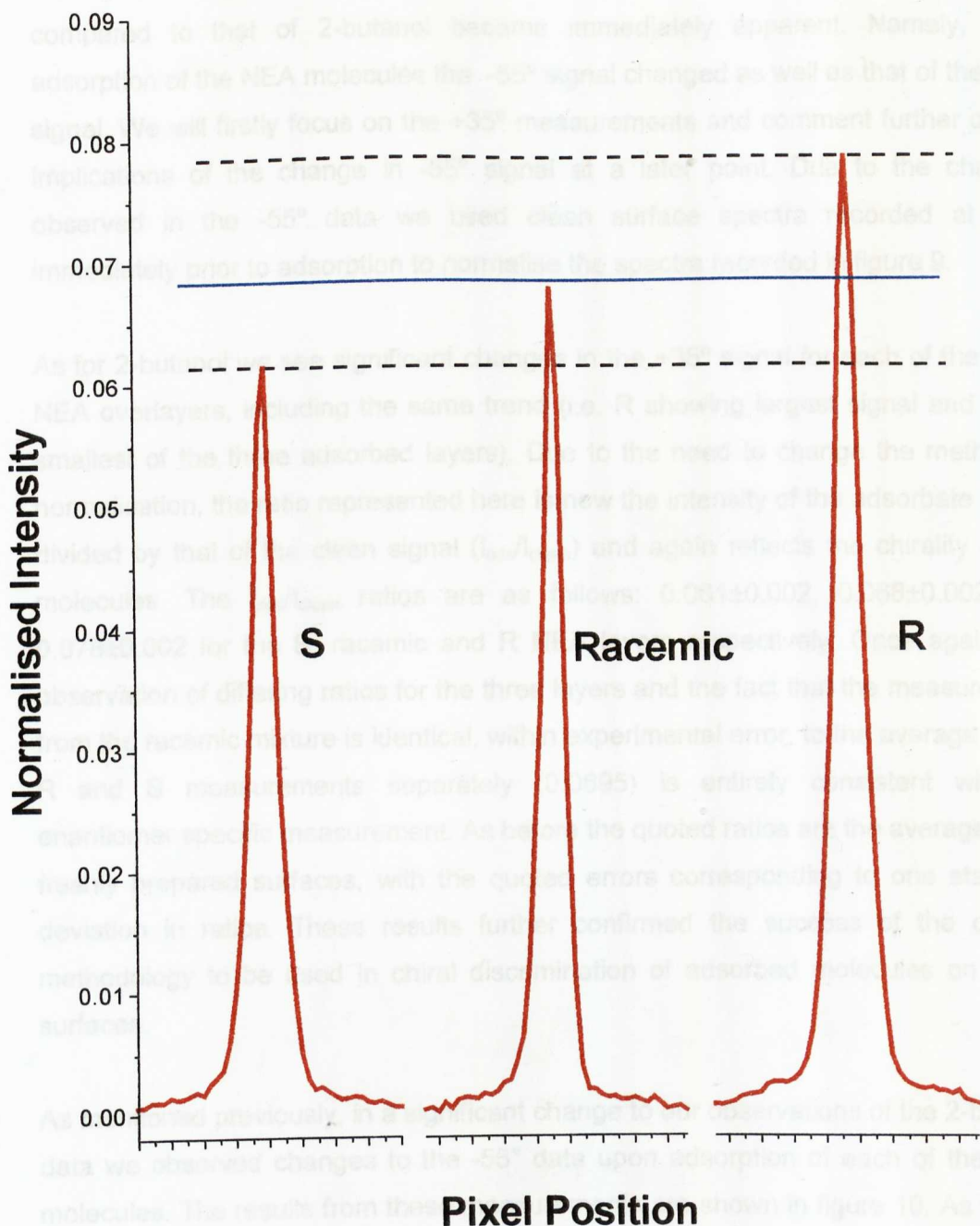


Figure 9. SHG signals monitored at $+35^\circ$ for a monolayer of S, R and racemic NEA. All the signals have been normalised against their respective $+35^\circ$ clean surface signals. Horizontal lines have been added to aid comparison.

While performing these measurements one significant difference to the -55° signal compared to that of 2-butanol became immediately apparent. Namely, upon adsorption of the NEA molecules the -55° signal changed as well as that of the $+35^\circ$ signal. We will firstly focus on the $+35^\circ$ measurements and comment further on the implications of the change in -55° signal at a later point. Due to the changes observed in the -55° data we used clean surface spectra recorded at $+35^\circ$ immediately prior to adsorption to normalise the spectra recorded in figure 9.

As for 2-butanol we see significant changes in the $+35^\circ$ signal for each of the three NEA overlayers, including the same trend (i.e. R showing largest signal and S the smallest of the three adsorbed layers). Due to the need to change the method of normalisation, the ratio represented here is now the intensity of the adsorbate signal divided by that of the clean signal ($I_{\text{ads}}/I_{\text{clean}}$) and again reflects the chirality of the molecules. The $I_{\text{ads}}/I_{\text{clean}}$ ratios are as follows: 0.061 ± 0.002 , 0.068 ± 0.002 and 0.078 ± 0.002 for the S, racemic and R NEA layers respectively. Once again, the observation of differing ratios for the three layers and the fact that the measurement from the racemic mixture is identical, within experimental error, to the average of the R and S measurements separately (0.0695) is entirely consistent with an enantiomer specific measurement. As before the quoted ratios are the averages of 5 freshly prepared surfaces, with the quoted errors corresponding to one standard deviation in ratios. These results further confirmed the success of the current methodology to be used in chiral discrimination of adsorbed molecules on metal surfaces.

As mentioned previously, in a significant change to our observations of the 2-butanol data we observed changes to the -55° data upon adsorption of each of the three molecules. The results from these measurements are shown in figure 10. As for the $+35^\circ$ data we observe significant changes in recorded signal for each of the three NEA overlayers. However, the changes we observe are not in the same sense as the previously recorded data from either 2-butanol or NEA at $+35^\circ$ and do not show the usual chiral characteristic of the average value from the R and the S measurements being identical to that from the clean surface. The ratio represented in these measurements is the intensity of the adsorbate signal divided by that of the clean signal ($I_{\text{ads}}/I_{\text{clean}}$) recorded at -55° . The $I_{\text{ads}}/I_{\text{clean}}$ ratios are as follows: 0.097 ± 0.004 , 0.085 ± 0.003 and 0.104 ± 0.003 for the S, racemic and R NEA layers respectively. As before the quoted ratios are the averages of 5 freshly prepared surfaces, with the quoted errors corresponding to one standard deviation in ratios.

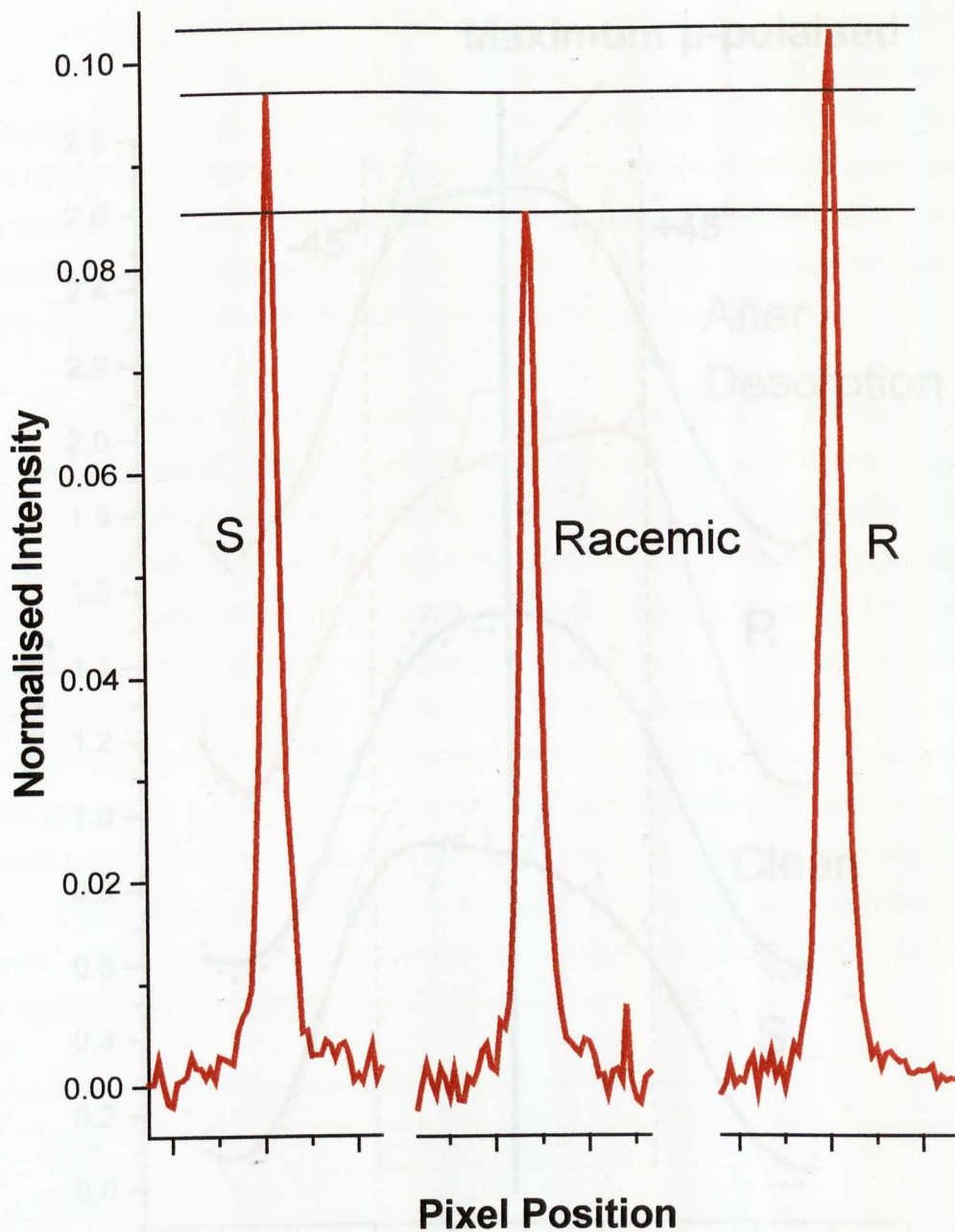


Figure 10. SHG signals monitored at -55° for a monolayer of S, R and racemic NEA. All the signals have been normalised against their respective -55° clean surface signals. Horizontal lines have been added to aid comparison.

The observation of a change in the metal dominated signal is interesting in that no similar changes were observed for 2-butanol, but the fact that the response is not the same as for our previous $+35^\circ$ measurements with a racemic measurement between that of the two enantiomers raises the question as to whether this is a true chiral effect. The observation is significant however, and encouraged us to investigate the metal response to NEA layers in greater detail. To do this, we repeat the same measurements described earlier on 2-butanol using p-polarised radiation on R and S NEA layers. The results of this are shown in figure 11.

The results of these experiments on 2-butanol produced identical spectra for both the R and S 2-butanol overlayers. For the NEA molecules however, figure 11 shows a number of differences between the R and the S enantiomers of NEA. Firstly, if we consider the profile recorded from the clean Cu(111) surface we can see that we have an essentially symmetric spectrum about the mid-point, the point of maximum p-polarisation. However, upon adsorption of either the S or R NEA molecules the spectra become distinctly less symmetric. This is particularly obvious around the points of $+45^\circ$ and -45° from the maximum for p-polarised radiation. In an attempt to clarify the results depicted in the spectra, we have quantified the spectra in two different ways. Firstly, we have calculated the ratio I_{+45}/I_{-45} from the intensity of the signal at the points shown on figure 11. Secondly, we measured the integrated area on each side of the maximum and used this to calculate a second ratio labelled I_+/I_- . The results of these measurements are displayed in table 1.

	I_{+45} / I_{-45}	I_{-45} / I_{+45}	I_+ / I_-	I_- / I_+
R-NEA	1.50 ± 0.10	0.67 ± 0.07	1.14 ± 0.06	0.88 ± 0.05
S-NEA	0.75 ± 0.07	1.33 ± 0.13	0.90 ± 0.06	1.11 ± 0.07

Table 1. Ratios of the intensity of the SHG signal at $+45^\circ$ and -45° from figure 11 and vice versa and similar ratios for the integrated area under the spectra.

Firstly, the ratios show clearly that we obtain different results for each of the adsorbate molecules. In addition to this, we also observe the measurements to have a chiral feature. For a true measurement of chirality, the results for the left and right handed molecules should mirror each other. In other words I_{+45}/I_{-45} for the R-NEA should produce the same value as taking a ratio of I_{-45}/I_{+45} from the S-NEA spectrum. As highlighted in table 1, we do indeed see this ratio for these measurements within experimental error. Additionally, we also see this in the

integrated area measurements, with these trends suggesting the observation is definitely a chiral effect.

After completion of measurements on the R and S NEA layers we then heated the crystal to 273 K to desorb the NEA overlayers. We then repeated the measurements just described. An example of these measurements is shown in figure 11 and shows a return to a symmetric profile about the p-polarised direction, consistent with the spectra obtained from clean Cu(111). Hence, the effects we observe on the metal are only present while in the presence of the adsorbed chiral layers.

8.3 Discussion

The aim of performing these experiments was to develop a new method of chiral discrimination to allow a wider range of chiral problems to be addressed than allowed by current methods. The initial experiments reported here have proved to be doubly successful in the sense that we have shown that the technique can not only be used in chiral discrimination of adsorbate species but can also be used to examine changes to the metal substrate.

In this chapter we have reported the results of two types of SHG measurement. The first of these used s-polarised radiation and the aim of the experiments was to monitor adsorbate chirality by reducing the SH_{metal} contribution to the overall SH signal. In the first instance, the measurements we have performed here on both 2-butanol and NEA at $+35^\circ$ show experimentally that the SH_{metal} signal can be minimised by the use of s-polarised fundamental radiation and careful choice of detection polarisation. Secondly, our data also shows that the technique can indeed be used for chiral discrimination, with the signals shown here recorded from R, S and racemic 2-butanol and NEA entirely consistent with a chiral measurement. In other words, we observe the magnitude of the signal from the racemic layer to be intermediate of the signal from the R and the S. This comes about as the chiral components of the susceptibilities being measured change sign but not magnitude. It is this change in sign going from left to right handed molecules that is observed in measurements and it is for this reason that the R and S signal is the same in magnitude but has different signs with respect to the racemic signal.

These results clearly show the technique can be used for the purposes of chiral discrimination and suggest further development would be worth while. Based on the precision of our measurements reported here on 2-butanol we estimate that enantiomeric excesses of 22% could be detected with the current experimental set up. While for the NEA molecule we estimate enantiomeric excesses of 23% could be detected. We believe that excesses >22 and 23% respectively, could be achieved by further work developing the system. Particularly, we believe the precision of the measurements could be improved by investigating further the most favourable out-going polarisations at which measurements could be made.

If we now turn our attention to the measurements of the metal substrate made at -55° and also using p-polarised light we observe a significantly different situation to that observed in the measurements just described. Measurements previously made in-resonance with the metal (already discussed in the introduction) have been shown to be particularly sensitive to the effects of adsorbates on the electronic structure of surfaces and the results we have presented here upon adsorption of NEA agree with these previous observations. However, we observe a significant difference in these experiments compared to those studying molecular adsorption previously. Namely, we observe a chiral response from the metal induced by the adsorption of chiral adsorbates.

Before considering this observation further we must address the issue of the origin of this observation. If the signal from the metal is the dominating contribution to the signal we are measuring then our observations represent a change to the electronic structure of the metal. However, if the SH_{abs} signal is comparable to that of the SH_{metal} then our observations could potentially be caused as a result of interference effects. To address this issue, we now consider the magnitude of each component to the overall signal (i.e. from the metal-adsorbate interface and the adsorbate-vacuum interface). The observed SH signal is determined by the second order susceptibility (χ^2) of the copper, χ^2_{Cu} , and NEA layer, χ^2_{NEA} . χ^2_{Cu} has been measured experimentally in a previous study and has a value of 1.54×10^{-12} esu [11]. The value of χ^2_{NEA} has never been measured or calculated previously but is determined from the hyperpolarizability (β) of each single molecule and the number density of the surface molecules. While β has never been measured for NEA, considerable experimental data does exist for a number of other mono-substituted aromatic compounds, such as benzene, stilbenes and polyphenyls [38,39]. For all cases,

$\beta \leq 10^{-30}$ have been obtained. In addition to these experimental measurements, the value for naphthalene has been calculated theoretically and has been shown to be of the same order of magnitude as for benzene [40]. Enhancements of χ^2 have been observed previously when electronic transitions of chiral films of the film coincide with the frequency of the SH radiation [41]. However, NEA is transparent at the wavelengths of both the incident and SH radiation and we therefore do not expect such effects to play a role in these experiments. Therefore, if we assume 10^{-30} is an upper limit for β and we use a value of $\sim 10^{14} \text{ cm}^{-2}$ [33] as a value of the surface molecular density, we obtain $\chi^2_{\text{NEA}} \leq 10^{-16}$ esu. Hence, we believe the SH signal produced by the copper to be significantly greater than that from the NEA layer. We therefore conclude that our observed change is produced by a change to the electronic structure of the metal surface and not by the effects of interference.

Turning our attention to the origin of our observed change to the SH_{metal} signal we believe that there are two possibilities. Firstly, the change could be as a result of a physical reconstruction of the Cu(111) surface and therefore also the electronic structure. Alternatively, purely a change to the electronic structure of the metal without physical reconstruction. However, we believe our results here suggest a physical reconstruction of the surface is unlikely and we therefore attribute the effect to a change in the surfaces electronic structure. This is based on the fact that firstly, as shown during the initial characterisation of NEA adsorption, NEA interacts only weakly with the Cu(111) surface. In addition to this, the cryogenic temperatures at which NEA is deposited would also suggest significant chiral restructuring (etching) of the surface would be unlikely. Finally, our SHG measurements also show that the chiral response imbued by the adsorbates on the metal is lost following desorption of the NEA after heating to 273 K. Previous work on adsorbate induced chiral restructuring of copper [42] has shown it involves the formation of chiral facets. These have associated chiral electronic states that remain on the surface after removal of the adsorbate and have been shown to be stable up to the annealing temperature of the metal (*ca.* 873 K). Hence, the fact our own observations show the chiral response of the metal is lost well below annealing temperatures again suggest the effect is electronic in nature. Hence, we believe the adsorption of NEA on Cu(111) results in the electronic structure of the metal becoming imbued with chirality, rather than the surface physically restructuring. This, in turn, must result in the symmetry associated with the electronic structure changing from that associated with the (111) face, C_{3v} , to one associated with chirality, C_{∞} . In turn, this change of

symmetry will result in a change in the second order susceptibility tensors associated with the metal and it is this change we have detected in our experiments.

Having established that we believe NEA instils chirality on to the electronic structure of the metal surface, we are left with one overriding question. Why do we observe this effect upon adsorption of NEA but not 2-butanol? This question may be of particular significance as it may provide a possible answer as to why only certain molecules have been successful as chiral modifiers. From the results of our initial characterisation experiments we know that although NEA has a stronger interaction with the surface than 2-butanol, both molecules interact only weakly with the copper surface. Hence, we do not believe the stronger interaction observed for NEA is sufficient to account for our observations. Therefore we must look beyond purely strength of interaction of the two molecules. Specifically, an examination of the level of contact between the molecules and the surface may shed light on the subject. As mentioned in the introduction section, there is no previous work in the literature examining the bonding of either molecule on the Cu(111) surface, so we have to rely on previous work performed on other surfaces. Consideration of this previous work suggests that the main interaction of the butanol molecule is through the lone pair of the oxygen atom, with the molecule in an upright geometry. This would result in the molecule having this as the only point of contact with the surface. The NEA molecule on the other hand will have a completely different adsorption geometry on the Cu(111) surface. The work of Lambert et al. has shown that NEA has a strong interaction between its aromatic rings and the surface. This interaction is a likely reason for the greater bond strength of NEA compared to 2-butanol but it does also result in the molecule being significantly inclined with respect to the surface normal. Additionally, an interaction between the lone pairs of the amine group has been suggested and in addition we believe a third interaction between the CH₃ group or H atom attached to the chiral centre is also likely although expected to be weak. A schematic diagram of the adsorption of both these molecules and the points of contact with the surface is shown in figure 12.

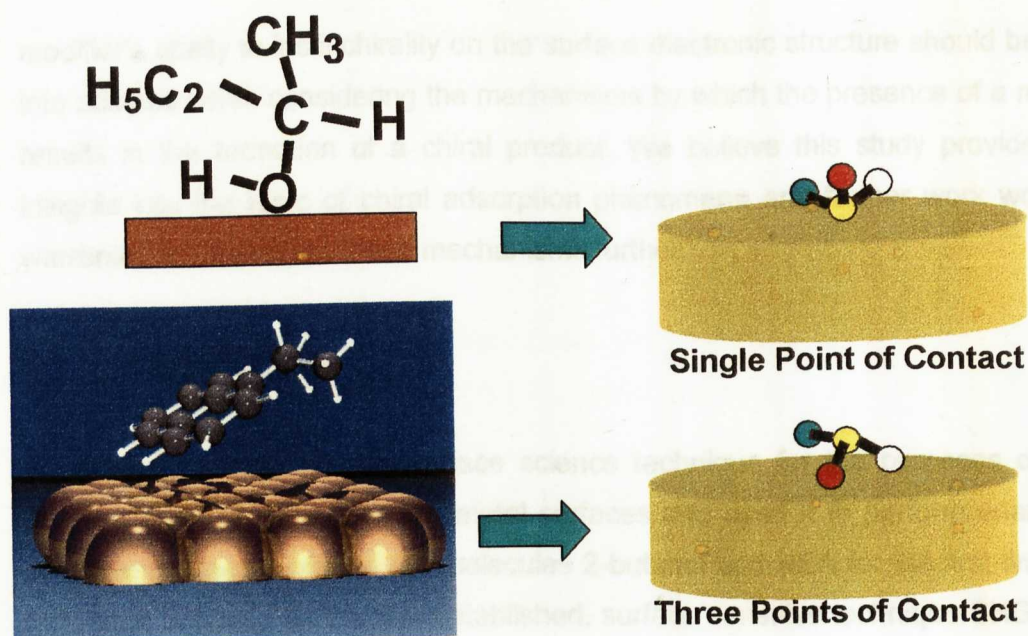


Figure 12. Schematic diagram showing proposed points of interaction between the Cu(111) surface and the 2-butanol and NEA molecules respectively.

We propose that it is the different adsorption geometry of the two molecules that can account for the instilling of chirality on the copper surface. Indeed, in some respects this may be a very simple answer to what has been considered to be a complicated question. For a molecule to impart chirality onto a surface, the surface must “feel” the chirality of that molecule. If the molecule only interacts with the surface at one point the three-dimensional chirality of that molecule cannot be transferred to the surface through only this single point. However, with increased contact the overall structure, the left or right handed “chiral footprint”, of the molecule can be transferred to the surface. Hence, while 2-butanol does not have the ability to imbue a “chiral footprint” on the surface, as a result of an adsorption geometry with only one point of contact with the Cu(111) surface. The adsorption geometry of NEA does result in the imparting of chirality on the surface through a “chiral footprint”.

These observations may be significant with respect to the mechanisms involved in enantioselective catalysis. Until now, previous work on chiral modifiers [43-47] has generally suggested mechanisms based on purely geometric arguments. These have suggested that the chiral modifier interacts directly with the achiral reactants, controlling the stereochemistry of the surface transition-state and therefore the chirality of the reaction products. Models of this type have been shown to be appropriate under certain circumstances but as yet a general mechanism has never been proposed. Hence, based on the results of this study, we suggest that a chiral

modifier's ability to instil chirality on the surface electronic structure should be taken into account when considering the mechanisms by which the presence of a modifier results in the formation of a chiral product. We believe this study provides new insights into the topic of chiral adsorption phenomena and further work would be warranted to investigate these mechanisms further.

8.4 Conclusions

We have developed a new surface science technique for the purposes of chiral discrimination of adsorbates on metal surfaces and used it to perform enantiomer sensitive measurements of the molecules 2-butanol and NEA for the first time. The technique is based on the well-established, surface sensitive technique SHG, which has already been shown to be sensitive to chirality although it has never been used on a metal surface before. The major complication of performing such measurements is posed by the large, usually dominating signal from the metal surface. However, this problem can be overcome by careful selection of in-going and out-going polarisation, which can be used to minimise the metal signal and allow detection of adsorbate SH signal.

Having developed the methodologies of the ES-SHG technique we then performed chiral discrimination measurements on R, S and Racemic 2-butanol and NEA overlayers on Cu(111). Using these systems, we have showed that the technique is successful in making chirally sensitive measurements of adsorbates. However, we have also shown that the technique can be sensitive to molecular induced chirality on the metal surface. In the presence of one enantiomer of the NEA molecule we observe the Cu(111) electronic structure adopting a chiral image related to the handedness of the molecule present. A similar response was not observed in the presence of either enantiomer of 2-butanol. On the basis of these measurements we propose the ability of a molecule to induce a chiral image on a metal surface may play an important role in determining a molecules success as a chiral modifier.

Having established methodologies and proved the technique to be successful, we believe we have opened up a vast avenue for the future study of chirality on metal surfaces. Of particular interest, stemming from the observations in this study would be to explore the hypothesis that molecules useful as chiral modifiers instil chirality on the metals electronic structure. Additionally, testing the methodologies further on

developing the technique further to investigate the origin of these measurements would be interesting to a wider community.

8.5 References

- [1] M.A. Keane and G. Webb, *J. Mol. Catal.* 73 (1992) 91
- [2] S.P. Griffiths, P. Johnston and P.B. Wells, *App. Catal. A: General*, 191 (2000) 193
- [3] G.P. Lopinski, D.J. Moffat, D.D.M. Wayner and R.A. Wolkow, *Nature* 392 (1998) 909
- [4] M. Böhlinger, W.D. Schneider and R. Berndt, *Angew. Chem. Int. Ed.* 39 (2000) 792
- [5] M.O. Lorenzo, C.J. Baddeley, C. Muryn and R. Raval, *Nature* 404 (2000) 376
- [6] H.W.K. Tom, C.M. Mate, X.D. Zhu, J.E. Crowell, T.F. Heinz, G.A. Somorjai and Y.R. Shen, *Phys. Rev. Lett.* 52 (1984) 348
- [7] S.G. Grubb, A.M. DeSantolo and R.B. Hall, *J. Phys. Chem.* 92 (1988) 1419
- [8] B. Bourguignon, W. Zheng, S. Carrez, F. Fournier, M.L. Gaillard and H. Dubost, *Surf. Sci.* 515 (2002) 567
- [9] C.Schwab, G. Meister, J. Woll, A. Gerlach and A. Goldmann, *Surf. Sci.* 457 (2000) 273
- [10] H.W.K. Tom and G.D. Aumiller, *Phys. Rev. B*, 33 (12) (1986) 8818
- [11] G. Lüpke, D.J. Bottomley and H.M. van Driel, *Phys. Rev. B*, 49 (24) (1994) 17303
- [12] M.Y. Jiang, G. Pajer and E. Burstein, *Sur. Sci.* 242 (1991) 306
- [13] C. Matranga and P. Guyot-Sionnest, *J. Chem. Phys.* 115 (20) (2001) 9503
- [14] J. Bloch, G. Lüpke, S. Janz and H.M. van Driel, *Phys. Rev. B*, 45 (20) (1992) 12011
- [15] H. Ishida, R. Mizoguchi, K. Onda, C. Hirose, S.S. Kano and A. Wada, *Surf. Sci.* 526 (2003) 201
- [16] M.J. Crawford, S. Haslam, J.M. Probert, Y.A. Gruzdkov and J.G. Frey, *Chem. Phys. Lett.* 230 (3) (1994) 260
- [17] M. Kauranen, T. Verbiest, J.J. Maki and A. Persoons, *J. Chem. Phys.* 101 (1994) 8193
- [18] J.M. Hicks and T. Petralli-Mallow, *Appl. Phys. B*, 68 (1999) 589
- [19] S. Sioncke, S van Elshocht, T. Verbiest, A. Persoons, M. Kauranen, K. E. S. Phillips and T.J. Katz, *J. Chem. Phys.* 113 (17) (2000) 7578

- [20] R. Stolle, M. Loddoch and G. Marowsky, *Nonlinear Opt.* 8 (1994) 79
- [21] T. Verbiest, M. Kauranen, J.J. Maki, M.N. Teerenstra, A.J. Schouten, R.J.M. Nolte and A. Persoons, *J. Chem. Phys.* 103 (18) (1995) 8296
- [22] B.J. Burke, A.J. Moad, M.A. Ploizzi and G.J. Simpson, *J. Am. Chem. Soc.* 125 (2003) 9111
- [23] M.C. Schanne-Klein, F. Hache, A. Roy, C. Flytzanis and C. Payraastre, *J. Chem. Phys.* 108 (22) (1998) 9436
- [24] F. Hache, H. Mesnil and M.C. Schanne-Klein, *J. Chem. Phys.* 115 (14) (2001) 6707
- [25] F. Hache, T. Boulesteix, M.C. Schanne-Klein, M. Alexandre, G. Lemerrier and C. Andraud, *J. Phys. Chem. B*, 107 (2003) 5261
- [26] M.C. Schanne-Klein, F. Hache, T. Brotin, C. Andraud and A. Collet, *Chem. Phys. Lett.* 338 (2001) 159
- [27] C.F. McFadden, P.S. Cremer and A.J. Gellman, *Langmuir* 12 (1996) 2483
- [28] R. Zhang, A. J. Gellman, *J. Phys. Chem.* 95 (1991) 7433
- [29] Q. Dai, A. J. Gellman, *Surf. Sci.* 257 (1991) 103
- [30] I. E. Wachs, R. Madix, *Appl. Surf. Sci.* 1 (1978) 303
- [31] I. E. Wachs, R. Madix, *Surf. Sci.* 76 (1978) 531
- [32] R. Zhang, PhD Thesis, University of Illinois (1992)
- [33] J.M. Bonello, F.J. Williams and R.M. Lambert, *J. Am. Chem. Soc.* 125 (2003) 2723
- [34] J. M. Bonello, E.C.H. Sykes, R. Lindsay, F.J. Williams, A. K. Santra and R. M. Lambert, *Surf. Sci.* 482-485 (2001) 207
- [35] M. J. Stephenson and R. M. Lambert, *J. Phys. Chem. B*, 105 (2001) 12832
- [36] Q-M. Xu, D. Wang, L-J. Wan, C-L. Bai and Y. Wang, *J. Am. Chem. Soc.* 124 (2002) 14300
- [37] J. E. Sipe, D. J. Moss and H. M. van Driel, *Phys. Rev. B*, 35 (1987) 1129
- [38] L.T. Cheng, W. Tam, S. H. Stevenson, G. R. Meredith, G. Rikken and S. R. Marder, *J. Phys. Chem.* 95 (1991) 10631
- [39] L. T. Cheng, W. Tam, S. R. Marder, A. E. Stiegman, G. Rikken and C. W. Spangler, *J. Phys. Chem.* 95 (1991) 10631
- [40] P. Norman, D. Jansson and H. Ågren, *Chem. Phys. Lett.* 268 (1997) 337
- [41] T. Verbiest, S. van Elshocht, M. Kauranen, L. Hellemans, J. Snauwaert, C. Nuckolls, T. J. Katz and A. Persoons, *Science* 282 (1998) 913
- [42] X. Zhao, *J. Am. Chem. Soc.* 122 (2000) 12584
- [43] W. A. Hofer, V. Humblot and R. Raval, *Surf. Sci.* 554 (2004) 141

- [44] H. U. Blaser, H. P. Jalett, W. Lottenbach and M. Studer, *J. Am. Chem. Soc.* 122 (2000) 12675
- [45] A. Baiker, *J. Mol. Catal. A: Chemical*, 155 (1997) 473
- [46] R.L. Augustine, S. K. Tanielyan and L. K. Doyle, *Tetrahedron Asymmetry*, 4(8) (1993) 1803
- [47] J. L. Margitfalvi and E. Tfist, *J. Mol. Catal. A: Chemical* 139 (1999) 81

Summary and Forward Look

The contents of this thesis have focussed on the study of a number of model adsorbate systems covering a variety of topics interesting to both the surface science and wider communities. In this summary we repeat a brief description of the results presented here and consider possible future work in related areas.

In the initial work presented in Chapter 4, we have performed the first ever structural study of the aromatic molecule furan and its non-aromatic equivalent, THF, adsorbed on the Cu(111) surface. Using the technique of NIXSW we determine THF to adopt an atop adsorption site with an oxygen to copper distance of 2.39 ± 0.04 , while furan adopts a displaced atop position with a distance of 3.08 ± 0.08 . TPD is consistent with these results showing THF to have a significantly stronger interaction with the surface than furan. We propose the displaced atop adsorption site attributed to furan is due to the effects of adsorbate-adsorbate interactions, which would be significant in comparison to the weak furan to copper interaction. Furthermore, we conclude that the significantly stronger adsorption observed for the THF molecule is due to the effects of C-H...Cu interactions, analogous to hydrogen bonding, between THF and the copper surface.

This chapter is a continuation of a long-term interest in our lab in both oxygen containing species and heterocycles and builds on this body of previous work. While current interest in simple systems of this type has diminished in the surface science community, this chapter highlights the fact that the study of these systems can continue to be of interest and produce unusual results. Hence, current interests in our lab aim to combine structural work of this type along with the other areas explored in this thesis such as chirality to provide quantitative structural information alongside other experiments.

In Chapter 5 of this thesis we perform initial characterisation experiments of both the S/Cu(111) and DMS/Cu(111) systems. While much of the work presented in this chapter represents our own characterisation of work performed previously, in addition we perform for the first time work function measurements of both systems alongside the first TPD study of DMS desorption from Cu(111). In work function measurements we determine the presence of increasing amounts of S to result in a linear increase in work function prior to formation of the $(\sqrt{7} \times \sqrt{7})R19.1^\circ$ structure

where we observe a sudden increase. This is consistent with formation of a CuS like structure up to $(\sqrt{7}\times\sqrt{7})R19.1^\circ$ formation where the significant reconstruction observed then results in a sudden increase in work function.

In the case of DMS we observe the opposite effect in work function measurements with a decrease in work function associated with increasing surface coverage of methyl thiolate. This is consistent with a strong molecular dipole anti-parallel to the Cu surface and is consistent with theory. During the desorption of DMS from the surface we conclude formation of methyl thiolate takes place followed by subsequent methyl thiolate dissociation above 325 K signalled by the desorption of methane and ethane from the surface.

While we have added some interesting additional information to the study of both of these systems, even prior to our own work, both systems could be considered to be some of the most extensively characterised in surface science. Hence, few opportunities exist to explore these systems further. However, as is about to be discussed, both systems continue to produce interesting work in other directions such as when used as co-adsorbates.

Chapter 6 continues from the work just discussed in chapter 5 and examines the adsorption of crotonaldehyde, butaldehyde, crotyl alcohol and 1-butanol on Cu(111) along with the effects of co-adsorption with S and methyl thiolate. Previous catalytic experiments studying the hydrogenation of crotonaldehyde have observed increased selectivity to crotyl alcohol formation in the presence of S and this chapter examines the mechanisms involved. In this chapter we observe the presence of S on the Cu(111) surface at any coverage to stabilise the adsorption of all four molecules on the surface. Additionally, the presence of S also results in significant increases in packing density on the surface. In the presence of methyl thiolate a significantly different effect is observed. While no stabilisation effects are observed for either aldehyde molecule, we observe the almost complete destabilisation of both of the alcohol molecules from the surface. Based on these observations we propose an electrostatic model to account for both the work reported here and that observed in catalytic measurements.

This chapter shows the use of surface science techniques in the study of catalytic systems, which could have direct applications in industry, and demonstrates that surface science can be used to rationalise catalytic measurements. The study of this

hydrogenation process continues to be of significant scientific interest and therefore would warrant an extension of the work presented here possibly to include other surfaces and co-adsorbates. Additionally, this chapter highlights the possible benefits that could be gained by the combined use of both surface science and catalytic techniques in studying catalytic processes.

The work presented in Chapter 7 represents an area of significant current interest and has been studied extensively using a number of different techniques. However, despite this large body of work, the system continues to remain very controversial. Therefore, we have performed the first study of aluminium oxide formation on NiAl(110) to examine the whole oxidation process from initial stages through to multiple oxidation and annealing cycles. In this chapter, we show that oxidation at room temperature results in the formation of a predominately amorphous aluminium oxide film and a small γ -like Al_2O_3 component. However, oxidation at elevated temperatures results in formation of a γ -like Al_2O_3 film. Annealing of this layer to 1273 K results in significant changes to the structure, with formation of an α -like Al_2O_3 film. However, we believe this layer to be inhomogeneous. Further to this work we also show that during multiple oxidation and annealing cycles the layer retains α -like Al_2O_3 character, but that the amount of aluminium in the layer increases with each cycle. This is consistent with the filling of Al^{3+} vacancies in the oxide layer.

Due to both the complexity and interest in this system further study would be warranted and indeed is necessary to obtain a fully developed and consistent model. In addition to this, general interest exists in a variety of oxide structures, including this one, for potential uses in nanotechnology applications. The techniques used during the course of this thesis and indeed many other surface science techniques are ideally suited for the study of nanotechnology systems and this may represent a new and interesting field for future surface science studies.

Finally, Chapter 8 details initial results following development of a new surface science/optics system for the study of chirality on metal surfaces. Using this technique we have performed the first ever chiral discrimination measurements of the 2-butanol/Cu(111) and NEA/Cu(111) systems. In addition to chiral discrimination of the adsorbed molecules we also show for the first time that the presence of a chiral molecule, NEA, can induce a chiral image of the electronic structure of the metal surface.

Summary and Forward Look

Following the development of this system and the methodologies associated with it we now have a unique probe of chiral systems. With this in mind current work in our lab is focussed on further development of this technique. Full characterisation of the systems being used for future chiral studies will draw on a number of aspects and techniques discussed in this thesis already such as TPD, NIXSW and photoemission and will be followed by further chiral measurements examining both adsorbate molecules and their effects on the underlying substrate. This work should continue from where this chapter ends and provide a body of work interesting to a wide audience.